BNWL-768

~~OFFICIAL USE ONLY~~

[redacted]

QUARTERLY PROGRESS REPORT
JANUARY, FEBRUARY, MARCH, 1968
REACTOR FUELS AND MATERIALS DEVELOPMENT PROGRAMS
FOR
FUELS AND MATERIALS BRANCH
OF
USAEC DIVISION OF REACTOR DEVELOPMENT AND TECHNOLOGY

JUNE 1968

[redacted]

AEC RESEARCH & DEVELOPMENT REPORT

~~OFFICIAL USE ONLY~~

BATTELLE NORTHWEST
BATTELLE MEMORIAL INSTITUTE PACIFIC NORTHWEST LABORATORY
BATTELLE BOULEVARD, P. O. BOX 999, RICHLAND, WASHINGTON 99352

BNWL-768

INFORMATION CONCERNING USE OF THIS REPORT

PATENT STATUS

This document copy, since it is transmitted in advance of patent clearance, is made available in confidence solely for use in performance of work under contracts with the U. S. Atomic Energy Commission. This document is not to be published nor its contents otherwise disseminated or used for purposes other than specified above before patent approval for such release or use has been secured, upon request, from the Chief, Chicago Patent Group, U. S. Atomic Energy Commission, 9800 So. Cass Ave., Argonne, Illinois.

PRELIMINARY REPORT

This report contains information of a preliminary nature prepared in the course of work under Atomic Energy Commission Contract AT(45-1)-1830. This information is subject to correction or modification upon the collection and evaluation of additional data.

LEGAL NOTICE

This report was prepared as an account of Government sponsored work. Neither the United States, nor the Commission, nor any person acting on behalf of the Commission:

A. Makes any warranty or representation, expressed or implied, with respect to the accuracy, completeness, or usefulness of the information contained in this report, or that the use of any information, apparatus, method, or process disclosed in this report may not infringe privately owned rights; or

B. Assumes any liabilities with respect to the use of, or for damages resulting from the use of any information, apparatus, method, or process disclosed in this report.

As used in the above, "person acting on behalf of the Commission" includes any employee or contractor of the Commission, or employee of such contractor, to the extent that such employee or contractor of the Commission, or employee of such contractor prepares, disseminates, or provides access to, any information pursuant to his employment or contract with the Commission, or his employment with such contractor.

PACIFIC NORTHWEST LABORATORY
RICHLAND, WASHINGTON
operated by
BATTELLE MEMORIAL INSTITUTE
for the
UNITED STATES ATOMIC ENERGY COMMISSION UNDER CONTRACT AT(45-1)-1830

PRINTED BY/FOR THE U.S. ATOMIC ENERGY COMMISSION

54-1950-016 (4-68)
ARC-RL RICHLAND, WASH.

BNWL-768

UC-25, Metals, Ceramics
and Materials
Special Distribution

QUARTERLY PROGRESS REPORT
JANUARY, FEBRUARY, MARCH, 1968
REACTOR FUELS AND MATERIALS DEVELOPMENT PROGRAMS
FOR
FUELS AND MATERIALS BRANCH
OF
USAEC DIVISION OF REACTOR DEVELOPMENT AND TECHNOLOGY

By

J. J. Cadwell

D. R. de Halas

R. E. Nightingale

D. C. Worlton

June 1968

PACIFIC NORTHWEST LABORATORY
RICHLAND, WASHINGTON

PREVIOUS QUARTERLY REPORTS

Quarter	Year	Report Number
	1966	
First		BNWL-CC-694
Second		BNWL-CC-761
Third		BNWL-CC-821
Fourth		BNWL-CC-957
	1967	
First		BNWL-435
Second		BNWL-473
Third		BNWL-658
Fourth		BNWL-668

TABLE OF CONTENTS

SUMMARY

NUCLEAR GRAPHITE

The reaction of grey boronated graphite with water vapor yields B_2O_3 and H_2 in the temperature range 700 to 900 °C and at water-vapor concentrations from 2700 to 39,000 vpm. The B_2O_3 subsequently reacts with water vapor to form a volatile boric acid and is thereby removed from the sample surface. Only at the highest temperatures and water-vapor concentrations is any CO_2 observed in the reaction products.

Further efforts to characterize the nongraphitic lace networks produced in TSX and AGOT-LS graphites by oxidation in the glow region of microwave-excited oxygen have resulted in lace structures which can be melted above 700 °C. The extent of the melted areas expands until virtually all the lace is melted at 1100 °C.

Additional microwave-excited oxidations with TSX and AGOT-LS graphite in the glow region indicate that the transient species responsible for saw-tooth formation is removed as oxygen pressure is increased and that impurities present in the graphite influence saw-tooth structure formation. Oxidation downstream from the glow region do not result in saw-tooth formation and the rate, which is about 1/100th that in the glow region at ambient temperatures, has a greater temperature coefficient than the oxidation rate in the glow. The principal structures produced by downstream oxidation are pits and channels.

A simplified method of calculating the contribution to bulk properties of preferred crystallite orientation is described. The results for TSGBF and TSX graphite are given as examples of extrusion textures with rotational symmetry throughout. Crystallites parallel to the surface of the extrusion are superposed on the otherwise symmetrical texture.

The yield of radiolytic reactions in inert-gas-cooled reactors is primarily dependent upon the efficiency of energy transfer from the excited helium to any reactive impurity which is present. The efficiency of the energy transfer is being studied by investigating the quenching of emission of light from helium excited by 2 MeV protons. The quenching efficiencies of the helium transitions, $3^3S \rightarrow 2^3P$ and $3^1P \rightarrow 2^1S$, by N_2, CO_2, and CO have been measured, and the results are given.

The proof-test capsule series in the GETR was terminated. The H-3-27 capsule was discharged after exposure to 1.5×10^{22} nvt ($E > 0.18$ MeV), with capsule temperatures ranging from 550 to 1100 °C. Several improved isotropic graphites displayed good dimensional stability to exposures of 10^{22} nvt. An irradiation

experiment to determine the effects of sample size and a low compressive stress on the turnaround behavior of graphite was initiated.

Three different irradiation experiments are being carried out in two Hanford reactors to investigate the effect of sample size on irradiation-induced contraction of graphite. Data are available on TSX graphite from two of these experiments to a maximum fast-neutron exposure of 1.6×10^{21} nvt (E > 0.18 MeV). These data indicate that the large blocks (4 in. x 5 3/8 in. x 17 1/2 in.) are contracting 25 to 30% faster than the small samples (0.43 in. diam x 3 in. long and 0.43 in. diam x 6 in. long) for directions both transverse and parallel to the extrusion axis. Other experiments are being initiated to determine the causes of size-effect; these include X-ray determination of crystallite orientation and possibly a study to determine the effect of high-temperature irradiation preceded by a brief exposure at low temperatures.

The GEH-13-14 capsule irradiated at temperatures from 800 to 1300 °C in the ETR was discharged in February 1968 with a maximum accumulated exposure of 6×10^{21} nvt (E > 0.18 MeV). Damage appears to be accumulating faster at these high temperatures than at lower temperatures. Two types of isotropic graphites are exhibiting stable behavior. The capsule will be recharged in May; it should accumulate exposures approaching 10^{22} nvt before the next discharge in September 1968.

An improved model was developed for explaining thermal-expansion hysteresis in nuclear graphite.

FUEL DEVELOPMENT FOR GAS-COOLED REACTORS - HTGR GRAPHITE STUDIES

Surface-area changes have been measured on four samples of graphite irradiated to about 1.94×10^{21} nvt (E > 0.18 MeV) at an average temperature of 916 °C. The changes were almost insignificantly small. The graphite samples will be reirradiated to determine if significant changes occur at higher doses.

NUCLEAR CERAMICS

Development of methods for preparation of thin foils of nuclear ceramic materials for transmission electron microscopy has continued. Considerable improvement in thinning UO_2 results from a combination of mechanical thinning and chemical polishing.

A scanning electron microscope to study the surface features of nuclear ceramic and graphite materials has been ordered, and delivery is expected by May 1, 1968.

Compatibility testing of hypostoichiometric $(U_{0.75}Pu_{0.25})O_{2-x}$, both helium-and sodium-bonded to

type 304 SS, has been completed. After heating for 1000 hr at 650 and 1000 °C, no incompatibility between the mixed oxide and sodium or clad was evident. Carbothermically produced uranium-plutonium nitrides were also tested in sodium-bonded stainless steel. No evidence of reaction was seen after 1000 hr at 1000 °C.

Studies on the growth of crystals of PuO_2 and UO_2-PuO_2 for basic property measurements were continued with the initiation of studies of the electron-beam floating-zone growth of UO_2 encapsulated in tungsten and rhenium. Crystal growth in tungsten is complicated by the solubility of the tungsten in molten UO_2 and the subsequent precipitation of tungsten metal particles in the crystals. Rhenium appears to be insoluble in molten UO_2 and should serve as the best container material for further growth studies.

The thermal diffusivity of sintered $(U_{0.75}Pu_{0.25})O_{2\pm x}$ can be expressed as a function of temperature and oxygen-to-metal ratio by the empirical relationship

$$\alpha = [0.110\ T - 1086\ (O/M) + 2175]^{-1},$$

$$(cm^2/sec) \quad .$$

where the temperature, T, is in °C (100 to 1200 °C) and O/M is the oxygen-to-metal ratio (1.92 to 2.00). Comparison with results for both UO_2 and PuO_2 indicate that plutonium content has no measurable effect on thermal diffusivity of mixed uranium-plutonium oxides.

The thermal diffusivity and thermal conductivity of pneumatically impacted stoichiometric PuO_2 (93.3% TD) from 100 to 1650 °C can be expressed by the empirical relationships

$$\alpha = \frac{1}{0.105\ T + 1.20} \quad , \quad (cm^2/sec)$$

and

$$K = \frac{1}{0.0269\ T + 2.53} \quad , \quad (W/cm\ °K) \quad ,$$

respectively.

A fuel capsule characterizing molten-zone solidification-rate effects on oxide fuel structure and impurity distribution failed in the 100-KE Snout facility. The incident, which had no adverse effect on reactor operation, was apparently caused by inadequate outgassing of the fuel after it was exposed to an organic solvent. The possibility of recurrent failures from this source in subsequent irradiations will be avoided by outgassing the fuel at 1000 °C immediately prior to capsule assembly.

Facilities for measuring properties of liquid UO_2-PuO_2 are nearing completion. Techniques for measuring change in volume on melting and liquid density were developed. Apparatus for measuring viscosity by the oscillating crucible technique at temperatures to approximately 3000 °C was designed and built.

Apparatus for measuring the sound velocity in solids by both the phase-comparison method and by a low-frequency resonance technique have been assembled. Measurements on a

polycrystalline sample of UO_2 are in agreement with previous work.

The thermal diffusivity from 200 to 1600 °C, of a mixed uranium-plutonium nitride sample obtained directly from mixed UO_2–20 wt% PuO_2 by the carbothermic reduction process agrees (within experimental error) with that of a metal-hydride-derived specimen.

FAST-REACTOR NITRIDES RESEARCH

Procedures have been developed which allow the reproducible synthesis of nitride compositions containing ∿1000 ppm oxygen and ∿2000 ppm carbon with variations of less than ∿0.06 wt% of any anion. The tungsten particle-bed reactor system developed for this work appears to be capable of continuous, long-term service under present operating conditions.

Nitrides obtained by carbothermic reduction of oxides were sintered to densities between ∿86% and ∿94% TD. The general procedures developed for sintering metal-derived nitrides were applied to the carbothermic material; variation of carbon content between ∿0.2 and 0.6 wt% had no significant effect on sintering behavior. A composition change involving reduction of carbon and oxygen content as a result of sintering was noted; minimum oxygen and carbon levels of 0.18 and 0.10 wt%, respectively, were obtained.

Preliminary studies on an advanced carbothermic synthesis method for mixed nitrides, starting with uranyl nitrate hexahydrate and sugar mixtures, were continued. Data on gas/liquid mass ratio for optimum operation of the spray-calciner system were gathered. Homogeneous, uniform particulate mixtures of UO_2 and carbon were obtained with controlled carbon contents in the range required for carbothermic reduction.

NONDESTRUCTIVE TESTING RESEARCH

EDDY CURRENT METHODS

The principal objective of the eddy current multiparameter nondestructive test studies now in progress is to develop techniques to obtain needed information about test specimens that cannot be obtained by using the conventional single frequency eddy current test equipment.

Electronic circuits were developed for simplifying and standardizing the instrument design for multiple-frequency multiparameter eddy current testers.

THERMAL METHODS

The program to develop a remote transient method for determining

surface thermal impedance values was continued this quarter. An automatic system for obtaining the impedance values for various sample materials has been constructed, and analysis of the data obtained with the test system indicates that the test technique is sensitive to material variations.

ULTRASONIC METHODS

Propagation of ultrasonic pulses in attenuating media is being studied to further the understanding of basic behavior.

The influence of frequency and grain size on reflection and transmission factors is demonstrated graphically.

METALLIC FUELS

The long term irradiation of three Th–2.5 wt% U–1.0 wt% Zr tubular fuel elements continues in the P-7 pressurized, hot water loop in the ETR. The exposures range from 11,200 to 20,300 MWd/T with corresponding fuel volume increases from 1.7 to 3.8%. The elements continue to show excellent performance with no evidence of warping, bowing or distortion. The maximum exposure element has experienced more than 814 effective days of irradiation under power reactor conditions at maximum fuel temperatures between 350 and 600 °C. In addition these elements have been removed from the reactor after each reactor cycle for interim examination in the reactor basin. The remarkable stability of these fuel elements under extreme conditions makes the Th-U alloy tubular fuel element a prime candidate for reactors requiring stable high exposure fuel.

Thirty-five hollow core uranium fuel elements 0.45 in. diam by 6.25 in. long and coextrusion clad with Zry-2 have been sucessfully irradiated in the ETR-M3 loop facility to rod average exposures ranging from 743 to 8740 MWd/T. These elements have 0.025 or 0.050 in. thick Zry-2 cladding and central voids of 5, 10, or 20% of the fuel volume. Interim examinations made in the ETR basin after each reactor cycle show that all the fuel elements have an accumulated volume decrease ranging from about -0.07 to -3.6%. Diameter measurements completed on 24 of the elements show both positive and negative changes, most changes being within the experimental error of the measurements. Micrometer measurements of fuel rod lengths made in the ETR canal indicate that up to 0.97% decreases in length have occurred. Sufficient length data have not been accumulated to establish a direct correlation of length change with volume change.

BASIC SWELLING STUDIES

Capsules P-11 (550 °C, 5000 psi, 0.27 to 90 at% BU) and P-18 (825 °C, 30 psi, 0.16 to 1.12 at% BU) were discharged after completing successful irradiations.

Detailed metallographic examination of high purity uranium specimens irradiated at 5000 psi to 0.22 at% BU at 450 °C and 0.82 at% BU at 425 to 430 °C, respectively, revealed that swelling is caused by microtearing and possibly fission gas porosity.

Postirradiation annealing of irradiated uranium at 900 °C for 100 hr in a vacuum resulted in a 31 to 33% volume increase, while heating to 1082 °C for three hours produced a 45 to 46% volume change. It has also been shown that heating irradiated uranium at 600 °C in a vacuum produces little or no volume change when the driving force for recrystallization is removed.

Two papers were presented at the 97th Annual Meeting of the AIME in New York City, which was held on February 26 to 29, 1968:

1. "Fission Gas Pores in Postirradiation Annealed Uranium" by R. D. Leggett, T. K. Bierlein, J. L. Brimhall and B. Mastel.
2. "Fission Gas Induced Swelling in Uranium at High Temperatures and Pressures" by G. L. Kulcinski, R. D. Leggett and C. R. Hann.

ATR GAS AND WATER LOOP OPERATION AND MAINTENANCE

PNL is proceeding with R&D programs designed to assist the various GCL vendors in their fabrication problems. In addition, work is underway to assist the AE and AEC in the acceptance standards required for the components in the vendors' plants.

Water chemistry for the ATR water loop is being completed. Test specimens and hanger rods are being prepared for startup of the ATR. A program document outlining the various tests to be completed in the water cooled loop is being published.

REACTOR FUELS AND MATERIALS

FAST-REACTOR DOSIMETRY AND DAMAGE ANALYSIS

SAND-II solutions for an EBR-II low-power reactor run show that the multiple-foil activation technique is well suited for fast-reactor flux and fluence measurements. In addition, the multiple-foil activation method has been used to obtain an evaluated differential cross section curve for the $^{27}Al(n,\alpha)^{24}Na$ reaction. Preliminary results indicate a fission-spectrum-averaged cross section of 0.764 mb.

Point-defect calculations for interstitial atoms in copper have been made by using a Morse potential modified to include up to third or fourth neighbor atoms. The ordering of energies for five interstitial

configurations is the same as found by using an unmodified Morse potential, although energy differences are larger. For all potential forms, the calculations yielded the result that the <100> split configuration is the most stable.

The correlated motion of vacancies has been introduced into the annealing simulation code ANNEAL, to make it applicable at elevated temperatures. The amended code is presently being checked out.

Calculations of binding energies are consistent with the suggestion that Stage III (150 C) annealing in irradiated molybdenum involves molybdenum interstitial atoms trapped by iron impurity atoms. Calculations using the DEFECT code yield 1.34 eV for the binding energy. The measured activation energy for Stage III annealing is 1.2 to 1.3 eV.

IRRADIATION DAMAGE TO REACTOR METALS

REACTOR METALS RESEARCH

Alloy Selection

A 500 lb quantity of 1/2 in. diam SS rod of alloy FV-548 has been obtained from Firth Vickers Stainless Steels, Ltd., England. Procurement of tubing material from the same heat as the rod is under negotiation.

Continuing the GE-APED superheat fuel-clad materials investigations, thermally aged controls for the alloy groups irradiated in the GETR were tensile tested at 704 °C. Results are compared with the tensile properties of the irradiated material.

Irradiation Facilities Operation

A total of 182 specimens were discharged from the ETR at the conclusion of Cycles 93 and 94. The variety included tensile, creep, charpy impact, DCB (double cantilever beam), thin foils, stress-to-rupture, and corrosion specimens.

Tensile data reports have been recorded, processed, and stored in the REM (Radiation Effects on Metals) computer program for 5506 individual tests.

Irradiation Damage to Stainless Steels

Annealed and cold-worked 348 SS irradiated in the G-7 loop to a fast fluence of 8.1×10^{21} n/cm^2 (E > 1 MeV) has been tested. The yield strengths are increased for irradiated specimens in the annealed condition at all test temperatures. The ductility is very low.

The tensile data on martensitic 410 SS irradiated at 60 and 290 °C are compiled.

Electron-Microscopy of ETR-Irradiated Stainless Steel

The electron microscopy examination continued on AISI type 304 SS irradiated in the ETR to 6×10^{21} n/cm^2

(E > 1 MeV) at 290 °C. The cavities, which are sufficient to cause the observed high temperature hardening, persist to the highest postirradiation heat treatment temperature, 1090 °C. Observations indicate that the cavities are stabilized and in equilibrium with the surface tension. However, the amount of helium gas produced by transmutation was less than one-tenth the amount required to balance the surface tension of the cavities. The same irradiated 304 SS was given a high-pressure high-temperature anneal and examined by electron microscopy. Preliminary analysis of the electron micrographs of the irradiated steel having the high-pressure high-temperature anneal showed that approximately 2×10^{13} cavities/cm^3 with an average diameter of 700 Å were still present. The results definitely indicate that the cavities do not respond like voids, but behave like gas-filled bubbles.

Irradiation Damage to Nickel-Base Alloys

Preliminary data from stress-rupture tests at 1350 °F on specimens of Hastelloy X-280, Inconel 600, and Inconel X-750 after irradiation at 1250 °F to a fast fluence of approximately 1×10^{20} n/cm^2 showed reductions in rupture life compared to controls ranging from a factor of 10 for Hastelloy X-280 and Inconel 600 to a factor of 300 for Inconel X-750.

Corresponding reductions after irradiations at 540 °F were only about a factor of three for all three alloys. The higher reductions after the 1250 °F irradiation are probably indicative of effects of combined thermal and irradiation-induced instabilities.

In-Reactor Measurements of Mechanical Properties

In-reactor and unirradiated control creep tests conducted on AISI Type 304 SS both showed similar discontinuous yielding upon loading. The in-reactor test fractured at 13% strain while the control test is still in progress.

A faster creep rate was measured for an annealed Zry-2 in-reactor creep test conducted at 315 °C and 10.6 kg/mm^2 (15,000 psi) stress than for a corresponding unirradiated control test.

In-reactor creep data for Zr–2.5 wt% Nb between 14- and 32-kg/mm^2 stress show little, if any, dependence of the creep rate on stress at 300 °C.

Grain Boundary Stabilization

A study of recrystallization and grain growth in metals containing small concentrations of inert gas has recently been initiated.

An apparatus for injecting helium atoms into nickel powder by ion bombardment has been set up and operated. The amount of helium introduced is dependent upon the time of bombardment and the potential used.

Nickel powder samples, with and without helium, are being compacted under different conditions, and the

recrystallization and grain growth characteristics of these materials will be investigated.

Fracture Studies

Fracture mechanics studies of A533-B quenched and tempered 12 in. plate material were initiated. The initial studies are directed at determining size effects of the Double Cantilever Beam specimen. Fracture toughness measurements at the 1/2 T position of this plate for 1/2 and 1 in. thick specimens yielded basic results whereby size criteria of the DCB specimen can be ascertained.

Heavy Section Steel

A paper entitled, "Dynamic Changes in the Internal Stress Fields of High Purity Iron", was presented at the AIME Annual Meeting in New York, February 26 to 29, 1968.

Work in progress, relating fracture toughness to work hardening behavior in the neighborhood of a crack tip, is described.

High Pressure Studies

The purpose of this phase of the program is to study the effects of ultra-high pressures (1,000 to 60,000 bars) on the production, retention, and subsequent microscopic configuration of the damage produced in irradiated solids. In addition, the high pressure synthesis of new phases and the high pressure alteration of mechanical properties will be investigated as possible methods of providing more radiation damage resistant materials for nuclear reactors.

In-Reactor Corrosion of Zirconium Alloys

Three lots of Zry-2, previously characterized in the Engineering Test Reactor G-7 loop in pH-10 LiOH, $\sim$1 ppm O_2, were exposed in the G-7 loop in pH-10 NH_4OH <0.05 ppm O_2. In-flux corrosion rates were only slightly accelerated on as-etched specimens. Corrosion rates were accelerated on all prefilmed specimens, but the response varied with prefilm treatment. In-flux hydrogen pickups were relatively low except on a specimen having a thick ($\sim$250 mg/dm^2) prefilm oxide.

FAST REACTOR SUPPORTING STUDIES

Fast Neutron Mechanisms

Nonisothermal gas evolution techniques have been developed and used to investigate the temperature-sensitive hydrogen effusion characteristics of the austenitic stainless steels over the 200 to 900 °C temperature range. The observed gas evolution behavior is not representative of a simple, matrix-diffusion controlled effusion process, and it is sensitive to small differences in alloy composition. In addition, cold-working significantly alters the normal effusion characteristics and appears to facilitate the gas evolution process.

EBR-II Irradiations

The effects of swelling in austenitic stainless steel induced by fast reactor exposure near one half the absolute melting point are being investigated. The greatest decrease in density measured to date is 0.34% for AISI 304L irradiated to 2.7×10^{22} n/cm^2 total EBR-II fluence near 800 °F.

Fuel Cladding Characterization

The purpose of this program is to determine the lot to lot variation of selected mechanical properties in two lots of AISI 304 SS tubing. The large number of biaxial tests to be run has necessitated a further modification of the CANEL test stands.

Structural Materials and Fuel Cladding Studies

Biaxial stress-to-rupture tests have been performed on FFTF prototype fuel clad material representing the as-received (slightly cold-worked) and annealed conditions of AISI type 304 SS. The test environment was 1400 °F (760 °C) helium.

Rupture strain for the as-received material was consistently greater than for the annealed material. The highly duplex grain size of the annealed material is noteworthy in comparison to the regular and somewhat finer grain size of the as-received condition.

Test Facilities

Construction is approximately 85% complete on a facility to test irradiated-and unirradiated-candidate structural and cladding materials in sodium and controlled gas atmosphere for the FFTF program. The transformer supplying power to this building will be moved next to the building. The three tests so far completed after alignment showed that the test frames have less than 10% bending moment.

A furnace liner containing sodium has been placed in service on the air environment creep test equipment to provide a longer uniform temperature hot zone in the test furnace. A test temperature of 1200 °F ± 1 °F and temperature gradient of ± 0.5 °F along a 2 in. sample was maintained during 500 hr of testing. The ASTM recommended specification for temperature control and temperature gradient at 1200 °F is ± 3 °F. Acceptance tests were carried out on the liquid metal loop in accordance with manufacturers recommendations. This section contains one unshielded test loop for test of prototype assemblies and control samples. An inert atmosphere glove-box for handling high purity alkali metals has passed the specified performance tests and will be shipped. A problem has been encountered in transferring and measuring sodium under reduced cover gas pressures in that dissolved helium must be outgassed from the liquid sodium before accurate measurements can be made.

NUCLEAR GRAPHITE

R. E. Nightingale

REACTION OF BORONATED GRAPHITE WITH WATER VAPOR

O. R. Sheard and R. E. Woodley

The use of boronated graphite as a control rod or shielding material in nuclear reactors requires a knowledge of its compatibility with other components of the reactor environment. Gases that can react with boronated graphite--thereby reducing its boron content and, hence, its neutron-absorbing properties--should normally be excluded from the reactor system. However, in practical reactor systems, gases such as water vapor are often unavoidably present in the atmosphere and their reactions with boronated graphite must, therefore be understood.

The reaction of grey boronated graphite with water vapor in helium has been studied over the temperature range from 700 to 900 °C with water-vapor concentrations from 2700 to 39,000 vpm. The reaction ordinarily takes place in two steps:

$$B_4C + 6H_2O \rightarrow 2\ B_2O_3 + C + 6H_2 \qquad (1)$$

and

$$B_2O_3 + H_2O \rightarrow \text{a volatile boric acid} \qquad (2)$$

The sample weight increases as molten B_2O_3 is formed by Reaction (1); but, as the thickness of the B_2O_3 layer increases, the rate of Reaction (1) rapidly decreases, as does the concentration of H_2 in the effluent gas. With the formation of B_2O_3, Reaction (2) commences and eventually a steady state is attained wherein the rates of formation and removal of B_2O_3 are equal. At this point, the sample weight decreases at a constant rate, and the concentration of H_2 in a flowing gas remains constant. The volatile boric acid condenses on the cooler downstream surfaces of the reaction vessel, including the sample suspension wire and makes continuous weight measurement impossible.

Under the most extreme reaction conditions investigated (i.e., $T \geq 850$ °C and $[H_2O(g)] = 39{,}000$ vpm) and only under these conditions, small concentrations of CO_2, amounting to about 30 vpm, were found in the effluent gas. It is not known whether this CO_2 arises from the oxidation of the graphite or the B_4C. It is very interesting, however, that the presence of boron almost completely inhibits the oxidation of graphite under conditions where the oxidation rate would normally be appreciable. Under the less extreme conditions of oxidation, no oxides of carbon are observed and the only gaseous product detected chromatographically is the H_2 resulting from Reaction (1).

ELECTRON MICROSCOPY STUDIES OF GAS-GRAPHITE REACTIONS

S. S. Jones

Although much effort has been expended upon the study of kinetics of

gas-graphite reactions, very little has been done to elucidate the microstructural changes that occur; the few studies conducted so far have dealt exclusively with single crystals. This study is designed to investigate the microstructural changes that occur during reactions of polycrystalline graphite, thus giving an increased understanding of the reactions occurring in a reactor environment.

Further efforts have been made to characterize the nongraphitic lace networks produced in TSX and AGOT-LS graphites by oxidation in the glow region of microwave-excited oxygen. Data were presented in an earlier Quarterly Progress Report[1] that indicated that these networks were very resistant to change by heat or thermal oxidation at 700 °C. More recently, this investigation has been continued by heating to temperatures up to 1100 °C in increments of 100 °C for approximately 10 to 15 min at each temperature. While very little change was observed at 700 °C, essentially all of the lace melted to form spherical globules at 1100 °C. Various sections of the lace melted at lower temperatures, and the extent of the melted area expanded until virtually all lace was melted when the temperature finally reached 1100 °C. The change in appearance of a typical lace area in AGOT-LS graphite as the temperature was increased is shown in Figures 3.1 through 3.5. The specimen for this experiment was prepared by an oxidation in microwave-excited oxygen which removed sufficient graphite to reveal the lace structures. Since the melted impurities were first made visible by an oxidation treatment, there was some concern as to whether the oxidation process had changed the oxidation state of these impurities. Further data on this subject were obtained by first heating an unoxidized meachanically-prepared disk specimen of AGOT-LS to 1100 °C and then observing the cooled specimen for evidence of previously melted impurities. While only small impurity areas could be observed in such a specimen, it was clear that the melting point of these impurities had been exceeded by this thermal treatment of the unoxidized specimen. Therefore, some relatively low-melting impurities must be present in the original AGOT-LS graphite. In fact, it was found recently that some of these impurities are sufficiently volatile to collect in the cooler ends of the oxidation tube following the high-temperature melting experiments. Thus, there is considerable evidence that at least some of the volatile impurities in AGOT-LS graphite remain even though the graphite was treated at a temperature of 2800 °C in the production process. Evidently, such volatile materials are trapped in the pore structure of large pieces of graphite during manufacture.

Additional microwave-excited oxidations have been done with TSX and AGOT-LS graphite in an attempt to get more detailed information about the features of oxidation attack in the glow region and downstream from the glow. In earlier

8,880X

FIGURE 3.1. Lace Network Impurity Areas in AGOT-LS Graphite Exposed to View by Removal of Graphite at Low Temperature with Glowing Microwave-Excited Oxygen and Followed by Thermal Treatment at 700 °C

FIGURE 3.2. Same Area as in Figure 3.1 but with Additional Thermal Treatment at 800 °C

8,880X

FIGURE 3.3. Same Area as in Figure 3.2 but with Additional Thermal Treatment at 900 °C

FIGURE 3.4. Same Area as in Figure 3.3 but with Additional Thermal Treatment at 1000 °C

FIGURE 3.5. Same Area as in Figure 3.4 but with Additional Thermal Treatment at 1100 °C

experiments, it was shown that the oxidation rate within the glow region varies approximately in direct proportion to oxygen pressure, and that the saw-tooth structure formation is enhanced by a positive charge on the specimen being oxidized. It has now been found that the formation of saw-teeth is greater at lower oxygen pressure (100 to 200 μ as contrasted with 500 to 1000 μ). Thus, it appears that a transient negatively charged species is responsible for tooth formation and that the concentration of this species is diminished, possibly by charge neutralization or by recombination, as the oxygen pressure is increased.

Further oxidations have been done in the microwave glow region to determine the influence of specimen location and the level of impurities present on the structural changes produced. While the rate of oxidation attack varied with the intensity of the glow in different parts of the glow region, no other significant change with respect to position was found. However, it was observed that impurities present in the graphite do affect saw-tooth structure formation. Saw-teeth always form more extensively in TSX than in AGOT-LS for the same degree of burnup. In the same graphite, either TSX or AGOT-LS, saw-tooth formation is less extensive at high burnup than at low burnup. Since the only difference between the two graphites is the substantially higher level of impurities in AGOT-LS, such impurities apparently tend to suppress saw-tooth formation in any part of the specimen where they occur in high concentration. Examination of the teeth themselves reveals, almost without exception, a small quantity of lace structure at the tooth tip (Figure 3.6). This lace can be melted by heating the specimen to 1100 °C in the same manner as that described above. Thus, it appears that a small element of impurity at the tip of all tooth structures is influential in the formation of such structures. Perhaps, by inhibiting oxidation at its immediate location, an element of impurity can cause the oxidation process to take place in such a controlled manner as to produce the observed structures.

Saw-tooth structures are not formed under the oxidizing conditions that exist downstream from the microwave glow region. At ambient temperatures, the downstream oxidation rate is about 1/100 of that in the glow region, and this rate difference can be reduced significantly by increasing the temperature for downstream oxidations. There appears to be a much lower temperature coefficient for oxidation in the glow itself. An effort has been made to compare microstructural changes in the glow region with those downstream from the glow at approximately the same specimen burnup. This burnup was restricted to the order of 1% weight loss due to low downstream oxidation rates. The principal structural feature observed from oxidations immediately outside the downstream boundary of the glow region is pit formation (Figure 3.7). The pits appear to decrease in concentration as the distance downstream increases. This microstructural

72,000X

FIGURE 3.6. Early Stage of Saw-Tooth Formation in TSX Graphite After Oxidation in Glowing Microwave-Excited Oxygen to the Extent of 1/2% Weight Loss Showing Tooth Structures Perpendicular to Plane of Page with Impurity Element in Tip of Each Tooth

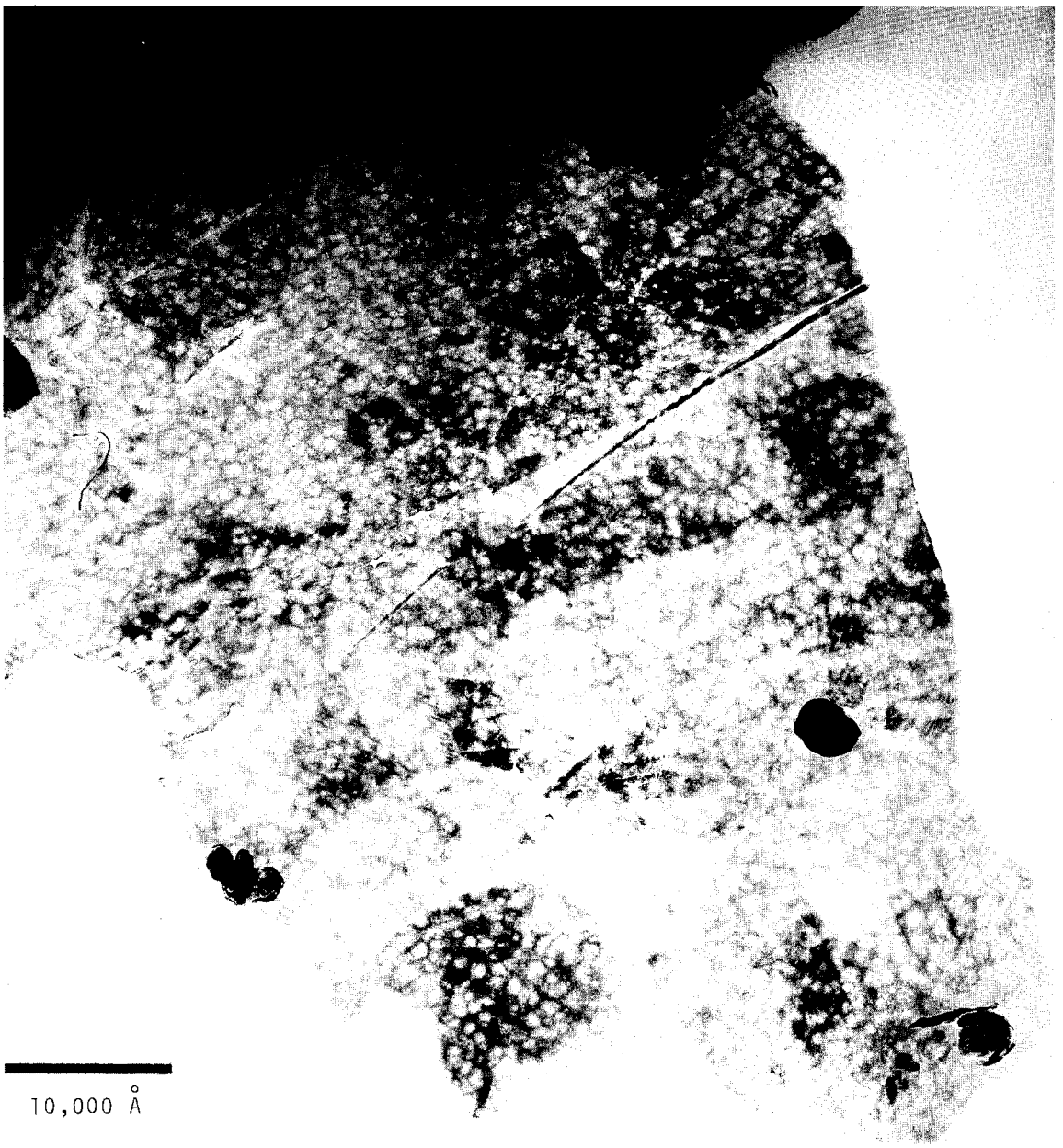

26,400X

FIGURE 3.7. Pit Formation in TSX Graphite Produced by Oxidation Immediately Downstream from Glowing Microwave-Excited Oxygen and Believed To Be Due to Oxygen-Atom Attack

change may be due to oxygen-atom attack. As the downstream distance increases and pit concentration is reduced (the pits also appear larger in diameter), channel formation is the most pronounced structural change (Figure 3.8). This form of oxidation attack seems to involve preferred oxidation at crystallite boundaries, and the principal oxidant may be ozone. The oxidation rate is increased with temperature and 2% burn-up is obtained with a TSX specimen in 1 hr at 500 °C. For unknown reasons, one AGOT-LS specimen incurred less than 1/2% weight loss by the same treatment.

X-RAY DIFFRACTION

P. G. Pallmer

The crystallite orientation of graphite is of interest because the directional properties, such as thermal expansion and radiation-induced dimensional changes, are directly related to the contributions of the individual crystallites to that property. The crystallite orientation is the basis for the study of orientation dependence of these properties and their modification by intercrystalline interations.

An intensity function, obtained by X-ray diffraction, measures the proportion of crystallites having the direction of the perpendicular to their layer planes within a particular solid angle. The form of the numerical or analytical integration of the contribution of the crystallites to a vector property in a given direction is well known,[2] but it is not necessarily convenient to carry out. A bulk property such as thermal expansion, α, would be related to the single-crystal properties α_a and α_c and the orientation parameter, R, by the equation

$$\alpha = \alpha_c + (\alpha_a - \alpha_c)R \quad .$$

If a simple analytic expression for the intensity distribution is not available, a point-by-point calculation and graphical integration are required. This procedure has been simplified by recognizing that the integral functions utilize the polynominal $P_2(\cos \phi)$ and an averaging or normalizing constant term, P_0, where

$$P_2 = 1/2(3 \cos^2 \phi - 1) \quad .$$

The value of P_2 varies from 1.0 at the axial direction to -0.5 in the transverse direction. The use of uniform intervals on the normalized coordinate $\cos \phi$, rather than the angle ϕ, is a further simplification inherent in this method. Because of the orthogonal characteristic of the functions, only those two components of the intensity distribution need be used. A graphical approximation is generally adequate for cases of rotational symmetry, while accurate values are easily obtained for any less symmetric or irregular distributions of intensity by a I(x) summation of the product $I(x) \cdot P_2(s)$. The integral orientation parameter is

8,880X

FIGURE 3.8. Channel Formation in AGOT-LS Graphite Produced by Oxidation Downstream from Glowing Microwave-Excited Oxygen Possibly Due to Ozone Attack

directly obtained from the magnitudes a_2 and a_o of the components as

$$R_z = 2/3(1 - a_2/5a_o) \quad .$$

The intensity distributions of extruded bars of TSX and TSGBF were measured by use of a pole-figure attachment to the X-ray diffractometer. The needle-coke filler of the TSX graphite had both a greater overall orientation and a subsidiary orientation toward the surface of the extrusion.

The orientation in a TSGBF graphite bar showed nearly exact rotational symmetry throughout. The complete orientation can be depicted by a polar plot (Figure 3.9) of the magnitude of the diffracted intensity from the (002) planes, or the c-axis direction, with angles measured from the extrusion direction as rotation axis. These values approximate the function 0.83 - 0.32 $P_2(\cos \phi)$ plotted in Figure 3.10. The compensating plus or minus deviations from the calculated values are immaterial for calculating the orientation parameter, but the closeness of fit indicates a simple mechanism for orienting grains in the extrusion process. The orientation parameter R, which is 2/3 for randomly oriented aggregates, was 0.72 in the extrusion direction and 0.64 in the transverse direction for TSGBF graphite.

TSX graphite with a fine-grain needle-coke filler shows greater anisotropy than the TSGBF, and near the surface of the extrusion the crystallites tend to align parallel to the surface. The variation of c-axis orientation in the transverse as well as two perpendicular longitudinal planes is depicted in Figure 3.11 by an isometric view of one octant bounded by the principal planes. At the center of the extrusion, there is no unique transverse direction and rotational symmetry is more closely approximated. The variations of all three perpendicular orientation parameters are shown in Figure 3.12.

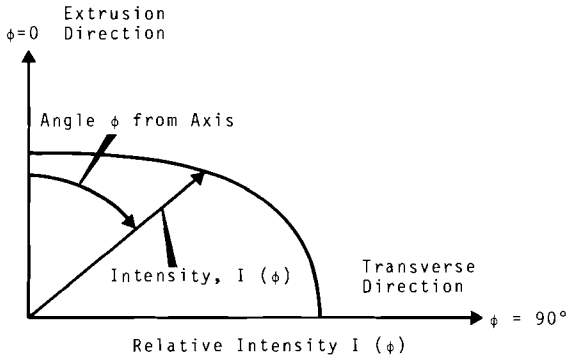

FIGURE 3.9. Variation of Defracted X-ray Intensity with Angle for TSGBF Graphite

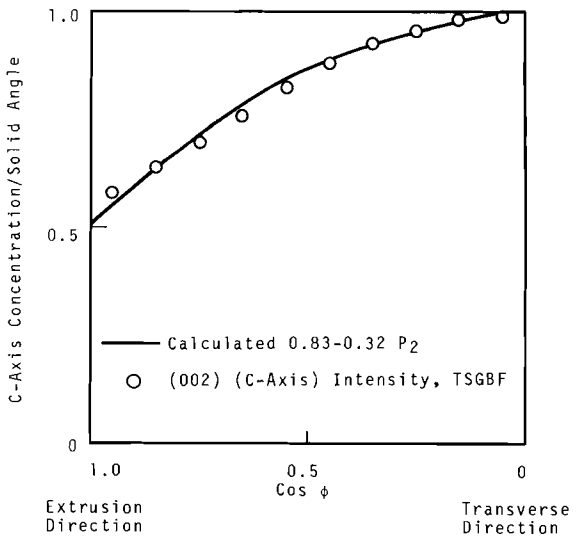

FIGURE 3.10. Crystallite Orientation in TSGBF Graphite Normalized to Unit Solid Angle

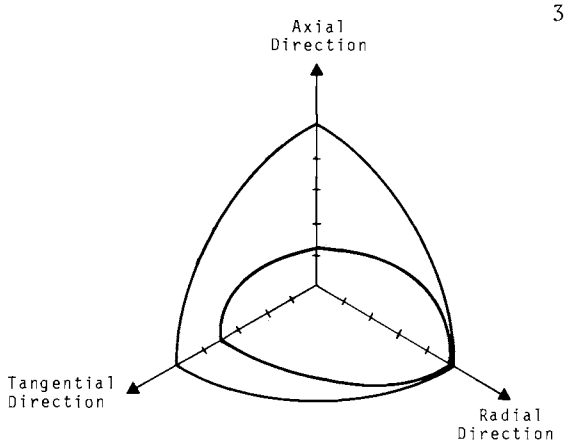

FIGURE 3.11. Crystallite Orientation near the Surface of a Bar of TSX Graphite

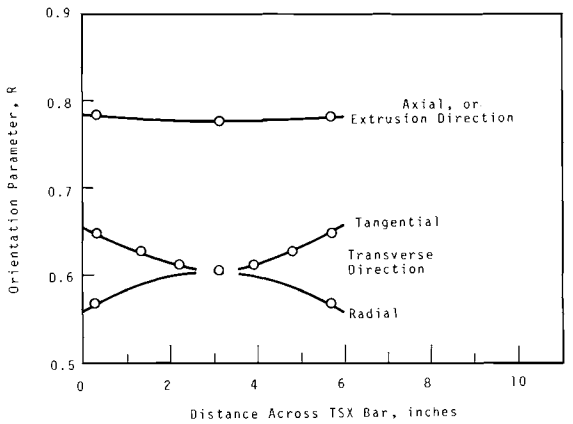

FIGURE 3.12. Orientation of TSX Graphite Extrusion

INERT-GAS-SENSITIZED RADIOLYSIS STUDIES

E. D. Jenson, R. L. Simons, and G. L. Tingey

Chemical reactions induced by radiation are of major importance in nuclear reactors. Although in many cases, the radiation chemistry of a reaction is fairly well understood in the pure reactant, a distinct gap does exist in the available information concerning the reaction when it occurs in the presence of large quantities of inert gas. The work reported here is being conducted to obtain information on the energy exchange from radiation-excited helium to impurities that may be present in the helium atmosphere of nuclear reactors. The apparatus and experimental procedures have been described earlier.(1)

The gas-leakage problems have been reduced, and the vacuum system is now capable of 10^{-6} mm Hg. Outgassing at this pressure overnight and passing the helium (nominally 99.9999% pure) through a molecular-sieve trap at liquid nitrogen temperatures have reduced the background emission to low levels. Even this treatment, however, is insufficient to completely remove nitrogen emissions. N_2^+ first negative bands at 5865, 5228, and 4709 Å are observed with intensities of 7, 30, and 470, respectively (on a scale of 1000). (The 4709 Å band head with an intensity of 470 is probably due mostly to the contribution of helium emission line on which it is superimposed.) In addition, two band systems at 5468 and 5506 Å, with intensities of 78 and 150 and degraded toward the red, are presently unidentified. A neon line at 5854 Å with an intensity of 230 is also observed.

The technique of studying the energy transfer is to monitor the light emission from a single helium line in a flowing gas system while the concentration of impurity gas changes. Helium is excited by exposure to a 1.5 to 2.0 MeV proton beam from a Van de Graaff positive-ion accelerator. De-excitation and neutralization of the helium then occur by light emission, collisions

with walls, free electrons or other helium atoms, and other means. In the presence of an impurity, gas de-excitation or quenching also occurs by collision and transfer of the energy to the impurity. Consequently, the emission of light from helium is reduced in the presence of impurity. In these studies, impurity gas is introduced into the helium stream by switching a helium stream through a tube, previously filled with the contaminant gas, into a magnetically stirred mixing chamber and then into the sample cell. Dilution of the contaminant occurs exponentially with time at a rate depending on the helium flow rate and the volume of the mixing chamber. The intensity of light emission from helium decreases when the impurity is introduced, and builds back up to its original intensity as the contaminant concentration approaches zero. Plotting the ratio of light intensity at zero contaminant concentration to that in the presence of contaminant for a given emission line-versus-impurity concentration gives a straight line whose slope is the ratio of the rate constants for emission to that for quenching.

A kinetic description of the process is as follows:

Quenching of Helium Emission by Added N_2, CO, and CO_2

Transition/ Quenching Gas	k_3/k_2 (ppm^{-1}) N_2	CO	CO_2
3^1p-2^1S (5016Å)		4.2×10^{-5}	5.1×10^{-5}
3^3S-2^3P (7065Å)	1.5×10^{-4}	1.4×10^{-4}	3.2×10^{-4}

He* represents all excited and ionized states produced by the proton beam, and He*i represents a selected excited state of helium. The average intensity, I_{imp}, of emission between proton bursts is given by $k_1(i)k_2/(k_2 + k_3[A])$ or $k_1(i)/\{1 + (k_3/k_2)[A]\}$, where $k_1(i)$ is the rate of formation of He*i by all modes and [A] is the concentration of impurity. When this expression is divided into that for no impurity present, [A] = 0, the following expression results: $I_o/I_{imp} = (1 + k_3/k_2)[A]$. Figure 3.13 shows a plot of I_o/I_{imp} as a function of [A]. A summary of qunching/emission-rate constants, k_3/k_2, obtained to date is given below.

Helium excitation	$He \xrightarrow{k_1} He^*$	(1)
Helium de-excitation	$He^*i \xrightarrow{k_2} He + h\nu$	(2)
Quenching	$He^*i + A \xrightarrow{k_3} He + I^*$	(3)

The total rate of loss of energy from the excited helium (emission plus quenching) is given by the sum of the rate of Reactions 2 and 3. The fractional emission intensity at a given contaminant concentration is given by

$$\text{Fractional emission} = I_{imp}/I_o = (1 + k_3/k_2[A]).$$

Figure 3.14 shows the relationship between concentration and percent quenching for carbon monoxide on the 5016Å (singlet) and 7065Å (triplet) emission lines.

From Figure 3.14, it is evident that although the ratio of the energy transferred from the excited singlet and triplet is constant for low concentration of CO, this ratio changes

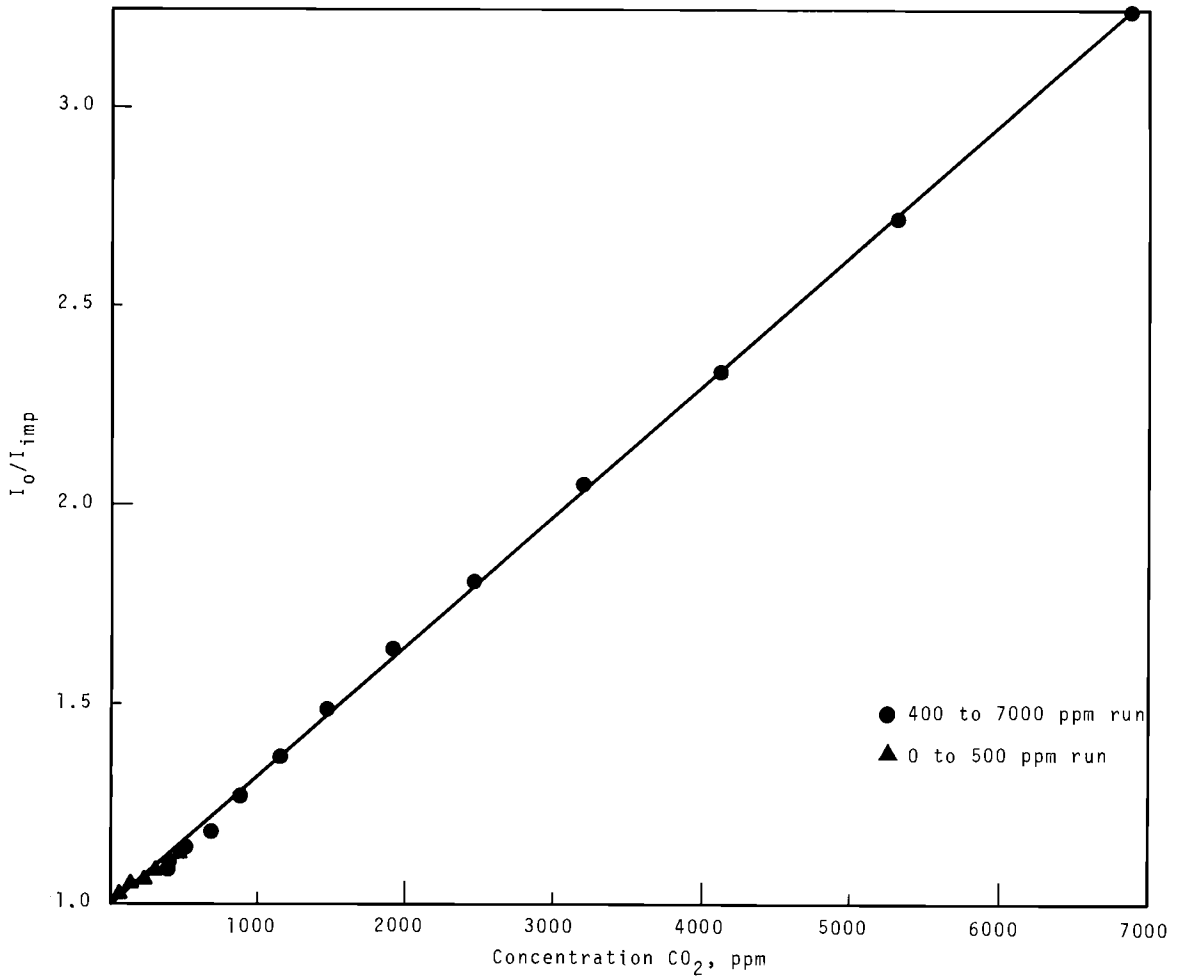

FIGURE 3.13. Quenching of the Helium Transition $3^3S \rightarrow 2^3P$ (7065 Å) by CO_2

and approaches one at higher CO concentrations. This change illustrates a property that may be very significant to radiation chemistry in general. Energy transferred from different excited states in an inert gas will likely excite the reactive molecule in different fashions and, thus, may produce different chemical reactions. Since the relative amount of energy transferred from various excited states is shown to be dependent upon the concentration of the reactive gas, the course of a radiolytic process may be likewise changed by varying that concentration. Further work is underway to investigate the energy transfer from other excited states of helium.

GRAPHITE IRRADIATIONS IN GETR

A. L. Pitner

The proof-test capsule series in the GETR was terminated after a maximum exposure of 1.5×10^{22} nvt (E > 0.18 MeV) had been accumulated on some samples. Irradiation temperatures ranged from 550 to 1100 °C, and several significant results were obtained.

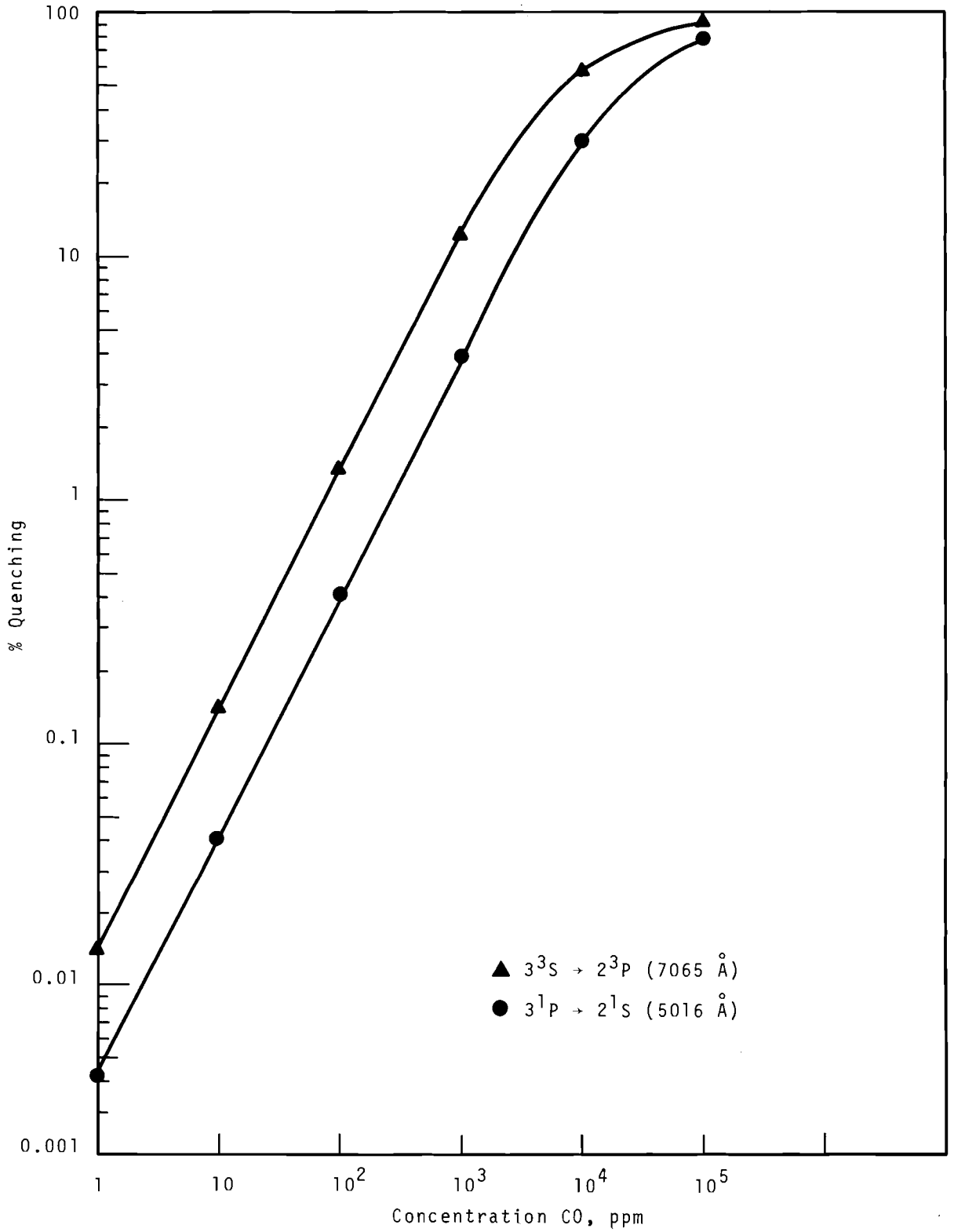

FIGURE 3.14. CO Quenching of the 5016 Å and 7065 Å Helium Lines

A transverse TSGBF sample expanded 50% from its virgin length at an exposure of 1.1×10^{22} nvt and temperature of 1000 °C. Although the sample is somewhat deteriorated after this high expansion, it is not warped and seems to still have good strength.

Two grades of Poco graphite were irradiated to maximum exposures of 1.1×10^{22} nvt. The grade designated by the manufacturer as AXZ-5Q1, which is isotropic with a density of 1.5 g/cm^3 and CTE of 6.7×10^{-6} $°C^{-1}$, showed very good dimensional stability to this exposure at a temperature of 1000 °C. It had contracted back to its original length after an initial expansion of 1.4% at 3×10^{21} nvt. Grade AXF-8Q1, also isotropic with a density of 1.8 g/cm^3 and CTE of 7.1×10^{-6} $°C^{-1}$, showed somewhat different behavior. After an initial expansion of 2% at 1000 °C, it remained at this value until an exposure of approximately 10^{22} nvt, where it now appears to be expanding again. Total expansion at 1.1×10^{22} nvt is 2.8%. Irradiation of these Poco samples will continue in an ETR capsule to better define the high-exposure trends.

Speer Grade RC5, an isotropic, nonneedle-coke graphite, was irradiated to an exposure of 1.5×10^{22} nvt at 1000 °C. In the parallel direction, it contracted to -2.5% before turning around at 8×10^{21} nvt. At an exposure of 1.5×10^{22}, it had not yet returned to its original length, but was still at -0.8% contraction. The transverse orientation behaved similarly and turned around at 8×10^{21} nvt after having contracted -1.2%. It returned to its original length after exposure to 1.1×10^{22} nvt.

Another Speer isotropic graphite, Grade 9650, also showed good dimensional stability. It expanded slowly to about 1% at an exposure of 7×10^{21} nvt and a temperature of 1050 °C. This graphite will also be investigated further in ETR irradiations.

Generally, the isotropic graphites show better dimensional integrity than conventional and needle-coke graphites. Contractions are less, and dimensional changes are still small at exposures where rapid, post-turnaround expansion is occurring in the conventional graphites.

The proof-test capsule series has been replaced with a compression-test series. Samples are all 1.75 in. diam x 2 in. long, and some are under a 50 psi compressive stress. Irradiation data will be obtained to define both the effect of sample size and a low compressive stress on the turnaround behavior of graphite. Preliminary results obtained from several large samples included in previous proof-test capsules indicated that the large samples contract at the same or possibly a slower rate than small samples (0.25 in. diam x 1.75 in. long). This is in direct contrast to what has been seen in reactors where large bars contract faster than small samples. The GETR irradiations, however, are conducted at higher temperatures, and maximum large-sample exposures thus far are less than 2×10^{21} nvt. Higher doses are required to identify the true

trends and determine whether this behavior persists. Upon discharge of the Capsule H-3-50 in May 1968, samples will have exposures to 5×10^{21} nvt and should provide the required data to resolve this question.

EFFECT OF SAMPLE SIZE ON GRAPHITE IRRADIATION BEHAVIOR

W. J. Gray

It has been reported[3,4] that irradiation-induced contraction of large graphite bars (i.e., sizes normally used in nuclear reactors) occurs at a rate two to three times faster than small test samples (typically 0.43 in. diam x 4 in. long). As a result of these observations, four irradiation experiments[5-8] were initiated to characterize the "size-effect" phenomenon; three of these experiments are still in progress.

Cox[9] reported the results for TSX graphite from the two size-effect experiments in the Hanford N-Reactor for a maximum fast-neutron exposure of 1.41×10^{21} nvt (E > 0.18 MeV). He found that the large blocks (4 in. x 5-3.8 in. x 17-1/2 in.) contracted 25 to 50% greater than the small samples (0.43 in. diam x 3 in. long and 0.43 in. diam x 6 in. long) in both the transverse and parallel directions.* At a fast-neutron exposure of 6.6×10^{20} nvt, he found no difference in contraction rates of samples taken from the edge and from the center of a bar.

The size-effect samples in the Hanford KE-Reactor[5] were measured after a fast-neutron exposure of about 4×10^{20} nvt. At this low exposure, no sample-size effect could be detected.

During the present quarter, the size-effect samples in N-Reactor were discharged and measured after a maximum fast-neutron exposure of 1.66×10^{21} nvt. The reason for discharging the samples after so brief an additional exposure was that they had been dropped during the charging process after the previous measurement, and some of the samples damaged by the drop had to be replaced. The contraction rates of the undamaged samples were in good agreement with those found by Cox.[9] In the transverse direction, contraction rates of samples taken from the edge of the bar were about 20% greater than those for samples taken from near the center. For the parallel direction, no difference was found between samples from the edge and center of the bar. As pointed out later, this is to be expected from variations in crystallite orientation within a bar of TSX graphite. Note that these are a different set of samples than those for which Cox compared data from the edge and center of a bar at an exposure of 6.6×10^{20} nvt.

The size-effect samples in the KE-Reactor were discharged for second length measurements after an exposure of about 1.5×10^{21} nvt now. Length measurements will be made, and the samples recharged for additional exposure.

---

* *Transverse and parallel to the extrusion axis of the graphite bar.*

It has been suggested[3] that variations in crystallite orientation within a graphite bar might partially account for the size-effect phenomenon. To investigate this possibility, an X-ray technique similar to that described by Bacon[10] is being used to determine the variation in crystallite orientation within a bar of TSX graphite. TSX graphite was chosen for the initial study because it is one of the types of graphites being used in the size-effect experiments discussed above. The X-ray results showed, within experimental error, no variation across the bar in the number of crystallites whose a axis is parallel to the extrusion axis. However, the crystallites tend to lie with their basal-planes parallel to the sides of the bar and, therefore, there is a variation across the bar with respect to any given edge. From the edge to the center of the bar, a smooth variation exists in orientation, i.e., there is no rapid change in orientation near the edge (no "skin").

Thermal-expansion coefficient measurements will also be made on the same bar of TSX graphite. These measurements, together with the X-ray data above, will be used to determine whether the accommodation coefficient[11] also varies across the bar. This information can then be used to calculate, to a first approximation, irradiation-induced contraction and, in particular, how this contraction varies across a bar of graphite.

Interestingly, the X-ray data suggest that there should be little or no change in irradiation-induced contraction across a bar of TSX graphite in the parallel direction. In the transverse direction, however, the contraction should be greater at the edge than it is near the center, and this is just what was observed in the N-Reactor experiment.

Another possible explanation for the greater rate of contraction of large reactor bars is the enhanced nucleation of radiation damage brought about by irradiating graphite for a brief period at low temperatures.[12,13]

Whether brief low-temperature operation during startups or other transients can increase the contraction by a factor of two or three is not known at this time.

HIGH-TEMPERATURE IRRADIATION IN THE ETR

A. L. Pitner

The GEH-13-14 high-temperature capsule was discharged from the ETR in February 1968, with a maximum accumulated exposure of 6×10^{21} nvt ($E > 0.18$ MeV). The capsule has a dual purpose: proof-testing several HTGR candidate graphites and accumulating high-temperature irradiation data on a variety of graphites for other advanced systems. Capsule temperatures range from 800 to 1300 °C.

Results from GEH-13-14 generally show accelerated damage at the higher temperatures. Initial contractions are greater, and turnaround apparently occurs sooner for most graphite types. This agrees with previous high-temperature irradiation data. Many

samples appear to be at or past turnaround; however, several graphite types have displayed good high-temperature stability. In particular, Poco graphite and Speer Grade 9650 graphite, both isotropic, have shown only small contractions or even slight expansions to the present doses. Additional irradiation is required to confirm whether this dimensional stability will continue to higher exposures.

Capsule GEH-13-15 will be charged in May for another three-cycle irradiation and will be discharged in September 1968. Maximum accumulated exposures at that time should approach 10^{22} nvt.

THERMAL-EXPANSION HYSTERESIS IN POLYCRYSTALLINE GRAPHITE

O. D. Slagle

In a previous quarterly program report,[14] measurements of thermal-expansion hysteresis in polycrystalline graphite were reported. It was found that a transverse sample of TSX graphite heated to 2400 °C had a difference in length between heating and cooling curves at 1800 °C of approximately 0.07%. A longitudinal sample similarly heated had no measurable hysteresis.

A model has been proposed by Buessem[15] to explain the thermal-expansion hysteresis observed in anisotropic ceramic materials. The model, shown in Figure 3.15, represents a constant-strain average of two crystallites in series, i.e., separated by a grain boundary. Buessem's method of introducing accommodation consists of assuming a temperature (T_o) at which stress buildup during cooling begins and a critical tensile strain (ε_c) at which a crystallite pair fails. As the model is cooled, those crystallite columns having the largest thermal contractions fail in tension; they are removed from the model when the difference between their thermal contraction and the average of the model is equal to the critical strain. In this manner the thermal-expansion coefficient of the model is progressively reduced. On reheating, if it is assumed that no recombination occurs until T_o is reached, the

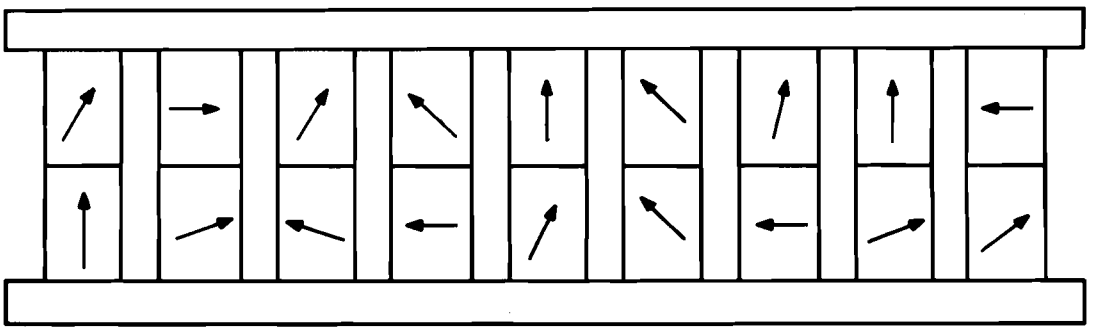

FIGURE 3.15. One-Dimensional Model Used in Analyzing Thermal-Expansion Hysteresis. Arrows depict the crystallite c-axis and are used to indicate randomness.

amount of thermal hysteresis expected can be easily determined.

This model was applied to TSX graphite, assuming T_o to be 2000 °C and ε_c to be 0.002 (Figure 3.16). The anomally predicted just above 1700 °C for the transverse orientation was not observed in the experimental curves. The room-temperature predictions of Buessem's model are also unreasonable. The number of columns remaining in the parallel sample would be 20%; that in the transverse sample would be only 5%. This extensive cracking is also reflected by the low calculated thermal expansion coefficients of 0.48 and 0.51 (x 10^{-6} $°C^{-1}$) for the parallel and transverse orientations, respectively. The respective measured values were 1.7 and 4.9 (x 10^{-6} $°C^{-1}$). Clearly, the Buessem's model results in too much c-axis accommodation when applied to polycrystalline graphite.

The extent of accommodation can be reduced by assuming that a column interacts only with its next nearest neighbor instead of directly with all the other columns. For this model,

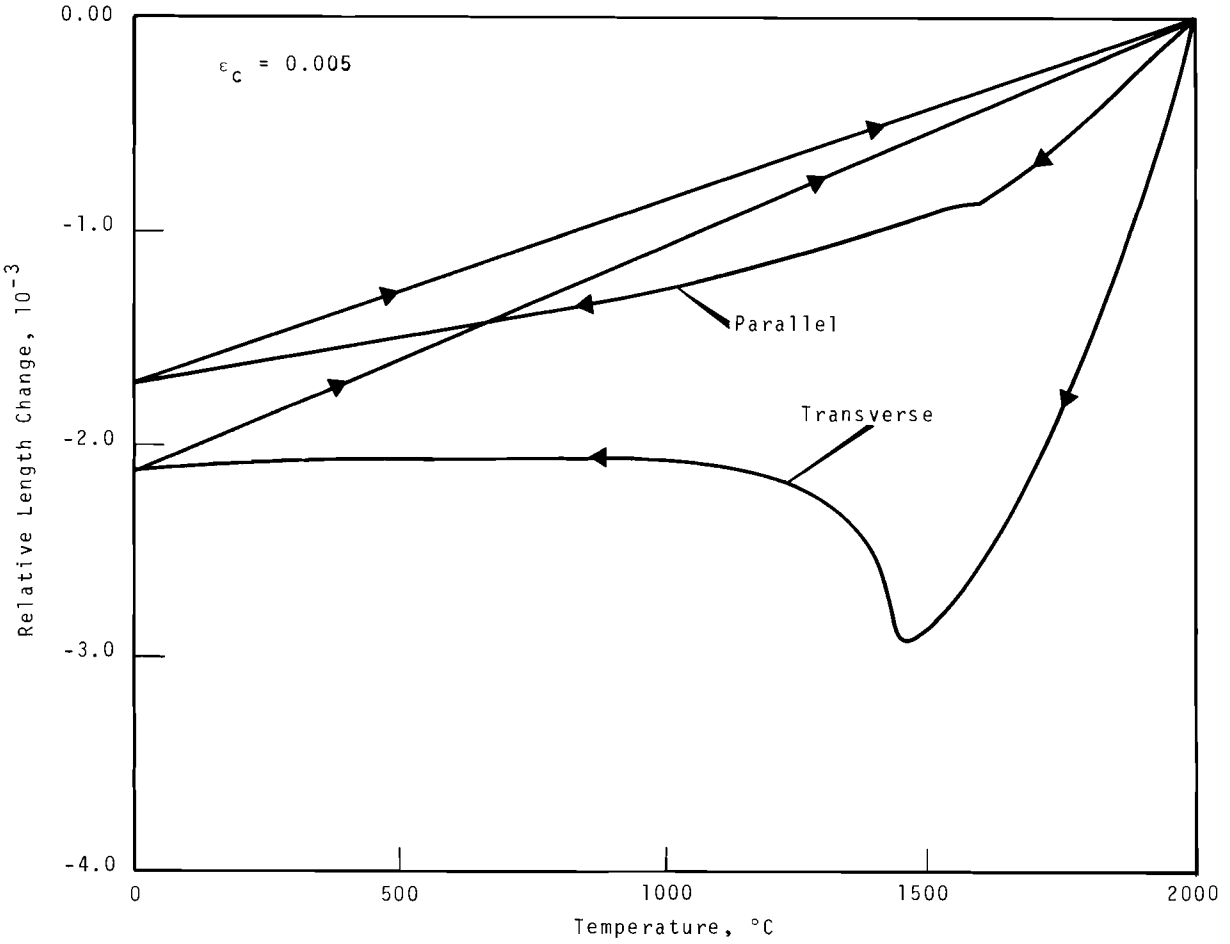

FIGURE 3.16. Thermal Hysteresis as Predicted Using Buessem's Method of Introducing Column Failure

accommodation is introduced by assigning to each column a probability that its next nearest neighbor will have a smaller thermal contraction and will impose a tensile strain on the column. This means of introducing accommodation has been quite successful in explaining room-temperature thermal-expansion coefficients and Young's moduli.[16] By choosing a difference in thermal contraction at which a column can be accommodated by its neighbor, a cooling curve can be determined.

Figure 3.17 gives the resulting curves obtained for this model by

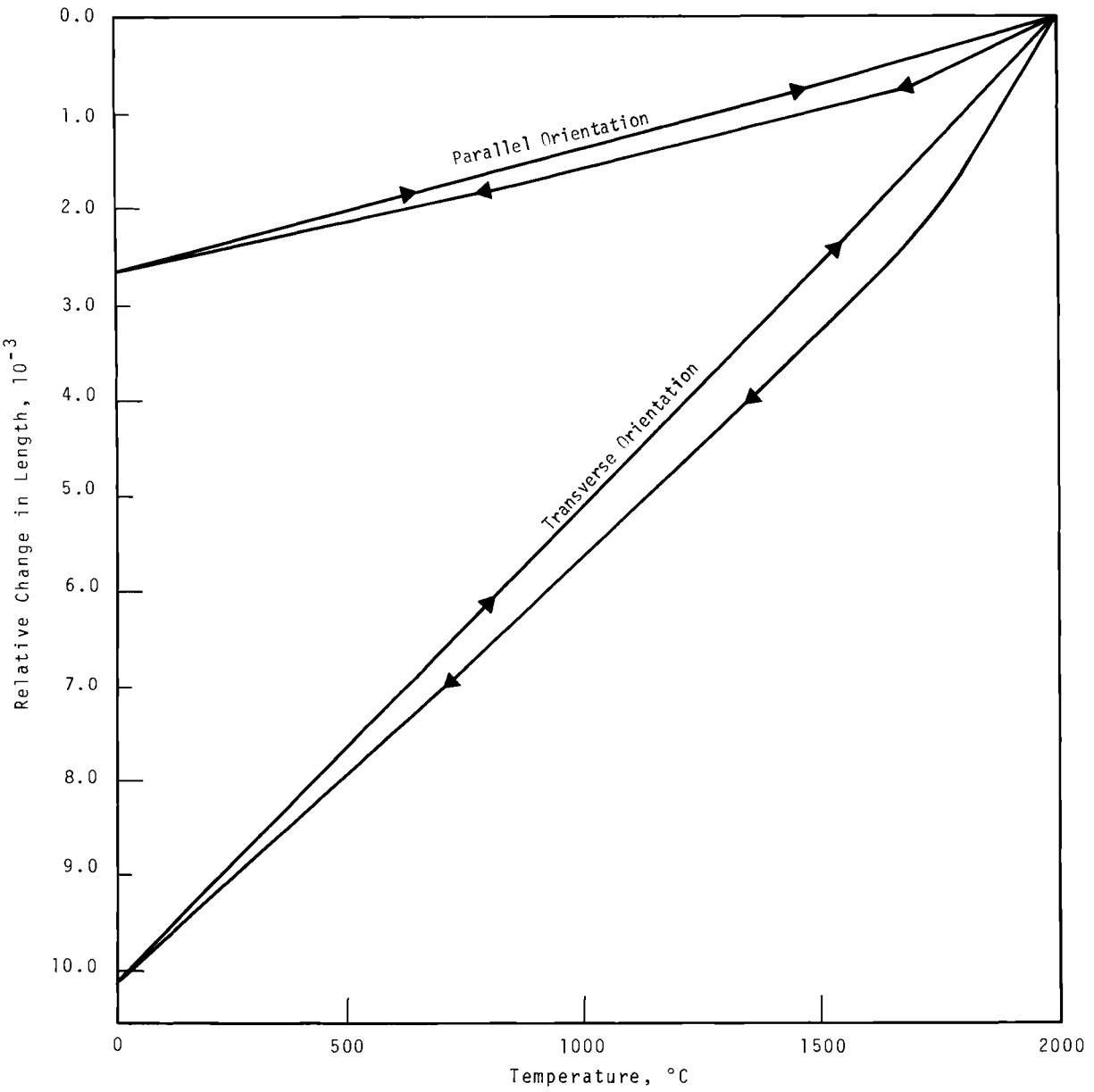

FIGURE 3.17. Thermal Hysteresis as Predicted when Accommodation is Assumed to Occur Only as an Interaction Between Next Nearest Neighbors

using the same parameters as before. These curves are in very good agreement with the experimental curves. The transverse orientation has a hysteresis at 1600 °C of 0.07% while the parallel orientation has a hysteresis of only 0.025%. These predictions are consistent with the experimental observations of no hysteresis for the parallel orientation since the predicted parallel hysteresis is within the experimental error. The refined model has 59% of the columns remaining at room temperature, which is a realistic number. The predicted thermal expansion coefficients are 1.35 and 5.1 ($\times 10^{-6}$ $°C^{-1}$) for the parallel and transverse orientations, respectively, and are in good agreement with the experimental values of 1.7 and 4.9 ($\times 10^{-6}$ $°C^{-1}$).

REFERENCES

1. *J. J. Cadwell, D. R. de Halas, R. E. Nightingale, and D. C. Worlton. Quarterly Progress Report, October, November, December 1967, Reactor Fuels and Materials Branch of USAEC Division of Reactor Development and Technology, BNWL-668. Pacific Northwest Laboratory, Richland, Washington, March 1968.*

2. *G. E. Bacon. J. Appl. Chem., vol. 6, p. 477. 1956.*

3. *R. E. Nightingale and E. M. Woodruff. "Radiation-Induced Dimensional Changes in Large Graphite Bars," Nucl. Sci. and Eng., vol. 19, p. 390. 1964.*

4. *W. C. Morgan. "Effect of Low Compressive Stress on Irradiation-Induced Dimensional Changes in Graphite," Carbon, vol. 1, p. 255. 1964.*

5. *L. O. Slind. An Experiment to Determine the Effect of Sample Size on the Irradiation-Induced Contraction of Graphite, HW-83734. General Electric Company, Richland, Washington, August 1964.*

6. *B. A. Ryan. Monitoring Dimensional Changes of Graphite in Ball Channel 60 at N-Reactor, HW-84503, General Electric Company, Richland, Washington, December 1964.*

7. *B. A. Ryan. Test for Monitoring Dimensional Changes of Graphite in Rod Channel 74 at N-Reactor, BNWL-56. Pacific Northwest Laboratory, Richland, Washington, April 1965.*

8. *J. W. Helm. Radiation-Induced Dimensional Changes of Graphite Effect of Sample Sizes Less Than One-Half Inch Diameter, BNWL-CC-399. Pacific Northwest Laboratory, Richland, Washington, December 1965.*

9. *J. H. Cox, Jr. Unpublished Data (NPR Graphite), Pacific Northwest Laboratory, Richland, Washington, August 1966. (Interim Report)*

10. *G. E. Bacon. "A Method for Determining the Degree of Orientation of Graphite," J. Appl. Chem., vol. 6, p. 477. 1956.*

11. *A. L. Sutton and V. C. Howard. "The Role of Porosity in the Accommodation of Thermal Expansion in Graphite," J. Nucl. Mater., vol. 7, p. 58. 1962.*

12. *W. N. Reynolds and P. A. Thrower. "Enhanced Nucleation of Radiation Damage in Graphite," Carbon, vol. 1, p. 185. 1964.*

13. *J. H. Cox and E. M. Woodruff. Irradiation-Induced Contraction of Graphites at High Temperature Following Cold Preirradiation and Intermittent Thermal Anneals, BNWL-215. Pacific Northwest Laboratory, Richland, Washington, January 1966.*

14. F. W. Albaugh, S. H. Bush, J. J. Cadwell, D. R. de Halas, and D. C. Worlton. Quarterly Progress Report, April, May, June, 1967, Reactor Fuels and Materials Branch of USAEC Divison of Reactor Development and Technology, BNWL-473. Pacific Northwest Laboratory, Richland, Washington, September, 1967.

15. W. R. Buessem. "Internal Ruptures and Recombinations in Anisotropic Ceramic Material," Mechanical Properties of Engineering Ceramics edited by W. W. Kriegel and H. Palmour III Interscience, New York, p. 127. 1961.

16. O. D. Slagle. Averaging Techniques in Polycrystalline Graphites, BNWL-SA-1237-Rev, Pacific Northwest Laboratory, Richland, Washington, August 14, 1967.

FUEL DEVELOPMENT FOR GAS-COOLED REACTORS - HTGR GRAPHITE STUDIES

R. E. Nightingale

GRAPHITE SURFACE-AREA MEASUREMENTS

R. E. Woodley

Surface-area measurements have been performed on four samples of graphite irradiated in capsule GEH-13-14 in the ETR. These measurements were made to determine if high-temperature irradiation results in surface-area changes, thus affect fission product adsorption and the rate of oxidation. The graphite samples have received a total integrated exposure of about 1.94 x 10^{21} nvt (E > 0.18 MeV) at an average temperature of approximately 916 °C. Weight losses to the samples during the irradiation averaged about 1 mg. The individual oxidation percentages, the surface areas, and the percent length change for the individual samples are included in the following table:

Surface-Area Changes in Graphite with Neutron Irradiation at 916 °C

Sample No.	Surface Area (m^2/g) Initial	Surface Area (m^2/g) Final[a]	Weight Change, %	Length Change, %
234-304	0.488	0.445 ± 0.003	-0.042	-0.702
66-9-212	0.290	0.281 ± 0.010	-0.036	-0.544
66-12-203	0.283	0.329 ± 0.012	-0.055	-0.444
NC8-358	0.510	0.484 ± 0.011	-0.017	-0.458

[a] *The limits of error given are the standard deviations.*

Generally, the surface-area changes are small. Because of the experimental error inherent in surface-area measurements, particularly for the small samples used here, it is difficult to ascertain whether the changes observed are real or merely an experimental uncertainty. Nevertheless it is interesting to note that three of the samples exhibit a small decrease in surface-area. This implies a decrease in microporosity caused perhaps by the expansion of crystallites into voids or the formation of pore blockages. The increased surface-area shown by the remaining sample is more difficult to explain. All of the samples lost small amounts of weight but certainly not enough to effect a measurable surface-area increase.

Because the initial surface-area values are based on only a single measurement (whereas, the final values are averages usually of three measurements and hence believed to be better established), these same samples will be reirradiated to determine if an additional, more significant change in surface-area will occur upon further exposure.

NUCLEAR CERAMICS

R. E. Nightingale

MICROSTRUCTURE AND TRANSMISSION ELECTRON MICROSCOPY OF NUCLEAR OXIDES

S. J. Mayhan and J. L. Daniel

Microstructural study of ceramic materials such as nuclear oxides is most meaningful if several modes of examination (e.g., petrography, surface structure, and internal crystallography) can be closely correlated without introduction of artifacts during specimen preparation. Therefore, development of methods for improved thin-foil preparation of ceramic materials for transmission electron microscopy has continued.

An earlier report[1] described the mechanical thinning methods under development. Further work now indicates that a combination of a light chemical thinning or etching treatment with mechanical thinning may reduce or eliminate the residue of grinding and polishing marks shown in previous specimens (Figure 5.1). The current procedure includes:

- Treating the precut specimen with 9:1 H_2O_2:H_2SO_4 for 4 min;
- Polishing one side, using careful metallographic procedures, followed by application of the H_2O_2-H_2SO_4 for 10 sec
- Polishing (rough and fine) the other side to a final thickness suitable for transmission
- Treating with H_2O_2-H_2SO_4 for 3 sec.

Some microstructural characteristics possibly attributable to the preparation procedure are still evident, but general quality is much improved. Evaluation of other chemical polishing reagents and methods of combination with the mechanical thinning is in progress.

SCANNING ELECTRON MICROSCOPE FOR NUCLEAR MATERIALS STUDY

J. L. Daniel

Following the favorable conclusions from evaluation of scanning electron microscopy for nuclear materials study, detailed performance specifications for an optimum instrument were prepared, and purchase procedures were initiated. The instrument will include the following features:

- Provisions included or available for images resulting from secondary, backscattered, transmitted and absorbed electrons, cathodluminescence, and emf differences
- Magnification range of at least 100 to 100,000X with primary beam voltage of at least 5 kV to 50 kV
- Image resolution of 250 Å or better
- Universal goniometer specimen stage
- Provisions for image recording by standard camera, Polaroid high-speed photography, and video tape
- Physical design adaptable to use of specially designed attachments for dynamic in-microscope experiments, and for examination of plutonium-bearing materials.

Delivery of the instrument is anticipated by May 1, 1968.

Neg J-4208 *16,000X*

Mechanically Thinned Only

Neg J-4671 *40,000X*

Neg J-4670 *40,000X*

Mechanically Thinned and Chemically Polished

FIGURE 5.1. Thin Sections of Sintered UO_2

COMPATIBILITY OF MIXED URANIUM-PLUTONIUM OXIDES AND NITRIDES WITH STAINLESS STEEL

F. M. Smith and J. L. Daniel

Some of the experiments referred to in the last Quarterly Progress Report[1] on the study of the compatibility of sodium and helium bonded uranium-plutonium mixed oxide (UO_2–25 wt% PuO_2) pellets with type 304 SS have been completed. These hypostoichiometric oxides (O/M = 1.96 and 1.97) were either helium- or sodium-bonded to 304

SS and heated for time periods ranging from 100 to 1000 hr at temperatures of 650 and 1000 °C. Inspection of these diffusion couples has been limited to ceramographic and metallographic techniques.

Reference oxide pellets showed a microstructure generally free of visible cracks at 75X magnification. Helium-bonded pellets heated at 650 °C for 1000 hr and 1000 °C for 1000 hr showed essentially the same microstructure as the reference pellets with only slightly more cracking. No interaction could be seen between the fuel and adjacent cladding. Sodium-bonded pellets showed a little more cracking near the edges probably a result of sodium penetration, but still no interaction between the fuel and cladding. Figures 5.2 and 5.3 show as-polished micrographs of the latter two couples. The peculiar layered material near the cladding and fuel surfaces is actually successive layers of mounting resin. No reaction layer is present in any specimen examined to date, and no evidence of incompatibility has been found. The differences in porosity shown in the fuel microstructures in these two figures are typical of that occurring in as-manufactured pellets.

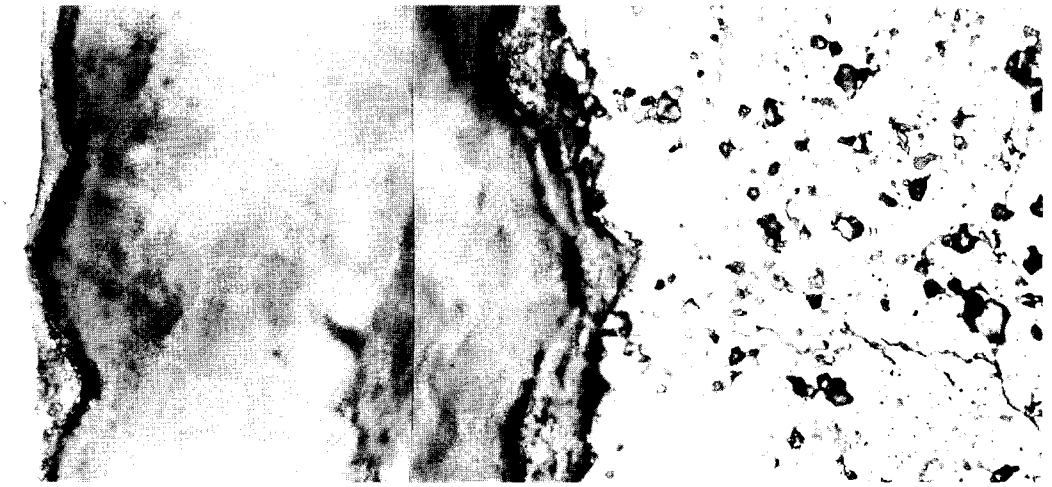

Neg 47249 *600X*

FIGURE 5.2. As-Polished Photomicrograph of Specimen 1-6. Diffusion Couple of UO_2—25 wt% PuO_2 (O/M = 1.96) Sodium Bonded to 304 SS and Heated to 650 °C for 1000 hr. Sodium Has Been Replaced by Epoxy Resin and Separates the Cladding on Left from Fuel on Right. No Reaction Layers Present on Either Fuel or Cladding. Observed Layers Resulted from Mounting Technique.

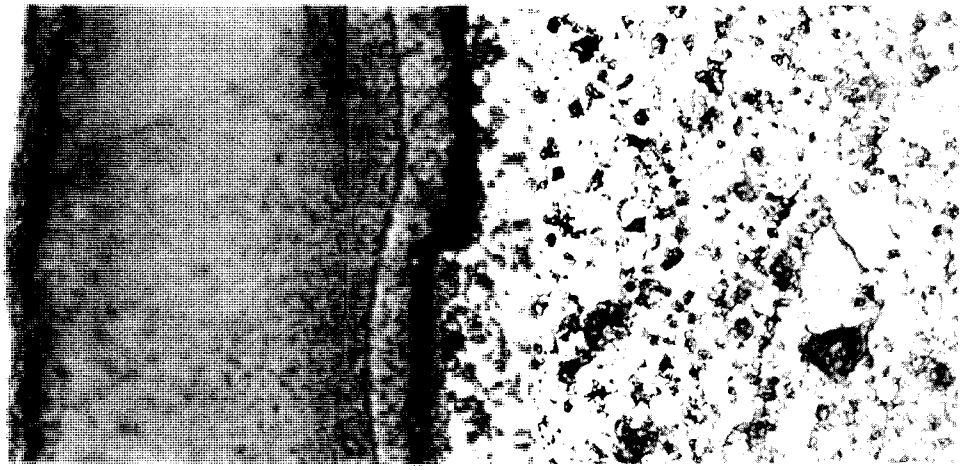

Neg 47254 600X

FIGURE 5.3. As-Polished Photomicrograph of Specimen 2-6. Diffusion Couple of UO_2–25 wt% PuO_2 (O/M = 1.96) Sodium Bonded to 304 SS and Heated to 1000 °C for 1000 hr. Sodium Has Been Removed and Replaced by Epoxy Resin Which Separates Cladding Left and Fuel Right. No Reaction Layers Present on Either Fuel or Cladding. Observed Layers Resulted from Mounting Technique.

The grain growth in the 304 SS cladding is of interest. Those capsules heated to 650 °C for 1000 hr show about 10 to 12 grains across the 16 mil capsule wall, which corresponds to ASTM grain Size 6. The capsules heated to 1000 °C exhibited a grain growth such that only two to three grains spanned the same wall thickness (ASTM grain Size 2). This results in a weakening of the capsule wall when operating at the higher temperatures. All of the oxide and nitride compatibility capsules examined have shown these same results.

Other test experiments with the mixed oxides are in various stages of completion; however, none of these have received as extensive a heat treatment as those discussed and are, therefore, expected to show no evidence of incompatibility.

In all the compatibility experiments discussed here and in previous reports,[1,2,3] direct contact of fuel and cladding material has only been incidental. Intimate contact would be more meaningful, and some method is needed to keep the fuel and cladding material in constant or pressure contact during the heating. Previously, at PNL (1966) pneumatic impaction has proven successful for compatibility experiments between promethium oxide and encapsulating materials, but control of stoichiometry is too difficult for such a method to be used with uranium-plutonium mixed oxides. To insure contact, a double restraining capsule has been made (Figure 5.4). It consists of an inner container of 304 SS or some other cladding candidate containing

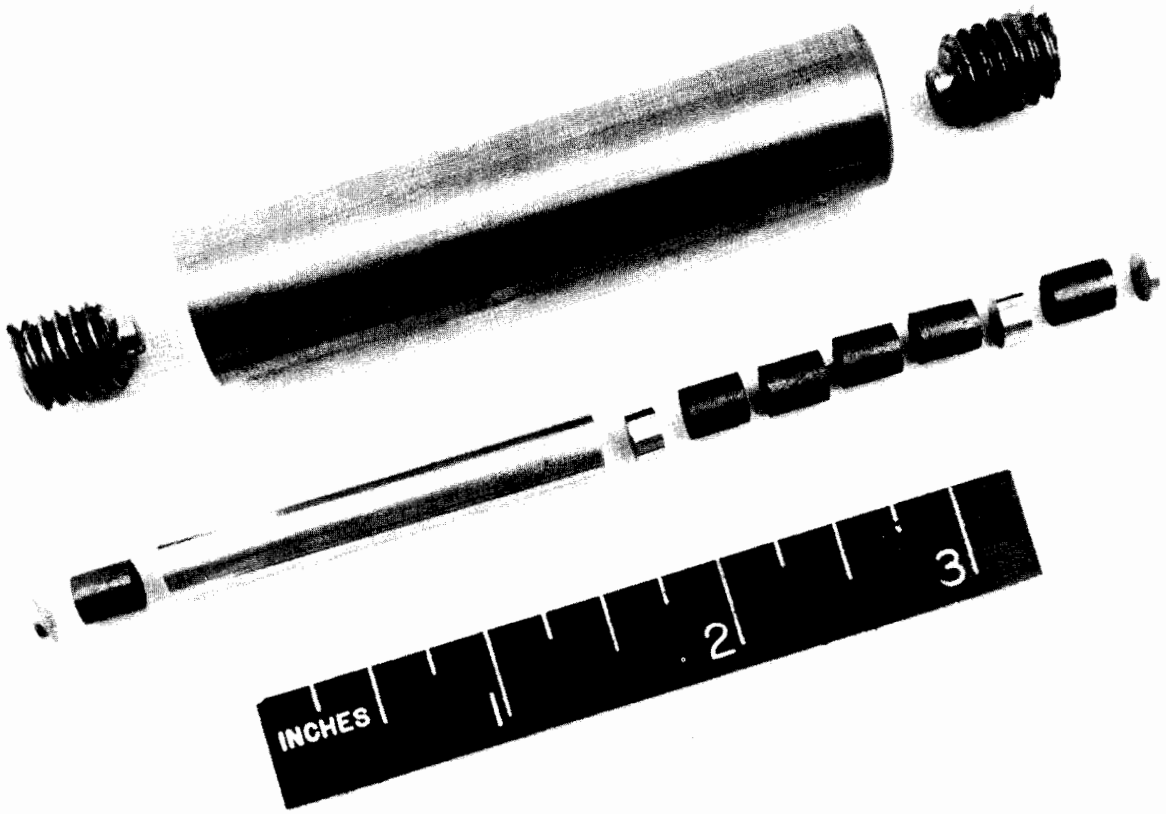

Neg 2680602

FIGURE 5.4. Restraining Capsule to Insure Intimate Contact Between the Fuel Pellets and Metal Disk Coupons of Cladding Material. Fuel Pellets and Metal Disk Coupons Are Loaded into Long Sleeve and Welded at Each End. Assembly Is Then Placed into Molybdenum Restraining Container (Top).

fuel and cladding-candidate disk coupons, and another restraining container of molybdenum metal. This is a modification of a technique used by Walter and Lahti[4] in their compatibility work. Since the molybdenum has about one-half the thermal expansion coefficient of 304 SS, the fuel and cladding disks are forced into intimate contact as the temperature is increased. Preliminary testing of this capsule is in progress.

Inspection of three, type 304 SS capsules containing UN–20 wt% PuN is essentially completed, and test conditions are summarized below:

Run No.	Temperature, °C	Time, hr	% TD	Bond	Carbon Content	Surface Preparation
A1	1000	1000	85.6	Na	3000 ppm	Centerless ground
A7	1000	100	85.6	Na	3000 ppm	Centerless ground
A2	1000	1000	~85.0	Na	300 ppm	Unground

These have been examined by both ceramography and metallography with the

sodium in place and also after removal. Comparison of the fuel microstructures with those obtained on the original sintered pellets before testing shows very little change. The minute cracks found in the oxides are not present in the nitrides, and the edge of the unground pellet is less irregular than those of the ground ones. Also, the fact that two of the pellets had a carbon concentration 10 times greater than the third pellet seemed to have no effect on the compatibility of the system. All three diffusion couples showed no interaction or evidence of incompatibility.

Other tests in this series, as listed in the last Quarterly Progress Report, are in progress and will be reported later. Besides these tests, others are in progress which use mixed nitrides prepared by the carbothermic process but with different variables. These tests will be done at the same temperatures used before (650 and 1000 °C), but the times will be extended up to 5000 hr.

GROWTH OF UO_2-PuO_2 SINGLE CRYSTALS

R. P. Nelson

Availability of sufficiently large PuO_2 and mixed UO_2-PuO_2 single crystals would provide possibilities for a wide range of basic property measurements free from the influence of microstructural features such as porosity and grain boundaries. Properties of direct importance to nuclear fuel performance, such as thermal conductivity and high-temperature creep behavior, and other properties of indirect importance, such as elastic modulus and electrical conductivity, are all dependent on microstructure. Measurements on single crystals will allow the separation of these extrinsic effects from the intrinsic properties that are dependent only on composition and stoichiometry.

The purpose of this work is to develop methods for the growth of UO_2-PuO_2 crystals for basic property studies. Although many techniques are available for crystal growth of refractory oxides, the most suitable must be chosen on the bases of the physical and chemical nature of the material and the probability that crystals of requisite size will result. Several different methods have been employed to produce UO_2, PuO_2, and other fluorite-structured oxide crystals; all seem to have inherent disadvantages. Large UO_2 crystals are commercially available through selective culling of large arc-melted batches. Nuclear criticality problems would seem to impose severe limitations on the size of a PuO_2 or UO_2-PuO_2 melt and, consequently, on the size of the crystal that would be produced from the slow cooling of such a melt.

UO_2 single crystals have also been produced in the laboratory by an induction-heated floating-zone method[5] and a vapor-transport method.[6] Both techniques require the separation of the larger crystals from a polycrystalline product, with the second method producing crystals that are characteristically small.

Several low-temperature methods have been studied. Both PuO_2[7]

and UO_2[8] crystals have been produced by electrodeposition, and PuO_2[7,9] and several fluorite structured oxides have been crystallized from molten solvents (flux growth). Crystals produced by these methods are characteristically small and often contain solvent inclusions.

In general, large, pure refractory oxide crystals of high perfection are most successfully grown by methods involving direct melting and solidification, e.g., Bridgman, Czochralski, and floating-zone methods. These techniques were considered the ones most likely to produce successful growth of compositions in the system UO_2-PuO_2, even though the high liquidus temperatures (2840 ± 20 °C for stoichiometric UO_2 to 2390 ± 20 °C for stoichiometric PuO_2)[10] and the relatively high oxygen partial pressures at the melting point (approximately 0.1 mm O_2 for stoichiometric UO_2)[11] place severe limitations on the choice of a suitable crucible material.

During the past year, work was begun on the growth of UO_2–PuO_2 compositions by the Bridgman, Czochralski, and floating-zone methods, using UO_2 and CeO_2 as stand-in materials. Initial growth studies have concentrated on the floating-zone growth of UO_2 via the electron-beam heating of the oxide contained in closed tungsten and rhenium capsules. Encapsulation is necessary to permit electron-beam heating of UO_2 which has a high vapor-pressure at the melting point. Tungsten and rhenium are the only refractory metals with melting points sufficiently high enough to use for encapsulation.

Electron-Beam Floating-Zone Growth of UO_2 in Tungsten

A series of growth experiments involving electron-beam heating and floating-zone growth of UO_2 encapsulated in tungsten have been completed. Polycrystalline UO_2 (95% TD) rods were contained in 0.250 in. ID x 0.020 in. wall x 2 in. long, chemically vapor-deposited (CVD) tungsten tubing with end closures made by electron-beam welding. The capsules were simple, right cylinders with no special end shape features for nucleation control. The UO_2 rods were chemically heat treated in Ar–8% H_2 atmosphere at 1850 °C for 1 hr to reduce the O/U to 2.00. Capsules formed in this manner were mounted vertically and scanned in a conventional electron-beam floating-zone system operated at 2.7 kV and beam currents of 200 to 400 mA. Successful growth experiments necessitated outgassed and leak-free capsules to prevent localized melting of the tungsten. Several capsules were outgassed by scanning at 2500 °C prior to UO_2 loading. This heat treatment also resulted in considerable grain growth in the tungsten. The internal temperature was maintained relatively constant by controlling the filament current, which maintained a constant capsule surface temperature under the beam as measured by a direct reading two-color optical pyrometer. By trial-and-error tests, UO_2 temperatures in the molten zone were maintained 50 to 100 °C above the melting point. Beam scans were made at 1 to 2 in./hr.

A typical result is shown in Figure 5.5. Single crystal growth

from multiple nucleation sites occurred, and individual grains up to 1 cm long x 2 to 3 mm wide were grown, but always in association with several other grains.

A significant amount of metal inclusions identified as tungsten by electron-microprobe spectroscopy was present in all the melted and solidified UO_2. The tungsten was present in two distinct forms (Figure 5.6) and was not distributed uniformily. A small portion of the tungsten was deposited as fine lines or strings of particles aligned parallel with the scan direction and fairly uniformily distributed throughout the solidified UO_2. A considerably larger volume of tungsten was deposited in much larger clusters. Occasionally, a large concentration of tungsten was present near the capsule edge, and deposition on the wall was evident (Figure 5.7).

The mechanism of tungsten transport and deposition in the molten UO_2 has been observed by other investigators,[12,13] but in one experiment where a single-crystal tungsten capsule was used,[13] no visible tungsten contamination was observed. Several possible mechanisms could account for the tungsten contamination:

- Errosion of tungsten grains through attack by molten UO_2 along grain boundaries at the capsule wall
- Chemical dissolution of tungsten in molten UO_2,

320X

FIGURE 5.6. Tungsten Inclusions in Single Crystal UO_2 Produced by Electron-Beam Floating-Zone Method. (Unetched)

25.6X

FIGURE 5.5. Crystal Growth Parallel to Scan Direction in UO_2 Produced by Electron-Beam Floating-Zone Method. (H_2SO_4 - H_2O_2 Etchant)

80X

FIGURE 5.7. Tungsten Inclusions in Single Crystal UO_2 Showing Deposition at Capsule Wall. (Unetched)

- Reaction of tungsten with excess oxygen in the UO_2 to form a tungsten oxide.

Errosion of wall grains could account for the large grains of tungsten in the UO_2 but not for the sintering of these grains together or to the wall, nor for the dispersion of fine tungsten particles. Furthermore, the increased tungsten grain size resulting from the outgassing heat treatment had no effect on the tungsten content or distribution, as might be expected if corrosion was the predominant mechanism. The last two mechanisms are the same since tungsten oxide would be expected to react with the molten UO_2. The solution of tungsten in molten UO_2 to form a liquid oxide solution has been suggested by Grossman.[14] The eutectic in this pseudo-binary system is probably very near the composition UO_2.

One might expect the solubility of tungsten to vary with the stoichiometry, but until the nature and extent of tungsten solubility in molten UO_2 is known as a function of stoichiometry, the contamination will prevent growth of useful UO_2 single crystals via this method. Measurements of the equilibrium solubility of tungsten in stoichiometric and hypostoichiometric liquid UO_2 are planned.

Electron-Beam Floating-Zone Growth of UO_2 in Rhenium

Growth studies via the electron-beam floating-zone method were extended to rhenium-encapsulated UO_2 to ascertain the growth behavior and the compatibility of UO_2 with rhenium. A 0.250 in. OD x 0.030 in. wall x 2.0 in. long rhenium capsule was fabricated by the rolling and electron-beam welding of 0.030 in. rhenium sheet. A polycrystalline UO_2 rod was heat treated and encapsulated in the manner used for the tungsten capsule.

Several attempts to float a molten zone failed almost immediately on UO_2 melting because of localized melting of the rhenium and gross escape of vapor leading to loss of vacuum and plasma discharge throughout the system. The presence of small defects in the weld region, which allowed escape of vapor, could account for this behavior. In the final experiment with the capsule reduced to 1 in. in length, a successful run was obtained. However, metallographic observation indicated that a molten zone had been moved only through a limited region in the center of the UO_2, producing a small region of columnar growth. Most significant was the apparent absence of rhenium metal inclusions, which was confirmed by spark-source mass spectrometry indicating less than 2 ppm rhenium in the melted region. Measurements of the equilibrium solubility of rhenium in UO_2 are planned. Further growth studies are in progress using CVD rhenium to minimize the possibility of failure through outgassing.

THERMAL DIFFUSIVITY OF $(Pu,U)O_{2\pm x}$

R. L. Gibby

The thermal diffusivity of sintered $(U_{0.75}Pu_{0.25})O_{2\pm x}$ was measured from 100 to 1200 °C as a function of oxygen-to-metal ratio from 1.93 to 2.00. Measurements were made with a laser heat-pulse apparatus.[15]

Properties of the specimens are given in Table 5.1, and results of the measurements are plotted in Figure 5.8.

The mixed-oxide solid-solution samples were prepared by blending PuO_2 and UO_2 powders in a ball mill for 72 hr, dry-pressing the blended powder into pellets, and sintering the pellets at approximately 1650 °C for 24 hr in an argon-8% hydrogen atmosphere.

Oxygen-to-metal ratios of the densified specimens were adjusted by reduction at temperatures from 1150 to 1600 °C in ultra-pure, liquid-nitrogen cold-trapped hydrogen. An oxygen-to-metal ratio of 1.93 was obtained by a 2 hr reduction at 1600 °C; a ratio of 1.97 was obtained after 1 hr at 1200 °C.

During the thermal-diffusivity measurements, the oxygen-to-metal ratio of the stoichiometric specimen was maintained in a flowing argon-8% hydrogen atmosphere passed over 0 °C water. The oxygen-to-metal ratios of the hypostoichiometric specimens were maintained by testing in a flowing atmosphere of dried argon-8% hydrogen.

Results of this study can be expressed by the empirical relationship

$$\alpha = [0.110\ T - 1086\ (O/M) + 2175]^{-1},\ (cm^2/sec)\ .$$

where the temperature, T, is in °C (100-1200 °C) and O/M is the oxygen-to-metal ratio (1.92-2.00). The calculated thermal diffusivities at temperatures of 200 and 1200 °C are compared with the experimental data in Figure 5.8. Small oxygen difficiencies apparently result in an appreciable reduction in thermal diffusivity at moderately low temperatures. At higher temperatures, Umklapp processes become more important, and, consequently, the effect of oxygen-to-metal ratio is not as important.

Table 5.1. Impurities of Mechanically Mixed $(U_{0.75}Pu_{0.25})O_{2.00}$

Lattice Parameter a_o:	(O/M = 2.000)	5.4515 Å	
	(O/M = 1.97)	5.4601	
	(O/M = 1.95)	5.4649	
	(O/M = 1.93)	5.4730	
wt% Plutonium:	21.6		
Density (% TD):	95.5		
Spectrochemical Analysis:			
Ag	<1 ppm	Na	2
Al	50	Ni	50
B	0.1	P	<50
Ca	1	Pb	2
Cr	<5	Si	12
Cu	20	Sn	5
Fe	120	V	<20
K	20	Zn	50
Mg	2		
Mn	2		
Mo	<5		

The thermal diffusivity of the mechanically mixed $(U_{0.75}Pu_{0.25})O_{2.00}$ (stoichiometric) specimen examined in this study was almost identical to that of a coprecipitated $(U_{0.80}Pu_{0.20})O_{2.00}$ (stoichiometric) specimen investigated previously.[16] Since both materials were good solid solutions, the results indicate that plutonium content has no measurable effect on thermal diffusivity of mixed uranium-plutonium oxides.

THERMAL DIFFUSIVITY OF PuO_2

R. L. Gibby

The thermal diffusivity of pneumatically impacted PuO_2 (93.3% TD) was determined from 100 to 1650 °C

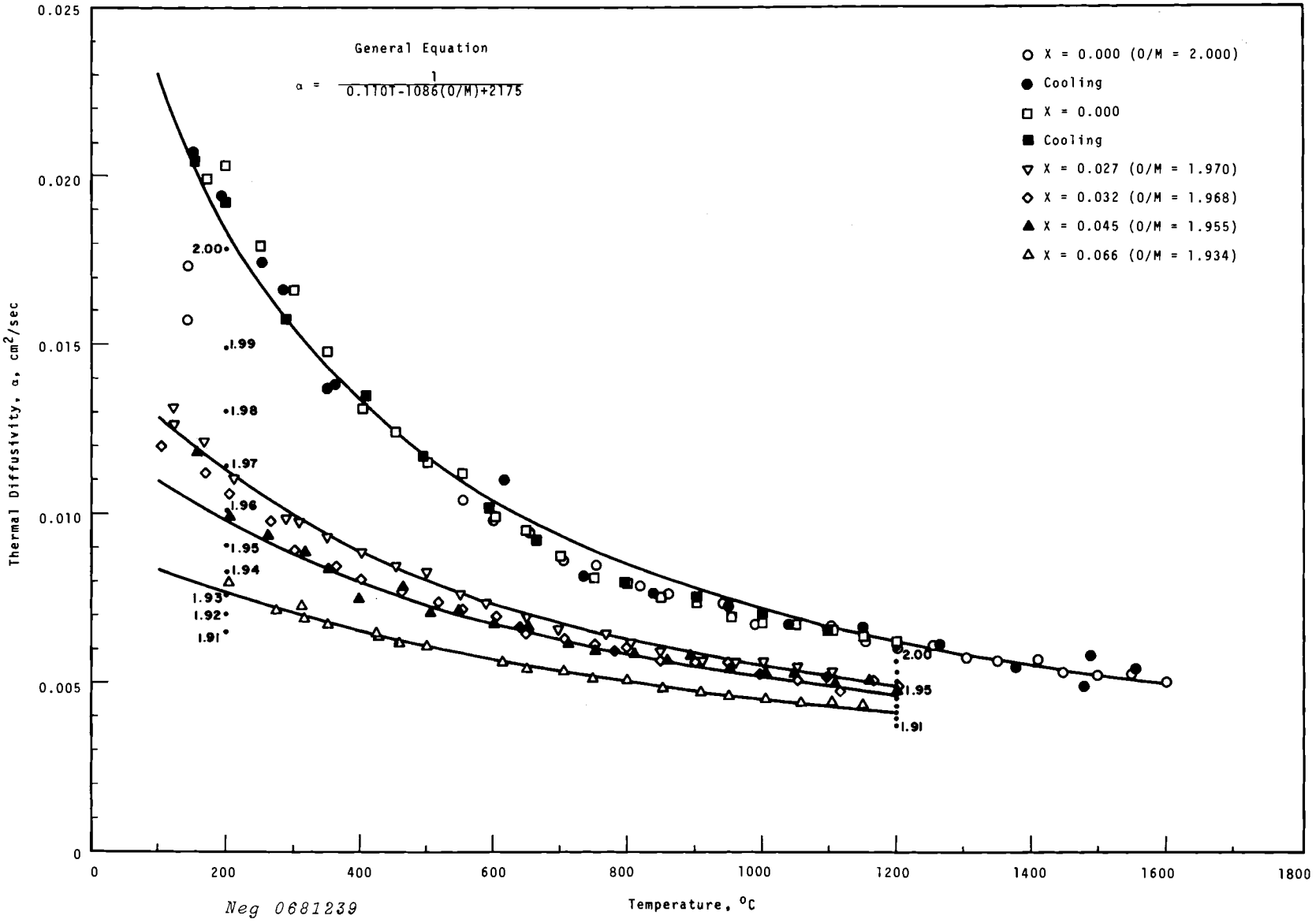

Neg 0681239

FIGURE 5.8. The Thermal Diffusivity of $(U_{0.75}Pu_{0.25})O_{2-x}$ as a Function of Oxygen-to-Metal Ratio (O/M)

by use of a laser heat-pulse apparatus.[15] The results from this study were used with reported heat-capacity data for PuO_2[17,18] to calculate thermal conductivity in the corresponding temperature range.

Measurements were made on two small specimens (∿0.63 cm diameter x 0.06 cm) which were cut from a larger piece of pneumatically impacted, high-purity PuO_2. One specimen was coated on both surfaces with a thin layer of colloidal graphite to prevent transmission of the ruby laser beam (λ = 0.6943 μ); the other specimen was left uncoated. The latter specimen was used for measurements above 1400 °C where it appears that PuO_2 becomes opaque to the laser beam. This also allowed thermal-diffusivity measurements on PuO_2 in an oxidizing atmosphere at high temperatures. The coated sample was heated in a reducing atmosphere (argon-8% hydrogen) to prevent oxidation of the graphite coating. Between 100 °C and ∿900 °C, the thermal diffusivity of the coated sample followed a reciprocal temperature relationship (Figure 5.9); however, above 900 °C, the data fell below this relationship, probably due to the formation of anion defects from oxygen losses from the sample. The data taken during cooling remained low to about 400 °C, where it returned to the original curve. This result is attributed to the precipitation of a second phase of lower oxygen composition (α-Pu_2O_3) with the corresponding return of the major PuO_2 phase to near stoichiometric oxygen composition. Such behavior is consistent with the reported Pu-O phase system.[19]

The uncoated sample was heated in air; below 1400 °C (as expected), the data were higher than the data taken on the coated samples because of some transmission of the laser beam through the sample. However, above 1400 °C, the results corresponded with the extrapolated reciprocal-temperature relationship determined at the lower temperatures. From these results, therefore, the thermal diffusivity of PuO_2 can be expressed between 100 to 1650 °C as a function of absolute temperature by the empirical relationship

$$\alpha = \frac{1}{0.105\ T + 1.20}\ (cm^2/sec) \quad ,$$

while the calculated thermal conductivity can be expressed by the relationship

$$K = \frac{1}{0.0269\ T + 2.53}\ (watts/cm°K) \quad .$$

This expression is plotted in Figure 5.10 along with the PuO_2 data of Lagedrost et al.,[20] determined in an identical manner, and the UO_2 data of Godfrey et al.,[21] measured directly with a radial heat-flow apparatus. The thermal conductivity of PuO_2 is nearly identical with that of UO_2. The higher thermal conductivity calculated for PuO_2 near 100 °C may be caused by the higher heat capacity of PuO_2 in this temperature range.

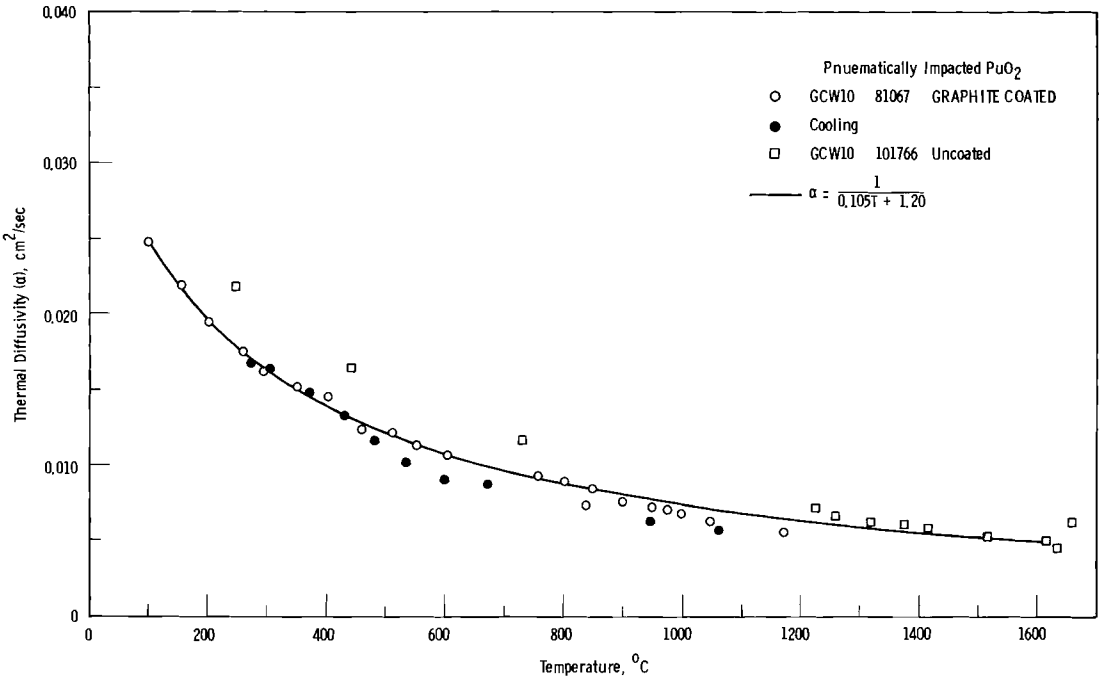

Neg 0680844-1

FIGURE 5.9. The Thermal Diffusivity of Pneumatically Impacted PuO_2 (93.3% TD).

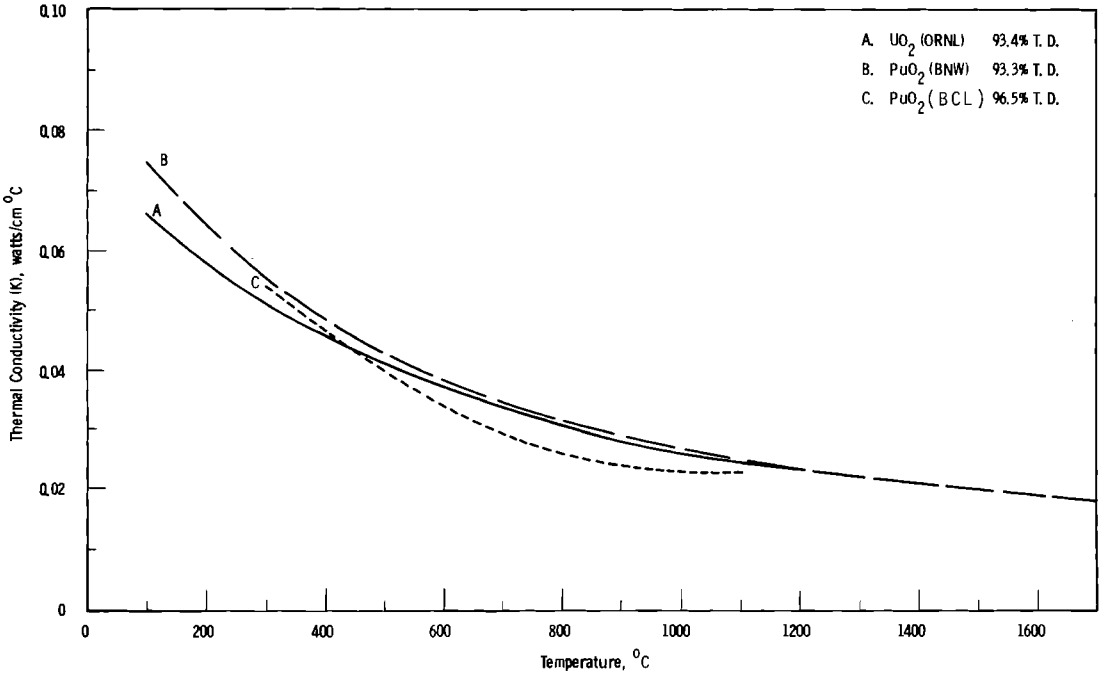

Neg 0680844-2

FIGURE 5.10. The Calculated Thermal Conductivity of Pneumatically Impacted PuO_2 (Curve B). Shown for Comparison Are the PuO_2 Data of Lagedrost et al. (Curve C) and the UO_2 Data of Godfrey et al. (Curve A)

COOLING-RATE EFFECTS IN MOLTEN-CENTER OXIDE FUELS

J. A. Christensen and R. R. Lewis

The sixth in a series of in-reactor experiments, designed to characterize molten-zone solidification-rate effects on oxide fuel structure and impurity distribution, failed in the 100-KE Snout facility. The failure consisted of loss of both bottom end plugs from the capsule which, together with approximately 400 g of UO_2, remained in the primary coolant system following capsule discharge. The incident had no adverse effect on reactor operation.

Postirradiation examination showed a simple shear failure of the welds that suggested a high internal pressure. Sufficiently high pressures would cause failure in the axial direction because of the high circumferential restraint imposed by a massive aluminum sleeve shrink-fitted onto each capsule. The fuel appeared to have operated at near the anticipated heat rating, and isotopic analysis confirmed the design fissile-atom content. The capsule contains two separate fueled compartments, only one of which failed. The sound compartment, which had bulged slightly, contained 500 cm^3 (STP) of gas. This was near the quantity required to exceed the longitudinal yield strength of the 304 SS clad. A gas analysis showed 96% CO and nearly 4% CO_2 in the sample. Origin of the carbonaceous contamination responsible for the released gas was not unequivocally identified. However, assembly records indicated a strong possibility of inadequate outgassing of the fuel after it was exposed to an organic solvent. The possibility of recurrent failures from this source in subsequent irradiations will be avoided by outgassing the fuel at 1000 °C immediately prior to capsule assembly.

PROPERTIES OF MOLTEN OXIDE FUELS

J. A. Christensen, D. I. Boget, and W. J. Woods

Facilities for measuring properties of liquid UO_2-PuO_2 are nearing completion. An 80 kW, programmed power supply with full range control from 0 to 2000 A was installed adjacent to the Shielded Materials Facility in 324 Building. Power is carried through copper bus bars and split copper bulk-head penetrations to the cell interior. The system provides adequate power for all high-temperature, remote experimentation contemplated. Techniques for measuring change in volume on melting and liquid density for UO_2-PuO_2 were developed. The method, which consists of measuring the liquid column height in a sealed, self-resistance-heated tungsten tube, was refined using sapphire (Al_2O_3) specimens. Reproducible results of satisfactory accuracy were obtained, and extension of the technique to UO_2-PuO_2 is in progress. Viscosity of refractory oxides is also under study. Apparatus for measuring viscosity by the oscillating crucible technique at temperatures to approximately 3000 °C was designed and built. A commercially available viscosimeter was procured

and will be modified for high-temperature applications. Both instruments are being checked out by using viscosity standards.

In-cell laboratory layout and space allocation are in progress, and a supporting out-of-cell high-temperature laboratory is nearly complete. Procurement of alpha-tight enclosures for both areas was initiated. The combined facility will have unique capabilities for high-temperature properties measurements on hazardous materials, including irradiated fuel materials.

ELASTIC PROPERTY MEASUREMENT ON NUCLEAR CERAMICS

O. D. Slagle

An apparatus for measuring the sound velocity in solids by the phase-comparison method has been assembled. Preliminary measurements of the longitudinal velocity of sound in fused silica gave a value within 0.4% of previous measurements.

Two single crystals of UO_2 have been oriented by use of a back-reflection Laue camera. The crystals are in the shape of rectangular prisms with sides (111); (11$\bar{2}$); (1$\bar{1}$0); and (100); (011); (0$\bar{1}$1). The crystals were slightly hyperstoichiometric, as indicated by a Widmanstätten precipitation of U_4O_9 in the UO_2 matrix. A preliminary study of these precipitates indicated that they are rod shaped and form along (111) planes. The oriented crystals will be reduced to $UO_{2.00}$ and used for studying single-crystal elastic constants in the system UO_{2+x}.

An apparatus for measuring elastic moduli of polycrystalline ceramics by a low-frequency resonance technique has also been assembled. Measurements on a polycrystalline sample of UO_2 are in agreement with previous work. Initial attempts to make measurements at temperatures to 1500 °C have not been successful.

THERMAL DIFFUSIVITY OF (U,Pu)N

R. L. Gibby and E. T. Weber

The thermal diffusivity of a mixed uranium-plutonium nitride sample was measured from 200 to 1600 °C by using a laser heat-pulse apparatus.[15] The sample (UPCN-2) was obtained from a sintered pellet fabricated from powder synthesized directly from mixed UO_2–20 wt% PuO_2 by the carbothermic reduction process. Specimen characteristics are given in Table 5.2, and the microstructure is shown in Figure 5.11. An oxide phase appears as a light grey inclusion in the unetched sample. Apparently, because of the high carbon content of this sample, a good etched microstructure was not obtained.

TABLE 5.2. Characteristics of Sintered Carbothermic Nitride Sample UPCN-2

Lattice Parameter	4.898 Å
U/Pu Ratio	4:1
Density	12.5 gm/cm^3
N_2	4.24 wt%
O_2	0.89 wt%
C	0.60 wt%

SPECTROCHEMICAL ANALYSIS

Element	Ag	Al	B	Ca	Cr	Cu	Fe	Mg	Mn	Na	Ni	P	Pb	Si
ppm	2	50	<0.1	<1	<25	20	20	<5	5	2	<10	<50	<1	5

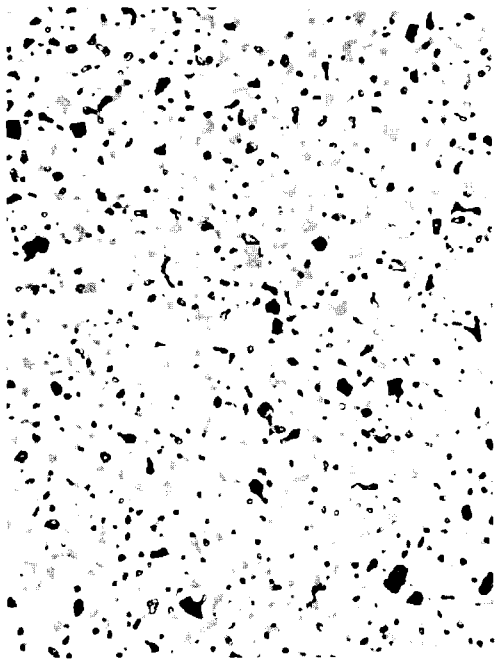

Neg 481B *600X*

a. Unetched

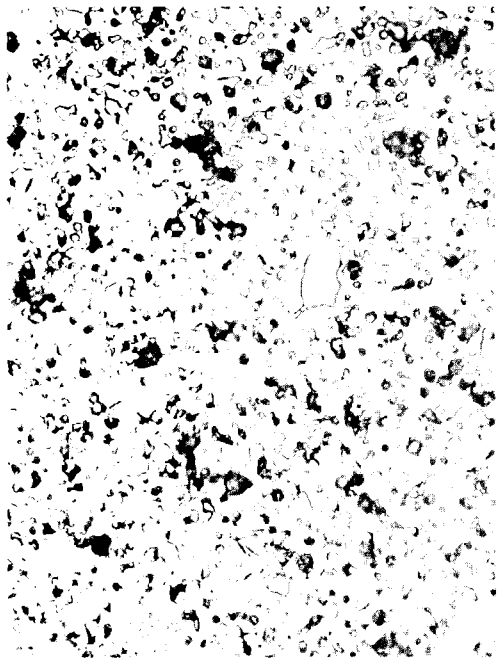

Neg 481D *600X*

b. Etched (H_2-HNO_3-HF Etchant)

FIGURE 5.11. Photomicrographs of Sintered Carbothermic Nitride Sample UPCN-2

The thermal-diffusivity data obtained in this study are shown in Figure 5.12. Shown for comparison are results reported previously[16] for mixed-nitride sample (UPN13-2) prepared from the metal-hydriding process. The carbothermic mixed-nitride specimen had a higher density (89% TD) than the metal-hydride-derived material (86% TD), but it also contained 6000 ppm carbon and 9000 ppm oxygen compared to 400 ppm carbon and approximately 3000 ppm oxygen for the metal-hydride-derived specimen. Results for the two samples are in good agreement when the amount of scatter present in the data is considered. The thermal-diffusivity data, taken on cooling of the carbothermic mixed-nitride sample, indicated that a compositional change (probably oxidation) occurred during the heating cycle, even though the sample was purposely heated in argon-8% hydrogen.

Thermal conductivity was calculated from results obtained by using UN heat capacity data;[3] the calculated thermal conductivities are shown as a function of temperature in Figure 5.13. Calculated thermal conductivity data for the metal-hydride-derived specimen[2] are again included for comparison. The difference between the thermal conductivities of the two materials at the lower temperatures is apparently related to the density difference

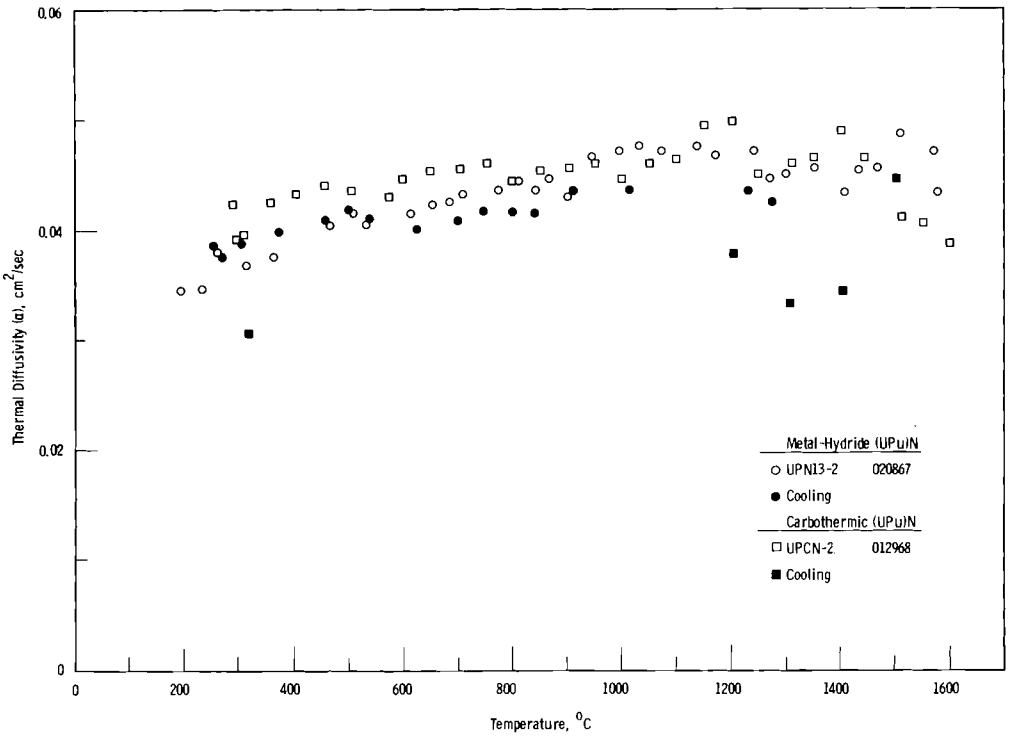

Neg 0680844-3

FIGURE 5.12. The Thermal Diffusivity of $(U_{0.20}Pu_{0.80})N$ Samples Prepared from the (1) the Metal-Hydride Process, (2) the Carbothermic Reduction of a Mixed Powder.

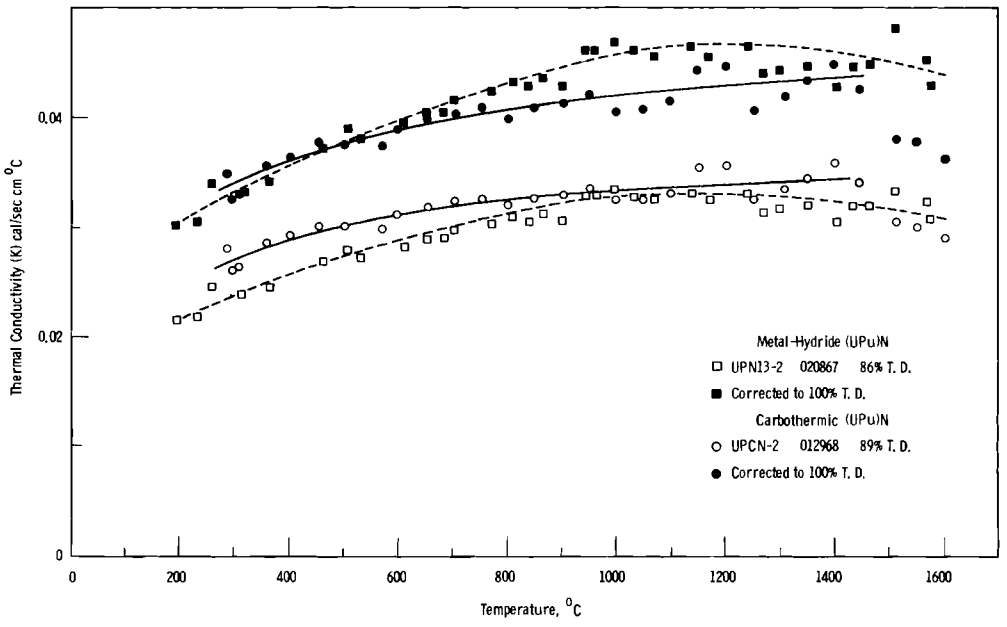

Neg 0680844-4

FIGURE 5.13. The Calculated Thermal Conductivity of $(U_{0.20}Pu_{0.80})N$ Samples. Results are also shown corrected to 100% TD.

since correction of the data to 100% TD[4] results in good agreement. At higher temperatures, oxidation of the carbothermic material is probably responsible for the difference.

References

1. J. J. Cadwell, D. R. de Halas, R. E. Nightingale, and D. C. Worlton. Quarterly Progress Report, October, November, December, 1967, Reactor Fuels and Materials Branch of USAEC Division of Reactor Development and Technology, BNWL-668. Pacific Northwest Laboratory, Richland, Washington, March 1968.

2. F. W. Albaugh, S. H. Bush, J. J. Cadwell, D. R. de Halas, and D. C. Worlton. Quarterly Progress Report, April, May, June, 1967, Reactor Fuels and Materials Branch of USAEC Division of Reactor Development and Technology, BNWL-473. Pacific Northwest Laboratory, Richland, Washington, September 1967.

3. J. J. Cadwell, D. R. de Halas, R. E. Nightingale, and D. C. Worlton. Quarterly Progress Report, July, August, September, 1967, Reactor Fuels and Materials Branch of USAEC Division of Reactor Development and Technology, BNWL-658. Pacific Northwest Laboratory, Richland, Washington, February 1968.

4. C. M. Walter and J. A. Lahti. Nuclear Applications, vol. 2, pp. 308-319. 1966.

5. A. T. Chapman and G. W. Clark. "Growth of UO_2 Single Crystals Using the Floating-Zone Technique," J. Am. Ceram. Soc., vol. 48 (9), pp. 494-95. 1965.

6. W. Van Lierde, R. Strumone, E. Smets and S. Amelinckx. "The Preparation of Uranium Oxide Single Crystals by Sublimation," J. Nucl. Matl., vol. 5, (2), pp. 250-253. 1962.

7. G. E. Benedict, K. M. Harmon, G. Jansen, Jr., L. K. Mudge, and F. A. Scott. "Production of Reactor Fuel Oxides from Molten Salt Solutions," New Nuclear Materials Including Non-Metallic Fuels, vol. I, pp. 21-36, IAEA, Vienna, 1963.

8. R. G. Robins. "Uranium Dioxide Single Crystals by Electrodeposition," J. Nucl. Matl., vol. 3, (3), pp. 294-301. 1961.

9. K. D. Phipps and D. B. Sullenger. "Plutonium Dioxide: Preparation of Single Crystals," Science, vol. 145, pp. 1048-49, September 4, 1964.

10. W. L. Lyon and W. E. Baily. "The Solid-Liquid Phase Diagram for the UO_2-PuO_2 System," J. Nucl. Matl., vol. 22, pp. 332-39. 1967.

11. R. E. Fryxell. Chemical Properties and Behavior of Urania Above 1500 °C, GEMP-439, General Electric Company, Cincinnati, Ohio. October 1966.

12. B. Weidenbaum and H. Hausner. "The Compatibility of Tungsten with Molten UO_2," Am. Nucl. Soc. Trans., vol. 8, p. 32. 1965.

13. D. T. Eash. "On the Compatibility of Tungsten with Molten UO_2," J. Nucl. Matl., vol. 19, pp. 196-97. 1966.

14. L. N. Grossman. "High Temperature Thermal Analysis of Ceramic Systems," Paper 34-B-66, 1966 Amer. Ceram. Soc. Annual Meeting, Basic Science Div., Washington, D. C., May 10, 1966.

15. F. W. Albaugh, S. H. Bush, J. J. Cadwell, D. R. de Halas, and D. C. Worlton. Quarterly Progress Report, January, February, March, 1966, Reactor Fuels and Materials Branch of USAEC Division of Reactor Development and Technology, BNWL-CC-694. Pacific Northwest Laboratory, Richland, Washington. June 1967.

16. F. W. Albaugh, S. H. Bush, J. J. Cadwell, D. R. de Halas, and D. C. Worlton. Quarterly Progress Report, January, February, March, 1967, Reactor Fuels and Materials Branch of USAEC Division of Reactor Development and Technology, BNWL-435. Pacific Northwest Laboratory, Richland, Washington. June 1967.

17. F. L. Oetting. "The Chemical Thermodynamics Properties of Plutonium Compounds," Chemical Reviews, vol. 67, no. 3, 1967.

18. T. K. Engel. "Heat Capacity of Plutonium Dioxide from 300 to 1100 °K," Pacific Coast Regional Meeting, American Ceramic Society, November 1-3, 1967, San Francisco, California.

19. T. D. Chikalla, C. E. McNeilly, and R. E. Skavdahl. "The Plutonium-Oxygen System," J. of Nuclear Materials, vol. 12, 2, pp. 131-141. 1964.

20. J. F. Lagedrost, D. F. Askey, V. W. Storhok and J. E. Gates. "Thermal Conductivity of PuO_2 as Determined from Thermal Diffusivity Measurements," Nuclear Applications, vol. 4, pp. 54-61. January 1968.

21. T. G. Godfrey, W. Fulkerson, T. G. Kollie, J. P. Moore, and D. L. McElroy. Thermal Conductivity of Uranium Dioxide and Armco Iron by an Improved Radial Heat Flow Technique, ORNL-3556, Oak Ridge National Laboratory, Oak Ridge, Tennessee. June 1964.

22. E. O. Speidel and D. L. Keller. Fabrication and Properties of Uranium Mononitride, BMI-1633, Battelle Memorial Institute, Columbus, Ohio. 1963.

23. A. Biancheria. "The Effect of Porosity on Thermal Conductivity of Ceramic Bodies," Trans. Am. Nucl. Soc., vol. 9, 1, June 1966.

FAST-REACTOR NITRIDES RESEARCH

R. E. Nightingale

SYNTHESIS OF MIXED URANIUM-PLUTONIUM NITRIDES BY CARBOTHERMIC REDUCTION OF OXIDES

E. T. Weber and W. O. Greenhalgh

A nitride fuel cycle for fast-breeder reactors based on synthesis of fuel material from the oxides, rather than from the pure metal, is potentially competitive with carbide and oxide fuel cycles. A technical basis for such a scheme exists with the application of the carbothermic reduction of oxides under nitrogen. This process is being adapted and developed for application to plutonium-bearing nitride fuel materials. The purpose of the present work is to demonstrate on a laboratory scale the feasibility for large-scale carbothermic synthesis of nitrides. Included in this approach is the evaluation of fuel material characteristics and behavior as a function of composition realized from the synthesis studies.

In our previous work on this synthesis method,[1] kinetic data were obtained on the overall reaction

$$MO_{2(s)} + 2\ C_{(s)} + 1/2\ N_{2(g)} \rightarrow MN_{(s)} + 2\ CO_{(g)} \quad ,$$

$$M = U \text{ and/or } (U+Pu) \quad .$$

These data were used to establish temperature range, time, and nitrogen gas-flow conditions for optimizing the conversion. A tungsten particle-bed reactor was developed and installed in a glove-box to provide optimum conditions for synthesis of approximately 50-g batches of (U,Pu) nitride. Descriptions of the reactor vessel, associated equipment, and material preparation methods have been given in previous reports.[1,2] Also, it was tentatively established that the use of alternating hydrogen and nitrogen purges through the reactant bed at temperatures of 1000 to 1200 °C is effective in removing both free and combined carbon after the primary conversion in nitrogen.

During this quarter, efforts were concentrated on two objectives: a) establishing reproducible synthesis of 50-g batches of mixed nitrides with compositions suitable for property and irradiation studies, and b) confirming the effectiveness of sequential hydrogen-nitrogen cycles in removing combined carbon from (U,Pu) carbonitrides.

Experimentation with the run procedures developed during work on the conversion of UO_2 to UN continued for the first three runs on U+Pu compositions. Material synthesized in these runs had oxygen contents from 0.04 to 0.82 wt% and carbon contents between 0.5 to 0.9 wt%. Problems with the apparatus compromised the first two runs, but the third run was properly conducted. The fourth run in the series (UPCN-4) involved an attempt to optimize the procedures on the basis of all previous experience. Changes from the

previous pattern, resulting in lower carbon levels in the run UPCN-4, were: a) a reduction in the amount of carbon in excess of stoichiometric requirements from ∿0.9 to ∿0.5 wt% and b) an increase in H_2 flow rates used during the cycles for removal of excess carbon.

A summary of the run conditions used in UPCN-4 is as follows:

1. The primary conversion of approximately 99.6% of the oxide to nitride or carbonitride was obtained at temperatures of 1600 to 1700 °C with nitrogen flow rates of approximately 40 cm^3/min/g (reactant) and was completed after 4 to 6 hr;
2. After reducing the temperature to approximately 1200 °C in either nitrogen or helium, hydrogen was passed through the bed at a flow rate of approximately 80 cm^3/min/g (reactant) for about 3 hr or until the evolution of methane from the reaction of hydrogen with excess free carbon was completed;
3. A nitrogen flow rate sufficient to displace the hydrogen was established without a temperature change and continued for 1 to 2 hr. This step allowed the displacement of combined carbon from the carbonitride solid solution primarily through formation of higher nitrides;
4. A second hydrogen purge similar to the previous one was used to remove the newly formed free carbon;
5. Temperature was increased to ∿1600 °C in a helium or argon purge to remove excess nitrogen and assure a uniform mononitride phase.

The batch preparation procedures for preparing particles were found to be of considerable importance to successful synthesis of homogeneous compositions with low carbon and oxygen content. An extremely poor result from run UPCN-5 was traced to an error in binder addition during particle preparation. Too little binder resulted in weak particles which were reduced to powder and entrained in the gas stream during the conversion. It is also probable that variations in the pattern of CO evolution between runs experiencing the same conditions were due to differences in particle characteristics.

The procedure used in run UPCN-4 was fixed as the standard for subsequent "production" runs. Material synthesized in these runs was to be sintered and used in property-and irradiation behavior-studies. Characteristics of the material synthesized in three of the four "production" runs and one "special" run are given in the following table, along with the characteristics of uranium nitride made previously, by using very similar procedures. The uniformity of carbon and oxygen contents in these materials confirms the reproducibility of the carbothermic synthesis technique using the procedures developed in this study. All the

Composition Data for Several Mixed Nitrides Synthesized by Carbothermic Reduction

Run	UCN-2	UPCN-4	UPCN-6	UPCN-7	UPCN-8[a]
N_2	4.84 wt%	5.22 wt%	5.30 wt%	5.38 wt%	5.32 wt%
O_2	0.04 wt%	0.10 wt%	0.08 wt%	0.19 wt%	0.14 wt%
C	0.25 wt%	0.17 wt%	0.18 wt%	0.22 wt%	0.28 wt%
U/Pu	(U only)	4.0	4.0	4.0	4.0
Lattice Parameter	4.890 Å	4.893 Å	4.893 Å	4.893 Å	4.894 Å

(a) *Run UPCN-8 was a "special" experimental run and conditions were not identical with those of UPCN-4, 6, and 7.*

material synthesized in the "production" runs was single-phase nitride with consistent lattice parameters.

A photograph of the as-synthesized nitride particles is shown in Figure 6.1. The microstructures of these particles were virtually identical with those for the UN particles reported previously.[2] An analysis of the U/Pu ratio obtained on the carbothermic nitrides was in good agreement with the starting U/Pu ratio, indicating little or no selective losses of plutonium during the conversion. At the present time, fourteen synthesis runs on both uranium and uranium-plutonium bearing compositions have been completed in the tungsten reactor system. There is no evidence of physical or chemical degradation of the reactor vessel as a result of the temperature cycling to 1700 °C or carbonaceous atmospheres of H_2, N_2, and He to which it has been subjected.

Besides the "production" runs, a separate experiment was conducted to

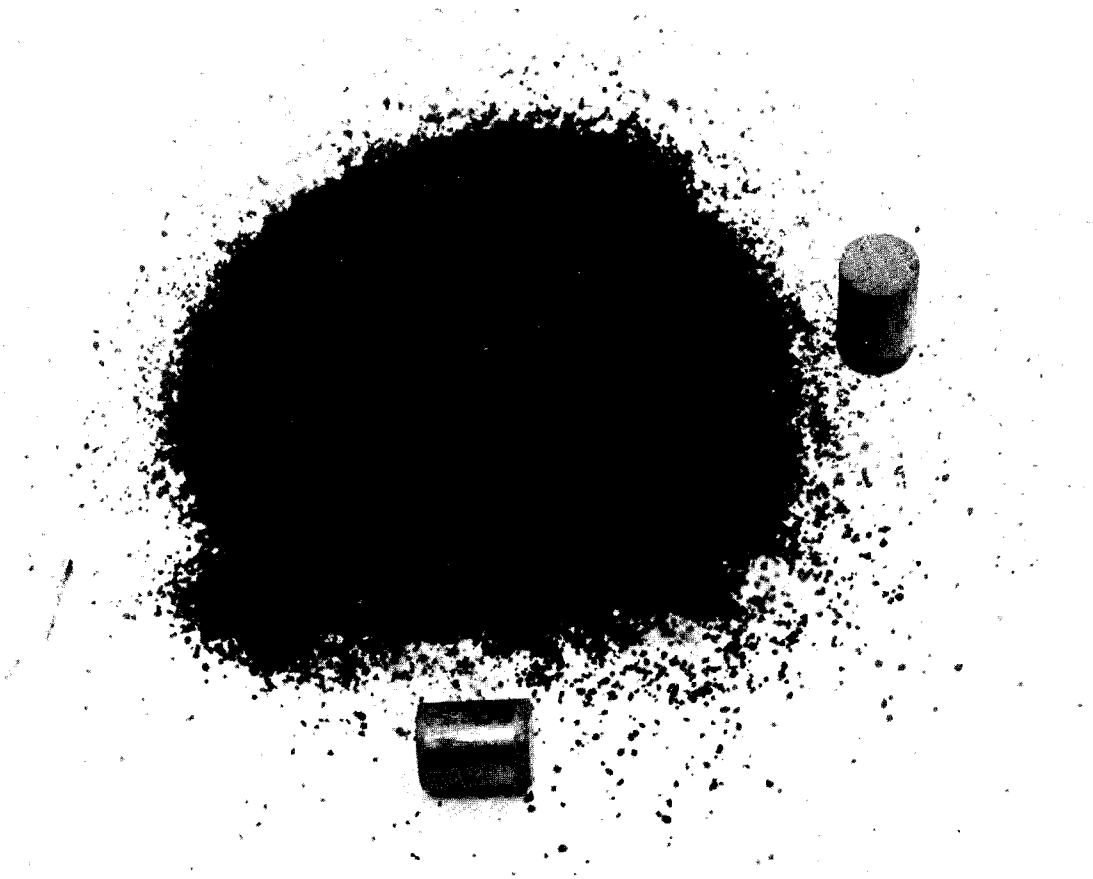

Neg 0680796-4

FIGURE 6.1. Particles of (U,Pu) Nitride from a Portion of One Batch Synthesized by Carbothermic Reduction. (Note: Pellets made from a previous run are 0.20 in. in diameter).

evaluate more closely the effectiveness of the hydrogen-nitrogen-hydrogen scheme for removal of both free and combined carbon. For this experiment (UPCN-8) the standard carbothermic cycle was run, but was divided into several sections. Cool-down of the furnace to ambient temperature and sampling of the bed material was imposed between Steps (1) and (2) [Sample A] between Steps (3) and (4) [Sample B] of the previously stated operating scheme. Sampling thusly, it was possible to determine the change in carbon content of the material as a result of the first hydrogen treatment and the subsequent nitrogen-hydrogen treatment. Characterization of the end product [Sample C] and the interim samples consisted of chemical and X-ray analyses. Also, the carbon monoxide and methane contents of the gases evolved during the various portions of the reaction were monitored and recorded.

The results of the analyses on the samples taken during the experiment are shown in the following table. It is immediately apparent that the hydrogen and nitrogen-hydrogen steps in the synthesis procedure are both effective in removing carbon. During the first hydrogen cycle, methane evolution was recorded immediately upon introduction of hydrogen. The rate of elution did not change for several hours, and then fell off in steps to zero. The total time to complete the reaction was approximately 7 hr.

Analytical Data From Experiment UPCN-8

	Sample A	Sample B	Sample C
N_2	4.76 wt%	4.92 wt%	5.32 wt%
O_2	0.10 wt%	0.09 wt%	0.14 wt%
C	1.35 wt%	0.68 wt%	0.28 wt%
Lattice Parameter	4.904 Å	4.900 Å	4.894 Å

The difference in carbon content between Samples B and C confirms the effectiveness of the nitrogen-hydrogen sequence in the removal of dissolved carbon from a carbonitride solid solution. After the nitrogen cycle at 1200 °C, evolution of methane was again recorded upon introduction of hydrogen. The marked reduction in lattice parameter between Samples B and C is indicative of the removal of carbon from the nitride lattice. It is also significant that the amount of carbon removed during this step (0.4 wt%) matches the gain in nitrogen content. The change in lattice parameter between Sample A and B was unexpected. This, of course, implies that a reaction occurs in hydrogen at 1200 °C, which results in the removal of combined carbon from the carbonitride lattice. No explanation for this result has been formulated.

The most significant results of this work on carbothermic synthesis of nitrides are summarized as follows:

- Procedures have been developed that allow the reproducible synthesis of nitride compositions containing ∿1000 ppm oxygen and ∿2000 ppm carbon with variations of less than ∿0.06 wt% of any anion.
- Approximately 150 g of carbothermic (U,Pu) nitrides have been synthesized with compositions suitable for use in evaluation of

properties and irradiation stability for potential fuel applications.

- The tungsten particle-bed reactor system developed for this work appears to be capable of continuous, long-term service under present operating conditions.
- The effectiveness of the nitrogen-hydrogen techniques (formulated on theoretical grounds) for removal of combined carbon from a carbonitride solid solution has been confirmed.

SINTERING OF MIXED NITRIDES OBTAINED BY CARBOTHERMIC REDUCTION

E. T. Weber

Sintering has been used to obtain dense samples for property and irradiation studies throughout our work on mixed nitrides. The procedures developed for densification of metal-derived nitrides were applied to carbothermic nitrides during this quarter. This work had two major objectives: 1) to densify samples of carbothermic nitrides for use in property measurements and as fuel for an irradiation experiment and 2) to determine whether the carbon and oxygen levels resulting from carbothermic synthesis would have a significant effect on sintering behavior relative to more pure nitrides. Approximately 150 g of usable mixed nitride pellets were obtained for use as samples.

The general procedures used in sintering the carbothermic nitrides were similar to those reported previously.[1,3] However, two different milling techniques were used to increase the activity of the powders prior to pressing. The techniques used were conventional dry ball milling for 92 to 96 hr and dry vibratory milling* for 3 hr, with tungsten carbide jars and balls used in both cases. Another departure from previous procedure was in the sintering cycle, where a vacuum outgassing period of approximately 30 min at either 1250 or 1400 °C was established, depending on whether the sintering atmosphere was helium or nitrogen. Green densities obtained in pressing near 60,000 psi were approximately 64 to 66% TD.

Materials obtained by carbothermic synthesis, including both UN and (U,Pu)N, were sintered to densities between 12.4 and 13.5 gm/cm^3 (approximately 87 to 95% TD). Densities measured on the basis of geometrical and fluid displacement volume measurements agreed within 0.2 gm/cm^3 in most cases. Sintering conditions and resulting densities for five batches of carbothermic nitrides are listed in Table 6.1.

From these data, it is apparent the carbothermic nitrides can be sintered to densities similar to those which have been reported for pure nitrides using similar sintering conditions.[1,4] Also, the 3 hr vibratory-milling operation is virtually equivalent to a 94 to 96 hr ball-milling operation. A comparison of the sintered densities indicates that the

* *Vibratory mill was a "Vibratom" laboratory vibrator manufactured by Shultz-O'Neill Company, Minneapolis.*

TABLE 6.1. Sintering Conditions for Carbothermic Nitrides

Run	Uranium Nitride		Uranium-Plutonium Nitride		
	UCN-1	UCN-2/4	UPCN-2	UPCN-4	UPCN-6/7
Milling Conditions					
Ball Mill (in argon), hr				96	94
Vibratory Mill (in argon), hr	2.5	3.0	3.0		
Sintering Cycle					
Offgas Temp, °C	1250	1250	1250	1400	1400
Sintering Temp, °C	1800	1800	1800	1900	1800
Sintering Time, hr	4	4	4	4	4
Sintering Atmosphere	Helium	Helium	Helium	Nitrogen	Nitrogen
Sintered Density					
Average					
gm/cm^3	12.8	13.0	12.4	13.3	12.6
% TD	∿90.0	∿91.5	∿87.0	∿94.0	∿89.0
Maximum					
gm/cm^3	13.0	13.1	12.5	13.5	12.8
% TD	∿91.5	∿92.5	∿88.0	∿95.0	∿90.0

uranium-only compositions sinter to slightly higher densities than the compositions containing plutonium under the same sintering conditions. It is also apparent that a 1900 °C sintering temperature yields higher densities than sintering at 1800 °C. However, such observations based on relative densities must be qualified on the possible influence of less highly controlled variables such as milling effectiveness, degree of oxidation, and condition of powder surface.

Composition data for the various materials before and after sintering are compared in Table 6.2. Both a uranium and a uranium-plutonium bearing composition with carbon contents in excess of 5000 ppm were included (Samples UCN-1 and UPCN-2). Results from a comparison of densities obtained with these compositions to those obtained for compositions with approximately 2000 ppm carbon indicate a possible but relatively insignificant effect of carbon content on sinterability. Under the presently employed processing conditions, some oxidation of the powder occurs during the milling and pressing operation. The increase in oxygen content shown in Table 6.2 for Samples UCN-2/4 and UPCN-2 represent the oxygen uptake between as-synthesized and sintered material. Oxygen contents listed for Samples UPCN-4 and UPCN-6/7 indicate that oxygen content in these compositions actually decreased as a result of the sintering cycle. The carbon content of these two samples and of UPCN-2 also shows a similar decrease.

TABLE 6.2. Compositions of Carbothermic Nitrides Before and After Sintering

Run	Component	As-Synthesized	Milled	Sintered
UCN-1	N_2, wt%	4.70		
	O_2, wt%	0.36		
	C, wt%	0.55		
	Lattice Parameter, Å	4.896		4.897
	U/Pu Ratio	U only		
UCN-2/4	N_2, wt%	4.77		4.41
	O_2, wt%	0.55		0.70
	C, wt%	0.35		0.70
	Lattice Parameter, Å	4.889		
	U/Pu Ratio	U only		
UPCN-2	N_2, wt%	4.50		4.24
	O_2, wt%	0.13		0.89
	C, wt%	0.81		0.60
	Lattice Parameter, Å	4.899		4.898
	U/Pu Ratio	4:1		
UPCN-4	N_2, wt%	5.22	5.34	5.27
	O_2, wt%	0.10	0.40	0.30
	C, wt%	0.17	0.18	0.11
	Lattice Parameter, Å	4.893		4.891
	U/Pu Ratio	4:1		4.05:1 (measured)
UPCN-6/7	N_2, wt%	5.20	5.34	5.33
	O_2, wt%	0.14	0.40	0.18
	C, wt%	0.20	0.20	0.10
	Lattice Parameter, Å	4.893		4.891
	U/Pu Ratio	4:1		

Since the reduction in both carbon and oxygen content is approximately the same, a probable mechanism for this effect is a further reaction (essentially carbothermic reduction) of carbon and oxygen yielding CO which is released during the high-vacuum offgas period at 1400 °C during sintering. The decrease in lattice parameter resulting from sintering these compositions may indicate removal of these impurities from the nitride crystal lattice. Although unanticipated, this phenomenon serves to further reduce the difference in composition between metal-derived and carbothermic nitrides. The sintered composition for samples from batch UPCN-6/7 represents oxygen and carbon levels which have been exceeded in metal-derived nitrides under some processing conditions.

Microstructures of the sintered carbothermic nitrides are virtually identical with those of metal-derived nitrides sintered to similar densities. Figure 6.2 shows etched microstructures from two the samples covered in the tables. The etching conditions were similar for both samples, but the sample containing approximately 6000 ppm carbon has responded differently to the chemical etchant. Unetched microstructures for the two compositions are identical except for the difference in volume of porosity and oxide phase.

Possible conclusions drawn from this very general work on sintering of nitrides obtained by carbothermic reduction are as follows:

- Sintered densities between 87 and 94% may be obtained on carbothermic nitrides with the methods developed for sintering metal-derived nitrides.
- Carbon contents to 0.8 wt% have a negligible influence on sintering behavior of U or (U, Pu) nitrides.
- A reduction in both carbon and oxygen levels occurs for carbothermic nitrides exposed to a high vacuum at temperatures between 1250 and 1400 °C during the sintering cycle.

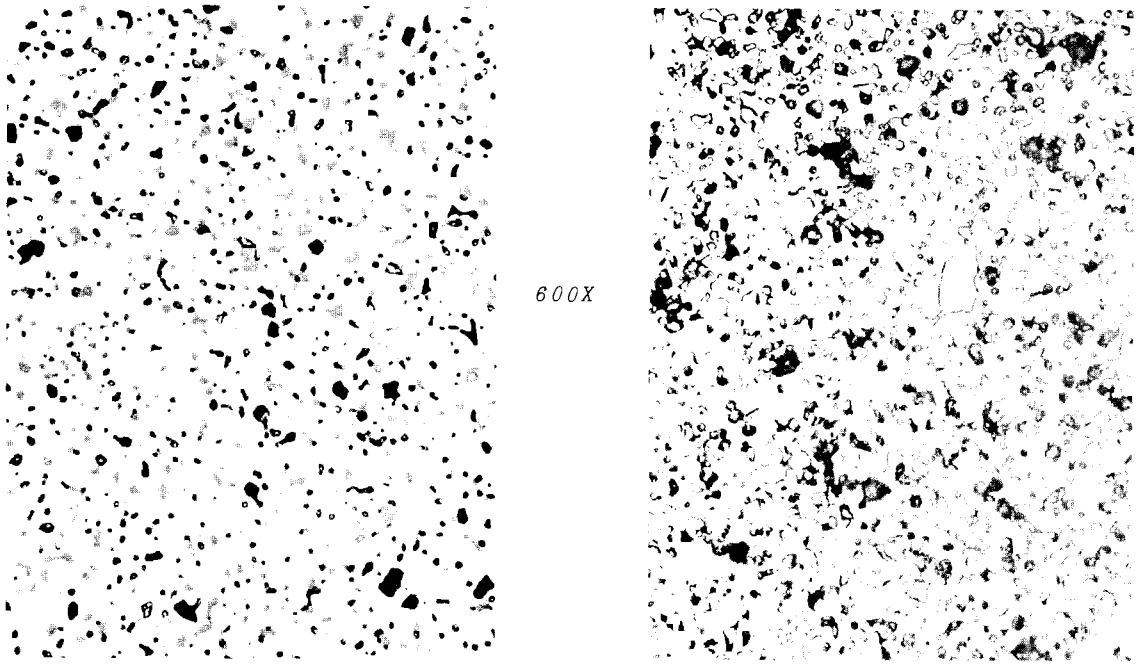

600X

Unetched *Etched*

(a) Sample UPCN-2 - Carbon Content ≈ 0.6 wt% (∿87% TD)

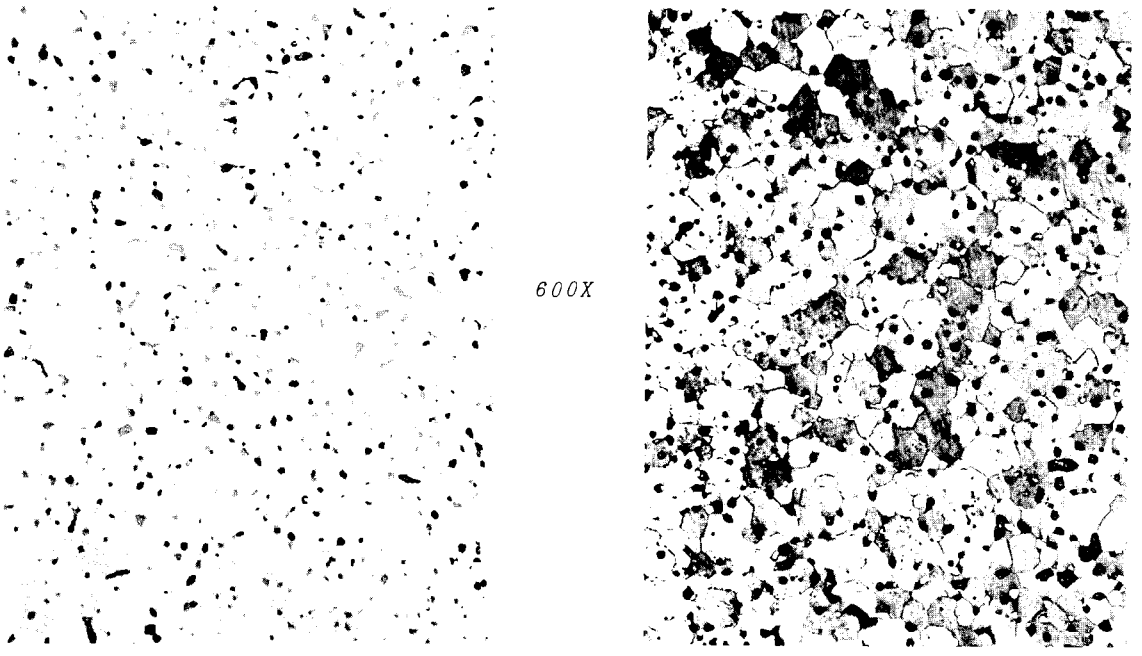

600X

Unetched *Etched*

(b) Sample UPCN-4 - Carbon Content ≈ 0.1 wt% (∿94% TD)

FIGURE 6.2. Microstructures of Sintered Carbothermic Nitrides. [Note effect of etchant on high carbon Sample (a) (H_2O-HNO_3-HF etchant)].

ADVANCED NITRIDE SYNTHESIS STUDIES*

E. A. Coppinger

A study is underway to determine the feasibility of starting with a uranyl nitrate hexahydrate (UNH) and sugar mixture to form UN by the carbothermic reaction. The study is also aimed at providing information so that a continuous process can be devised to produce UN-PuN mixtures by the same approach. Initial work on limiting conditions, modification of a spray reactor, and sugar solubility in aqueous UNH-HNO_3 solutions was reported earlier.[5]

The primary objective of the experimental program has been to determine if an intimate mixture of UO_2 and carbon can be obtained by calcining UNH with sugar in a nitrogen atmosphere in a spray reactor. An intimate mixture of UO_2 and carbon can be used as an intermediate in the production of UN by the carbothermic route. Also, once formation of an intimate mixture of UO_2 and carbon has been demonstrated, operation of a spray calciner at higher temperatures in nitrogen atmospheres could lead to a one-step process that produces mixed nitride.

Eight experimental runs were made during the quarter. An 8 in. diam by 10 ft long spray reactor was used at temperatures of 600 to 800 °C. In these runs, powder characteristics and carbon content were investigated primarily as a function of the sugar/uranium weight ratio in the feed, and the gas/liquid mass ratio at the feed nozzle. In all eight runs, a lump-free powder with a fairly uniform particle size was produced. When the sugar/uranium weight ratio was 1.27, 1.50, and 1.92, the average carbon content in the powder was 5.4, 9.0, and 12.6 wt%, respectively. For this series of runs, the gas/liquid mass ratio was maintained between 1.0 and 1.4. This series of runs marks the first time the carbon content has approached or exceeded the stoichiometric amount required for subsequent UN production (8.16%) without the formation of large brownish lumps in the product.

Earlier runs, during the previous two quarters, resulted in the formation of heterogeneous mixtures of fine black powder and brownish agglomerates when gas/liquid mass ratios of about 0.3 to 0.6 were used in conjunction with sugar/uranium ratios above 0.86. Thus, the data obtained this quarter illustrate the importance of using high gas-flow rates to provide adequate atomization of the very viscous feed solution.

Further analytical work, including X-ray diffraction and thermogravimetric tests, is underway for the powders. The powders are also being tested as intermediates in UN production.

* *Although related to the Fast-Reactor Nitrides Program, this study is supported by the 1% discretionary AEC Funds.*

REFERENCES

1. *J. J. Cadwell, D. R. de Halas, R. E. Nightingale and D. C. Worlton. Quarterly Progress Report, July-September 1967, Reactor Fuels and Materials Branch of USAEC Division of Reactor Development and Technology, BNWL-658. Pacific Northwest Laboratory, Richland, Washington, February, 1968.*

2. *J. J. Cadwell, D. R. de Halas, R. E. Nightingale and D. C. Worlton. Quarterly Progress Report, October-December 1967, Reactor Fuels and Materials Branch of USAEC Division of Reactor Development and Technology, BNWL-668. Pacific Northwest Laboratory, Richland, Washington, March, 1968.*

3. *F. W. Albaugh, S. H. Bush, J. J. Cadwell, D. R. de Halas, and D. C. Worlton. Quarterly Progress Report, January-March 1967, Reactor Fuels and Materials Branch of USAEC Division of Reactor Development and Technology, BNWL-435. Pacific Northwest Laboratory, Richland, Washington, June, 1967.*

4. *M. A. Goodyear, R. A. Smith, and D. E. Kizer. Progress Relating to Civilian Applications During October Through December 1967, p. A-3, BMI-1826, Battelle Memorial Institute, Columbus, Ohio, January, 1968.*

5. *F. W. Albaugh, S. H. Bush, J. J. Cadwell, D. R. de Halas, and D. C. Worlton. Quarterly Progress Report, April-June 1967, Reactor Fuels and Materials Branch of USAEC Division of Reactor Development and Technology, BNWL-473. Pacific Northwest Laboratory, Richland, Washington, September, 1967.*

NONDESTRUCTIVE TESTING

J. C. Spanner

EDDY CURRENT METHODS

MULTIPARAMETER STUDIES

H. L. Libby

The principal objective of the eddy-current multiparameter nondestructive test studies now in progress is to develop techniques for gathering needed information about test specimens not obtainable by use of conventional single-frequency eddy-current test equipment. The need for such techniques in the nuclear field increases as the serviceability requirements of materials and parts become more stringent, and as more specialized inspection problems arise due to related technological advances.

Electronic circuits were developed for simplifying and standardizing the instrument design for multiple-frequency multiparameter eddy current testers. Techniques were also developed for applying the multiparameter test principles to pulsed eddy-current test systems. Advances made in both of these areas have inventions potential so details will be reported after patent clearance.

THERMAL METHODS

REMOTE TRANSIENT METHOD FOR SURFACE THERMAL IMPEDANCE DETERMINATION

J. D. Jensen

The program to develop a remote infrared transient method for determining the surface thermal impedance values for a wide range of materials was continued this quarter. The radiometer drift problem mentioned last quarter has been largely overcome by use of an electronic system that substitutes an artificially-generated linear run-down for the trailing edge of the temperature transient function. Construction of this system was completed this quarter, and preliminary data obtained for a variety of materials indicate that the system is extremely sensitive to small differences in the thermal properties of the materials.

The simulation system supplying the linear rundown is composed of time delay circuits, a sample-and-hold circuit, and an operational integrating amplifier. The initial portion of the temperature transient is processed by the Laplace transformation circuits in the usual manner. After an initial time delay (which is adjustable to accommodate a variety of test samples), a sample of the value of the transient function at the instant is obtained and stored by the sample-and-hold circuit. The sample value is converted to a dc level which is integrated by the operational integrating amplifier. The resulting linear ramp is then substituted for the trailing edge of the temperature transient function and is fed directly to the Laplace transformation circuits. The surface thermal impedance plots then obtained demonstrate the required convergence properties.

Figure 7.1 shows the measured, surface thermal impedance values for a large number of materials, ranging from materials with high thermal conductivities to materials with very low thermal conductivities. The data points shown on the plot are normalized to the teflon sample. A line from the origin to a particular point represents the normalized magnitude of the impedance, while the angle between the line and the real axis represents the impedance phase angle. Differentiation of the various materials is quite evident, which indicates that the test technique is very sensitive to material variation.

Analytical work performed this quarter indicated that the observed error in impedance phase angle, due to simulation of the trailing edge of the temperature transient function, was approximately five degrees.

ULTRASONIC METHODS

BASIC STUDIES OF ULTRASONIC WAVES

C. E. Fitch, Jr., and F. L. Becker

Propagation of ultrasonic pulses in attenuating media is being studied to further the understanding of basic behavior. Ways to mathematically represent broad frequency band signals are still being sought; however, no conclusive results have yet been produced. Meanwhile, other aspects of the wave studies, which were heretofore temporarily discontinued, are being reactivated.

The wave analysis computer program output includes reflection- and transmission-factor data graphically plotted over any range of wave incident angles. Some errors in the plotting routine existed in the past, but these have now been corrected.

To explore the effects of losses on the reflection- and transmission-factors, attenuation coefficients for both longitudinal and shear waves must be known over a range of frequencies. Experimental data for both types of waves are available for only a few materials. Of these limited data, none have apparently been corrected for shear wave diffraction effects. The correction for longitudinal wave diffraction effects has been the subject of many studies in the literature, and calculating techniques are available. Similar methods are not available for shear wave corrections, although an experimental method has been devised.[1] Full utilization of this new method has not yet been undertaken.

It is instructive to examine the effects of attenuation on the reflection and transmission factors by making some unverified assumptions about the way in which waves attenuate due to grain scattering since this is the major source of losses in granular materials. Grain scattering formulas and tables have been provided in the literature.[2] These scattering values apparently can be used for commercial materials if average grain volumes and diameters are known. The averages are obtained by analysis of photomicrographs of actual grain structures. Here again, experimental data are limited.

If it has been assumed that all grains are spherical and of the same

diameter and the tables and procedures in Reference (2) are used, scattering factors can be obtained and attenuation curves plotted for a number of materials and grain sizes. To illustrate the methods, longitudinal and shear-wave scattering factors for three grain sizes were calculated for nickel (Table 7.1).

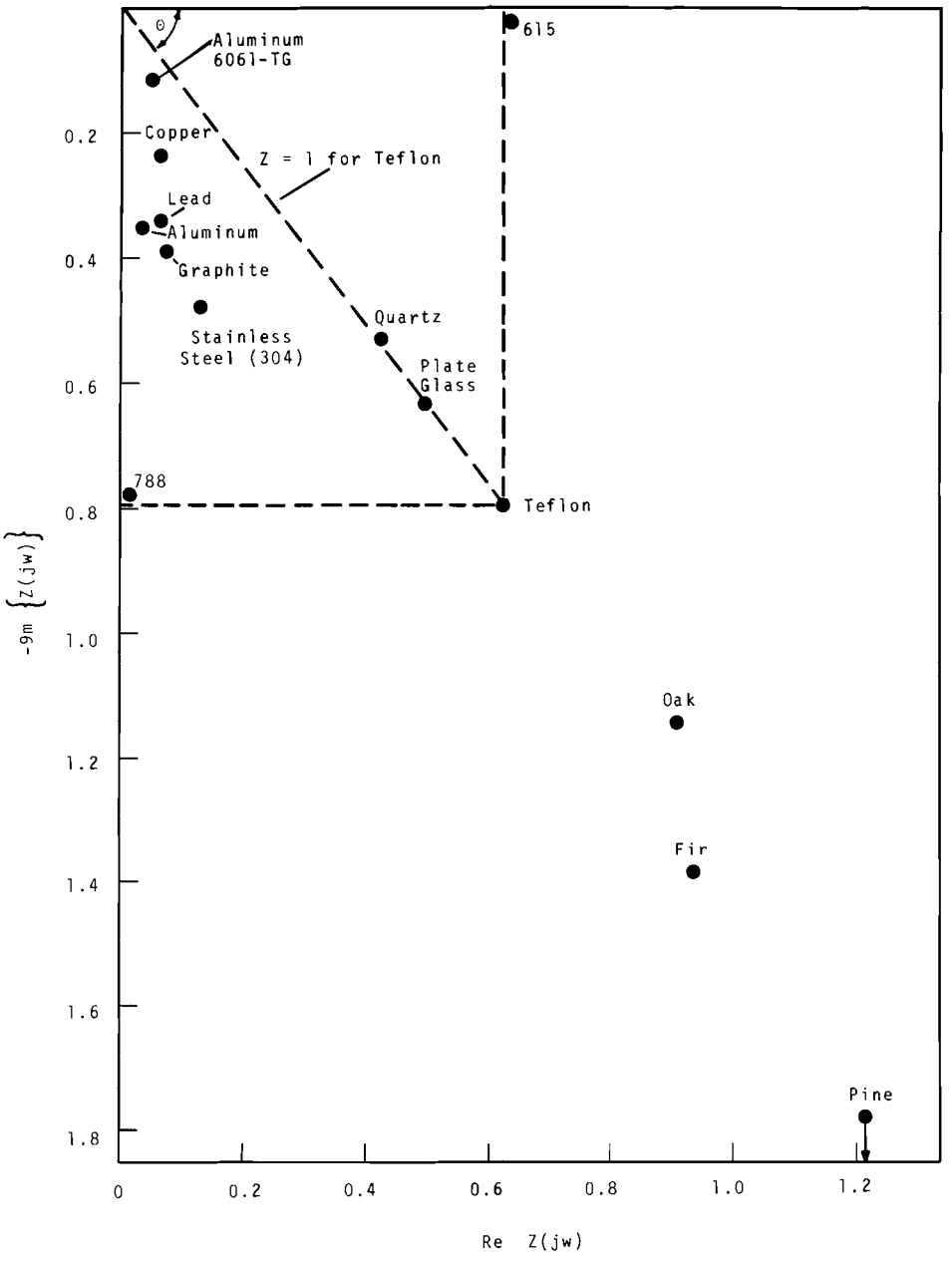

FIGURE 7.1. Thermal Surface Impedance Values for Materials Ranging from Good Conductors to Good Insulators

TABLE 7.1. Scattering Factors for Nickel

$\alpha_{R\ell}$(dB/ft)	α_{Rs}(dB/ft)	$\alpha_{s\ell}$(dB/ft)	α_{ss}(dB/ft)	f(MHz)	Grain Diameter, in.
4.8×10^{-3}				0.378	0.010
	1.77×10^{-3}			0.187	0.010
		1.62×10^{3}		37.8	0.010
			1.66×10^{4}	18.7	0.010
9.6×10^{-3}				0.757	0.005
	3.54×10^{-3}			0.375	0.005
		3.24×10^{3}		75.7	0.005
			3.33×10^{4}	37.5	0.005
4.8×10^{-2}				3.78	0.001
	1.77×10^{-2}			1.87	0.001
		1.62×10^{4}		378	0.001
			1.66×10^{5}	187	0.001

$V\ell = 2.377 \times 10^{5}$ in./sec.
$Vs = 1.178 \times 10^{5}$ in./sec.
$\rho = 0.322$ lb/in.^{3}

The first and second columns give the attenuation factor for longitudinal and shear waves having a wave length such that conventional Rayleigh scattering (proportional to the fourth power of frequency) takes place. The third and fourth columns are longitudinal and shear attenuation factors for stochastic[2] scattering (proportional to the second power of frequency). The fifth column gives the frequencies for the above factors by using the assumed grain diameters shown in column six and the stated velocities and density.

The method used to plot the attenuation at any frequency is given in Reference 2. Briefly, the Rayleigh points are established on log-log paper, and then vertical lines are erected from the stochastic frequencies. The center of a circle is found such that the circle passes through the Rayleigh point and its corresponding stochastic frequency line at a slope of two. This then establishes arcs of circles which have the slope of four (fourth power scattering) at the Rayleigh points and the slope of two (second power scattering) at the stochastic frequencies. These arcs together with the Rayleigh and stochastic points are plotted in Figure 7.2. Using these plots, attenuation at any frequency can be obtained and used to examine its effect on the reflection and transmission factors.

As an example, the reflection and transmission factors were plotted in Figures 7.3, 7.4, and 7.5 for a water-nickel interface at a frequency of 20 MHz for the three grain sizes

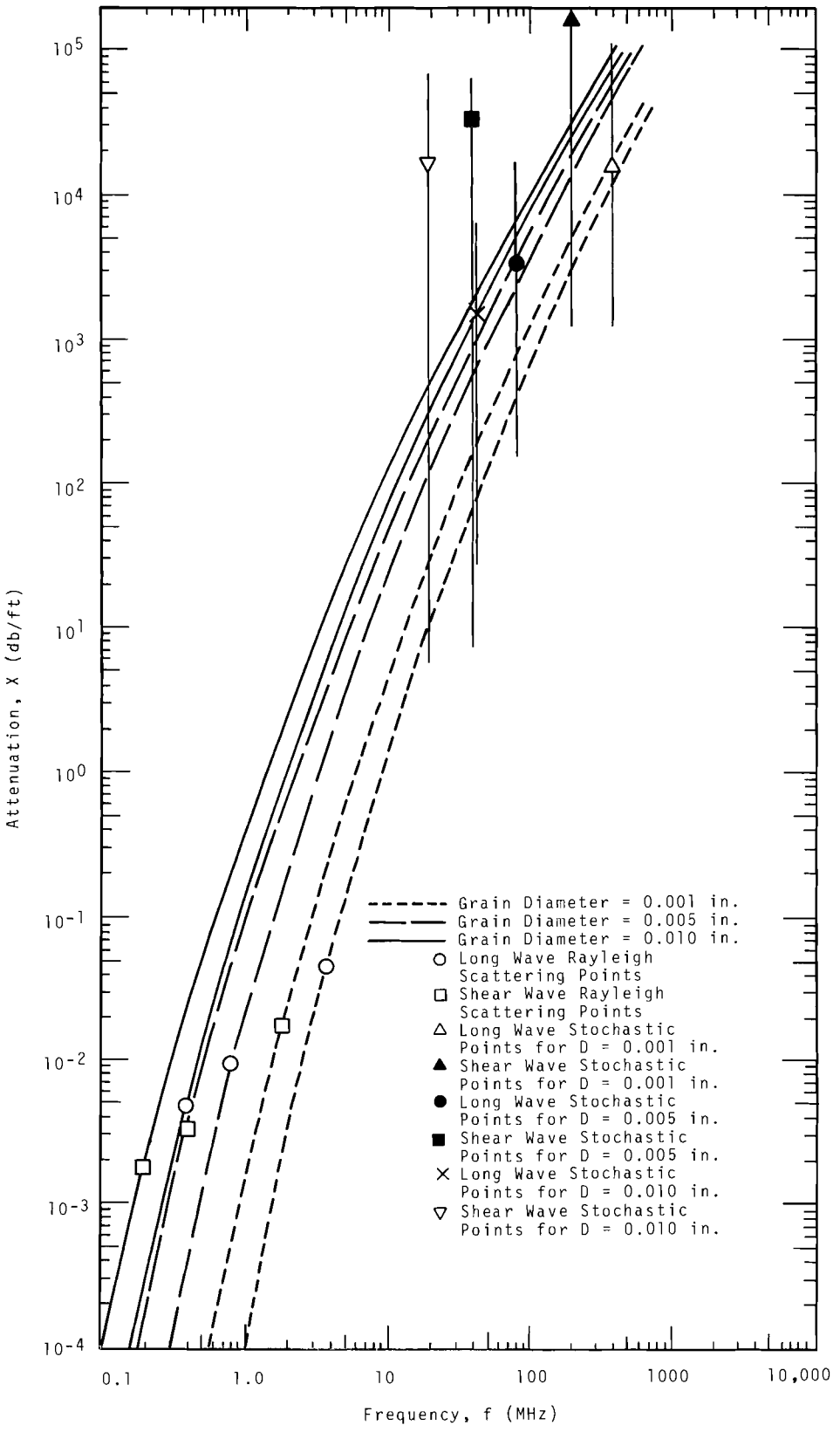

FIGURE 7.2. Nickel Attenuation for Three Grain Sizes

shown in Table 7.1. These graphs are for longitudinal waves incident from the water to the nickel at incident angles ranging from 0 to 45°. The reflected longitudinal wave is labeled R_ℓ, the transmitted shear wave T_s, and the transmitted longitudinal wave T_ℓ. Only minor differences are observable in the curves except near the surface wave critical angle (32.2°) where the reflected wave decreases in amplitude progressively with increasing grain size.

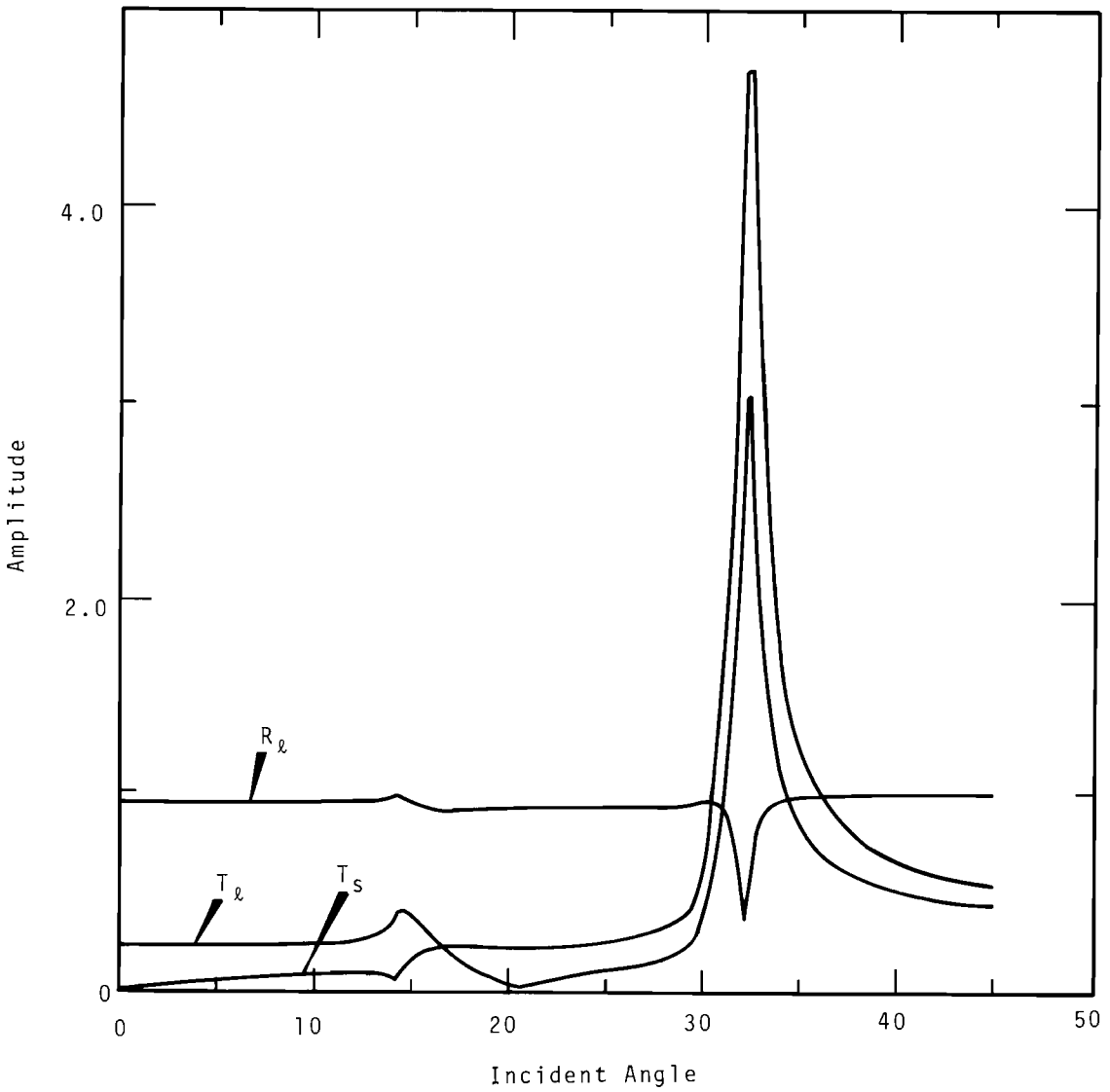

FIGURE 7.3. Reflection and Transmission Factors from Water to Nickel, D = 0.010 and f = 20 MHz

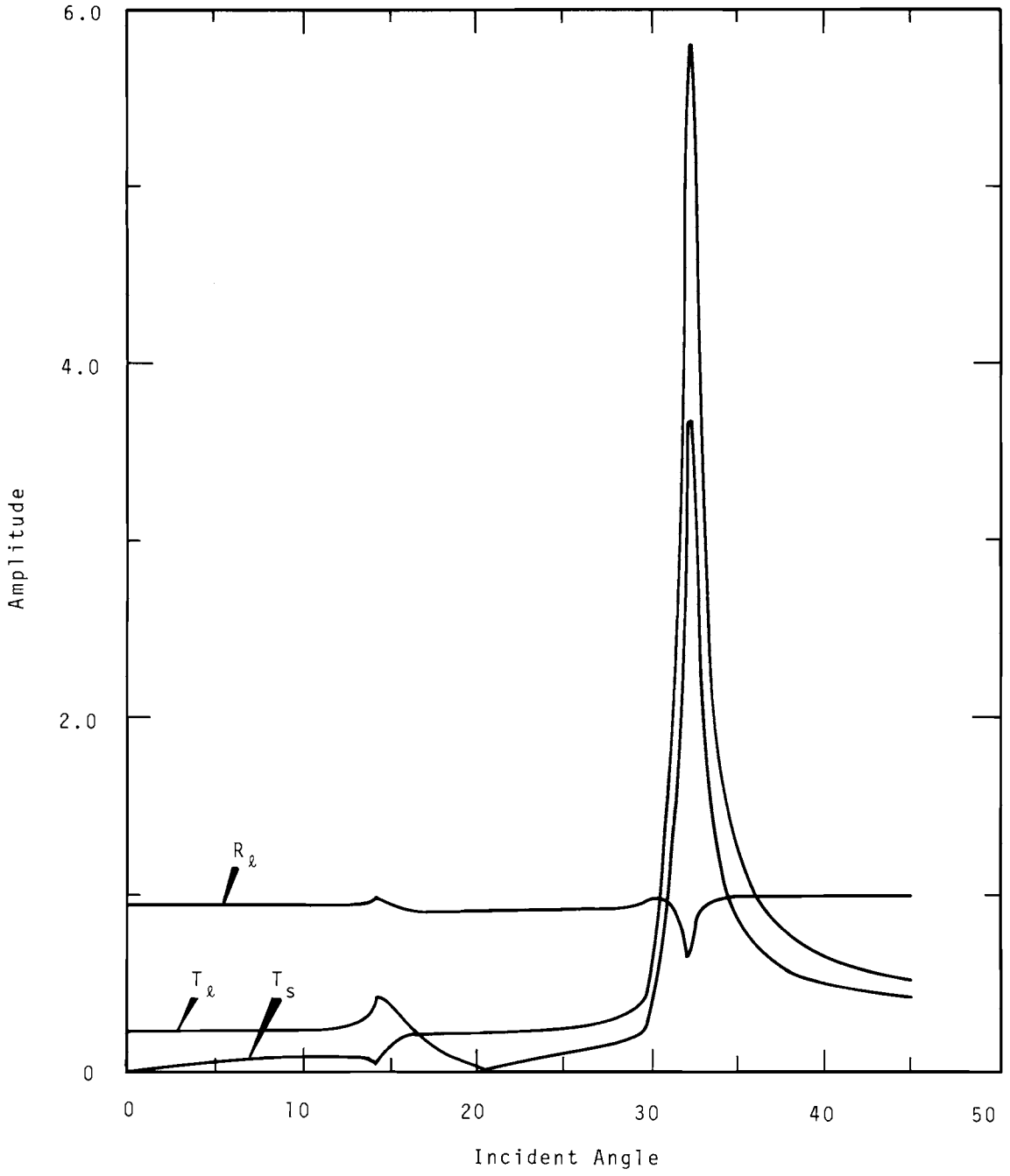

FIGURE 7.4. Reflection and Transmission Factors from Water to Nickel, D = 0.005 in. and f = 20 MHz

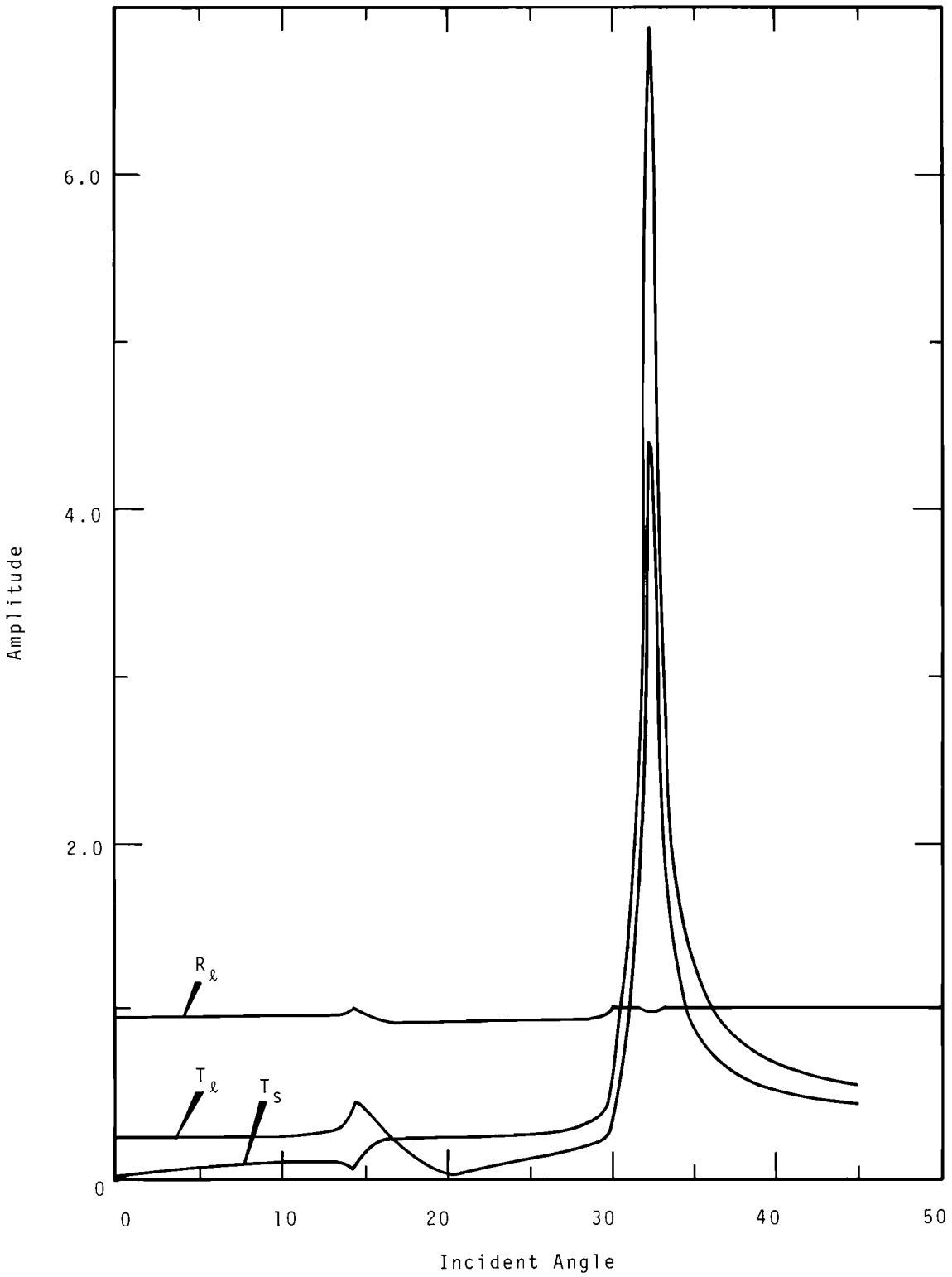

FIGURE 7.5. Reflection and Transmission Factors from Water to Nickel, D = 0.001 in. and f = 20 MHz

In Figures 7.6 and 7.7, the reflection and transmission factors are plotted for shear and longitudinal waves incident from within the nickel to the water interface again at a frequency of 20 MHz. Reflection and transmission factors again are labeled R and T with subscripts appropriate to the type of wave. The graphs in Figures 7.6 and 7.7 are for a grain diameter of 0.010 in. and only minor differences are observable for the other grain sizes. It is noted that the wave amplitudes near the surface wave critical angle in Figures 7.6 and 7.7 increase beyond the range of the ordinates chosen. To show the entire graphs, Figures 7.8, 7.9, and 7.10 present the same information as Figures 7.3, 7.6, and 7.7, but the ordinate has now been increased to enable amplitudes to be completely examined and the absissa increased to include all incident angles from 0 to 90°.

The above graphs can then be used to obtain information about the expected wave amplitudes for most testing applications involving nickel. Of course, assumptions have been made about grain sizes and shapes and the way in which attenuation curves are established. Also, low frequency absorption caused by effects other than scattering has been disregarded. However, the graphs do illustrate that except for points near the critical angles and for highly attenuating media, reflection and transmission factors are not seriously influenced by attenuation. Materials other than nickel can also be examined by use of the information in Reference 2.

The critical angle reflection factors, as stated above, are the most significant changes observed for the various grain sizes. Considerable effort has been expended to better understand this condition and to evaluate its usefulness as a NDT tool. It has been shown[3] that the depth of the reflection factor dip (Figures 7.3, 7.4, and 7.5) depend predominantly on the attenuation of shear waves. Correlation between measured and calculated factors has also been demonstrated.[3]

To better understand the relationship between attenuation and the reflection factors, several materials have been studied by calculating the reflection factors in the area around the critical angle at several frequencies. Attenuation data for nickel were obtained from Figure 7.2; data for iron, brass (30% zinc) and iron-30 nickel were calculated by the same method. Diffraction corrected attenuation factors are available for 304 SS and were used in these calculations. Figure 7.11 shows the reflection factors for 0.01, 0.005, and 0.001 in. grain-size nickel versus shear wave attenuation. The minimums occur at 2.3, 6.0, and approximately 30×10^3 db/ft of shear wave attenuation. Figures 7.12 and 7.13 likewise present this information for Fe–30Ni, 304 SS, brass and iron.

A summary of pertinent details from Figures 7.11, 7.12, and 7.13 and other sources is contained in Table 7.2.

In analyzing Table 7.2, several factors appear to form a pattern that

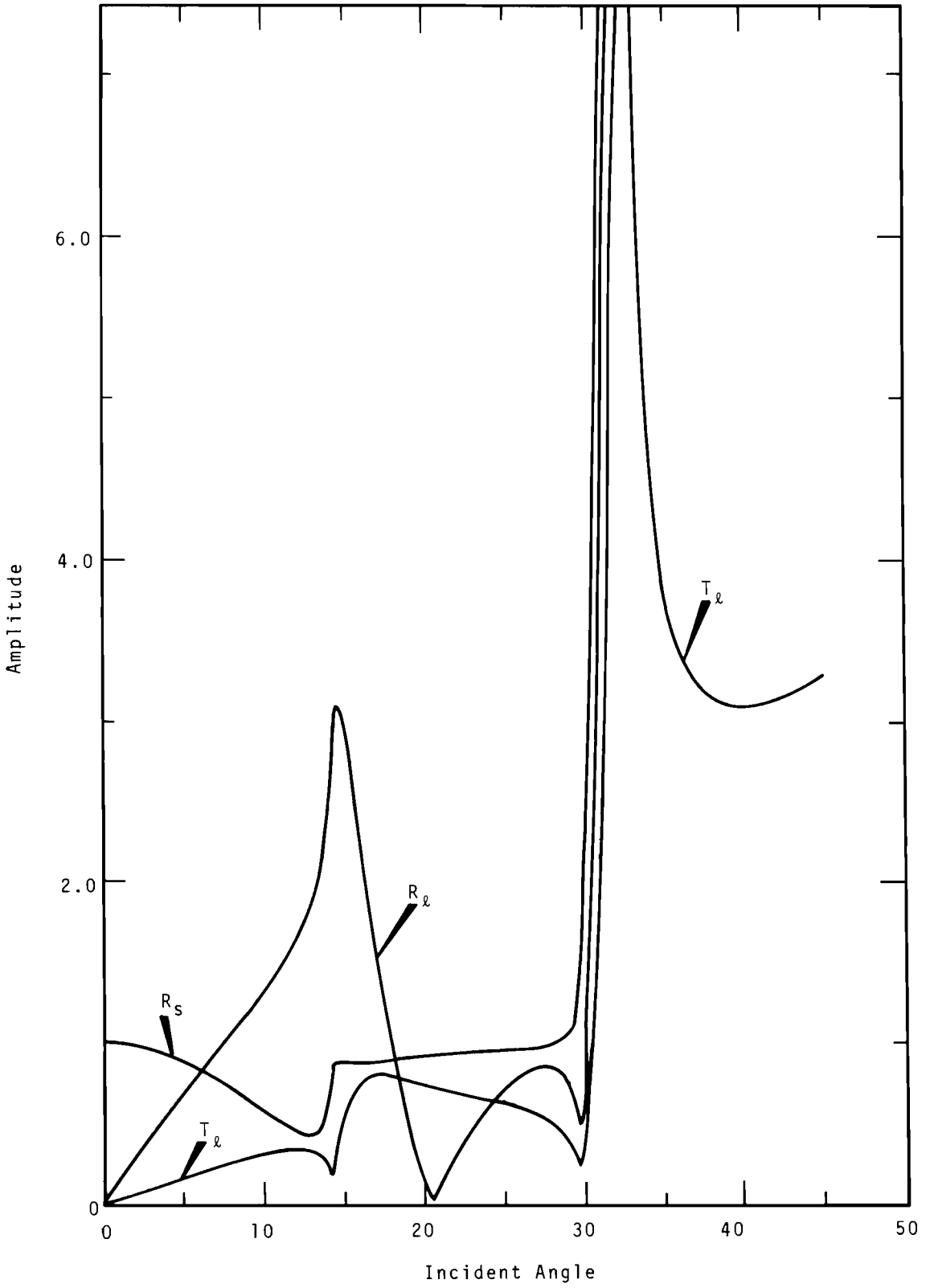

FIGURE 7.6. Shear Wave Reflection and Transmission Factors from Nickel to Water, D = 0.010 in. and f = 20 MHz

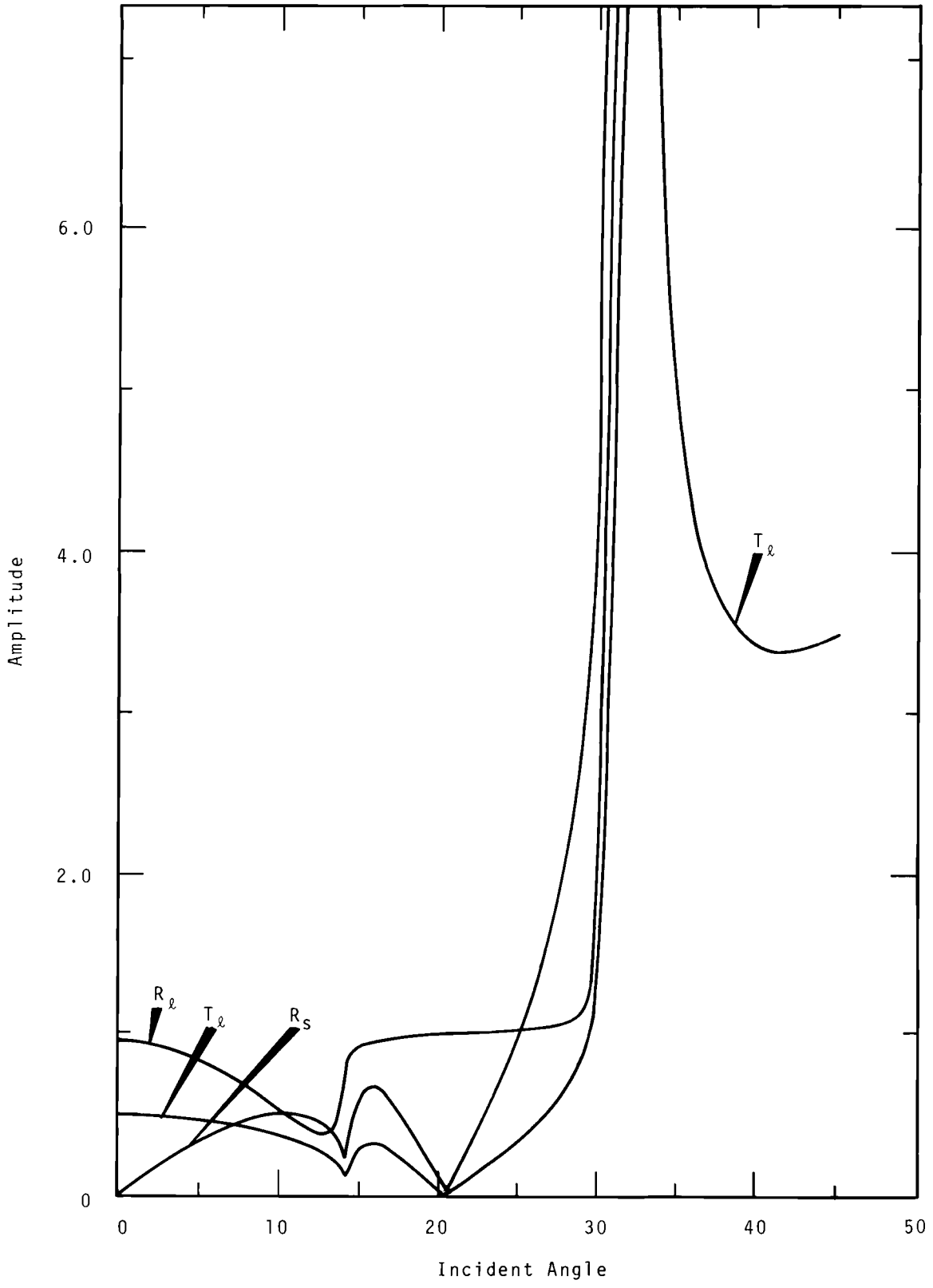

FIGURE 7.7. Longitudinal Wave Reflection and Transmission Factors from Nickel to Water, D = 0.010 in. and f = 20 MHz

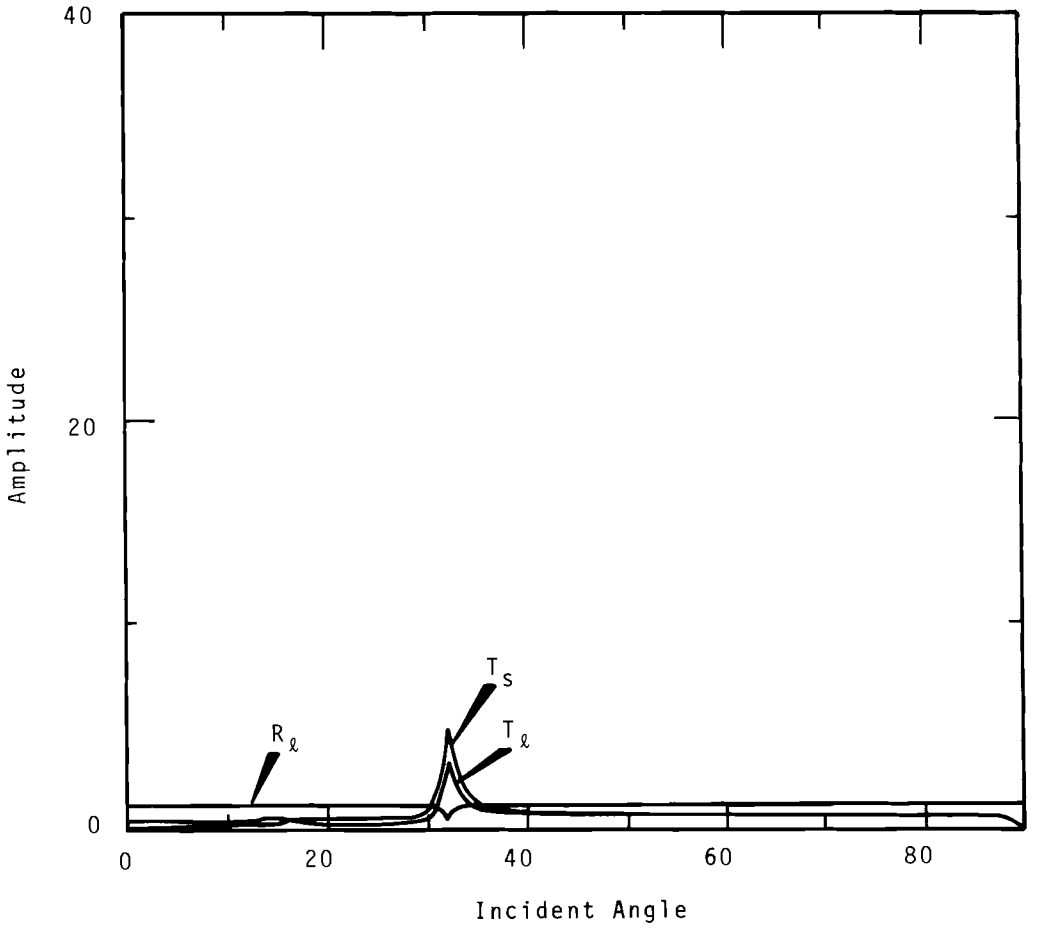

FIGURE 7.8. Same as Figure 7.2 Except for Scale Changes

may help to predict the frequency of minimum reflection, f_m. They are as follows:

- The minimum does not occur at the same attenuation or frequency even for the same material of different grain sizes.
- α_s at the minimum varies inversely with attenuation. Except for brass, Columns 2 and 5 appear to obey this pattern.
- The attenuation per wavelength at the minimum α_s min/λ is approximately equal for different grain sizes of the same material.
- α_s min/λ falls within a narrow range, 0.572 ± 0.044 db for all of the materials except brass which was 1.36.

The above are only empirical relationships. A thorough analytical study is needed to fully explain the phenomenon.

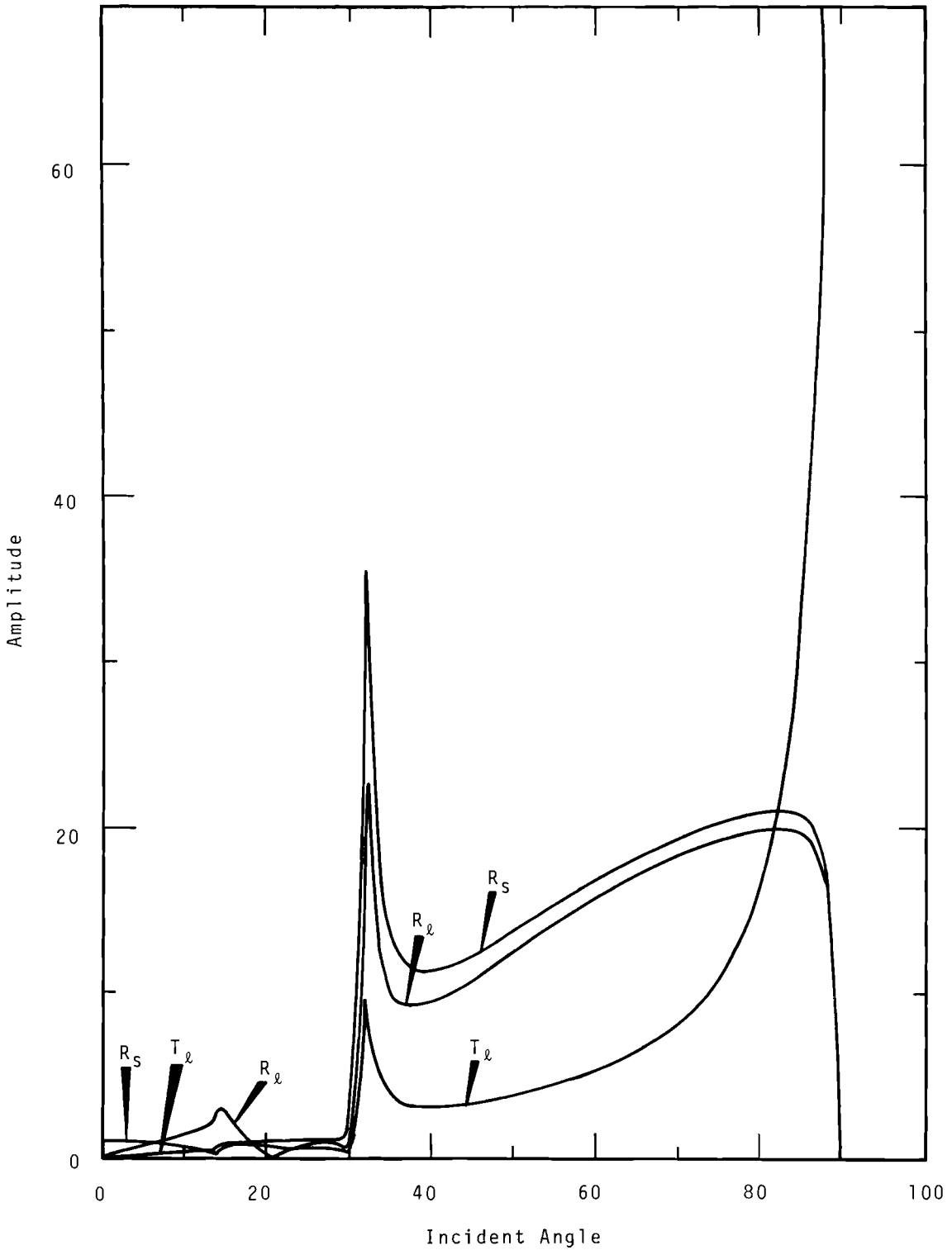

FIGURE 7.9. Same as Figure 7.5 Except for Scale Changes

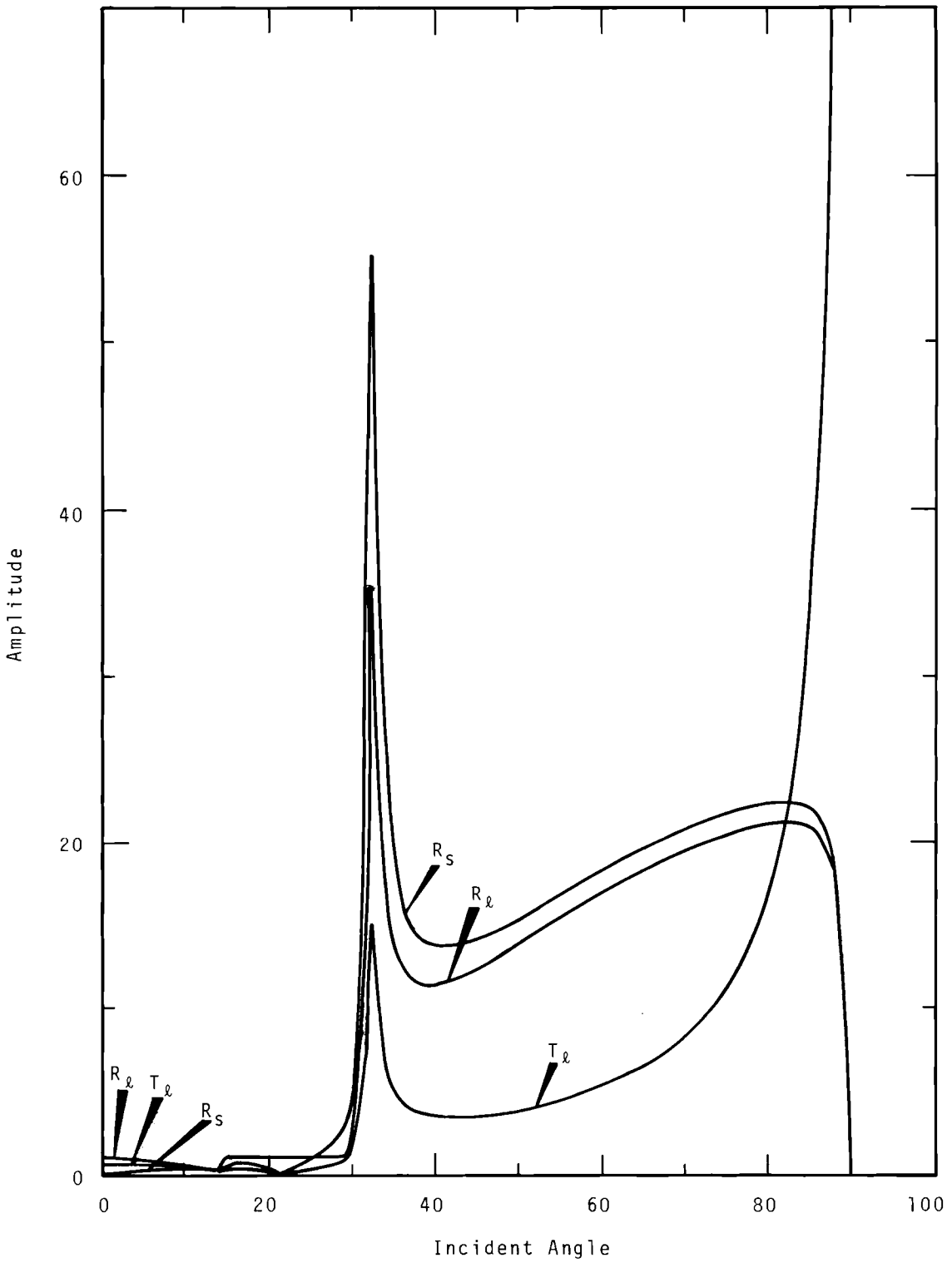

FIGURE 7.10. Same as Figure 7.6 Except for Scale Changes

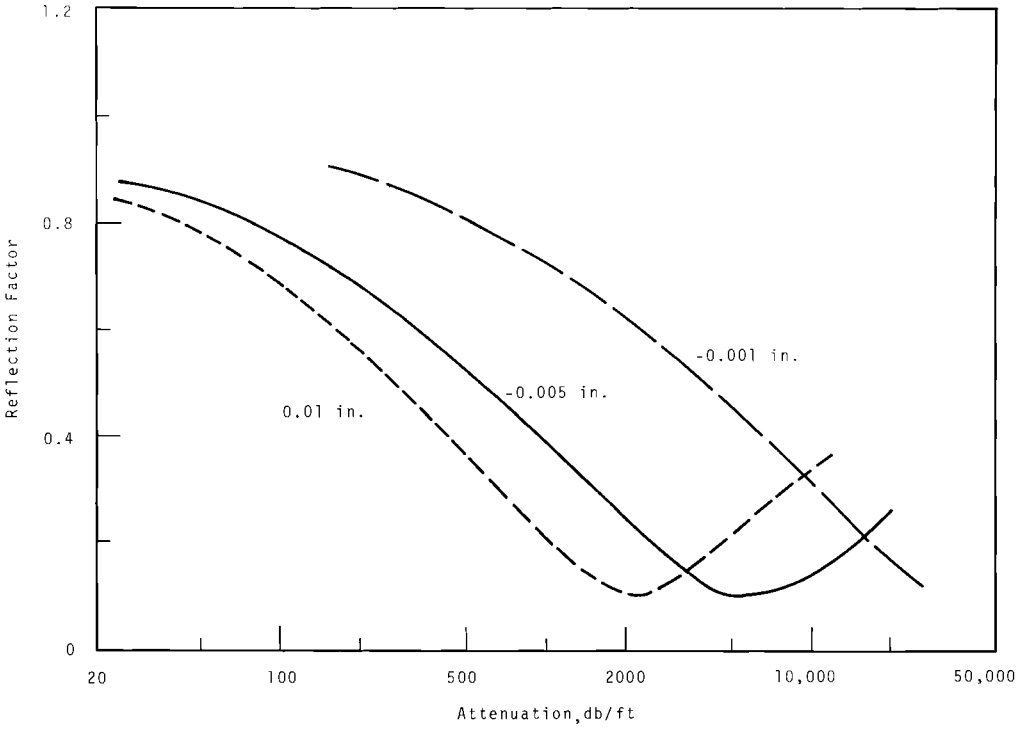

FIGURE 7.11. Reflection Factor Versus Shear Wave Attenuation at a Water Nickel Interface. Nickel with Average Grain Sizes of 0.01, 0.005, and 0.001 in. is Shown.

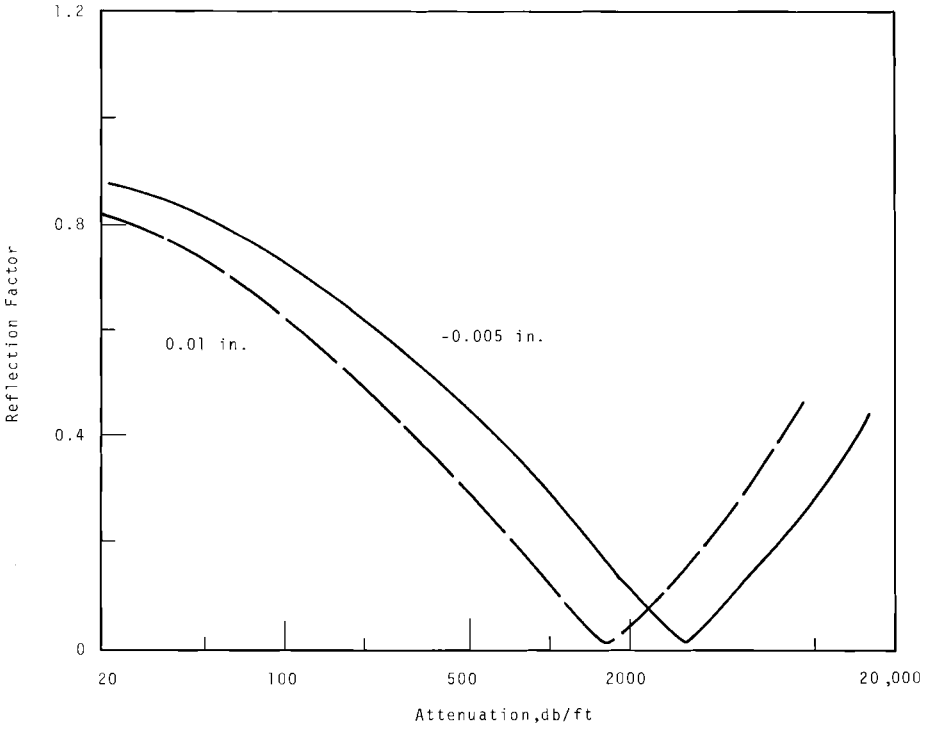

FIGURE 7.12. Reflection Factor Versus Shear Wave Attenuation at a Water Fe30Ni Interface. Fe30Ni with Average Grain Sizes of 0.01 and 0.005 is Shown

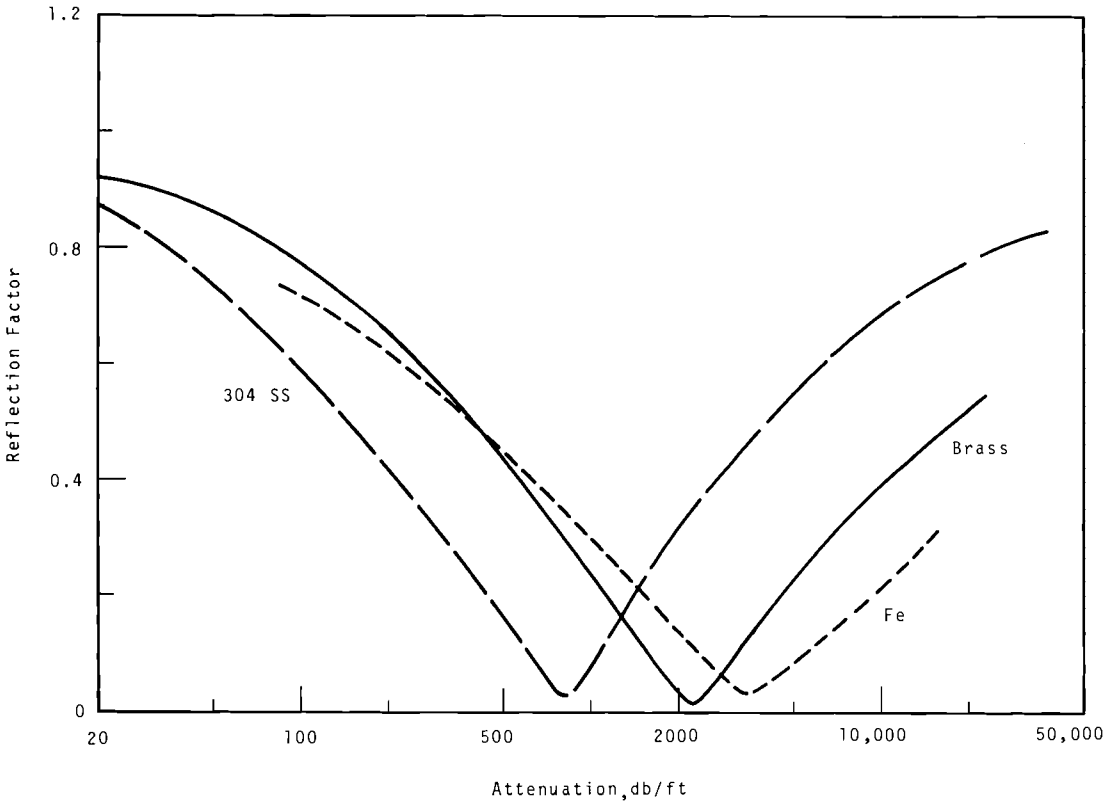

FIGURE 7.13. Reflection Factor Versus Shear Wave Attenuation for a Water Metal Interface. 304 SS, Brass and Iron are Shown.

TABLE 7.2. Pertinent Details from Figures 7.11, 7.12, 7.13, and Other Sources

Material and Grain Size in Inches		σ (a)	α_s (b), db/ft	fm, (c) MHz	$10^{-3}\lambda_m$ (d) in.	α_s (e) at minimum, db/ft	α_s (f) min/λ db
Fe30Ni:	0.01	0.2055	950	25	4.35	1,600	0.58
	0.05	0.2055	510	50	2.18	3,200	0.581
304 SS:	0.003	0.29	3,000	13	9.5	780	0.616
Fe:	0.01	0.2955	360	65	1.95	3,500	0.568
Ni:	0.01	0.337	540	42.5	2.94	3,350	0.542
	0.05	0.337	240	120	0.98	6,700	0.546
	0.001	0.337	30	>400	----	>30,000	-----
Brass:	0.002	0.354	9,000	11.5	7.11	2,300	1.36

(a) σ: *Poissons ratio found from the ratio of shear and longitudinal velocities.*

(b) α_s, *at 20 MHz: the shear wave attenuation at 20 MHz. This frequency was chosen to compare the relative attenuation of each material.*

(c) f_m: *the frequency at which the critical angle reflection factor is a minimum.*

(d) λ_m: *the wavelength of shear waves at* f_m.

(e) α_s *at min.: the attenuation of shear waves at* f_m *in db per foot.*

(f) α_s *min./*λ*: attenuation per wavelength found from Columns 4 and 5.*

In Figure 7.14, the reflection factor versus frequency is plotted for the three grain sizes of nickel. If for instance, it is desired to detect different grain sizes, signal ratios of 1, 3.9, and 9 could be obtained for grain sizes of 0.01, 0.05, and 0.001 in., respectively at 40 MHz. Other materials may give better signal ratios because the minimums approach closer to 0 as shown in Figures 7.12 and 7.13. It would be possible to make the method insensitive to velocity gradients by sweeping through the critical angle. The indication would pertain only to the surface layer approximately 3 wavelengths thick; in this case, about 0.12 in.

Other possible applications and analytical investigations will be considered during the coming quarter.

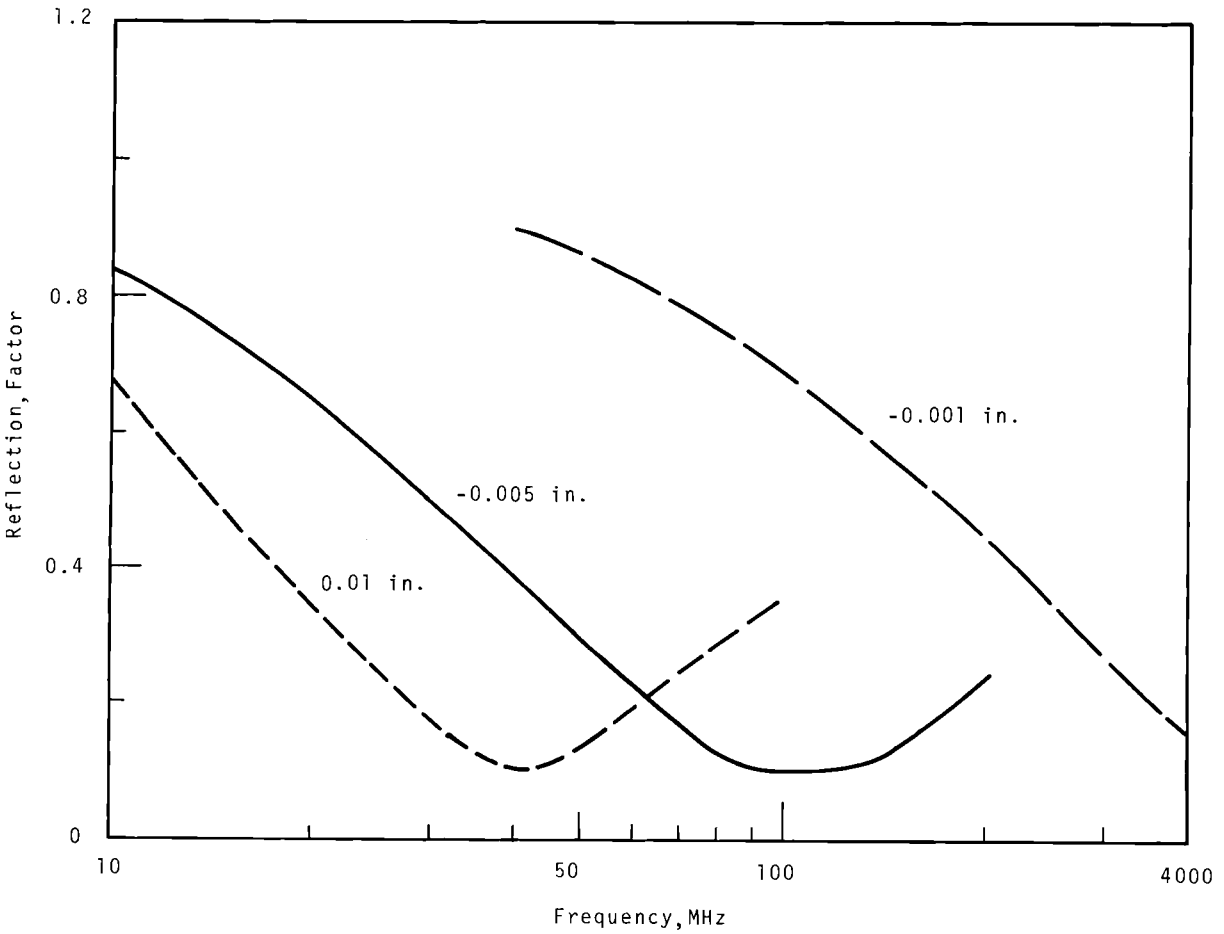

FIGURE 7.14. Reflection Factor Versus Frequency at a Water Nickel Interface. Nickel with Average Grain Sizes of 0.01, 0.005, and 0.001 in. is Shown.

DETECTION OF IRRADIATION INDUCED SHIFT IN Nil-DUCTILITY-TRANSITION TEMPERATURE

D. O. Hunter

Irradiated steel specimens are being studied by using ultrasonic techniques to determine if a correlation exists between the nondestructive measurements and irradiation damage--particularly as manifested by a shift in the brittle-ductile transition temperature.

As a follow-up to the previously reported successful critical angle measurements, measurements were made of changes in shear velocity on forty available irradiated specimens. A number of technique improvements were made, and repetitive measurements were averaged to enhance accuracy; but despite this, the possible error of as much as ±0.2% remains rather high relative to the measured changes shown in the attached curves. The percentage change in velocity measured for a given specimen is shown as "X"% but it may actually be "X" ±0.2%. A few measurements had 0% change, but due to the indicated error factor, the validity of these measurements is open to question. Two main sources of measurement error are: (1) difficulty in making exact dimensional measurements of the highly radioactive specimens, some of which were slightly damaged during de-encapsulation and subsequent handling, and (2) measurements made on 36 nonirradiated control specimens that strongly indicate velocity variations of up to about 0.13% existed in the specimens before irradiation.

Despite the possible error, the trend of shear velocity change with radiation exposure shows clearly. Velocity change as a function of neutron fluence >1 MeV for the four materials families are shown in Figures 7.15-7.18. Specimens exposed at low temperatures (<350 °F) generally show, a greater decrease in velocity as exposure increases. Specimens irradiated at high temperatures (>610 °F) exhibit a reduced velocity increase as exposure increases, but in most cases--even at the highest exposure measured--the net effect is still a velocity increase relative to non-irradiated material.

The rate of velocity change for the stainless steel family irradiated at low temperature is seen to exceed that of the carbon steel families. Note also that the high temperature irradiated stainless steel specimens have a greater net increase in velocity than do the carbon steel specimens.

Inflections in the curves for low-temperature irradiated carbon steel specimens occur at about 1.3×10^{19} nvt > 1 MeV. These specimens are unique in that they received two cycles of exposure instead of one; they were exposed in a region of the reactor where thermal to fast neutron ratio was about 15 to 1 versus 3 to 1 for the groups irradiated to 1.0×10^{20} nvt > 1 MeV; and they are also the most recently exposed specimens by about six months.

Although conclusions from these data would be premature; some possibilities are as follows:

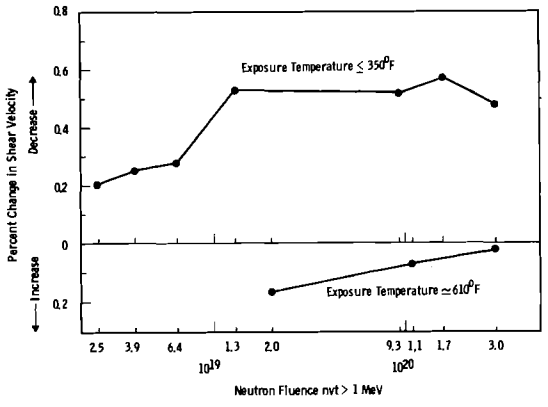

FIGURE 7.15. Change in Shear Velocity for Irradiated A302B Carbon Steel cut from Top of 4 in. Plate

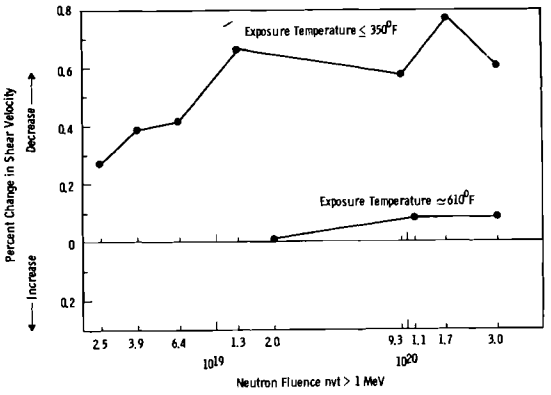

FIGURE 7.16. Change in Shear Velocity for Irradiated A302B Carbon Steel cut from Middle of 4 in. Plate

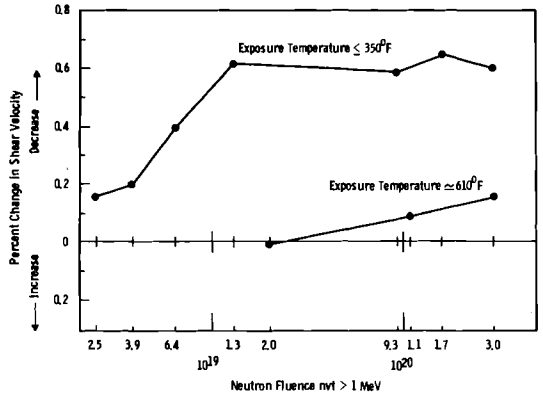

FIGURE 7.17. Change in Shear Velocity for Irradiated A542-II Carbon Steel cut from Top of 6 in. Plate

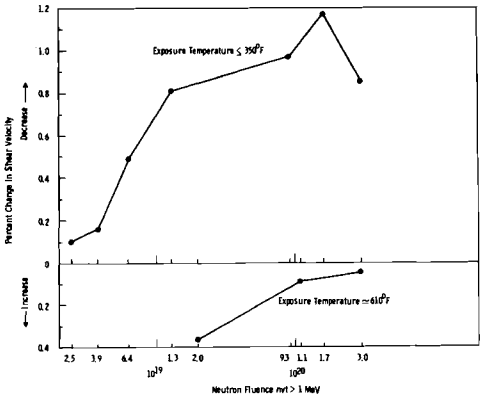

FIGURE 7.18. Change in Shear Velocity for Irradiated 304 SS

- Since shear velocity changes generally indicate changes in the modulus of rigidity, it would appear that at least two physical damage mechanisms are occurring--one causing an apparent softening and the other an apparent stiffening. Irradiation exposure and temperature help determine which is the dominant mechanism.
- Lower-energy neutrons appear to play a role in the damage mechanism(s) experienced during low temperature exposure.
- The measured changes in shear velocity do not correlate directly with a shift in the brittle-ductile transition temperature because the 304 SS specimens exhibited a greater change than did the carbon steel specimens. However, it is known that irradiation does not degrade the impact properties of austenitic stainless steel as it does carbon steels.

Electrostatic Transducer Development

R. W. Smith

Work is in progress to develop an electrostatic transducer to fill the need for a high temperature, broadband transducer. A technique that uses a liquid metal as the couplant

and front electrode of the transducer is being investigated. High-vacuum deposition equipment, capable of producing high quality dielectric layers, is also being readied for use in fabricating an electrostatic transducer of a different design.

The electrostatic or capacitive transducer used as a receiver is essentially a biased capacitor. A sound wave modulates the distance between the capacitor plates and thus varies the capacitance. The capacitance change ΔC is

$$\Delta C \simeq C \left(\frac{\Delta d}{d}\right), \quad (\Delta d << d)$$

where C is the quiescent transducer capacitance, and $\frac{\Delta d}{d}$ is the strain in the dielectric.

Figure 7.19 shows a biasing arrangement. If the transducer capacitance $C >> C_i$, and if $\frac{R_B R_i}{R_B + R_i} C >> \frac{1}{f}$ (f is the frequency), then the signal voltage developed, ΔV, is given by

$$\Delta V \simeq -V\left(\frac{\Delta d}{d}\right)$$

where V is the bias voltage.

To the extent that the assumptions above are valid:

- The signal voltage is proportional to the bias voltage, and the bias voltage is limited by the dielectric strength of the spacer between the capacitor plates.
- For maximum signal the dielectric should have a low Youngs Modulus. An example of a good dielectric is a gas.

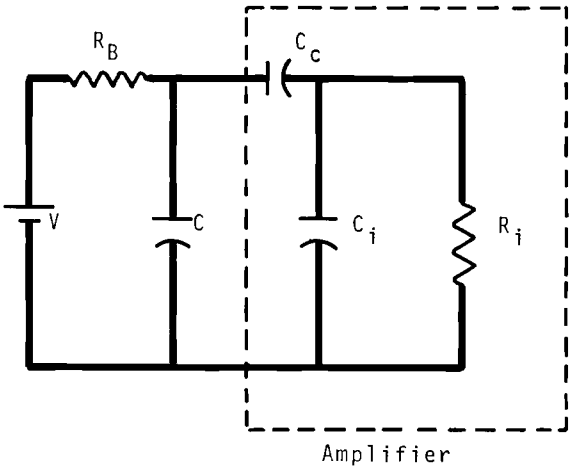

FIGURE 7.19. Biasing Arrangement for the Electrostatic Transducer

- Providing that $C >> C_i$ is valid, the amplitude of the signal voltage is independent of the quiescent capacitance.

The low frequency limit for the electrostatic transducer is a function of the amplifier input resistance R in. The input resistance can fall off as f^{-1}, and the signal voltage will not be degraded. For a transducer capacitance of 100pf and a low frequency cutoff of 1 kHz an input impedance of the order of 100 MΩ would be required.

No bias is used when the electrostatic transducer is used as a transmitter. The capacitor plates attract each other with a force per unit area, p, given by:

$$p = \frac{\varepsilon E^2}{2}$$

where E is the applied voltage. The sound transmitted should have a fundamental frequency that is twice the driving frequency if the driving voltage is sinusoidal.

A problem in fabricating the electrostatic transducer is that the distance between the plates must be very small and closely controlled. One fabrication technique used to minimize this problem is a thin dielectric layer vacuum deposited on a metal sphere. Thus, the backing member (the metal sphere) is always aligned with the front electrode. To make a sensitive transducer in this manner, the dielectric must be quite thin. The pressure at the point of contact is quite high; consequently, the delicate dielectric layer breaks down easily. High-vacuum equipment capable of producing high purity dielectric layers is now being readied and may solve the problem of the dielectric breakdown.

Another approach to the alignment problem is the use of a liquid metal couplant between the dielectric layer and the test piece. Since the liquid metal makes intimate contact with the dielectric layer, a thicker, more stable dielectric layer can thus be used, and the transducer can be biased at a higher voltage. This concept is now being investigated. Two electrostatic transducers with mercury to couple to the test piece were fabricated and tested, with the mercury column also serving as the front electrode. These transducers were quite sensitive and could easily pick up small sounds in the room. When they were used on an acoustic emission test, however, they appeared to be primarily sensitive to lower frequencies in the audio range. The tests conducted thus far have used mica as the dielectric layer. As a receiver, the electrostatic transducer has good sensitivity in the 1 to 5 MHz range; no testing has been done outside this range as yet. The electrostatic transducer appears to be a poor transmitter because with both transducers being driven by the same pulser, the signal received from an electrostatic transmitter has been more than 40 db below the signal received from a PZT-5 transmitter.

Thus far, tests to measure transducer frequency response have been inconclusive, primarily because of the difficulty in generating either a constant or a known amplitude pressure wave over several decades of frequency. In addition, test fixtures at audio frequencies are necessarily large to avoid standing wave problems. Three test fixtures were fabricated that aid in the evaluation of dielectric layers for the electrostatic transducer. One fixture is a solid brass cylinder, 4 in. long, by 1 in. diam, and the others are hollow nylon cylinders holding a mercury column. The transmitting transducer is placed at one end of the column and the receiving transducer at the other end. The fixtures facilitate the evaluation of dielectric layers for frequencies above several hundred kHz.

REFERENCES

1. *C. E. Fitch, Jr. "New Methods for Measuring Ultrasonic Attenuation," JASA, vol. 40, no. 5, pp. 989-997. November 1966.*

2. *E. P. Papdakis. "Revised Grain-Scattering Formulas and Tables," JASA, vol. 37, no. 4, pp. 703-710. April 1965.*

3. *J. J. Cadwell, D. R. de Halas, R. E. Nightingale, and D. C. Worlton. Quarterly Progress Report, July, August, September, 1967, Reactor Fuels and Materials Branch of USAEC Division of Reactor Development and Technology, BNWL-658. Pacific Northwest Laboratory, Richland, Washington, February 1968.*

METALLIC FUELS

R. D. Leggett

The inherent high density, mechanical strength, high thermal conductivity, and low fabrication costs associated with metallic fuels combine to make the goal of improving swelling resistance and corrosion resistance of fuel elements worthwhile.

The Metallic Fuels Program is combining the fundamental concepts obtained from various metallic fuel research efforts with the knowledge gained from the actual operating behavior of metallic fuels to develop fuel elements exhibiting superior in-reactor performance. This program includes studies of thorium and uranium base alloys irradiated as prototype fuel elements in pressurized hot water loops as well as studies of clad rods irradiated in temperature-monitored, NaK-filled capsules. Both material parameters and fuel element design parameters are being evaluated.

THORIUM BASE ALLOYS

R. K. Marshall, J. W. Goffard

The use of metallic thorium as a fertile material in the fuel of a nuclear reactor offers the advantages of long life and high specific power operation. The isotropic crystal structure of thorium obviates concern over irradiation "growth" or "growth induced" swelling which are important considerations for anisotropic fuels such as uranium. The high melting point (1750 °C) of thorium is also an advantage because fission gas swelling would be expected to be minimal below about 800 °C (0.53 of the absolute melting temperature). Furthermore, thorium possesses excellent thermal conductivity (about twice that of stainless steel). Thus, high specific powers and surface heat fluxes can be achieved without undue regard that the fuel temperatures will become excessive. The present program is engaged in evaluating the suitability of prototype thorium-uranium elements under power reactor operating conditions.

Irradiation Testing

Three thorium–2.5 wt% U(93.2% ^{235}U)–1.0 wt% Zr tubular fuel elements clad in Zircaloy-2 are under irradiation in the P-7 loop in the ETR under simulated power reactor conditions. The P-7 loop is normally operated at 260 °C and maintained at pH 9-10 with LiOH. Three other fuel elements irradiated in the M-3 loop are being stored in the viewing basin at the ETR site.

The current status of the six test elements is summarized in Table 8.1. The reported fuel swelling values vary from -0.5% to 3.8% with accumulated exposures varying from 2500 to 20,300 MWd/T. The fuel volume increases are obtained by weighing the fuel elements in water during reactor shutdowns. The rate of swelling is roughly 2% per 10,000 MWd/T, which is slightly greater than

TABLE 8.1. Irradiation Data on Th-2.5 wt% U-1 wt% Zr Fuel Elements

GEH-10	Percent Fuel Swelling	Burnup Fissions/cm^3 (MWd/T)	Burnup at.%	Surface Temp, °C	Max. Core Temp, °C	Specific Power, W/g	Surface Heat Flux Btu/hr/ft^2	Thermal Cycles[a]
65[a]	3.8	6.9×10^{20} (20,300)	2.3	295	445	34	4.9×10^5	403
64[a]	2.2	4.8×10^{20} (14,200)	1.6	285	405	26	3.8×10^5	342
71[a]	1.7	3.8×10^{20} (11,200)	1.3	295	465	38	5.5×10^5	203
72[b]	0.1	1.5×10^{20} (4,300)	0.49	300	490	43	6.2×10^5	103
70[b]	-0.5	1.3×10^{20} (3,900)	0.45	295	470	39	5.6×10^5	103
84[b]	0.1	0.9×10^{20} (2,500)	0.29	290	440	33	4.8×10^5	58

(a) *A thermal cycle is defined as a change from 90 to 100% of maximum power to 0 to 10% of reactor power and return to 90 to 100% of reactor power.*

(b) *Temperatures, corrected for oxide buildup, and heat generation conditions during ETR Cycle 93.*

(c) *Temperatures, not corrected for oxide buildup, and heat generation conditions during ETR Cycle 84.*

the value calculated by considering the conversion of thorium-233 atoms to more dense uranium-233 atoms and the conversion of uranium atoms to less dense fission product atoms.

The maximum exposure element, GEH-10-65, has experienced more than 814 effective days of irradiation at maximum fuel temperatures between 350 and 600 °C and has undergone more than 400 full power thermal cycles. There is no evidence of warpage, bowing, or distortion. The temperature history and cumulative swelling of the maximum exposure element is shown in Figure 8.1 as a function of exposure.

HIGH EXPOSURE URANIUM IRRADIATION TEST

R. K. Marshall and J. W. Weber

Irradiation studies have shown that uranium swelling can be reduced significantly by external pressure and by appropriate alloying additions to uranium to produce increased solid solution and second phase intermetallic precipitates. It has also been observed that under irradiation, uranium takes on plastic characteristics.

A fuel element irradiation test has been designed which capitalizes on these known characteristics. The fuel specimens, incorporating a void in the center of the uranium, are coextrusion clad with Zircaloy-2 (Zry-2). The combined effect of the uranium plasticity and the restraints from the cladding and the pressurized loop will direct the uranium swelling inward where it will be accommodated by the central hole.

The fuel specimens are 0.45 in. OD by 6.25 in. long including end caps. Two thicknesses of Zry-2 cladding, 0.025 and 0.050 in. and three uranium void volumes, nominally 5, 10 and 20%, are combined in this test. Two uranium alloys,

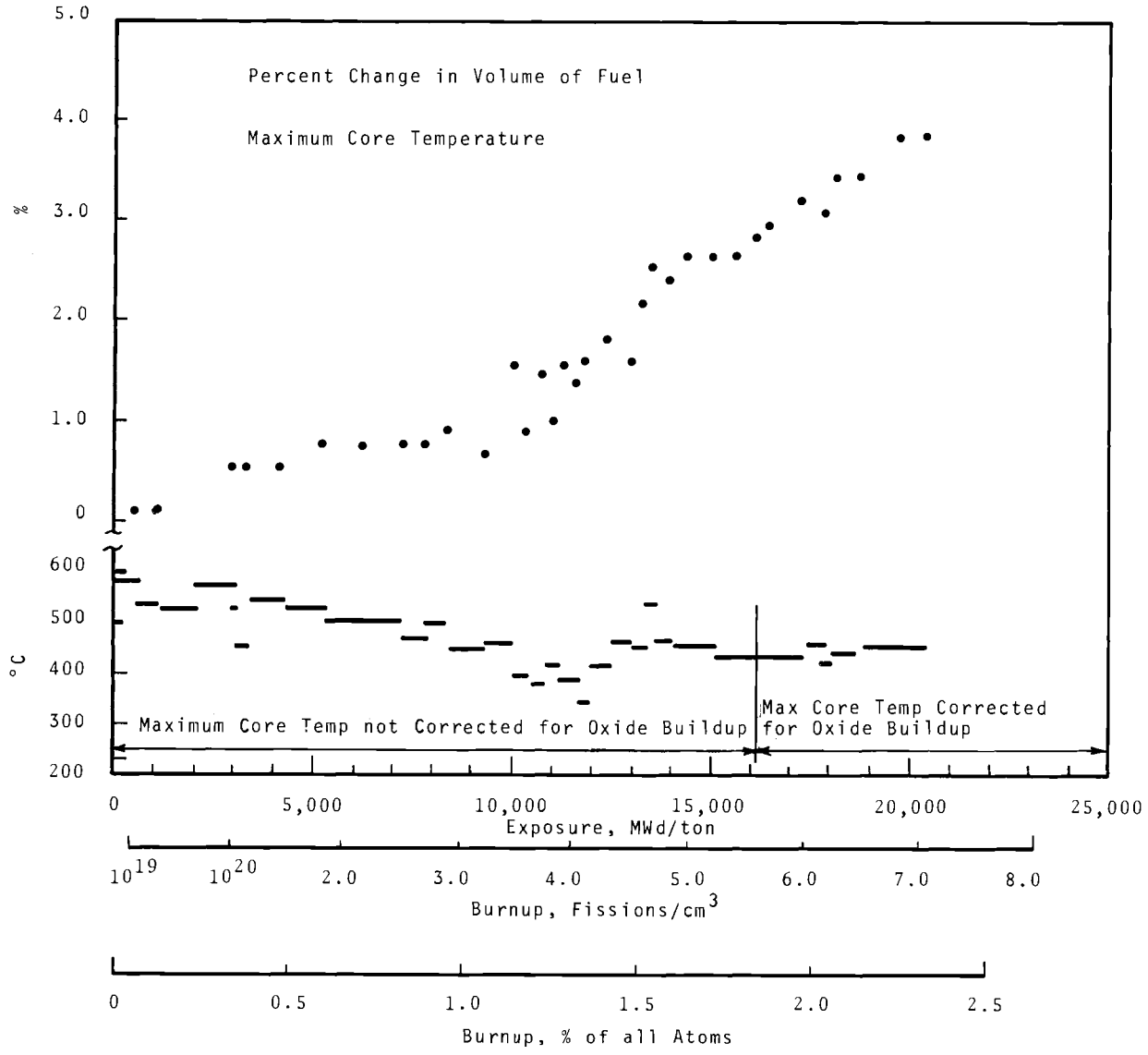

FIGURE 8.1. Swelling Behavior of Th–U–Zircaloy Fuel Element GEH–10–65 LiOH Demineralizer

U + 150 ppm Fe-100 ppm Si and U + 350 ppm Fe-800 ppm Al, are utilized in the study to establish the influence of alloying additions on the performance of this type fuel element.

Fabrication

Fabrication of the Zry-2 fuel elements through coextrusion, drilling of the central hole, and brazing and welding of the end caps has been

described in previous quarterly reports.[1,2] Preirradiation characterization of the elements consists of dimensional measurements of length, diameter and warp, and determination of bulk fuel-element density by dry and submerged weight. Volume of the central hole is determined, prior to brazing in the end caps, by measuring the weight of CCl_4 required to fill the hole. Eleven additional fuel elements have been fabricated and shipped to the ETR to replace some of those now under irradiation.

Irradiation Testing

The test was designed for irradiation in the ETR M-3 water loop. This facility operates with a water temperature of 260 °C at 2,000 psi. The pH is controlled at 9-10 by NH_4OH. The 6.25 in. long rods are supported in an assembly consisting of four clusters of 6 rods in hexagonal arrays.

A total of 35 elements have been irradiated over a period of 9 cycles. The exposures range from a maximum of 5.2×10^{20} fissions/cm^3 (8740 MWd/T) to a minimum of 0.45×10^{20} fissions/cm^3 (743 MWd/T). The maximum fuel temperatures range from 545 to 360 °C. At the end of each irradiation cycle, the elements are removed from the basket and holder assembly for weight measurements, warp measurements, and visual examination in the ETR basin.

The weight measurements are used to calculate a volume change in the rods for each cycle of irradiation. During the examination at the end of Cycle 93, the 24 elements irradiated were measured for diameter and length changes using C-type micrometers located in the ETR canal. A check of the measuring system using a stainless standard showed that the error of measurement should be less than -0.001 and +0.002 in.

Presented in Table 8.2 are the irradiation temperature, the accumulated exposure, the accumulated volume change, and the single throw warp for the 35 irradiated rods as of the end of ETR cycle 93. Included, also, is the alloy composition, the cladding thickness, and the preirradiation central void volume of each rod. Figures 8.2 through 8.6 show the volume change as a function of exposure. Each figure represents a single set of nominal void volume and cladding thickness, while each curve represents the volume change with progressive exposure on a single fuel element. From the first interim volume change data point obtained, each element has shown and continued to show a volume decrease. The accumulated volume changes range now from -0.07 to -3.64%. There were no significant changes in the trends of the curves of volume changes over the last cycle of irradiation. Elements of both cladding thicknesses in all three void volumes show that the volume decrease tends to stop and reverse after some amount of exposure. The curves for the high exposure elements of 0.050 and 0.025 in. Zircaloy-2 cladding with 10 and 20% initial void (Figures 8.3, 8.4, 8.6 and 8.7) extrapolate to exposures

TABLE 8.2. Irradiation Data on Hollow Core, Metallic Uranium Fuel Elements

GEH-10	Preirrad. Uranium Void Volume, %	Zry-2 Cladding Thickness, in.	Alloy(a)	Temperatures Max. Core, °C	Temperatures Fuel Surface, °C	Accumulated Volume Change, %	Single Throw Warp, in.	Accumulated Exposure, MWd/T
129	23.8	0.025	1	415	360	-1.00	0-0.025	2568
103	21.5	0.025	1	385	345	-0.63	0-0.025	4280
102	20.5	0.025	1	380	340	-0.82	0-0.025	6035
128	18.3	0.025	1	410	355	-1.01	0-0.025	1748
101	18.2	0.025	1	375	330	-0.48	0-0.025	5131
104	15.5	0.025	1	380	335	-0.84	0-0.025	5131
105	7.7	0.025	1	370	320	-0.21	0-0.025	988
109	28.4	0.050	1	425	385	-0.38	0-0.025	8462
151	26.0	0.050	1	495	450	-0.99	0-0.025	2917
108	25.2	0.050	1	445	405	-0.38	0-0.025	5254
110	16.5	0.050	1	440	395	-0.83	0-0.025	6571
107	11.8	0.050	1	445	400	-0.99	0-0.025	7281
111	8.7	0.050	1	430	380	-0.37	~0	5475
112	7.3	0.050	1	435	385	-0.07	0-0.025	3684
130	4.9	0.050	1	510	435	-0.60	0-0.025	1545
127	22.2	0.025	2	450	385	-1.95	0-0.025	1725
120	21.2	0.025	2	405	355	-1.60	0.025	6986
121	21.1	0.025	2	460	400	-1.74	0.025-0.050	4013
146	12.8	0.025	2	435	375	-2.22	0.025	4473
122	11.4	0.025	2	390	335	-1.67	0.025	3582
150	10.6	0.025	2	380	325	-1.57	0.025	3231
119	10.4	0.025	2	425	355	-1.63	0.025-0.050	5142
124	5.0	0.025	2	410	345	-1.31	0-0.025	4714
123	4.7	0.025	2	420	345	-1.35	0-0.025	3082
125	4.4	0.025	2	400	335	-1.05	0.025	1916
152	22.9	0.050	2	507	452	-3.64	0.025-0.050	743
114	22.6	0.050	2	445	400	-0.83	0.025	8743
131	19.3	0.050	2	545	475	-2.90	0.025-0.050	2290
115	18.9	0.050	2	470	425	-2.21	0.025-0.050	5433
113	16.4	0.050	2	440	395	-0.81	0-0.025	7446
116	14.7	0.050	2	490	428	-1.49	0-0.025	1772
153	9.8	0.050	2	400	345	-0.91	0.025-0.050	5191
117	6.0	0.050	2	450	395	-0.83	0-0.025	3709
118	5.9	0.050	2	440	390	-1.40	0-0.025	5434
133	5.6	0.050	2	500	430	-1.71	0-0.025	1526

(a) *Alloy Compositions:*

1. *U + 350 ppm Fe + 800 ppm Al*
2. *U + 150 ppm Fe + 100 ppm Si*

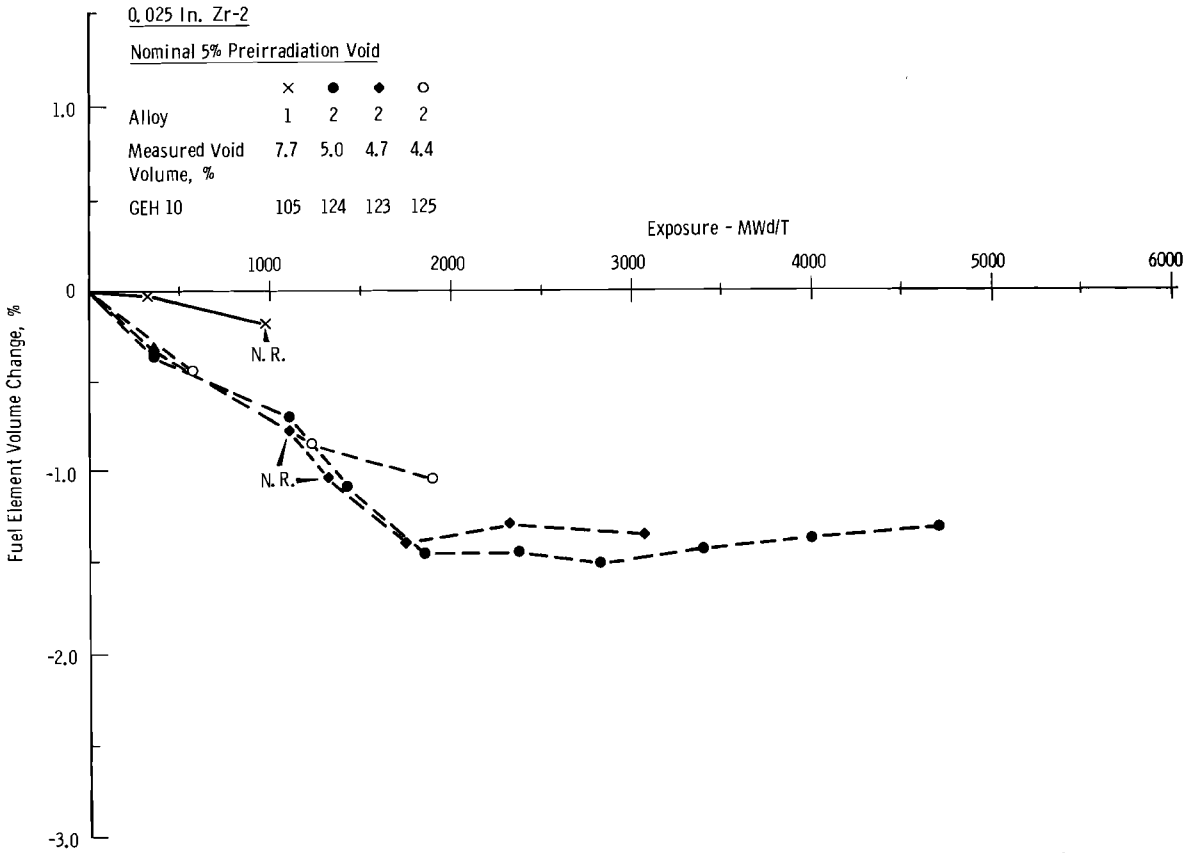

FIGURE 8.2. 0.025 in. Zry-2 Nominal 5% Preirradiation Void

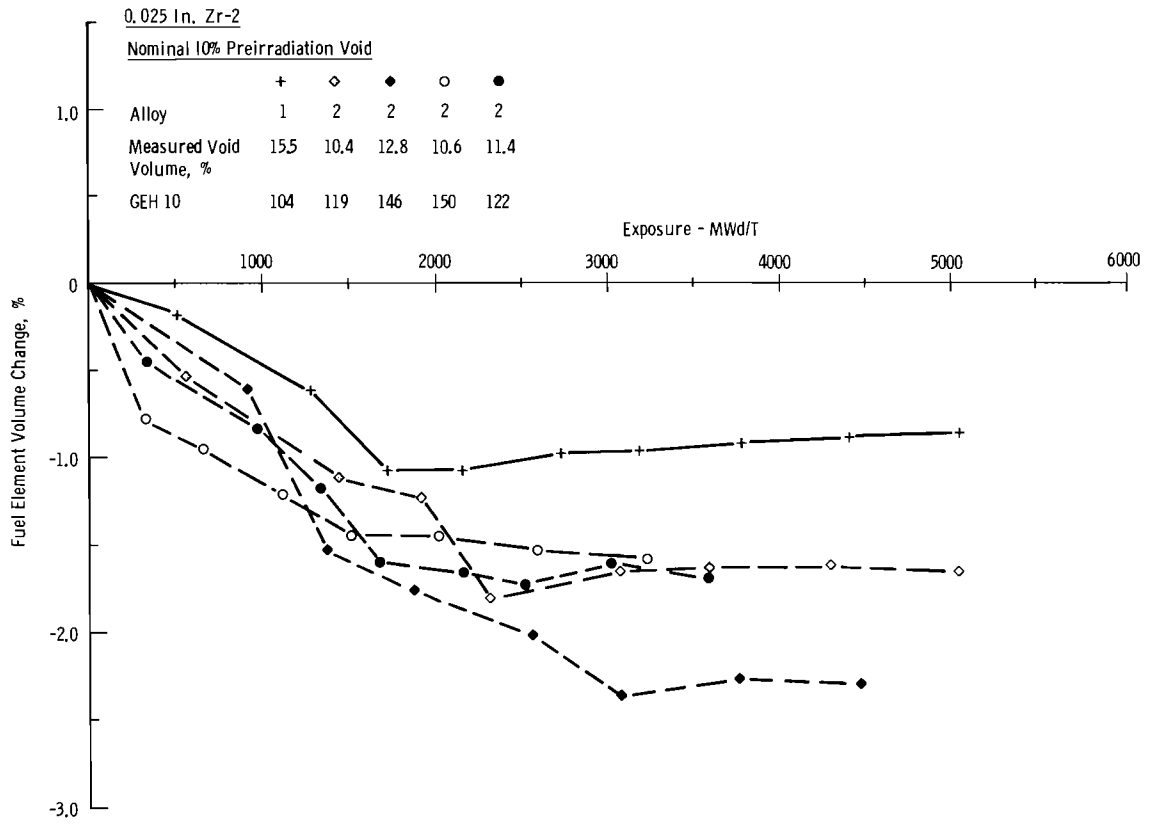

FIGURE 8.3. 0.025 in. Zry-2 Nominal 10% Preirradiation Void

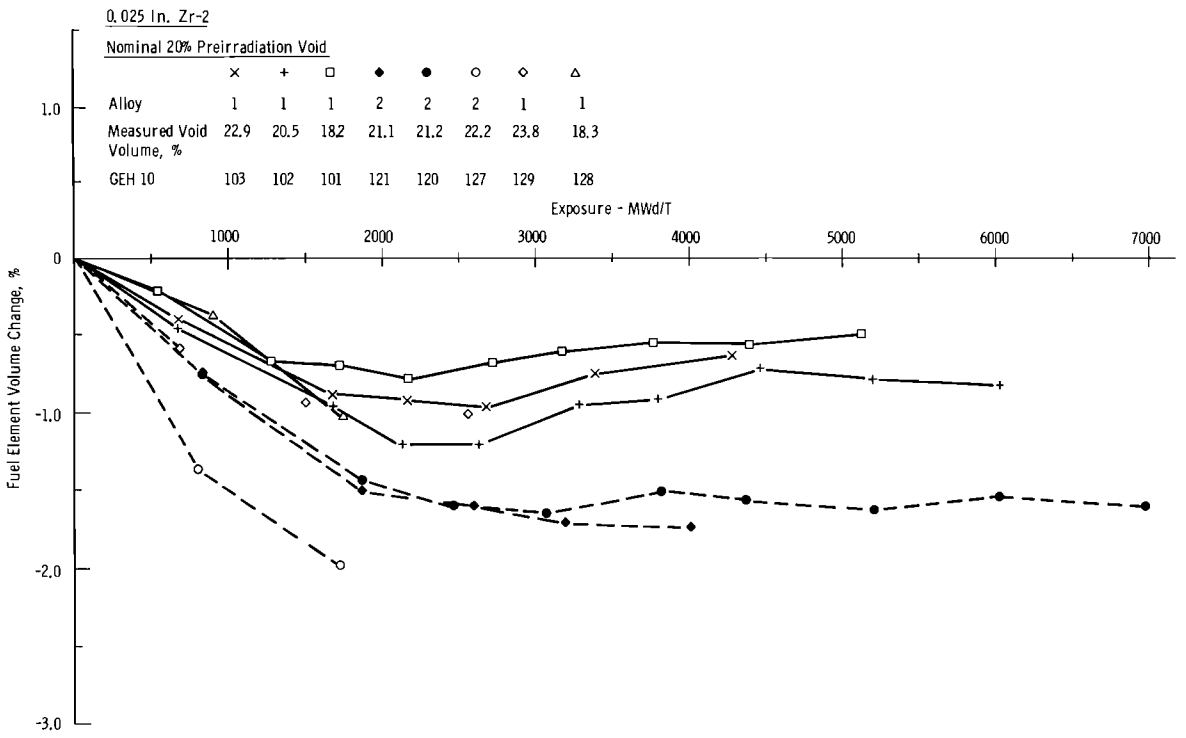

FIGURE 8.4. 0.025 in. Zry-2 Nominal 20% Preirradiation Void

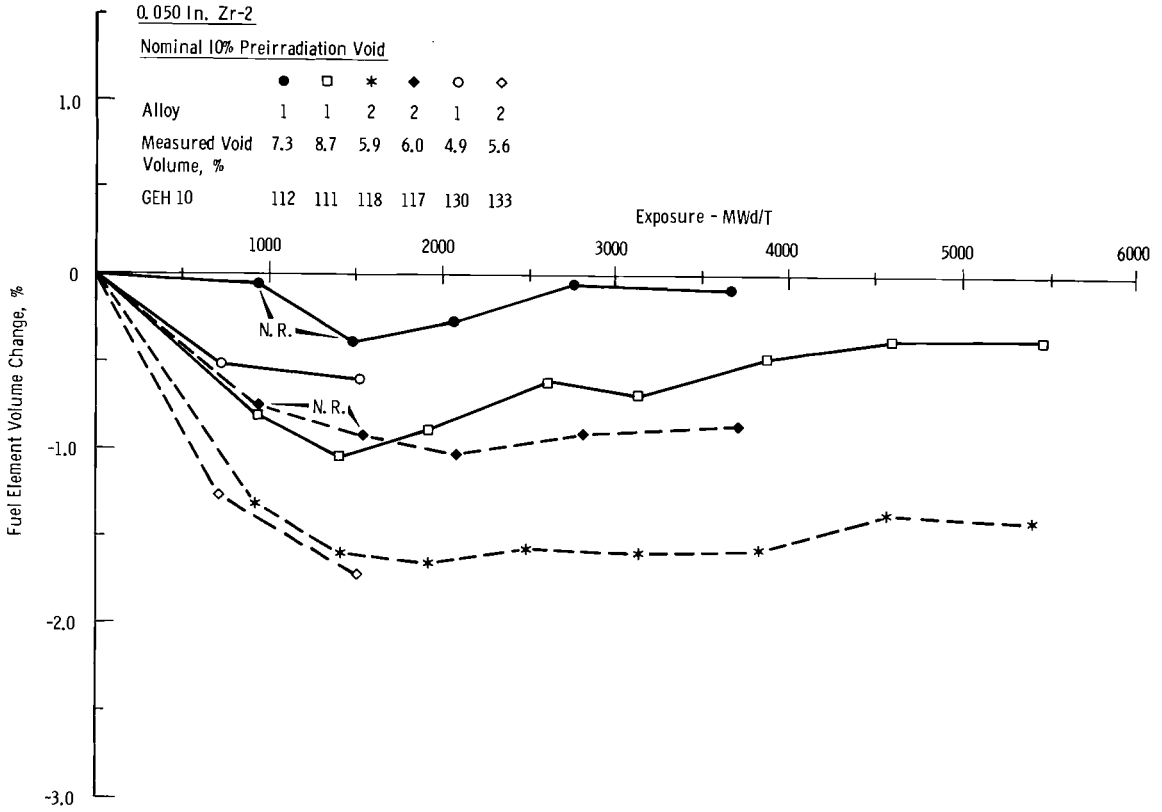

FIGURE 8.5. 0.050 in. Zry-2 Nominal 5% Preirradiation Void

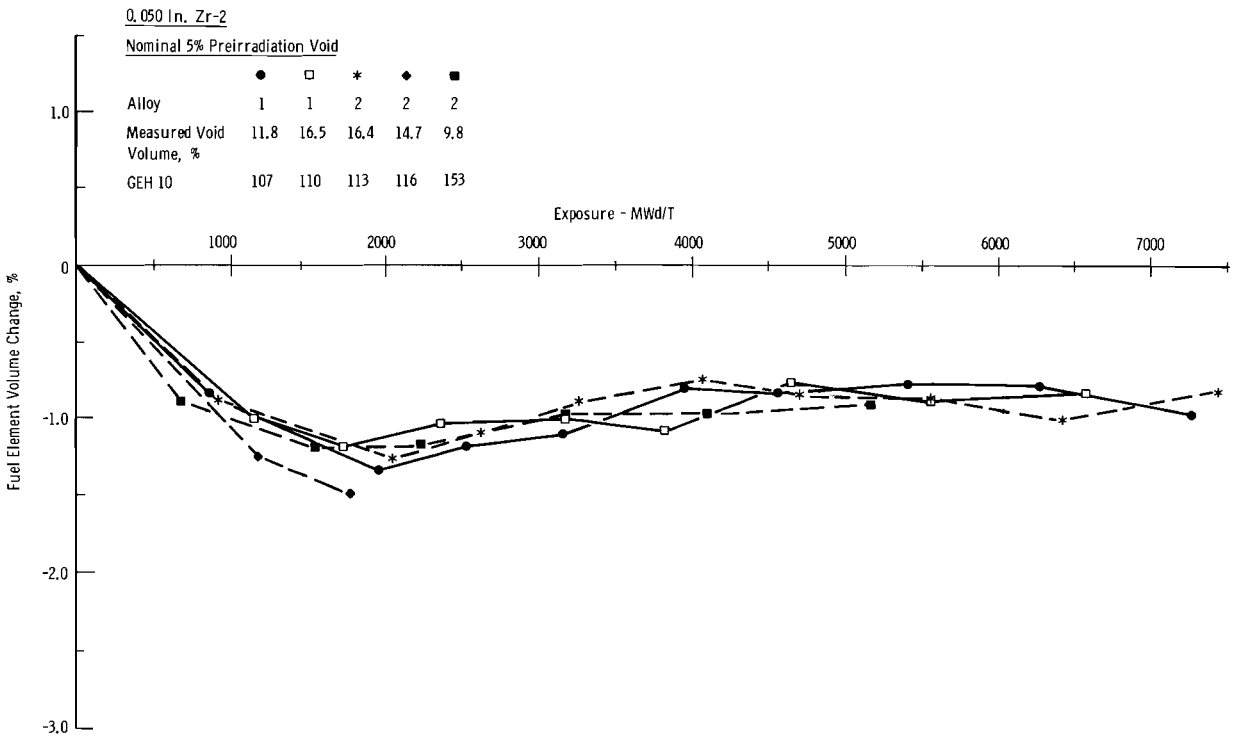

FIGURE 8.6. 0.050 in. Zry-2 Nominal 10% Preirradiation Void

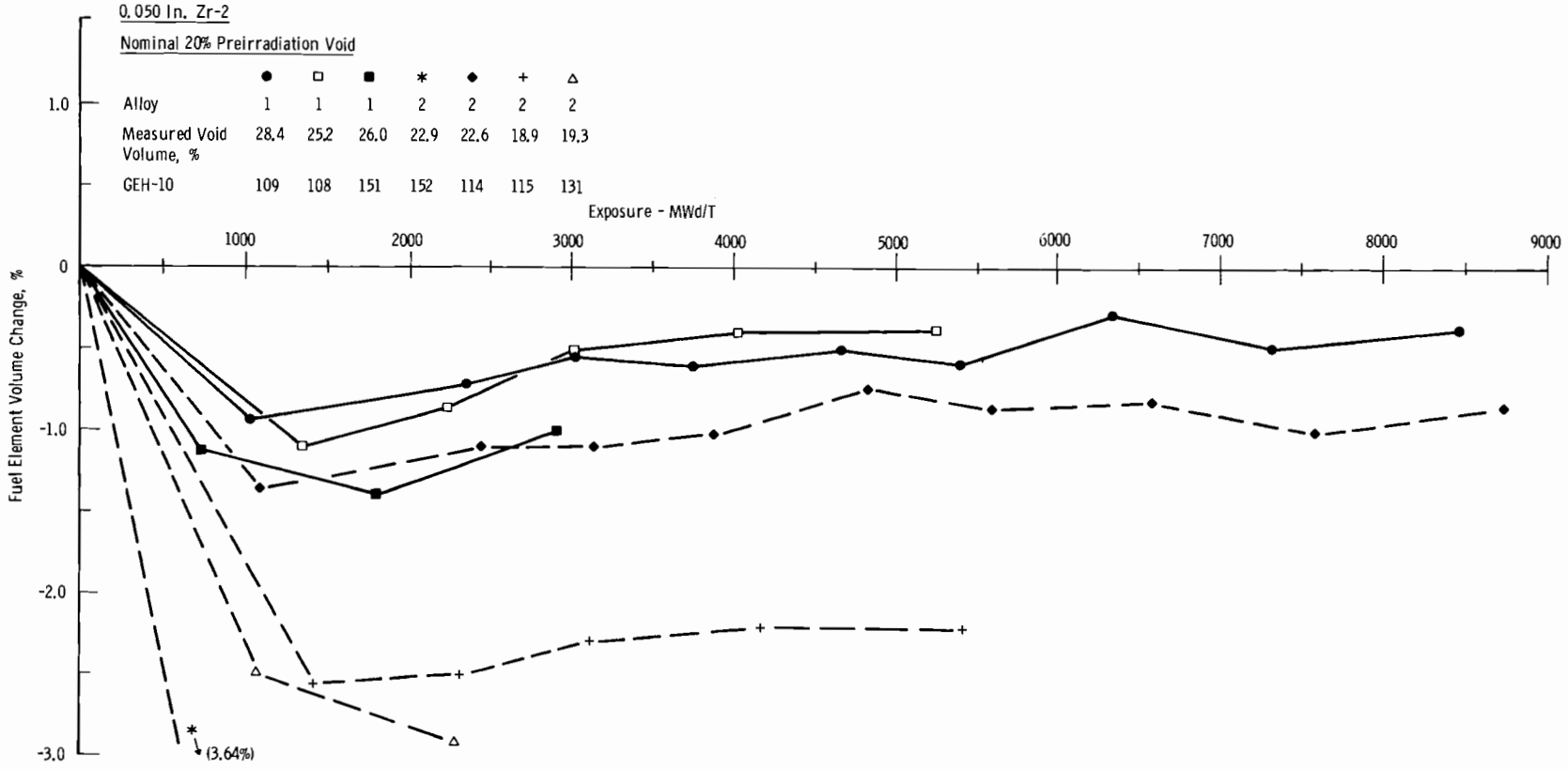

FIGURE 8.7. 0.050 in. Zry-2 Nominal 20% Preirradiation Void

greater than 10,000 MWd/T before the external volumes again reach their preirradiation volume. As reported in a previous quarterly,[3] the reversal of volume change is not believed to be caused by the collapse and filling of the internal voids as shown by pictures from neutron radiography.

In the last quarterly[4] it was reported that the maximum diametrical change was +0.006 in. on Element 119. Measurements on this element after the last cycle failed to show the 0.006 in. ΔD. At the end of the cycle, the ΔD was about 0.003 in. Element 115 now has the maximum OD increase which is +0.0035 in. In general, the measured diameters showed little significant change in their average compared to preirradiation diameters.

A micrometer was placed in the ETR canal to measure fuel rod lengths. The lengths measured on all rods irradiated during Cycle 93 showed accumulated length changes from -0.03 to -0.97%. Sufficient length data have not been accumulated to establish a direct correlation of length change with volume change.

The elements continue to demonstrate excellent behavior, with no end in sight, and there are no indications that these elements will not continue this performance.

REFERENCES

1. *F. W. Albaugh, S. H. Bush, J. J. Cadwell, D. R. de Halas, and D. C. Worlton. Quarterly Progress Report, July, August, September, 1966, Reactor Fuels and Materials Branch of USAEC Division of Reactor Development and Technology, BNWL-CC-821. Pacific Northwest Laboratory, Richland, Washington, December 1966.*

2. *F. W. Albaugh, S. H. Bush, J. J. Cadwell, D. R. de Halas, and D. C. Worlton. Quarterly Progress Report, October, November, December, 1966, Reactor Fuels and Materials Branch of USAEC Division of Reactor Development and Technology, BNWL-CC-957. Pacific Northwest Laboratory, Richland, Washington March 1967.*

3. *F. W. Albaugh, S. H. Bush, J. J. Cadwell, D. R. de Halas, and D. C. Worlton. Quarterly Progress Report, July, August, September, 1967, Reactor Fuels and Materials Branch of USAEC Division of Reactor Development and Technology, BNWL-658. Pacific Northwest Laboratory, Richland, Washington, February 1968.*

4. *F. W. Albaugh, S. H. Bush, J. J. Cadwell, D. R. de Halas, and D. C. Worlton. Quarterly Progress Report, October, November, December, 1967, Reactor Fuels and Materials Branch of USAEC Division of Reactor Development and Technology, BNWL-668. Pacific Northwest Laboratory, Richland, Washington, March 1968.*

BASIC SWELLING STUDIES

R. D. Leggett

When fissionable metals are irradiated, the ordered metallic structure is perturbed in a number of ways. High energy neutrons and fission fragments collide with metal atoms, knocking them out of their structural positions. The resultant defects, vacancies, interstitials, dislocation loops, etc., can adversely affect metallic properties. Similarly, the fission products generated, some of which are noble gases, may be incompatible with the structure and so precipitate or coalesce as second phase inclusions or gas pores. Furthermore, the high localized temperatures associated with the fission event can cause anisotropic fissionable metals such as uranium to drastically change shape in accordance with the crystallography of the specimens.

These effects and their interactions are being studied with regard to the influence of irradiation variables such as the specimen temperature, burnup, burnup rate, and external pressure, and with regard to the influence of metallurgical variables such as composition, structure, and geometry. The data thus far obtained on this program have established that, contrary to previous beliefs, swelling at low burnup in alpha uranium is due to mechanical processes associated with the irradiation "growth" phenomena and with fission event induced defects rather than with the agglomeration and growth of fission gas pores. This is manifested as a maximum in the swelling-temperature curve in the 400 to 600 °C range. Swelling continues to decrease above 600 °C up to about 700 °C. Above 700 °C, fission gas swelling begins to occur. A few tenths of a percent alloying addition or an applied external pressure have been found to be effective in overcoming this "mechanical" type of swelling. Efforts are continuing to better define the basic mechanisms involved and the interrelationship between burnup, temperature, pressure and metallurgical state. Fundamental information developed by this program will provide a basis for engineering exploitation of the many beneficial attributes of metal fuels for use in reactor applications.

IRRADIATION PROGRAM

C. R. Hann, R. K. Marshall

Capsules P-18 (825 °C, 50 psi, 01.–0.7 at.% BU) and P-11 (550 °C, 5000 psi, 0.2–0.8 at.% BU) were discharged after successfully reaching their goal exposures. A tandem assembly of three, controlled temperature-pressure capsules (P-12, P-13, and P-17) will be charged during the next reactor outage. The status of currently active capsules is indicated in Table 9.1 with specimen arrangements described in Tables 9.2, 9.3, 9.4, 9.5, and 9.6.

TABLE 9.1. Capsule Status

Capsule Number	Control Temp, °C	Control Pressure, psi	Goal[a] BU, at.%	Status
P-10	450	5000	0.2 - 0.8	Under examination in Radiometallurgy
P-11	550	5000	0.2 - 0.8	Discharged
P-12	625	5000	0.2 - 0.8	Ready to charge
P-13	700	5000	0.2 - 0.8	Ready to charge
P-14	700	500	0.2 - 0.8	Discharged
P-15	700	1000	0.2 - 0.8	Under examination in Radiometallurgy
P-16	625	1000	0.35 - 0.7	Discharged
P-17	825	5000	0.2 - 1.5	Ready to charge
P-18	825	50	0.1 - 0.7	Discharged
P-19	825	50	0.2 - 1.5	Under construction
P-20	725	50	0.2 - 1.5	Under construction

(a) *Different burnups are achieved in a single capsule by including specimens of various enrichments.*

TABLE 9.2. Specimen Arrangement in Swelling Capsules P-10 through P-15

Specimen Number	Alloy Designation	Composition (Additions in ppm)	Heat Treatment[a]	^{235}U, %
A-1	E-2	U + 109 Fe–30 Al–36 Si–53 C	AE	2.88
A-2	E-2	U + 109 Fe–30 Al–36 Si–53 C	BQ	2.88
B-1	U+Fe-Si	U + 140 Fe–25 Al–95 Si–400 C	AE	0.72
B-2	U+Fe-Si	U + 140 Fe–25 Al–95 Si–400 C	BQ	0.72
C-1	Hi P	U + 64 Fe–25 Al–25 Si–6C	AE	0.72
C-2	Hi P	U + 64 Fe–25 Al–25 Si–6C	BQ	0.72
D-1	U+Fe-Al-Si	U + 407 Fe–645 Al–95 Si–500 C	AE	0.72
D-2	U+Fe-Al-Si	U + 407 Fe–645 Al–95 Si–500 C	BQ	0.72
E-1	WEB	U + 393 Fe–807 Al–32 Si–402 C	AE	1.47
E-2	WEB	U + 393 Fe–807 Al–32 Si–402 C	BQ	1.47
F-1	E-1	U + 98 Fe–11 Al–34 Si–56 C	AE	1.44
F-2	E-1	U + 98 Fe–11 Al–34 Si–56 C	BQ	1.44

(a) *AE: As-extruded*
BQ: 730 °C-15 min-Oil Quench

TABLE 9.3. Specimen Arrangement in Swelling Capsule P-16

Specimen Number	Alloy Designation	Composition (Additions in ppm)	Heat Treatment[a]	^{235}U, %
A-1	E-1	U + 98 Fe–11 Al–34 Si–56 C	AE	1.44
A-2	E-1	U + 98 Fe–11 Al–34 Si–56 C	BQ	1.44
B-1	E-1	U + 98 Fe–11 Al–34 Si–56 C	AE	1.44
B-2	E-1	U + 98 Fe–11 Al–34 Si–56 C	BQ	1.44
C-1	U + Fe-Al-Si	U + 407 Fe–645 Al–95 Si–500 C	AE	0.72
C-2	U + Fe-Al-Si	U + 407 Fe–645 Al–95 Si–500 C	BQ	0.72
D-1	WEB	U + 393 Fe–807 Al–32 Si–402 C	AE	1.47
D-2	WEB	U + 393 Fe–807 Al–32 Si–402 C	BQ	1.47
E-1	U + Fe-Al-Si	U + 407 Fe–645 Al–95 Si–400 C	AE	0.72
E-2	U + Fe-Al-Si	U + 407 Fe–645 Al–95 Si–400 C	BQ	0.72
F-1	WEB	U + 393 Fe–807 Al–32 Si–402 C	AE	1.47
F-2	WEB	U + 393 Fe–807 Al–32 Si–402 C	BQ	1.47

(a) *AE: As-extruded*
BQ: 730 °C-15 min-Oil Quench

TABLE 9.4. Specimen Arrangement in Swelling Capsules P-17 and P-18

Specimen Number	Alloy Designation	Compositions (Additions in ppm)	Metallurgical Condition[a]	^{235}U, %
A-1	Th–5.4 wt% U	Analysis incomplete	A	93
A-2	E-2	U + 109 Fe–30 Al–36 Si–53 C	AE	2.88
B-1	Th–1 wt% U	Analysis incomplete	B	93
B-2	Th–1 wt% U	Analysis incomplete	C	93
C-1	Hi P	U + 64 Fe–25 Al–25 Si–6 C	AE	0.72
C-2	Hi P	U + 64 Fe–25 Al–25 Si–6 C	BQ	0.72
D-1	U + Fe-Si	U +140 Fe–25 Al–95 Si–400 C	AE	0.72
D-2	U + Fe-Al-Si	U +407 Fe–645 Al–95 Si–500 C	AE	0.72
E-1	E-1	U + 98 Fe–11 Al–34 Si–56 C	AE	1.44
E-2	WEB	U +393 Fe–807 Al–32 Si–402 C	AE[b]	1.47
F-1	Th–3.85 wt% U	Analysis incomplete	D	93
F-2	Th–3.85 wt% U	Analysis incomplete	C	93

(a) *A: Extruded and cold swaged*
B: Hot rolled, cold rolled and cold swaged
C: 850 °C-2 hr-FC
D: Hot rolled and cold swaged
AE: As-extruded
BQ: 730 °C-15 min-Oil Quench

(b) *BQ: In capsule P-18*

TABLE 9.5. Specimen Arrangement in Swelling Capsule P-19

Specimen Number	Alloy Designation	Compositions (Additions in ppm)	Metallurgical Condition(a)	^{235}U, %
A-1	Th–5.4 wt% U	Analysis incomplete	A	93
A-2	Th–5.4 wt% U	Analysis incomplete	C	93
B-1	Th–1 wt% U	Analysis incomplete	B	93
B-2	Th–1 wt% U	Analysis incomplete	C	93
C-1	U + Fe-Al-Si	U + 407 Fe–645 Al–95 Si–500 C	AE	0.72
C-2	U + Fe-Si	U + 140 Fe–25 Al–95 Si–400 C	AE	0.72
D-1	Th–3.85 wt% U	Analysis incomplete	D	93
D-2	Th–3.85 wt% U	Analysis incomplete	C	93
E-1	Th–1 wt% U	Analysis incomplete	B	93
E-2	Th–1 wt% U	Analysis incomplete	C	93
F-1	U_3Si (3.6 wt% Si)	-	E	0.72
F-2	U_3Si (4.0 wt% Si)	-	E	0.72

(a) *A: Extruded and cold swaged*
B: Hot rolled, cold rolled, and cold swaged
C: 850 °C - 2 hr - FC
D: Hot rolled and cold swaged
E: 800 °C for several days - FC
AE: As-extruded

TABLE 9.6. Specimen Arrangement in Swelling Capsule P-20

Specimen Number	Alloy Designation	Compositions (Additions in ppm)	Metallurgical Condition(a)	^{235}U, %
A-1	Th–5.4 wt% U	Analysis incomplete	A	93
A-2	Th–5.4 wt% U	Analysis incomplete	C	93
B-1	E-2	U + 109 Fe–30 Al–36 Si–53 C	AE	2.88
B-2	E-2	U + 109 Fe–30 Al–36 Si–53 C	BQ	2.88
C-1	E-1	U + 98 Fe–11 Al–34 Si–56 C	AE	1.44
C-2	WEB	U + 393 Fe–807 Al–32 Si–402 C	AE	1.47
D-1	Th–3.85 wt% U	Analysis incomplete	D	93
D-2	Th–3.85 wt% U	Analysis incomplete	C	93
E-1	Th–1 wt% U	Analysis incomplete	B	93
E-2	Th–1 wt% U	Analysis incomplete	C	93
F-1	U_3 Si (3.6 wt% Si)	-	E	0.72
F-2	U_3 Si (4.0 wt% Si)	-	E	0.72

(a) *A: Extruded and cold swaged*
B: Hot rolled, cold rolled, and cold swaged
C: 850 °C - 2 hr - FC
D: Hot rolled and cold swaged
E: 800 °C for several days - FC
AE: As-extruded
BQ: 730 °C - 15 min-Oil Quench

Several capsules listed in Table 9.1 contain nickel, iron, molybdenum and rhenium foils; molybdenum and rhenium length change rods; and molybdeunum and iron tensile rods for the purposes of another program.

The above irradiation capsules will provide data needed to evaluate the effects of temperature (alpha, beta, and gamma phase in uranium base alloys), pressure, burnup, burnup rate, and minor alloying additives on the irradiation behavior of uranium and thorium-uranium alloys.

POSTIRRADIATION EXAMINATION

C. R. Hann, B. Mastel

The irradiation history and measured swelling were previously reported[1] for specimens recovered from capsule P-10 (450 °C, 5000 psi, 0.2–0.8 at.% BU). The metallurgical histories and compositions of the specimens are summarized in Table 9.2. Irradiation temperatures ranged from 405 to 460 °C while estimated burnups ranged from 0.22 to 0.82 at.%. The burnup range was achieved with samples of different enrichment. All specimens were identical in geometry, i.e., a split tube 1/2 in. OD x 0.030 in. wall with lengths varying from 3/8 to 5/8 in.

Optical micrographs of specimen P-10-C1 are shown in Figure 9.1. The small equiaxed grains of the preirradiation microstructure have been distorted by irradiation growth processes, but the large grain boundary tears, occurring in uranium irradiated at lower pressures to comparable burnups in the 400 to 525 °C temperature range, are not present.

Electron micrographs obtained from negative replicas are depicted in Figures 9.2, 9.3, and 9.4. Individual grains are discernible and heterogeneously distributed porosity is apparent. A few tears occur, but most of the porosity appears as spherical-shaped voids. It is not known at this time whether the spherical voids are filled with gas or are merely small tears.

Representative optical micrographs of specimen P-10-A1 are shown in Figure 9.5. Comparison of Figure 9.5 with Figure 9.1 reveals the pronounced effect of a factor-of-four difference in burnup. No grain structure is apparent in Figure 9.5, and the black areas are microtears which are resolved in the electron micrographs of Figures 9.6, 9.7, and 9.8. In contrast to P-10-C1, most of the porosity in P-10-A1 appears as small tears, with very few grain boundaries evident. This difference in porosity could be caused by subtle temperature effects either during irradiation or during reactor downtimes. P-10-C1 operated at 450 °C (reactor up) and 300 °C (reactor down) while P-10-A1 operated at 425 to 430 °C (reactor up) and 205 to 210 °C (reactor down). Additional metallography on a specimen at an intermediate burnup (0.43 at.%) might resolve this point. High pressure annealing at 5000 psi might also establish whether fission gas swelling or tear sintering is occurring. Quantitative measurements will be made to determine the size-frequency relationship of the porosity and its contribution to the total volume increase. A paper entitled "Fission

A paper entitled "Fission Gas Pores in Postirradiation Annealed Uranium" was presented on February 26-29, 1968 at the 97th Annual Meeting of the AIME in New York City.

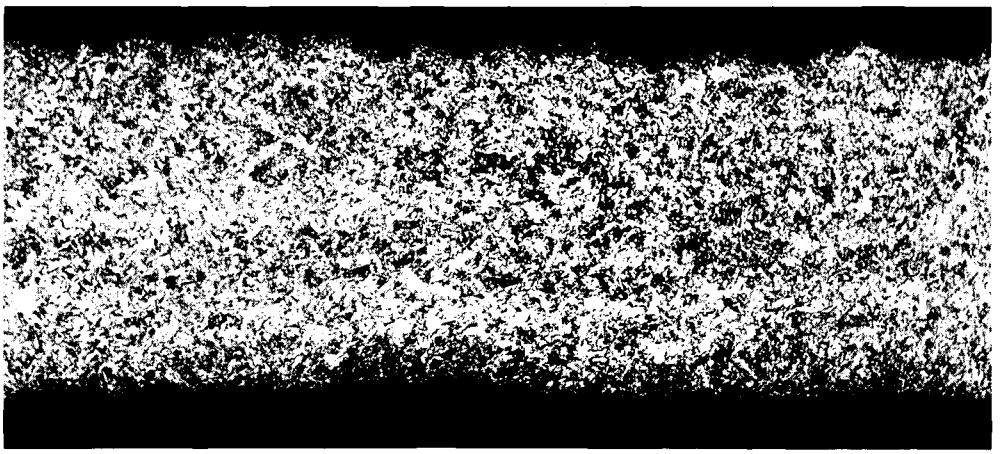

E4847 *60X*

Etched (Ion Bombardment)

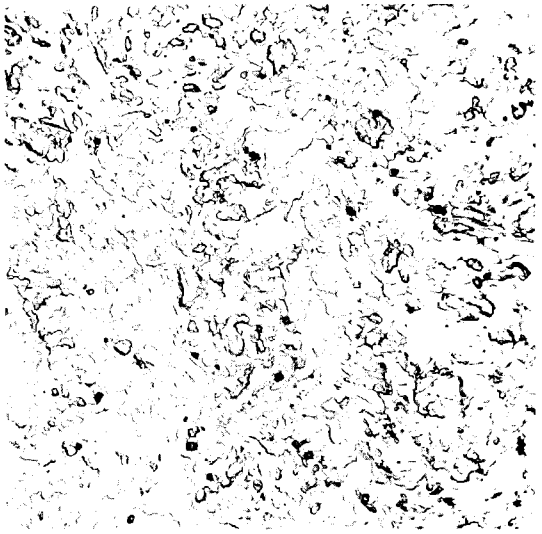

E4848 *200X*

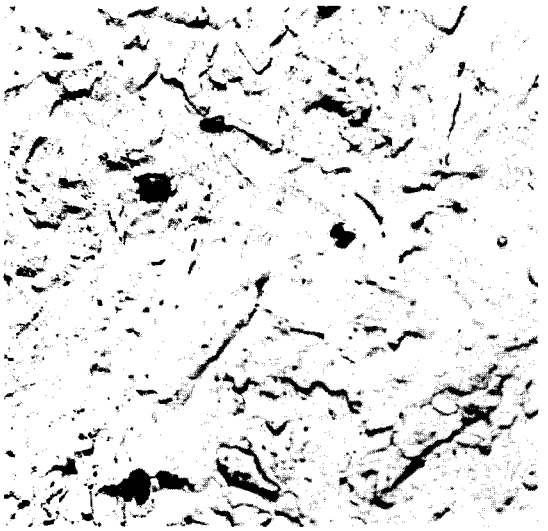

E4849 *600X*

Etched (Ion Bombardment)

FIGURE 9.1. High Purity Uranium Specimen P-10-C1 Irradiated at 450 °C and 5000 psi to 0.22 at.% BU ($\Delta V/V = 2.5$)

5499A 2960X

FIGURE 9.2. High Purity Uranium Specimen P-10-C1 Irradiated at 450 °C and 5000 psi to 0.22 at.% BU (%ΔV/V = 2.5)

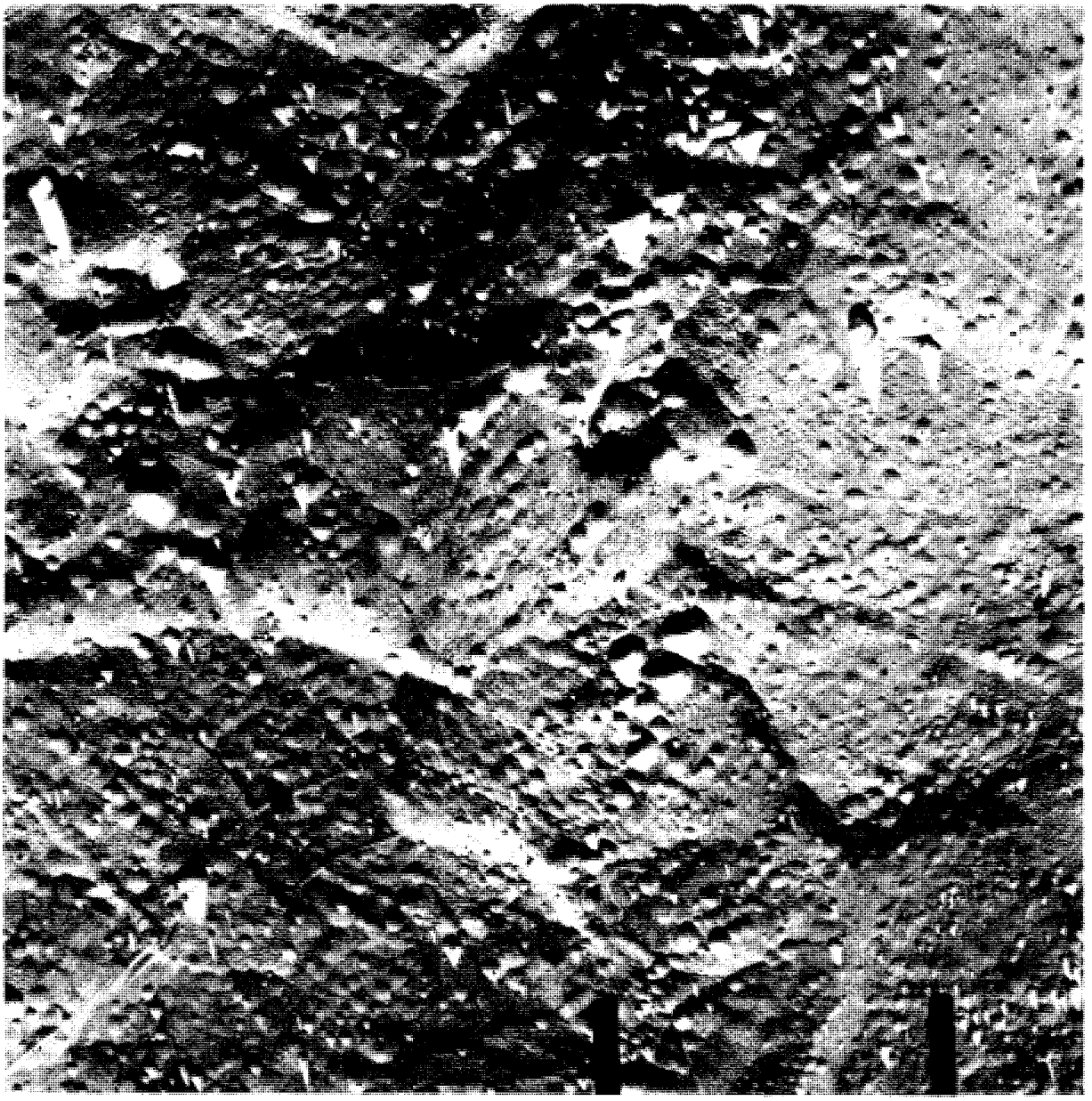

5499B 4640X

FIGURE 9.3. Same Area as Figure 9.2

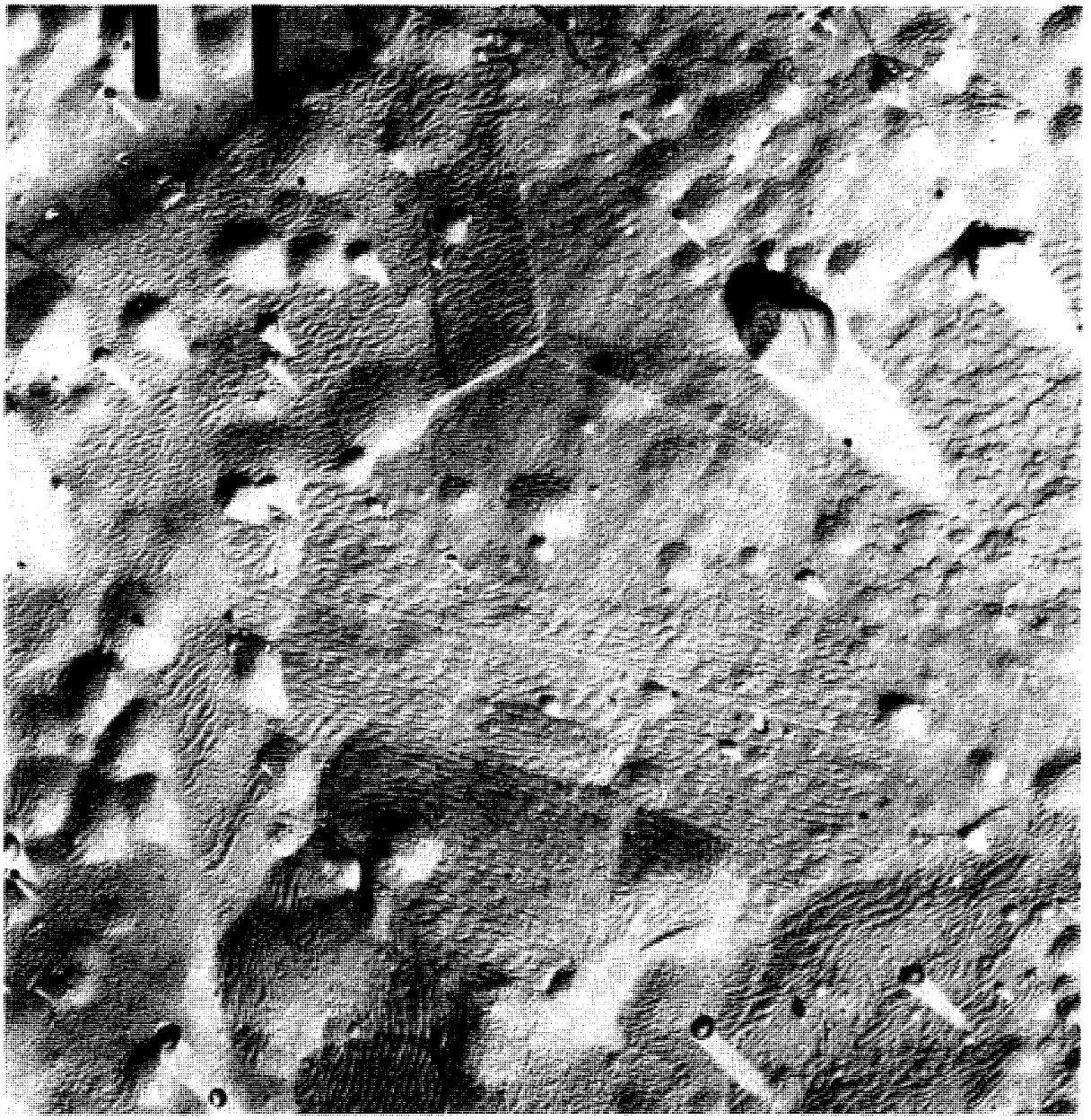

5999C *14,000X*

FIGURE 9.4. Same Area as Figures 9.2 and 9.3

E4853 *60X*

Etched (Ion Bombardment)

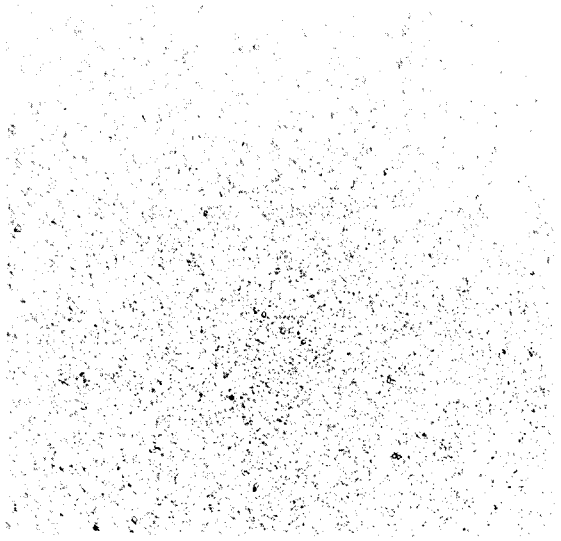

E4854 *200X*

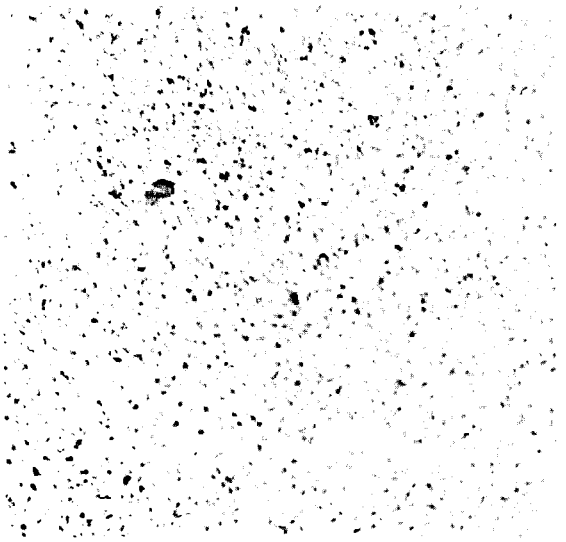

E4855 *600X*

Etched (Ion Bombardment)

FIGURE 9.5. High Purity Uranium Specimen P-10-A1 Irradiated at 425-430 °C and 5000 psi to 0.82 at.% BU (%ΔV/V = 4.4)

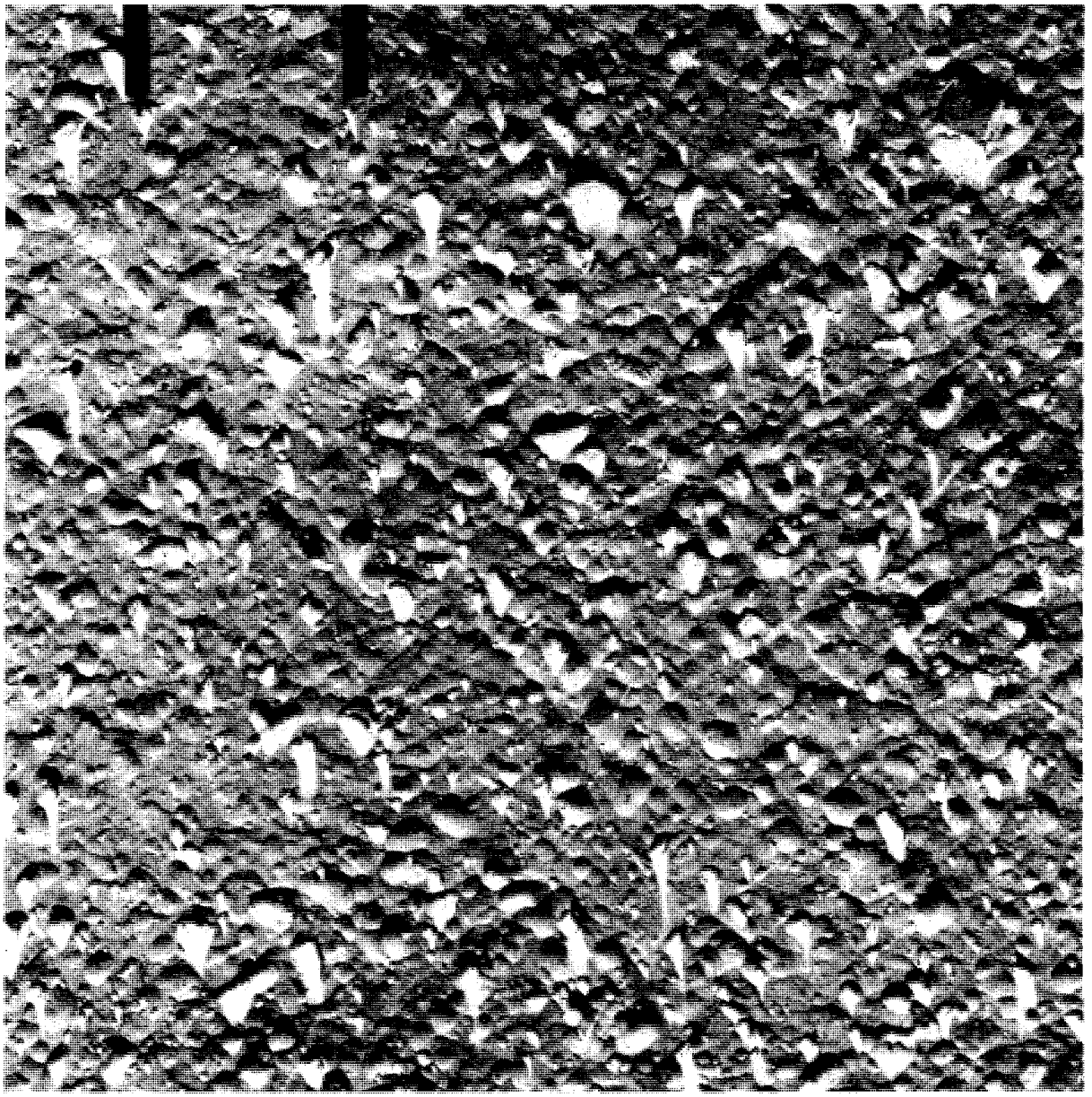

5495D 2840X

FIGURE 9.6. High Purity Uranium Specimen P-10-A1 Irradiated at 425-430 °C and 5000 psi to 0.82 at.% BU (%ΔV/V = 4.4)

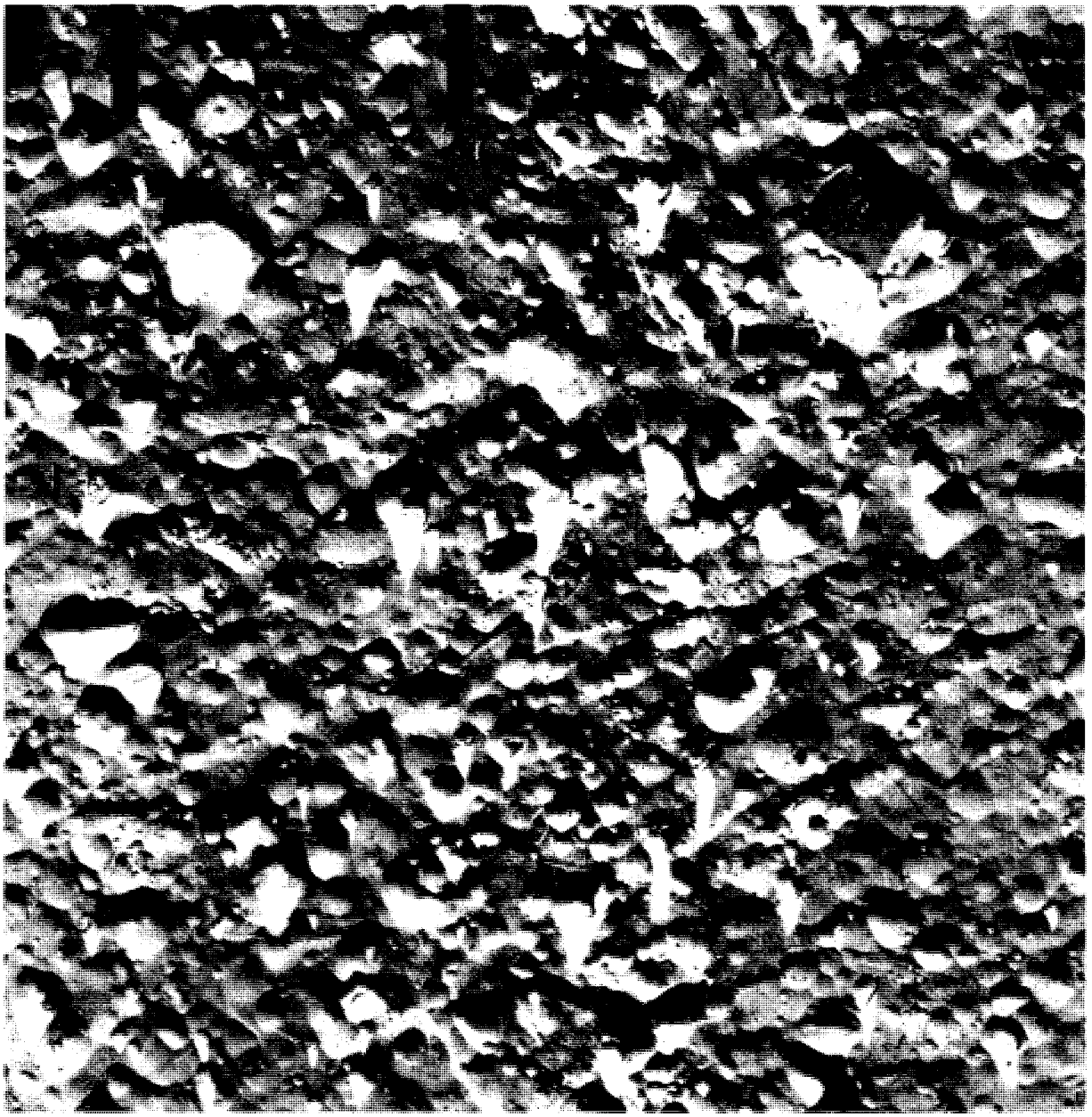

5495E 4600X

FIGURE 9.7. Same Area as Figure 9.6

5496A 15,600X

FIGURE 9.8. Same Area as Figures 9.6 and 9.7

HIGH PRESSURE, POSTIRRADIATION ANNEALING

G. L. Kulcinski

The purposes of this study are to determine the effect of hydrostatic pressure on: 1) the fission gas induced swelling in uranium, 2) the healing of irradiation produced microtears in irradiated uranium, and 3) the diffusion of fission gases in uranium and Zircaloy-2 cladding.

Fission Gas Swelling in Gamma Uranium

A paper entitled "Fission Gas Induced Swelling in Uranium at High Temperatures and Pressures" was presented at the 97th Annual Meeting of the AIME held on February 26-29, 1968 in New York City.

As indicated in the previous quarterly,[2] density measurements have been repeated on several samples that were contaminated by an oxide surface layer after the capsule unloading (Table 9.7). In all the cases of the low-carbon high-purity material, the swelling was drastically reduced after 900 °C high pressure anneals. This result is similar to that reported earlier[2] for samples that had swelled because of pulse anneals to 600 °C after irradiation. Therefore, the reversibility of swelling in uranium does not seem to depend on whether the sample has swelled during irradiation or as a result of a postirradiation anneal.

Several vacuum anneals were performed this quarter on samples in the as-irradiated state, as well as those which had been annealed under pressure (Table 9.8).

The sample P1A16-3, heated to 600 °C for 1/2 hr after a 900 °C-100 hr-340 bar anneal, showed essentially no further increase in swelling after the high pressure anneal, which is significant because this very same sample had undergone 11% swelling when originally heated to 600 °C for 5 hr. Metallographic examination after the first vacuum anneal showed that most of the bubbles were found on the boundaries of the newly recrystallized grains. Since high temperature anneals in the gamma phase should remove the strain in the lattice caused by irradiation at a low temperature, one would not expect subsequent annealing in the high alpha region to promote recrystallization. Therefore, it appears that 600 °C is not a high enough temperature to cause fission gas swelling in the absence of a driving force for bubble coalescence, such as recrystallization.

The results of vacuum annealing as-irradiated specimens (1A4, 1A5) at 900 °C for 100 hr show that volume increases on the order of 31 to 32% occur. This agrees fairly well with previously reported data for 0.41% burnup material annealed at 880 °C for 100 hr.[3] The swelling in the latter case was 29%. A sample having undergone a previous high temperature-pressure anneal (PB3) swelled approximately the same as the as-irradiated samples during 900 °C vacuum annealing. This indicated

TABLE 9.7. Density Measurements and R Values of Samples Subjected to Postirradiation Pressure Annealing at 900 °C After Irradiation at Elevated Temperatures and Pressures

Sample No.	Irradiation Condition	Annealing Press. Bars	Burnup, %	Density g/cm^3 After Irrad.	Density g/cm^3 After Press. Test	R[a] After Irrad.	R[a] After Press. Test
T12	575 °C - 1000 psi[b]	1000	0.15	18.15	(d)	32	--
T22	575 °C - 1000 psi[c]	1000	0.15	16.87	18.90	85	4
TA3	550 °C - 500 psi[b]	340	0.16	18.40	18.84	19	4
TB3	550 °C - 500 psi[c]	340	0.16	15.32	18.74	152	10
TA4	550 °C - 500 psi[b]	110	0.16	18.77	18.63	7	11
TB4	550 °C - 500 psi[c]	110	0.16	16.23	18.60	107	14

(a) *(% $\Delta V/V_o$)/% Burnup.*
(b) *High carbon, high purity uranium.*
(c) *Low carbon, high purity uranium.*
(d) *Destroyed during measurement.*

TABLE 9.8. Swelling Induced in 0.37% Burnup Uranium as a Result of Postirradiation Vacuum Annealing

Sample No.	Temp, °C	Time, hr	Density, g/cm^3	$\frac{\Delta V}{V_o}$, %	R[a]
P1A16-3[b]	600	1/2	18.52	2.3	6
1A4	900	100	14.35	32.1	87
1A5	900	100	14.44	31.3	85
PB3[c]	900	100	14.22	33.3	90
1A6	1082	3	13.01	45.5	123
1A7	1082	3	12.93	46.5	125
PC3[c]	1082	3	13.09	44.7	121
P1A14-2[d]	1082	1/2	12.39	53.0	143

(a) *(% $\Delta V/V_o$)/% Burnup.*
(b) *After successive anneals at 600 °C, 5 hr in a vacuum and 900 °C for 100 hr under 340 bars pressure.*
(c) *After 900 °C, 100 hr, 340 bar anneal.*
(d) *After successive anneals at 600 °C for 1/2 hr in vacuum, and 900 °C for 100 hr under 1000 bars pressure.*

that fission gas swelling is essentially a reversible phenomena at sufficiently high temperatures.

The results of a 1082 °C anneal for 3 hr showed that both samples in the as-irradiated case, as well as samples that had undergone a previous 340 bar anneal, swell about the same amount (~45 to 46%). A sample that had shown reversible swelling previously (P1A14-2) displayed a 53% volume increase at 1082 °C for 1/2 hr. Since the sample is so porous at this point, the accuracy of the density measurements is questionable, and it is not certain that this sample showed any increased swelling, as compared to the other samples (1A6, 1A7, and PC3) annealed at 1082 °C for 3 hr.

A compilation of data obtained thus far is shown graphically in Figure 9.9, where the percentage volume increase found as a result of 100 hr 900 °C anneals is plotted versus the annealing pressure. Of

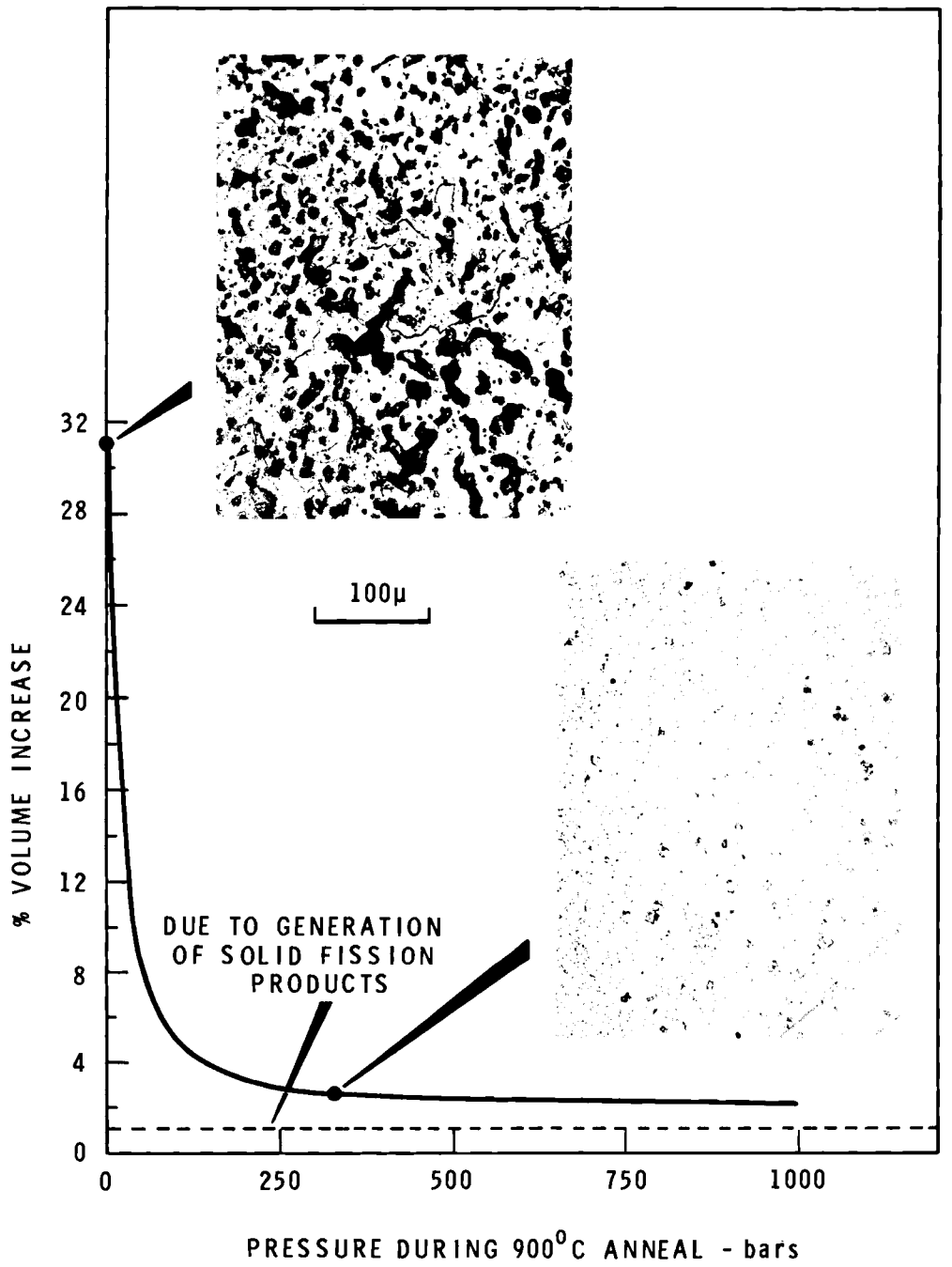

Neg 0680952

FIGURE 9.9. Effect of Hydrostatic Pressure on Fission Gas Induced Swelling in Irradiated Uranium

particular importance is the extreme sensitivity of the swelling to pressures below ~100 bars and the general leveling out of the curve by ~300 bars. The dotted line represents the contribution to be expected from the solid fission products. The inserts show the microstructures of the samples after vacuum and 340-bar anneals. Whereas considerable coalescence and rather large bubble size (5 to 10 μ in diameter) is noted in the vacuum annealed sample, the structure after a 340 bar anneal shows no observable bubbles at a magnification of 250X. The fine background of black spots is caused by an increased amount of second phase precipitation.

Metallography of the pressure annealed samples is continuing.

References

1. *J. J. Cadwell, D. R. de Halas, R. E. Nightingale and D. C. Worlton. Quarterly Progress Report, July, August, September, 1967, Reactor Fuels and Materials Branch of USAEC Division of Reactor Development and Technology, BNWL-658. Pacific Northwest Laboratory, Richland, Washington, February 1968.*

2. *J. J. Cadwell, D. R. de Halas, R. E. Nightingale and D. C. Worlton. Quarterly Progress Report, October, November, December, 1967, Reactor Fuels and Materials Branch of USAEC Division of Reactor Development and Technology, BNWL-668. Pacific Northwest Laboratory, Richland, Washington, March 1968.*

3. *T. K. Bierlein, B. Mastel, and R. D. Leggett. Metallographic Observations of Swelling in Uranium, HW-63848, USAEC, Richland, Washington, 1960.*

ATR GAS AND WATER LOOP OPERATION AND MAINTENANCE

J. E. Minor

ATR GAS LOOP SUPPORT

J. E. Minor

Gas-Cooled-Loop Design Review

The design of the lower specimen train portion of the Gas Cooled Loop (GCL) inpile tube has been under review. The design of the specimen containers required that the original hanger-rod design be changed to a plate-type hanger. Vendor response to the incorporation of these changes into the existing inpile tube order indicated that additional design effort should be made. Such an effort would simplify the configuration and thus obtain a workable assembly at a more reasonable cost. The design change was modified as necessary to include only those portions of the lower specimen train present in the original order. The portions requiring redesign will be procured separately by BNW on a procurement directive to AEC-RLO. An estimate to perform this work is currently being prepared for submittal to AEC-ID.

All cognizant agencies have agreed to the final draft of the HSW Clean Room and Quality Control Procedures. Because of the change in GCL funding, the clean rooms that have been constructed will probably be used for component storage.

Analyses of the GCL Loop primary and regeneration heat exchangers were performed and reported by Idaho Nuclear Corporation. Their results indicate that flow-induced vibrations in these units are of such limited amplitude and frequency that no vibration difficulty is expected.

Vendor Data Review

Vendor data reviewed include submittals from manufacturers of the primary circulators, purification train, heat exchanger and miscellaneous smaller equipment. The data have been generally acceptable. The heat exchanger manufacturer has submitted revisions to his welding procedures to permit use of recently procured automatic welding equipment. Presently, the only area in question is his proposal to make all the tube-to-tube sheet welds without filler metal. He was requested to submit chemical analyses for the actual components to be welded for evaluation so that the probability of obtaining acceptable welds by this means could be determined. The results of this evaluation should be available within a few weeks. One item, concerning welding in the analytical panel, requires some R&D effort prior to preparation of a recommendation. Sample components are enroute to PNL for development of an acceptable method for joining 303 SS to 304.

Meetings

On January 10, A.M., a meeting was held with INC, AEC-ID, and BNW at the

Time	pH		Oxygen (ppm)
19:54	10.16		8.75
22:08	--	Yellow Water	--

The loop was cooled down and the test was terminated. The yellow water sample, indicating chromate, was qualitatively analyzed, and chromium was verified and estimated at about 10 ppm. A trace of iron was found and estimated at 1 ppm. Nickel was not found and sodium showed about 0.1 ppm. At first it was believed that sodium dichromate inhibited HDW (high-pressure demineralized water, 240 psig) leaked into the loop because HDW is used to cool the shell side of the three heat exchangers and the three primary circulation pumps. However, because the loop was at 2000 psig, no makeup water had been added, and the leak rate was small, the possibility of HDW leakage was discounted. Investigation revealed that similar yellow water incidents have been seen in other loops when excess oxygen was in the water. It is now believed that chromate was formed from the stainless steel piping in the loop, the chemical reactions being in two steps:

$$2Cr + 3H_2O \text{ -- } Cr_2O_3 + 3H_2 \qquad (1)$$

$$2Cr_2O_3 + 3O_2 + 4H_2O \text{ -- } 4H_2CrO_4 \qquad (2)$$

Chromic acid was formed which ionized to give free chromate ion and the yellow colored water.

Later, a fourth water chemistry test was run with the loop filled with LDW, pressurized to 2000 psig, heated to 540 °F, and circulated at 60 gpm. Before the loop was heated, the oxygen was reduced from 8 ppm to 4.25 ppm by degassing for a few hours. A side flow of 1.5 gpm was flowing through the purification ion exchangers. The following results were recorded:

Time	pH	Oxygen (ppm)	Date
10:30	10.05	4.25	2-12-68
11:22	--	4.35	2-12-68
13:30	10.03	4.20	2-12-68
09:00	10.08	4.20	2-13-68
10:09	10.06	1.85	2-13-68

The system was degassed after 09:00 and the oxygen content was reduced as shown. Prior to that time, little change in pH or oxygen concentration was noted.

Another similar test is planned with the reactor at about 100 MW to see what effect neutrons have on the oxygen level.

A tilt table and work tray were shipped from Richland to the ATR. The 3 by 5 ft tray and 24 ft long tilt table will soon be installed in the ATR canal and will be used to assemble and disassemble loop sample trains.

Spare parts that have been ordered are being delivered to the NRTS site. Such parts, which will help insure continuous operation of the ATR pressurized water loop, include spare thermocouples, gaskets, valves, packing, diaphragms and related items.

REACTOR FUELS AND MATERIALS
FAST REACTOR DOSIMETRY AND DAMAGE ANALYSIS

R. E. Nightingale

FAST-REACTOR NEUTRON SPECTRA AND FOIL-ACTIVATION CROSS SECTION EVALUATION*

W. N. McElroy, J. L. Jackson, and J. A. Ulseth

The SAND-II code[1] has been used to calculate neutron spectra from multiple-foil activation data for an EBR-II low-power (∿20 kW) reactor run. The reactions utilized were $^{63}Cu(n,\gamma)$, $^{45}Sc(n,\gamma)$, $^{235}U(n,f)$, $^{58}Ni(n,p)$, $^{238}U(n,f)$, $^{54}Fe(n,p)$, $^{46}Ti(n,p)$, and $^{27}Al(n,\alpha)$. Different combinations of these reactions and initial input spectral approximations were used to determine six solutions to test the uniqueness of the iterative solution. The results for the neutron integral flux above seven specified energy values are presented in Table 11.1.

The variation in integral flux values for the six solutions given in Table 11.1 is rather small, which shows that the multiple-foil technique is well suited for fast-reactor flux and fluence measurements. The uncertainties in foil reaction cross sections and the dependence of the iterative solution on the input spectral approximation do not appear to introduce uncertainties of more than about ±10% (one standard deviation) in integral flux values.

In a previous report,[2] the application of the multiple-foil activation method to evaluation of the differential cross section for the $^{54}Fe(n,p)^{54}Mn$ reaction was discussed. The method involves irradiating identical foils in each of "m" different neutron environments, determining the corresponding values of saturated activities, and then solving a set of activation integral equations for the magnitude and shape of the differential cross section.

Preliminary results have also been obtained for the differential cross section of the $^{27}Al(n,\alpha)^{24}Na$ reaction, and they are presented in Figure 11.1 and tabulated in Table 11.2. The shaded area in the figure represents the envelope of solutions for the CAND-II (Cross Section Analysis by Neutron Detectors - II code) based on all the initial approximations listed in the figure legend. The results are derived from the use of a total of 11 reference spectra. Because three of the spectra used are very similar, the results shown in Figure 11.1 are in effect based on nine spectra. The most reasonable solution should be from the initial approximation representing a best fit through all available differential data. The CAND-II solution based on this best-fit input is identified by the solid curve in the figure. Most of the monoenergetic differential cross sec-

* *The cross section evaluation studies are funded in part under the AEC Special Studies Account.*

TABLE 11.1. SAND-II Integral Flux Comparison EBR-II Low Power (20 kW) RUN #1 (Core Center - Row 1, Reactor Midplane)

Run #	SAND-II Input Spectral Approximation	Foils Used (Total of 8)	No. of Iterations to Achieve 20% Diff. Solution	Absolute Value of Integral Flux (n/cm^2-sec) Above Specified Energies (MeV)						
				10^{-3}	10^{-2}	0.18	0.5	1	3	5
1	Constant $\geq 10^{-2}$ E Form $<10^{-2}$	All	15	1.228×10^{12}	1.213×10^{12}	1.037×10^{12}	7.494×10^{11}	3.613×10^{11}	6.392×10^{10}	1.898×10^{10}
2	Mach-I[a]	All	20	1.169×10^{12}	1.159×10^{12}	0.920×10^{12}	5.478×10^{11}	2.846×10^{11}	6.156×10^{10}	1.975×10^{10}
3	Monte Carlo[b]	All	9	1.073×10^{12}	1.054×10^{12}	0.803×10^{12}	5.802×10^{11}	3.100×10^{11}	6.305×10^{10}	1.652×10^{10}
4	Transport	All	18	1.159×10^{12}	1.149×10^{12}	0.909×10^{12}	5.558×10^{11}	2.895×10^{11}	6.411×10^{10}	1.810×10^{10}
5	Transport	^{235}U Out	11	1.304×10^{12}	1.297×10^{12}	1.068×10^{12}	6.677×10^{11}	3.159×10^{11}	6.500×10^{10}	1.750×10^{10}
6	Transport	^{63}Cu, ^{45}Sc Out	1	1.086×10^{12}	1.084×10^{12}	0.854×10^{12}	5.347×10^{11}	3.030×10^{11}	6.465×10^{10}	1.593×10^{10}
	Average Value of RUNS 2 Through 6[c]			1.16×10^{12}	1.15×10^{12}	0.911×10^{12}	5.77×10^{11}	3.01×10^{11}	6.37×10^{10}	1.76×10^{10}
	Standard Deviation[d]			$\pm 0.09 \times 10^{12}$	$\pm 0.09 \times 10^{12}$	$\pm 0.10 \times 10^{12}$	$\pm 0.53 \times 10^{11}$	$\pm 0.13 \times 10^{11}$	$\pm 0.14 \times 10^{10}$	$\pm 0.15 \times 10^{10}$

(a) *Private communication from F. Kirn, ANL-Idaho.*

(b) *Private communication from J. Moteff, GE.*

(c) *The SAND-II run with the constant flux used as input was not expected to be as reliable as the other runs and was not included in the average -- RUN #1 was used mainly to establish the adequacy of the foil set in providing a unique solution.*

(d) *This standard deviation is a reflection of errors resulting from using different input spectral approximations, different foil sets, and a solution criterion of 20% which reflects the errors associated with the measurement of the foil activities.*

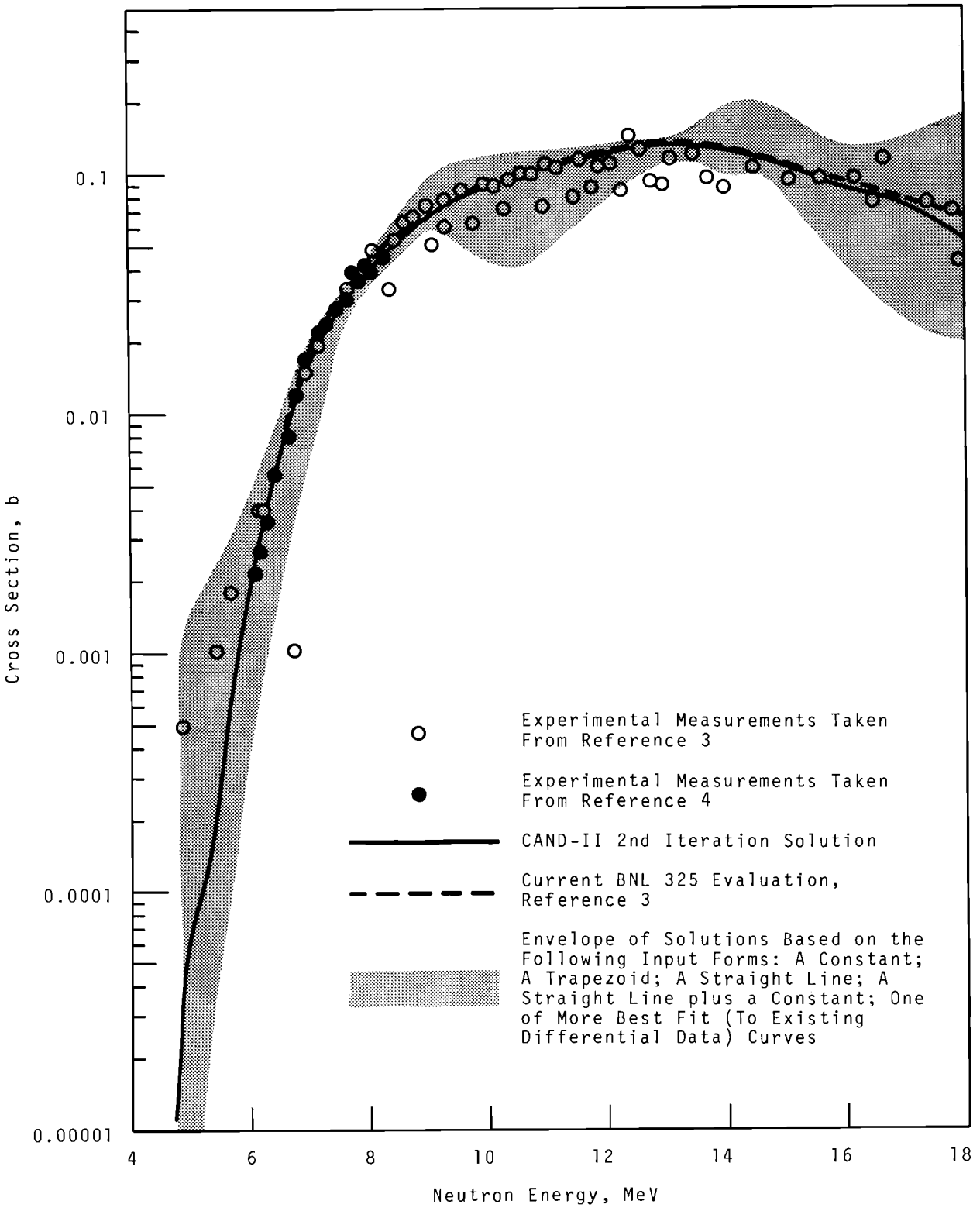

FIGURE 11.1. CAND-II Solution for $^{27}Al(n,\alpha)^{24}Na$ Reaction Cross Section

tion measurements reported in the literature, as well as the current BNL-325 evaluated cross section curve, are also shown in Figure 11.1.[3,4]

The solution envelope broadens at higher energies, (Figure 11.1). This indicates lower reliability for the differential solution with increasing energy and is associated with the lack of high-energy neutrons, and lack of adequate differences among the 11 reference spectra. Although the CAND-II solution based on the best-fit input should be the best evaluation, it is only approximately correct in differential form. Nevertheless, the iterative process does adjust the input differential form and magnitude so as to produce consistency with the integral activity measurements -- a necessary condition that is not currently satisfied for most cross-section evaluations reported in Reference 3.

Calculated values of fission-averaged cross section ($\bar{\sigma}^f$) based on the data in Table 11.2 for four forms of the fission spectrum are presented in Table 11.3.* Zijp has provided a summary of previously reported values of $\bar{\sigma}^f$ for $^{27}Al(n,\alpha)^{24}Na$.[5] The values range from 0.44 to 0.85 mb and are based on direct integral measurements in different types of neutron environments and/or on calculations using various evaluated differential cross section curves and one of the four forms of the fission spectrum. Fabry has recently reported measured absolute values of fission-averaged cross sections for $^{27}Al(n,\alpha)^{24}Na$ and other reactions.[6]

Fabry's values provide a self consistent set which are, perhaps,

TABLE 11.2. $^{27}Al(n,\alpha)^{24}Na$ Evaluated Differential Cross Sections

Neutron Energy, MeV	Cross Section, b
4.6	0.00(a)
4.8	2.19×10^{-5}
5.0	6.47
5.2	1.04×10^{-4}
5.4	1.78
5.6	4.68
5.8	9.73
6.0	1.79×10^{-3}
6.2	3.07
6.4	4.74
6.6	7.78
6.8	1.21×10^{-2}
7.0	1.69
7.1	1.92
7.2	2.13
7.3	2.10
7.4	2.22
7.5	2.68
7.6	3.11
7.7	3.14
7.8	3.12
7.9	3.59
8.0	4.31
8.1	4.43
8.2	4.24
8.3	4.24
8.4	4.68
8.5	4.98
9.0	6.66
9.5	7.76
10.0	8.70
10.5	9.56
11.0	1.04×10^{-1}
12.0	1.20
13.0	1.32
14.0	1.26
15.0	1.06
16.0	8.63×10^{-2}
17.0	7.33
18.0	6.15

(a) *Assigned Value*

* *Grundl's 50-group tabulated data were used for the fifth specified form.*

TABLE 11.3. Calculated Fission-Averaged Cross Sections for $^{27}Al(n,\alpha)^{24}Na$

$\phi^f(E)$ - Fission Form[1]	Fission-Averaged Cross Section, mb[a]
Watt	0.663
Frye	0.606
Cranberg	0.683
SAND-II[b]	0.764
Grundle Multigroup Fluxes	0.76[c]

(a) $$\bar{\sigma}^f = \frac{\int_0^\infty \sigma(E)\ \phi^f(E)\ dE}{\int_0^\infty \phi^f(E)\ dE}$$

(b) *This form was derived with SAND-II using a selected combination of Fabry's and Grundl's measured values of saturated activities.*

(c) *Using Grundl's group fluxes and group-averaged cross sections based on a Cranberg weighting, Reference 9.*

the most accurate available. His absolute results are presented in Table 11.4. The relative results reported by Bresesti, Grundl, and Boldeman are also shown in Table 11.4. These latter values, except for Grundl's, have been renormalized to agree with Fabry's absolute results. [Because of the large error bar on Fabry's $^{235}U(n,f)$ result, Grundl's results were not renormalized.]

For the $^{27}Al(n,\alpha)$ reaction, the calculated value of fission-averaged cross section based on the CAND-II evaluated differential cross section and the SAND-II form of the fission spectrum agrees well with Fabry's value of 0.78 and Grundl's value of 0.76 mb. Current ASTM procedures for measuring neutron flux by activation detectors[7] recommend a value of 0.60 mb for ^{27}Al (n,α) and Zijp[5] recommends a value of 0.61 mb. These values are in serious disagreement with the integral results determined by Fabry, Grundl, and the SAND-II - CAND-II codes.

To establish consistency between the more recent differential and integral cross-section data for the $^{27}Al(n,\alpha)^{24}Na$ reaction, it is necessary to use the SAND-II (or Grundl) form of the fission spectrum. This immediately raises the possibility that the fission spectrum representations by the Watt, Frye, and Cranberg forms are incorrect. A multiple-foil activation test in a slightly degraded fission spectrum is being planned to investigate this possibility further and to obtain additional experimental activity data for the evaluation of the cross section for the $^{27}Al(n,\alpha)$ and other reactions of interest for fast-reactor dosimetry.

POINT-DEFECT CALCULATIONS: EFFECT OF INTERATOMIC POTENTIAL TYPE AND RANGE

A. DePino, Jr.

These calculations have the goal of increasing confidence in defect configuration energy calculations using computer simulation techniques. The literature contains calculations based on a variety of types and

TABLE 11.4. Summary of Measured Values of Fission Averaged Cross Sections[a]

Reaction	Fabry	Bresesti[8]	Grundl[9]	Boldeman[10]
$^{27}Al(n,\alpha)^{24}Na$	0.78 ± 0.03	0.78[b]	0.753	0.74
$^{54}Fe(n,p)^{54}Mn$	∿87.6[c]	83.2	-	81.5
$^{58}Ni(n,p)^{58}Co$[d]	∿121[c]	123	-	119
$^{32}S(n,p)^{32}P$	74 ± 3	-	-	74[b]
$^{115}In(n,n')^{115m}In$	200 ± 10	198	-	-
$^{237}Np(n,f)$	-	-	1367	-
$^{232}Th(n,f)$	-	-	-	-
$^{238}U(n,f)$	353 ± 30[c]	-	326	-
$^{235}U(n,f)$	1335 ±130[c]	-	1253[b]	-
$^{197}Au(n,\gamma)^{198}Au$	74 ± 3	-	-	-
$^{115}In(n,\gamma)^{116m}In$	122 ± 6	-	-	-
$^{63}Cu(n,\gamma)^{64}Cu$	10.8[c]	-	-	-

(a) *Measured in ^{235}U converter assemblies.*

(b) *Value assumed for normalization of other results.*

(c) *Private communication to W. N. McElroy, March 1968.*

(d) *Reaction cross section for total production of ^{58}Co.*

ranges of the assumed interatomic potential. Determining the relative sensitivity of various defect configuration energies to assumptions about the potential should lead to more confidence in the technique.

In this work, Morse potentials, modified to limit the range to either third or fourth nearest neighbor atoms, are being used. Sohm[11] determined these potentials for a number of metals. The potentials help fill the gap between the pure repulsive (Born-Mayer) and long-range (Morse) potentials. The Born-Mayer and Morse potentials (Figure 11.2) have been the most extensively used in published work.

The third neighbor modified Morse potential was used in the initial calculations carried out for copper--the subject of much theoretical and experimental work. Five equilibrium interstitial configurations have been examined to date: body-centered interstitial (0);<100>split interstitial (H_o); <110>split interstitial (H_c); activated crowdion (C); and, tetrahedral interstitial (T).

All results indicate that H_o is the most stable configuration. Table 11.5 lists the five interstitial configuration energies relative to H_o; the table also includes energies computed with an unmodified Morse potential,[12] and a Born-Mayer potential.[12]

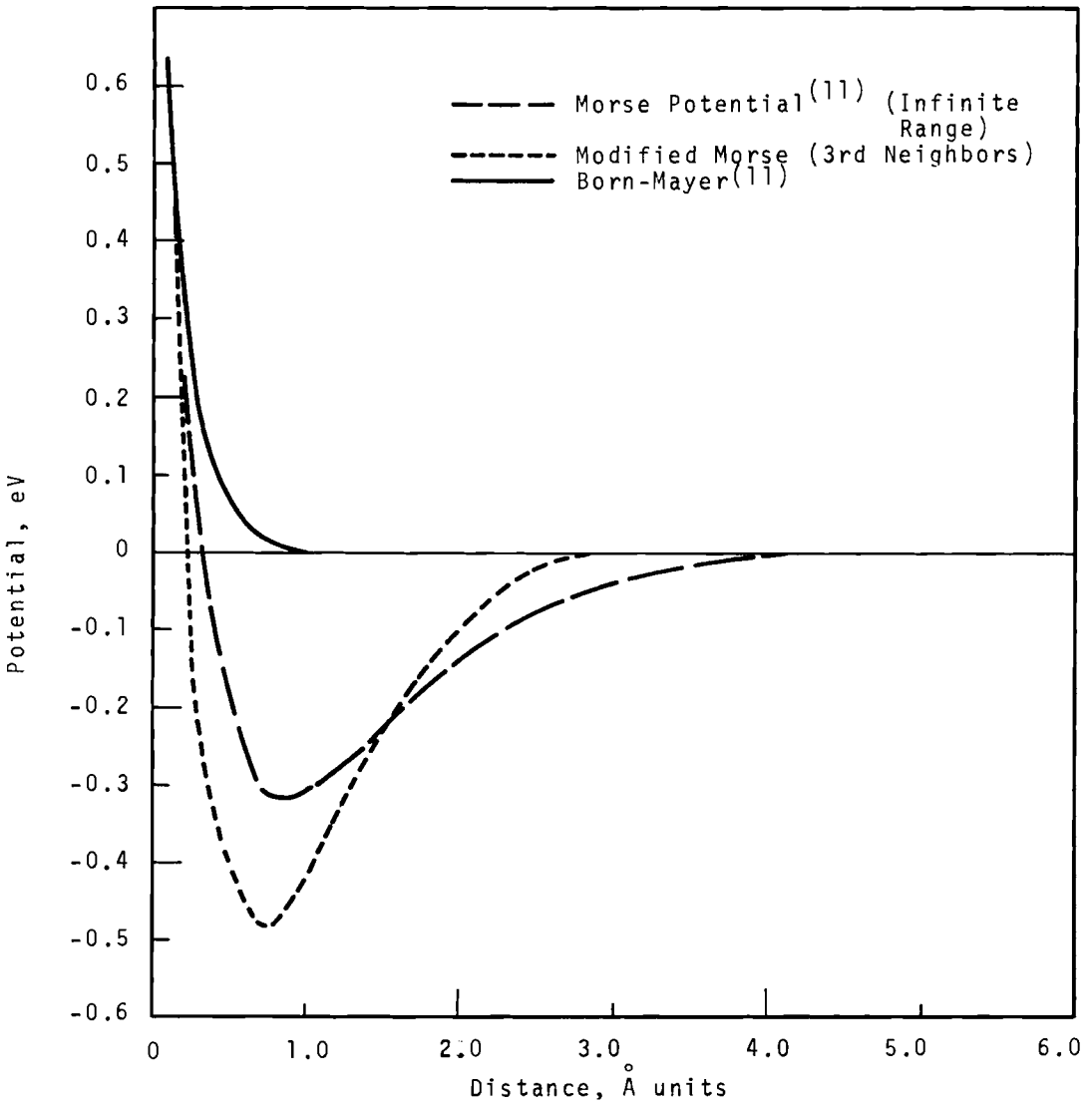

FIGURE 11.2. Interatomic Potentials

TABLE 11.5. Energy of Formation of Interstitial Configurations in Copper

Type	Morse Potential (3rd Neighbor) Energy Above Stable, eV	Morse (Long Infinite Range)(11) Energy Above Stable, eV	Born-Mayer(11) Energy Above Stable, eV
H_O (body-centered)	0.00	0.00	0.00
H_C	0.42	0.15	0.21
C	0.43	0.16	0.22
O	0.56	0.21	0.13
T	0.57	0.31	0.42

Results from the use of the modified Morse potential agree with those from an infinite-range Morse potential in the ordering of the configuration energies, but the energy differences are generally larger for the former.

Several calculations have been made with the fourth-neighbor modified Morse potential. The difference between the energy for the T configuration (which produced the most strain in the lattice) and the energy for the H_o configuration decreased by ~0.1 eV relative to the third-neighbor calculation. A decrease was anticipated since the infinite-range Morse potential gave lower energies than the third-neighbor potential.

These calculations were made by using an FCC lattice model containing 1687 atoms. An assumption in the calculations is that the introduction of an interstitial causes only a limited number of atoms to move from their equilibrium lattice positions. The moveable atoms comprise what is termed the crystallite. Surrounding the crystallite is a mantle of immoveable atoms representing the remainder of the crystal lattice. Because the thickness of the mantle must be greater than or equal to the range of the interatomic potential, the crystallite contained 365 atoms for the potentials used here.

Clearly, the mantle could influence the resulting energies for configurations whose strain fields extend to the mantle, but this was checked by reducing the number of moveable atoms to 171 atoms. The energy differences in the H_o and T configurations were increased by 0.04 eV and 0.1 eV, respectively, over the 365 atom crystallite. The net change of 0.06 eV is considered small enough to insure the validity of the results of the calculations, since all other configurations would experience smaller changes than the T configuration.

COMPUTER SIMULATION OF CRYSTALLINE DEFECTS

D. G. Doran, A. DePino, Jr., and L. A. Lawrence

To simulate radiation damage at finite temperatures, annealing of the primary damage must be included. This is presently handled by the code ANNEAL, developed at GE-NMPO by J. R. Beeler and D. G. Besco; it is independent of the codes (CASCADE-CLUSTER) that simulate primary damage at 0 °K. The original version of ANNEAL allowed interstitial migration only and, hence, applied only at low temperatures. Including vacancy migration in the code will make the simulation apply at elevated temperatures.

To do this requires the determination of activation energies for the correlated (i.e., nonrandom) motion of a vacancy in the vicinity of other vacancies. Some of the necessary information is either directly available in the literature or is suggested by published results.[13] More data have been obtained by application of the code DEFECT.[14]

The determination of the migration energy of an isolated vacancy with DEFECT is straightforward because, by symmetry, the saddle point lies along a <111> direction joining two nearest neighbors. One then simply determines the configuration energy as a function of the position of the vacancy (actually, an atom is moved) along this line. To facilitate this computation, the code was modified (reducing computer time by 50%) so that a series of cases could be obtained in one computer run. The relaxed coordinates of the atoms corresponding to one position of the vacancy serve as the input coordinates for the computation at the next position.

The determination of the migration energy is more difficult when a migrating vacancy is in the vicinity of one or more vacancies. The symmetry of the previous case is lost, and the saddle point no longer lies along a line joining the nearest neighbor sites. Several techniques were tried to minimize the computer time needed to locate the saddle point. The adopted procedure consists of starting the migrating atom on the line joining nearest neighbor sites near where the saddle point is expected to be and of holding one coordinate of this atom constant to allow the other coordinates (and those of all other atoms) to relax to equilibrium values. Succeeding steps consist of changing all coordinates of the migrating atom by the same increment (i.e., it is moved slightly along <111>) and again allowing relaxation holding the same coordinate fixed. A minimum of 5 or 6 steps is needed to define a saddle point.

This technique has been applied to α-iron (using Johnson's potential) to supplement published results. In addition, several key quantities were recomputed. The published value of 0.68 eV for the computed migration energy of an isolated vacancy was corroborated; however, several published values indicating a relatively long-range interaction between two vacancies could not be. If $V_2(n)$ represents a pair of vacancies that are n^{th} neighbors, the calculated activation energies for $V_2(9) \rightarrow V_2(4)$ and $V_2(4) \rightarrow V_2(9)$ are 0.65 and 0.76 eV, respectively, compared to published values of 0.53 and 0.66 eV. Similarly, calculated activation energies for $V_2(8) \rightarrow V_2(4)$ and $V_2(4) \rightarrow V_2(8)$ were 0.67 and 0.73 eV, respectively, compared to published values of 0.63 and 0.57 eV.

Based on these results and published results for tri- and tetravacancies, the first attempt to treat correlated motion of vacancies included only a few short-range interactions. Hence, a number of DEFECT runs were made to study the migration of a vacancy from a 4^{th} to a 2^{nd} neighbor of the closest member of a nearby cluster for various cluster sizes and orientations. The activation energy was found to be ∿0.42 eV for all configurations. A similar study of the 5^{th} to 1^{st} neighbor transition gave ∿0.58 eV.

This information on correlated motion of vacancies has been programmed

into ANNEAL by D. G.Besco. Because interstitials are so much more mobile than vacancies in α-iron, they were treated independently. That is, the interstitials reached a quasi-equilibrium configuration before any vacancy migration occurred, and this configuration was frozen in while the vacancies migrated. The effects of this simplification will be critically examined when the amended code becomes operational.

Each vacancy is given the opportunity to move during a time step equal to one-tenth the average time between jumps of an isolated vacancy. The motion of a single vacancy is correlated only with respect to other vacancies that are 5^{th} neighbors or closer. The motion of a vacancy in a cluster, i.e., a vacancy with at least one 1^{st} or 2^{nd} neighbor, is correlated only with respect to other members of the cluster.

The amended code has been compiled and checkout runs are in progress.

COMPUTER SIMULATION OF DEFECTS IN SOLIDS

L. A. Lawrence

The computer code DEFECT has been applied to the problem of calculating the binding energy in molybdenum of an molybdenum interstitial trapped by an iron impurity atom. An molybdenum interstitial trapped by an iron impurity has been suggested[15] as the source of Stage III (+150 °C) annealing of neutron irradiated molybdenum. The activation energy for Stage III annealing is 1.2 - 1.3 eV. The calculations will tell whether the binding energy involved in the proposed mechanism is consistent with the measurements.

The binding energy was calculated in the following way. Molybdenum potential was generated that was consistent with the physical properties of the lattice, and this potential was used to determine the stable configuration of a molybdenum interstitial in a molybdenum lattice. A molybdenum lattice atom was replaced by an iron atom, and the most stable configuration of the iron impurity atom with the molybdenum interstitial was found. The binding energy for this configuration was then calculated.

The Mo-Mo potential was generated from elastic constants data using Johnson's method[16] and high-pressure compressibility data.[17] The cutoff distance for the potential was varied until DEFECT calculations of the formation and migration energies for a single vacancy agreed with the experimental values.[18] Johnson's[16] Fe-Fe potential was used for the impurity atom. The Mo-Fe interaction potential was constructed using the method of Rimmer and Cottrell[19] to combine the Mo-Mo and Fe-Fe potentials.

Three molybdenum interstitial configurations were investigated for a lattice containing no impurities. They were the <110> split, <111> split, and the activated crowdion. The <110> split interstitial was the most stable; its formation energy of 8.52 eV was 0.38 eV below that of the

<111> split, and 0.33 eV below that of the activated crowdion.

Substituting an iron atom for an molybdenum atom changed the configurational energy by 1.11 eV.

Several orientations of the iron substitutional impurity relative to the molybdenum interstitial were investigated. The [110] split molybdenum interstitial with the iron along the [111] direction at a nearest neighbor lattice site was metastable with a binding energy of 0.78 eV. The activated crowdion with the iron along the [111] direction at a nearest neighbor lattice site was a more energetically favorable configuration with a binding energy of 1.34 eV. The [111] split molybdenum interstitial with the iron along the [111] direction at a nearest neighbor lattice site was not stable; it migrated to the more favorable configuration of an activated crowdion.

The value of 1.34 eV obtained for the binding energy is close to the activation energy of 1.2 - 1.3 eV found in Stage III annealing of neutron irradiated molybdenum.[20] The results are consistent with the suggestion that Stage III annealing involves the release of molybdenum interstitial atoms trapped to iron impurity atoms.

COMPUTER SIMULATION OF RADIATION DAMAGE BEHAVIOR

G. E. Russcher

Work during this quarter primarily involved the use of computer simulation techniques for the assessment of the relative damaging power of irradiations in the DFR, FTR, EBR-II, and ETR for void generation in fuel clad. This effort, sponsored by the FFTF project, was possible because work under this program had put in place the capability for performing computer studies of damage processes.

The adaptation of the codes to damage correlation continued with the addition of the SATURATION link to the CASCADE CLUSTER series. With the SATURATION link, the input to the CASCADE CLUSTER series need not be the perfect lattice but, instead the state generated when the damage patterns from individual knock-on atoms overlap. The damaged lattice should be more typical of the situation encountered in long-term radiation experiments, thus, the addition of the SATURATION link should make the simulation more realistic.

The CASCADE CLUSTER programs were adapted to the bcc lattice. Since the original formulation was solely for the fcc lattice, results from α-iron generated with SPECTRA could not be used in further investigations; however, this adaptation will permit that study. In addition, improved potential data for iron were incorporated into the program. The potential is a combination of the Bohr scattering potential with Born-Mayer potentials in the manner of Erginsoy and Vineyard.[21] These improvements and adaptations widen the scope of the CASCADE CLUSTER programs.

REFERENCES

1. W. N. McElroy et al. A Computer-Automated Iterative Method for Neutron Flux Spectra Determination by Foil Activation, Volumes I, II, III, and IV, AFWL-TR-67-41, Air Force Weapons Laboratory, Kirtland AFB, New Mexico. September 1967.

2. J. J. Cadwell, D. R. de Halas, R. E. Nightingale, and D. C. Worlton. Quarterly Progress Report, October, November, December, 1967, Reactor Fuels and Materials Branch of USAEC Division of Reactor Development and Technology, BNWL-668. Pacific Northwest Laboratory, Richland, Washington, March 1968.

3. J. R. Stehn et al. Neutron Cross Sections, BNL-325, Brookhaven National Laboratory, Long Island, New York. Second Edition, Supplement No. 2. 1965-1966.

4. H. Liskien and A. Paulsen. Compilation of Cross-Sections for Some Neutron Induced Threshold Reactions, EUR 119.e, European Atomic Energy Community, Euratom. 1963-1967.

5. W. L. Zijp. Review of Activation Methods for the Determination of Fast Neutron Spectra, RCN-37, Reactor Centrum Nederland. May 1965.

6. A. Fabry. "Test of the Uranium-235 Thermal Fission Spectrum Reprentations by Means of Activation Detectors," Nucleoniks, vol. 10, (5) p. 280. 1967.

7. ASTM, "Measuring Neutron Flux by Radioactivation Techniques," ASTM Designation: E261-65T. 1965.

8. A. M. Bresesti, M. Bresesti, and R. A. Rydin. "Threshold Detector Cross-Section Intercalibration in a Pure Fission Spectrum," NSE vol. 29, pp. 7-14. 1967.

9. J. Grundl. "A Study of Fission-Neutron Spectra with High-Energy Activation Detectors -- Part II, Fission Spectra," NSE vol. 31, pp. 191-206. 1968.

10. J. W. Boldeman. "Fission Spectrum Averaged Cross Sections of Threshold Reactions," J. Nucl. Eng., Part A/B, vol. 18, pp. 417-424. 1964.

11. L. R. Sohm. M.S. Thesis, Clarkson College of Technology.

12. R. A. Johnson. "Comparison of F.C.C. Interstitial Calculations," J. Phys. Chem. Solids, vol. 28, pp. 275-277. 1967.

13. J. R. Beeler, Jr. and R. A. Johnson. "Vacancy Clusters in α-Iron," Phys. Rev., vol. 136, p. 677. 1967.

14. J. J. Cadwell, D. R. de Halas, R. E. Nightingale, and D. C. Worlton. Quarterly Progress Report, July, August, September, 1967, Reactor Fuels and Materials Branch of USAEC Division of Reactor Development and Technology, BNWL-658. Pacific Northwest Laboratory, Richland, Washington, February 1968.

15. G. L. Kulcinski. Unpublished Data, Pacific Northwest Laboratory, Richland, Washington, (personal communication). 1967.

16. R. A. Johnson. "Interstitials and Vacancies in α-Iron," Phys. Rev., vol. 134, p. A 1329. 1964.

17. D. G. Doran. A Contribution to the Determination of Interatomic Potentials for Computer Simulation Studies, BNWL-SA-1648, Pacific Northwest Laboratory Richland, Washington, 1968.

18. J. D. Meakin, A. Lawley, and R. C. Koo. "Vacancies in Quenched Molybdenum Crystals," Appl. Phys. Ltrs., vol. 5, p. 133. 1964.

19. D. E. Rimmer and A. H. Cottrell. "The Solution of Inert Gas Atoms in Metals," Phil Mag., vol. 2, p. 1345. 1957.

20. D. E. Peacock and A. A. Johnson. "Stage III Recovery in Neutron Irradiated Molybdenum and Niobium," Phil. Mag., vol. 8, p. 563. 1963.

21. C. Erginsoy, G. H. Vineyard and A. Englert. "Dynamics of Radiation Damage in a Body-Centered Cubic Lattice," Physical Review, vol. 133 (2A), pp. A595-A606. January 1964.

IRRADIATION DAMAGE TO REACTOR METALS

REACTOR METALS RESEARCH

ALLOY EVALUATION

K. R. Wheeler and J. H. Hoage

The purpose of this program is to study, on a limited basis, materials potentially useful for reactor application. From such cursory examination, the more promising alloys can be studied in depth.

A British stainless steel FV-548, which has a composition similar to 316 SS but includes a nominal 1% NB in its chemistry, has shown smaller ductility changes than 316 when irradiated to high fast fluence levels.[1] Five hundred pounds of 1/2 in. diam rod of FV-548 (Heat #49625) have been procured from Firth Vickers Stainless Steels, Ltd., for inclusion in the Radiation Effects program. Negotiations are also underway to obtain 300 ft of FV-548 tubing (0.250 in. OD x 0.016 in. wall) to be fabricated from the same heat (#49625) as the rod material. Additionally, a 500 lb heat of stainless steel 3/8 in. diam rod with the nominal FV-548 chemistry was obtained on an experimental basis from the Allegheny Ludlum Research Center. Randomly selected rods from both producers are now being characterized for structure, chemistry, and mechanical properties.

As reported in previous quarterly reports, specimens of ten alloys residual from the GE-APED superheat fuel-clad materials investigations are undergoing tensile properties evaluation at PNL. Alloys involved in that phase of the testing program irradiated in the GETR are Incoloy 825 and 801, In 102, Inconel 718, Incoloy 804, Hastelloy F, and René 62.

The tensile properties at 1300 °F (704 °C) of the thermally aged control materials are reported in Table 12.1, as a continuance of the program. For comparison, the 1300 °F (704 °C) tensile properties of the same alloys in the irradiated condition are shown in Table 12.2. As can be seen, both irradiated and control materials have the same time-temperature history. The response of these alloys to elevated temperature exposure has been well documented.[2] In general, each of these alloys shows a degree of metastability with increased hardness and lower ductility after prolonged exposure to temperatures above 1000 °F (538 °C). Each alloy (as discussed below) varies in its chemistry and the type of precipitate structure created in the dynamics of the aging process.

Incoloy 801

This alloy is basically Incoloy 800 with a percent addition of titanium to increase strength. The alloy appears to have reached its thermal aging peak in the shorter aging at 1000 °F (538 °C), with indications of overaging at longer times and higher temperatures. The ductility is reduced drastically after irradiation.

TABLE 12.1. Effect of Pretest Thermal Aging on the 1300 °F (704 °C) Tensile Properties of Selected Nickel-Base Alloys

Spec. Number	Material	Exposure Time, hr	Aging Temp, °F	0.2% YS, ksi	UTS, ksi	% UE	% TE	% RA
D 60	Incoloy 801	620	1000	47.73	55.45	8.38	28.19	31.82
D 61	Incoloy 801	620	1000	36.44	41.95	9.01	26.90	23.73
D 70	Incoloy 801	620	1300	44.19	54.88	11.98	28.44	37.21
D 76	Incoloy 801	620	1300	42.33	52.84	10.46	32.76	27.27
D 50	Incoloy 801	5200	1000	41.28	58.72	16.40	30.93	32.56
D 51	Incoloy 801	5200	1000	41.48	59.09	15.13	32.51	37.50
D 47	Incoloy 801	5200	1300	38.07	51.14	11.11	34.30	44.32
D 48	Incoloy 801	5200	1300	36.93	50.91	11.40	36.97	42.05
E 60	Incoloy 804	620	1000	45.90	58.20	10.02	24.35	28.69
E 61	Incoloy 804	620	1000	50.00	62.29	8.32	20.36	27.12
E 70	Incoloy 804	620	1300	42.28	56.10	8.14	24.43	32.52
E 71	Incoloy 804	620	1300	42.98	57.44	8.33	25.58	35.54
B 62	Incoloy 825	620	1000	37.98	55.43	12.25	47.79	63.57
B 63	Incoloy 825	620	1000	36.82	53.88	13.56	50.77	60.47
B 70	Incoloy 825	620	1300	35.38	53.46	15.24	48.55	64.62
B 71	Incoloy 825	620	1300	37.11	54.69	15.74	49.85	64.06
B 40	Incoloy 825	5200	1300	38.46	56.15	10.94	36.46	48.46
B 42	Incoloy 825	5200	1300	40.00	56.92	9.81	36.70	45.38
H 60	Hastelloy F	620	1000	47.64	65.75	18.12	45.64	47.24
H 61	Hastelloy F	620	1000	48.85	64.00	10.51	46.58	45.38
H 70	Hastelloy F	620	1300	51.18	70.87	8.72	31.64	44.09
H 71	Hastelloy F	620	1300	49.22	68.45	9.45	29.38	41.09
A 60	Inconel 718	620	1000	127.12	138.98	4.81	19.13	23.73
A 71	Inconel 718	620	1300	114.50	125.20	2.49	18.88	31.30
J 60	Rene 62	620	1000	132.84	147.76	3.93	12.29	28.36
J 61	Rene 62	620	1000	143.41	158.91	3.30	17.30	31.78
J 70	Rene 62	620	1300	131.06	151.06	5.45	17.14	35.61
J 71	Rene 62	620	1300	128.78	149.24	5.63	16.94	33.33
M 37	In 102	5200	1000	63.01	83.74	11.10	53.85	70.73
M 38	In 102	5200	1000	60.33	80.17	11.61	50.13	73.55

Incoloy 804

Additions of chromium and nickel with decrease in iron content provide the difference in chemistry between this material and Incoloy 800. Its thermal response is essentially the same as Incoloy 801, with post-irradiation ductility again severely reduced. Precipitates in this alloy are more extensive than the 801 modification, a condition no doubt contributing to its low irradiated ductility.

Incoloy 825

This alloy with its molybdenum and increased nickel content tends to form a sigma phase type structure with a trace of matrix carbide after exposure to 1400 °F (760 °C). The evidence for this can be seen by the downward trend in ductility after thermal aging for 5200 hr at 1300 °F (704 °C).

The ductility of Inconel 825, however, after elevated temperature irradiation is still several percent

TABLE 12.2. Effect of a Mixed Spectrum Neutron Irradiation[a] on the 1300 °F (704 °C) Tensile Properties of Selected Nickel-Base Alloys

Specimen Number	Material	Exposure Time, hr	Fast Fluence, n/cm^2	Thermal Fluence, n/cm^2	Irrad. Temp, °F	0.2% YS, psi x 1000	UTS, psi x 1000	%UE[b]	%TE[c]	%RA[d]
A-2	Inconel 718	630	3.6×10^{20}	2.6×10^{20}	1300	95.8	95.8	0.74	0.80	6.15
B-3	Incoloy 825	630	4.0×10^{20}	2.8×10^{20}	1300	36.9	50.6	8.75	10.43	13.08
B-4	Incoloy 825	630	4.0×10^{20}	2.8×10^{20}	1300	36.2	50.3	6.09	7.77	16.28
B-21	Incoloy 825	5200	1.3×10^{21}	3.4×10^{21}	1300	43.1	52.8	5.06	6.35	10.77
B-22	Incoloy 825	5200	1.6×10^{21}	4.2×10^{21}	1300	39.5	53.1	5.47	6.16	11.63
D-5	Incoloy 801	630	2.6×10^{20}	1.7×10^{20}	1300	45.8	49.3	1.15	1.76	9.09
D-6	Incoloy 801	630	2.9×10^{20}	2.1×10^{20}	1300	42.2	42.8	0.85	2.76	15.56
D-21	Incoloy 801	5200	0.4×10^{21}	0.6×10^{21}	1000	39.9	44.6	1.64	2.36	6.98
D-22	Incoloy 801	5200	0.4×10^{21}	0.6×10^{21}	1000	39.3	43.3	1.42	2.18	11.11
E-1	Incoloy 804	630	3.6×10^{20}	2.6×10^{20}	1300	38.7	41.7	0.79	0.94	10.48
E-2	Incoloy 804	630	3.6×10^{20}	2.6×10^{20}	1300	38.1	39.9	0.72	0.79	8.06
H-1	Hastelloy F	630	3.6×10^{20}	2.6×10^{20}	1300	53.8	65.6	7.71	14.37	17.74
H-2	Hastelloy F	630	3.6×10^{20}	2.6×10^{20}	1300	52.8	65.1	5.61	12.95	18.11
J-2	Rene 62	630	2.9×10^{20}	2.1×10^{20}	1300	106.9	133.6	8.73	9.42	12.98
J-3	Rene 62	630	2.9×10^{20}	2.1×10^{20}	1300	131.3	132.0	0.91	1.09	10.69

(a) Irradiated in GETR
(b) *Uniform Elongation*
(c) *Total Elongation*
(d) *Reduction in Area*

greater than that observed in Incoloy 801 and 804 with the same irradiation history.

Hastelloy F

The high (7%) molybdenum content of Hastelloy F produces an extensive precipitation of a Laves phase (Fe_2Mo). The structure appears not to be affected by radiation, since strength and uniform elongation values are comparable for both irradiated material and controls with the same time-at-temperature history. There is, however, a sharp reduction in total elongation due to irradiation.

Inconel 718 and René 62

Both alloys are precipitation hardenable by a gamma prime type micro-constituent, with the development of considerable strength accompanied by lower ductility values. As can be seen, these alloys, although maintaining 4 or 5% uniform elongation in the aged condition, drop to approximately 1% after irradiation.

In 102

This nickel-base material, alloyed generously with refractory (Nb, Mo, W) additions, was developed for

long time service to 1200 °F (649 °C) with a high degree of structural stability.[3] The alloy, however, does evidence an aging reaction after exposure to elevated temperature for extended periods of time. At 1300 °F (704 °C) test temperature, the tensile ductility of In 102 is nominally 60%, as compared to 50% for aged material. Almost no irradiated data are available for In 102. Experience and results have shown the irradiated material to be extremely notch sensitive. All three tensile samples of In 102 irradiated at 1000 °F (538 °C) to an approximate fast fluence level of 1×10^{21} n/cm^2 fractured in the gripping tabs before attaining the 0.2% yield point of the material. Attempts will be made to verify these results with additional tests.

In general, all alloys reported here have shown a ductility loss caused by prolonged thermal exposure. When irradiation and temperature effects are combined, the resulting ductility loss, with few exceptions, is extremely large.

IRRADIATION FACILITIES OPERATION

R. W. Barker

The purpose of this phase of the program is to provide for the timely accomplishment of irradiation, testing, and subsequent processing of the data obtained from a variety of reactor structural materials. Irradiations will be performed in aqueous, gaseous, and molten metal environments. Elevated temperature irradiations and tests will be emphasized. Special testing techniques, applicable to either irradiated or unirradiated specimens, will be developed.

Facilities Operation

The experiments discharged from the various Engineering Test Reactor (ETR) core positions for Cycles 93 and 94 are given in Tables 12.3 and 12.4, along with the estimated neutron fluxes and exposures.

The operating history of the ETR and the G-7 hot water loop for Cycle 92 is given in Table 12.5. Loop operation was normal for this cycle. The history for the out-of-reactor loop is given in Table 12.6.

Data Processing

One hundred and thirty-four tensile data reports have been added to the Radiation Effects on Metals (REM) computer program during the quarter, which raises the accumulative total to 5506.

IRRADIATION DAMAGE TO STAINLESS STEELS

A. J. Lovell

The purpose of this program is to determine the combined effects of neutron irradiation and environment on stainless steels. Irradiation-induced mechanical property changes are determined as a function of fast- and thermal-neutron fluence, temperature and environment of irradiation, and postirradiation test temperatures and environments. Emphases are placed on tensile and

TABLE 12.3. Summary of Experiments Discharged at the Conclusion of ETR Cycle 93

Experiment Designation	No. of Specimens	Type of Specimens	Estimated Flux, $n/cm^2/sec$(a)	Estimated Exposure, n/cm^2(a)
GEH-20-33	18	348 SS Tensiles	10.3×10^{13}	8.1×10^{21}
266	18	Zr-2 Corrosion Tabs	10.0×10^{13}	1.1×10^{21}
269	6	304 SS Creep	10.6×10^{13}	1.3×10^{21}
271	6	304 SS Stress-Rupture	1.0×10^{13}	3.7×10^{19}
272	6	304 SS Stress-Rupture	10.4×10^{13}	1.07×10^{21}
283	3	Carbon Steel Charpy	2.5×10^{13}	9.4×10^{19}
284	3	Carbon Steel Charpy	3.7×10^{13}	1.27×10^{20}
308	6	Fe Foils	8.0×10^{13}	1.94×10^{20}
309	6	Fe Foils	7.5×10^{13}	2.75×10^{20}
GEH-14-698	6	Fe Foils	1.1×10^{13}	3.2×10^{20}
699	6	Fe Foils	1.1×10^{13}	3.2×10^{20}

(a) *Neutrons with energies greater than 1 MeV.*

NOTE: Total specimens discharged, Cycle 93 = 84.
Total specimens discharged, ETR G-7 Loop, Cycle 93 = 72.

TABLE 12.4. Summary of Experiments Discharged at the Conclusion of ETR Cycle 94

Experiment Designation	No. of Specimens	Type of Specimens	Estimated Flux, $n/cm^2/sec$(a)	Estimated Exposure, n/cm^2(a)
GEH-20-79	18	AM 350 Tensile	10.3×10^{13}	8.1×10^{21}
273	6	304 SS Stress-Rupture	10.6×10^{13}	1.1×10^{21}
277	6	19-9 DL Tensile	10.9×10^{13}	1.0×10^{21}
278	6	19-9 DL Tensile	6.0×10^{13}	5.5×10^{20}
280	6	304 SS Creep	11.1×10^{13}	1.0×10^{21}
287	22	JS 700 Tensiles	10.0×10^{13}	2.5×10^{20}
310	6	"A" Ni Foils	2.5×10^{13}	6.0×10^{19}
311	6	"A" Ni Foils	3.7×10^{13}	9.0×10^{19}
GEH-14-696	5	Mild Steel Impact Spec.	0.35×10^{13}	1.9×10^{19}
697	4	A-302 B DCB	0.3×10^{13}	1.6×10^{19}
762	6	"A" Ni Foils	$\sim 2.1 \times 10^{13}$	6.2×10^{19}
766	6	"A" Ni Foils	$\sim 3.1 \times 10^{13}$	9.1×10^{19}

(a) *Neutrons with energies greater than 1 MeV.*

NOTE: Total specimens discharged, Cycle 94 = 98.
Total specimens discharged, ETR G-7 loop, Cycle 94 = 76.
Total specimens discharged, ETR G-7 loop, to date = 3386.

TABLE 12.5. Summary of Operating History for ETR and G-7 Hot Water Loop, ETR Cycles 92 and 93

Operating History	ETR Cycle Number	
1. Reactor History	92	93
Startup[a]	10-12-67	12-7-67
End of Cycle	11-26-67	1-30-68
Megawatt Days	5949	5966
Effective Days at 175 MW	34.0	34.1
Number of Scrams[b]	11	19
Number of Shutdowns	3	5
2. G-7 Hot Water Loop History		
Maximum Temperature	525 °F	532 °F
Effective Days Above 200 °F	35.5	35.6
Effective Days at Oper. Temp.	33.0	31.2
Operating Efficiency[c]	104.4%	104.4%
Temperature Efficiency[d]	93.0%	87.7%

(a) *Includes flux runs at low power.*

(b) *Power drops below half of full power (175 MW) with immediate recovery.*

(c) *Effective days of loop operation above 200 °F (95 °C) relative to effective days of reactor operation at 175 MW.*

(d) *Effective days of loop operation between 500 and 550 °F (260 and 290 °C) relative to days of operation above 200 °F (95 °C).*

TABLE 12.6. Summary of Operating History and Discharge Schedule for Out-of-Reactor Loop, ETR Cycles 92 and 93

1. TIME-TEMPERATURE SUMMARY

Temperature	Time, hr	
	Cycle 92	Cycle 93
200 °C (392 °F)	20.4	50.6
218 °C (424 °F)	12.1	15.8
246 °C (475 °F)	26.5	42.1
282 °C (540 °F)	792.0	746.6
TOTAL TIME	851.0	855.1

2. SPECIMEN DISCHARGES: Material, Specimen Type, and Number.

Cycle 92	Type 304 SS	Creep	6
Cycle 93	Type 348 SS	Tensile	18
		TOTAL[a]	24

(a) *Total specimens discharged to date = 1461.*

creep investigations and on studies of the mechanisms of irradiation-induced property changes.

Annealed rolling and transverse, and 25% cold-worked transverse AISI 348 specimens have been irradiated at 290 °C, in the G-7 loop, to a fast neutron fluence of 8.1×10^{21} (E > 1 MeV). This fluence represents 1080 full power days in the Engineering Test Reactor (ETR) G-7 hot water loop. After being exposed to the irradiation in the pH 10 water at 2000 psia, the specimens were coated with a rather adherent corrosion layer. No evidence of localized pitting or attack was apparent.

The tensile testing is partially completed. The effects of test temperatures on the strength of the annealed specimens after irradiation are shown in Figure 12.1. The

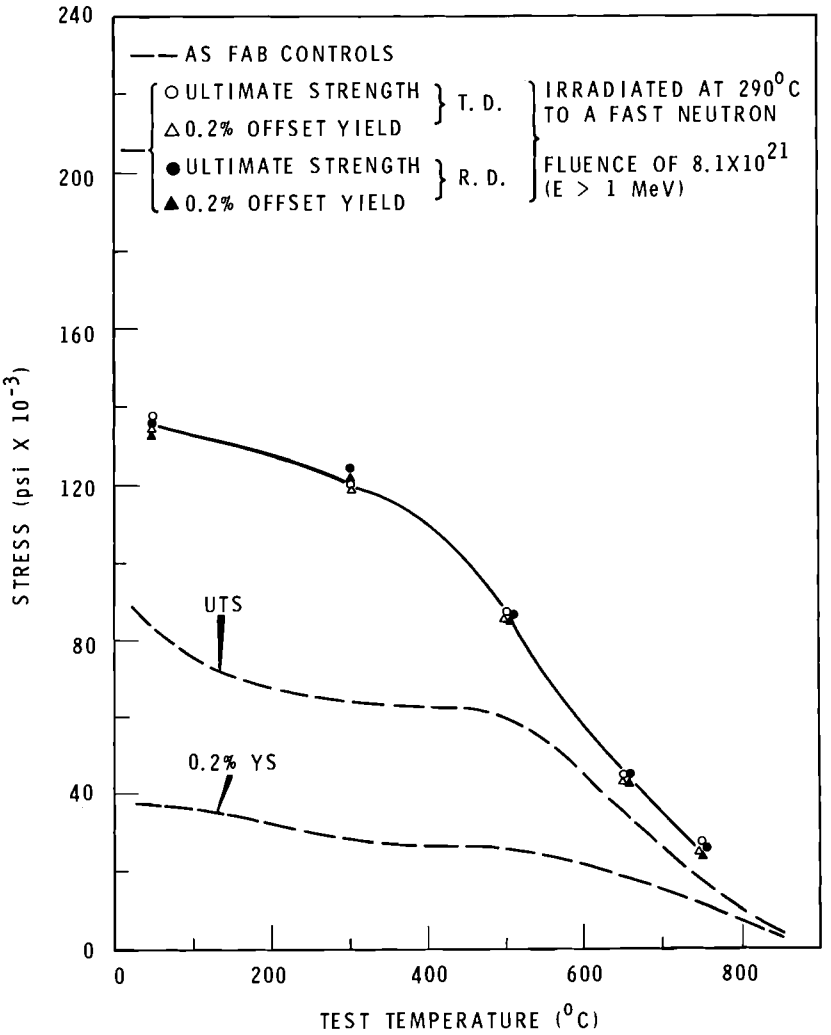

FIGURE 12.1. The Effect of Test Temperature on the Strength of Irradiated AISI 348 Flat SS Specimens in the Annealed Condition

increase of the yield strength over the as-fabricated values was observed at all test temperatures up to and including the 750 °C test. The ductility was very low for all irradiated specimens (Figure 12.2).

The effect of test temperatures on the strength of AM-350 in the double-aged condition after an out-of-reactor age and after irradiation to 6.4 x 10^{21} (E > 1 MeV) is shown in Figure 12.3. There was a strengthening of the yield strength at all test temperatures in the 300 to 600 °C range. Figure 12.4 shows that the uniforms and totals for all irradiated specimens were lower at all test temperatures.

The data generated on martensitic AISI 410 SS are consolidated in Table 12.7. Irradiation at 60 °C were in the ETR core where the water

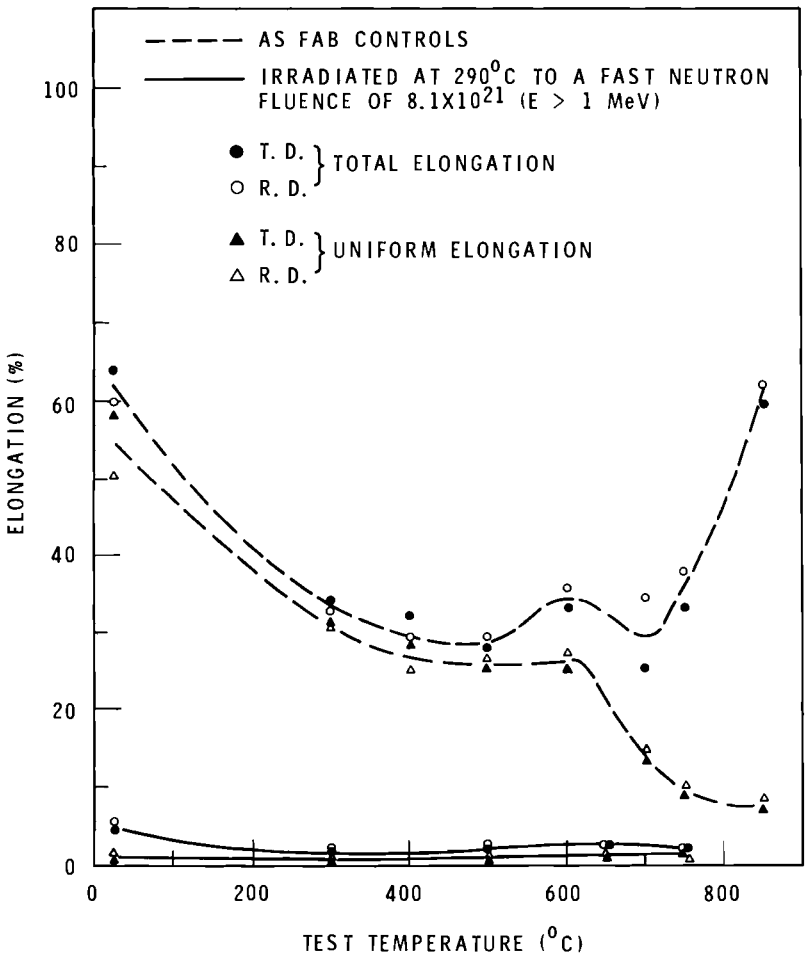

Neg 0680963-1

FIGURE 12.2. The Effect of Test Temperature on the Ductility of Irradiated AISI 348 Flat SS Specimens in the Annealed Condition

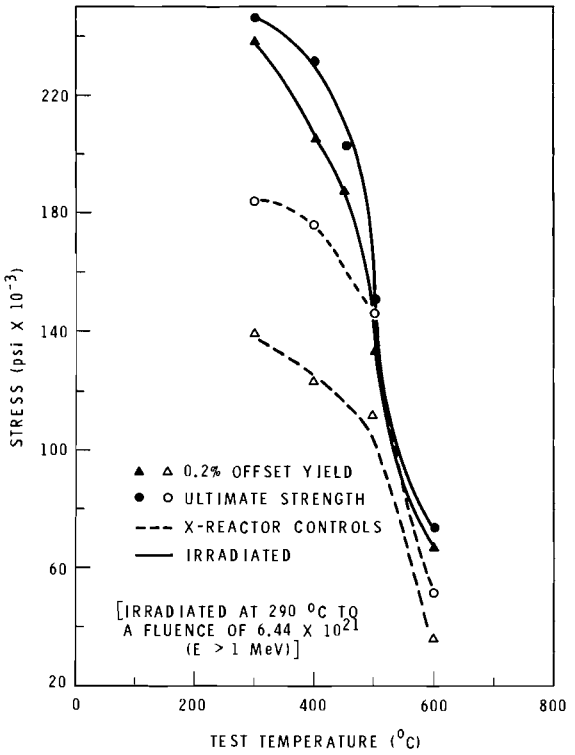

Neg 0680763

FIGURE 12.3. Effect of Test Temperature on the Strength of Irradiated AM-350 in the Double Aged Condition

pH and pressure ranges are 5.5 to 6.5 and 165 to 200 psia. The 290 °C irradiations were in the G-7 hot water loop.

The limited data after irradiation at 60 °C showed increased yield strength with neutron fluence, and decreased ductility with neutron fluence for room temperature tests.

The change in strength with neutron fluence for room temperature and 600 °C test temperatures after a 290 °C irradiation is shown in Figure 12.5. The strength increased with fluence for room temperature tests. The 600 °C test first indicated a small decrease with fluence to 1 x 10^{20} but an increase thereafter. The effect of fluence on ductility is shown in Figure 12.6. The room-temperature test shows decreased uniform and total elongation with increasing fluence. The attempt to test at room temperature after a

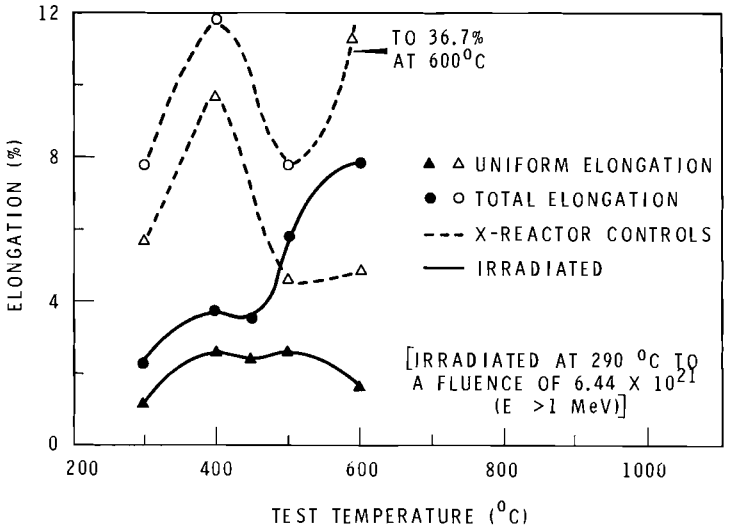

Neg 0680368-4

FIGURE 12.4. The Effect of Test Temperature on the Ductility of Irradiated AM-350 SS in the Double Aged Condition

TABLE 12.7. Tensile Properties of Martensitic 410 SS

IRRADIATION DATA			TENSILE DATA						
Fluence (E > 1 MeV)	Irr. Temp, °C	Test Temp, °C	Strength KPSI PEL	0.2% YS	UTS	Percent Strain Uniform	Total	Reduction of Area, %	Plastic Work, ft-lb
		RT	118.7	140.4	173.5	4.48	6.75	55.6	40.74
		RT	115.0	141.0	175.0	4.84	7.27	57.0	44.86
		RT	95.0	128.0	175.5	5.53	8.79	47.0	47.47
		RT	120.0	147.5	172.7	6.02	8.71	39.0	49.06
		RT	112.5	147.0	169.5	5.53	7.85	45.5	43.65
		RT	53.0	137.9	167.5	4.14	7.04	55.7	37.66
		RT	32.2	140.1	174.5	4.80	8.62	62.9	48.46
		RT	42.1	136.1	170.3	5.81	9.59	63.4	52.95
		RT	29.6	131.8	167.5	5.04	7.97	58.6	43.28
		RT	34.3	136.0	170.3	5.77	9.81	57.8	54.99
		RT	44.6	141.1	174.5	5.24	8.69	57.4	49.13
		RT	87.1	140.5	174.6	5.48	8.02	55.2	50.09
		RT	117.5	140.7	173.7	5.17	7.81	61.0	48.24
		RT	115.0	141.0	175.0	4.84	7.27	57.0	44.86
		RT	118.8	141.1	174.0	3.87	6.30	52.0	38.69
		RT	118.7	138.9	172.7	4.65	6.99	50.5	42.00
		RT	88.4	136.9	173.0	4.98	7.63	53.0	40.95
		RT	99.8	137.9	171.2	5.17	7.87	51.0	44.41
		RT	84.2	135.5	169.7	5.17	7.84	52.0	41.90
		300	92.5	140.5	190.2	7.02	9.10	42.5	54.05
		400	64.4	125.0	182.7	9.59	12.21	42.6	72.25
		500	49.0	112.7	157.1	6.14	9.68	42.6	49.63
		600	11.2	31.3	40.7	2.99	21.79	90.23	26.01
1.72×10^{20}	60	RT	73.0	168.5	198.0	2.52	7.67	45.0	25.92
1.72×10^{20}	60	RT	82.6	163.8	185.9	2.53	2.94	19.2	16.57
6.37×10^{20}	60	RT	106.4	182.5	201.2	1.79	7.31	20.4	13.43
1.10×10^{21}	60	RT	104.8	170.3	182.1	1.19	1.25	28.8	5.53
1.10×10^{21}	60	RT	97.6	180.5	193.9	1.41	1.82	20.5	9.37
3.70×10^{19}	290	RT	62.5	175.0	196.7	3.64	6.49	40.5	40.43
3.70×10^{19}	290	RT	133.0	168.7	194.1	3.79	6.51	47.8	40.43
3.70×10^{19}	290	RT	96.2	178.8	201.9	3.73	6.88	49.5	45.79
3.70×10^{19}	290	RT	86.6	182.2	201.2	4.03	6.95	50.5	45.06
4.50×10^{19}	290	RT	81.9	159.3	183.4	2.59	4.97	41.7	27.98
4.50×10^{19}	290	RT	114.2	170.6	230.2	4.35	6.74	42.1	47.35
4.50×10^{19}	290	RT	128.6	181.9	216.7	6.24	9.37	43.3	68.29
4.50×10^{19}	290	450	57.9	103.3	139.7	8.95	11.68	41.6	56.49
4.50×10^{19}	290	600	15.0	25.1	30.4	3.00	26.36	89.4	20.52
4.50×10^{19}	290	500	13.6	22.8	30.2	3.73	19.96	86.9	17.03
1.01×10^{20}	290	RT	121.9	193.3	215.5	2.53	4.74	36.7	34.14
1.01×10^{20}	290	RT	109.1	194.8	218.2	2.76	5.17	40.9	37.55
1.01×10^{20}	290	450	41.3	85.6	95.2	1.62	6.46	63.9	19.07
1.01×10^{20}	290	450	56.1	93.5	100.5	0.93	4.75	65.0	14.36
1.01×10^{20}	290	600	7.9	14.3	18.4	4.95	38.72	86.2	20.44
1.01×10^{20}	290	600	8.9	18.0	23.4	3.15	31.38	88.7	19.50
1.01×10^{20}	290	600	12.8	20.2	25.1	4.53	25.52	94.0	19.64
1.05×10^{20}	290	RT	137.1	185.2	210.7	2.49	6.34	39.5	44.28
1.05×10^{20}	290	RT	98.2	178.6	206.0	3.91	6.68	42.9	48.42
1.05×10^{20}	290	450	60.2	118.7	155.6	6.54	9.84	45.6	50.50
1.05×10^{20}	290	450	53.9	116.7	153.7	7.09	10.33	43.6	51.45
1.05×10^{20}	290	600	11.2	20.1	25.9	3.45	33.64	90.2	22.32
1.05×10^{20}	290	600	12.9	25.2	26.6	1.42	25.85	90.1	17.29
1.19×10^{20}	290	RT	130.7	180.9	208.8	3.70	3.76	1.9	25.52
1.19×10^{20}	290	RT	125.0	184.0	212.6	4.73	7.77	40.6	55.67
1.19×10^{20}	290	450	87.1	129.2	169.4	8.53	12.05	44.5	68.86
1.19×10^{20}	290	450	48.2	107.1	145.2	8.36	11.55	46.3	58.82
1.19×10^{20}	290	600	12.7	22.4	27.7	3.68	36.24	89.0	25.71
1.19×10^{20}	290	600	10.0	21.7	26.8	3.89	34.25	89.5	24.32
2.40×10^{20}	290	RT	87.4	189.3	213.6	3.08	5.32	45.6	36.34
2.40×10^{20}	290	RT	91.3	192.3	217.5	2.92	5.29	45.2	37.27
2.40×10^{20}	290	300	101.2	166.2	195.7	3.23	5.26	32.0	31.22
2.40×10^{20}	290	300	74.6	154.7	191.3	4.44	6.57	35.3	38.96
2.50×10^{20}	290	RT	120.0	202.5	229.5	3.19	3.30	27.5	21.84
2.50×10^{20}	290	RT	139.4	204.8	215.6	2.48	4.75	43.7	32.41
2.50×10^{20}	290	300	86.8	157.6	197.8	4.08	4.53	31.2	38.78
2.50×10^{20}	290	300	72.7	155.0	194.7	3.77	5.73	37.5	34.48
2.50×10^{20}	290	450	51.9	126.2	167.5	8.19	11.35	46.2	63.86
2.50×10^{20}	290	600	13.3	26.5	31.8	3.43	26.54	90.0	22.69
6.44×10^{21}	290	400	115.4	187.0	205.0	1.79	3.75	39.9	23.35
6.44×10^{21}	290	450	76.2	175.0	182.5	1.81	3.99	41.0	21.71
6.44×10^{21}	290	500	70.4	146.9	156.3	1.88	4.67	40.8	24.07
6.44×10^{21}	290	600	19.4	45.8	50.7	1.27	12.19	74.1	16.63

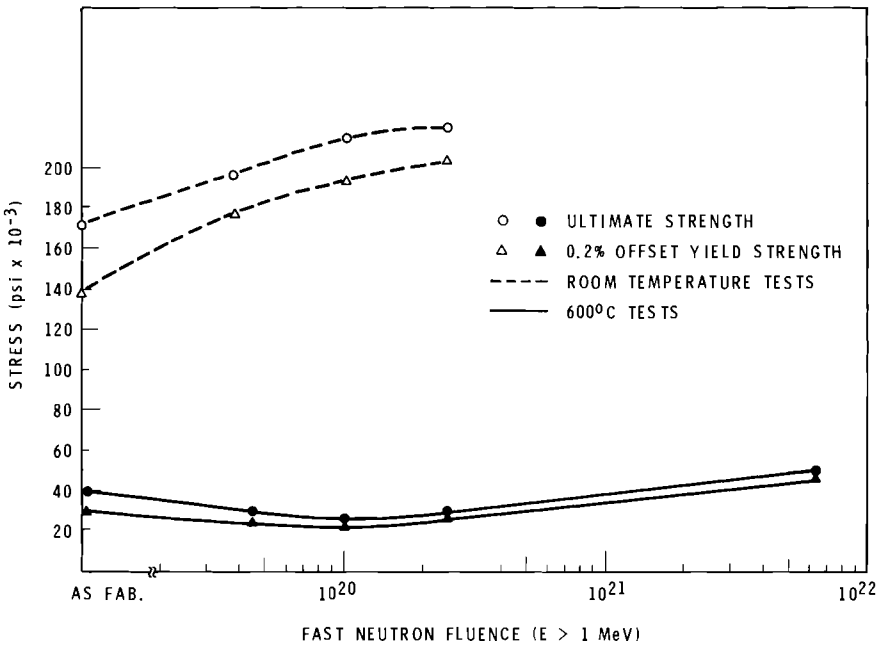

Neg 0680625-2

FIGURE 12.5. The Effect of Neutron Exposure at 290 °C on the Strength of Martensitic AISI 410 SS

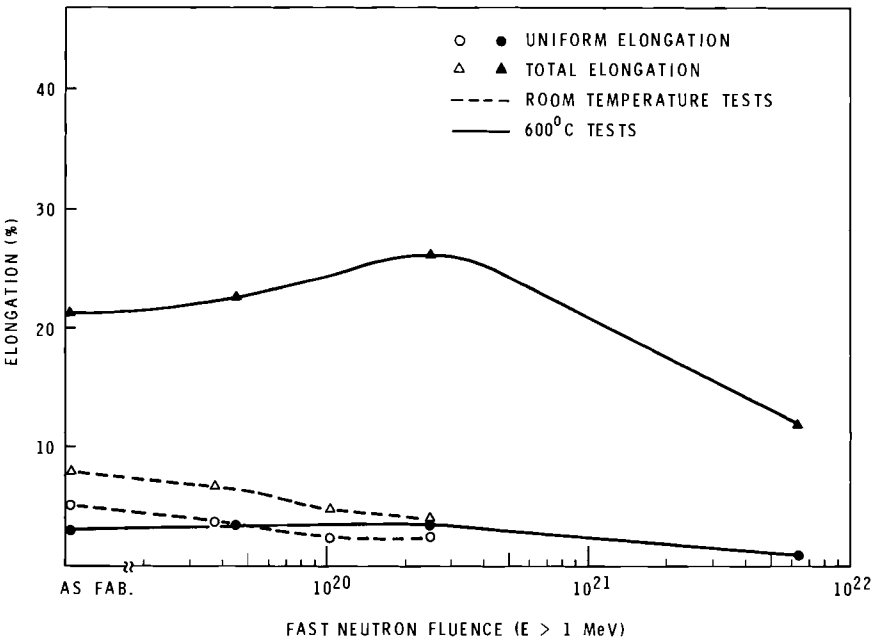

Neg 0680625

FIGURE 12.6. The Effect of Neutron Exposure at 290 °C on the Ductility of Martensitic AISI 410 SS

fluence of 6.4 x 10^{21} was not successful. The specimen became prematurely brittle at the extensometer points. In the 600 °C test, the ductility increased with increasing fluence but then decreased. It appears that the softening effect of the 290 °C age on the 600 °C tensile properties outweighed the hardening effect of the irradiation up to moderate fluence. So, as the fluence went to a higher value, the irradiation hardening outweighed the aging effects on the tensile properties.

The effect of test temperatures on the strength of the martensitic 410 irradiated at 290 °C to a fast fluence of 6.4 x 10^{21} is shown in Figure 12.7, while the ductility-versus-test temperature is presented in Figure 12.8. At all test temperatures, the yield strengths are greater and the ductilities less for irradiated specimens.

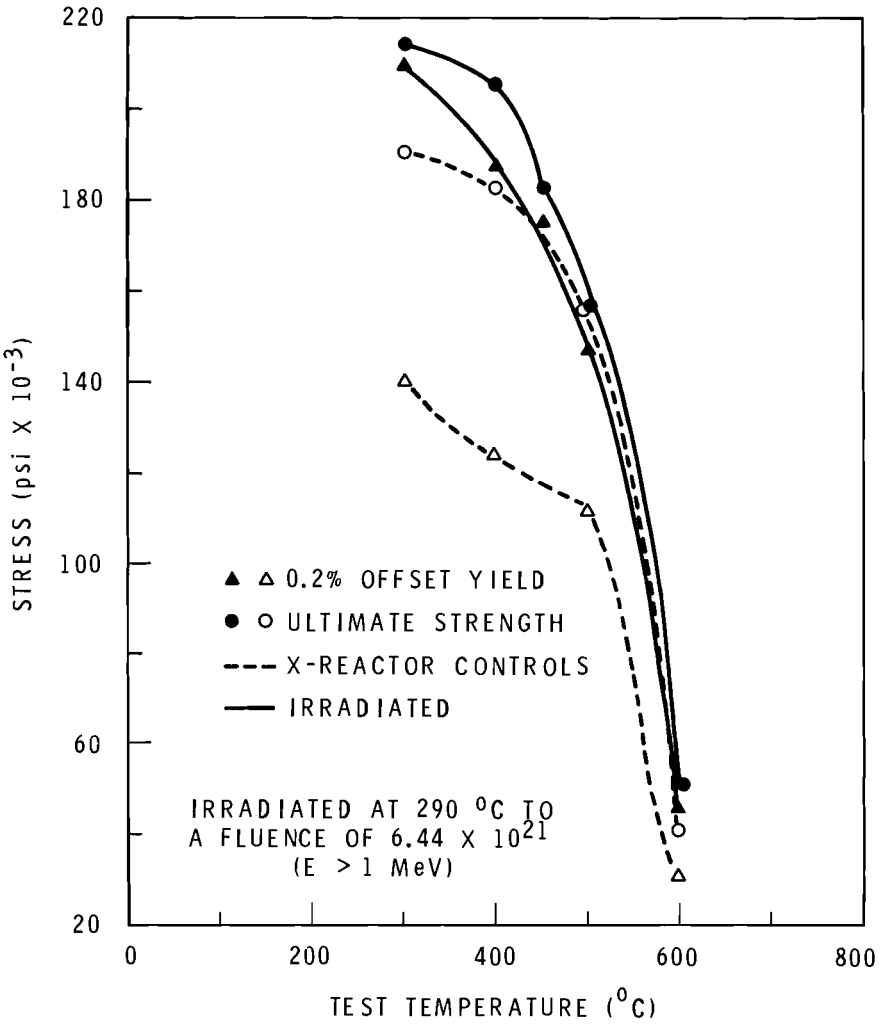

Neg 0680368-2

FIGURE 12.7. The Effect of Test Temperature on the Strength of Irradiated 410 SS in the Martensitic Condition

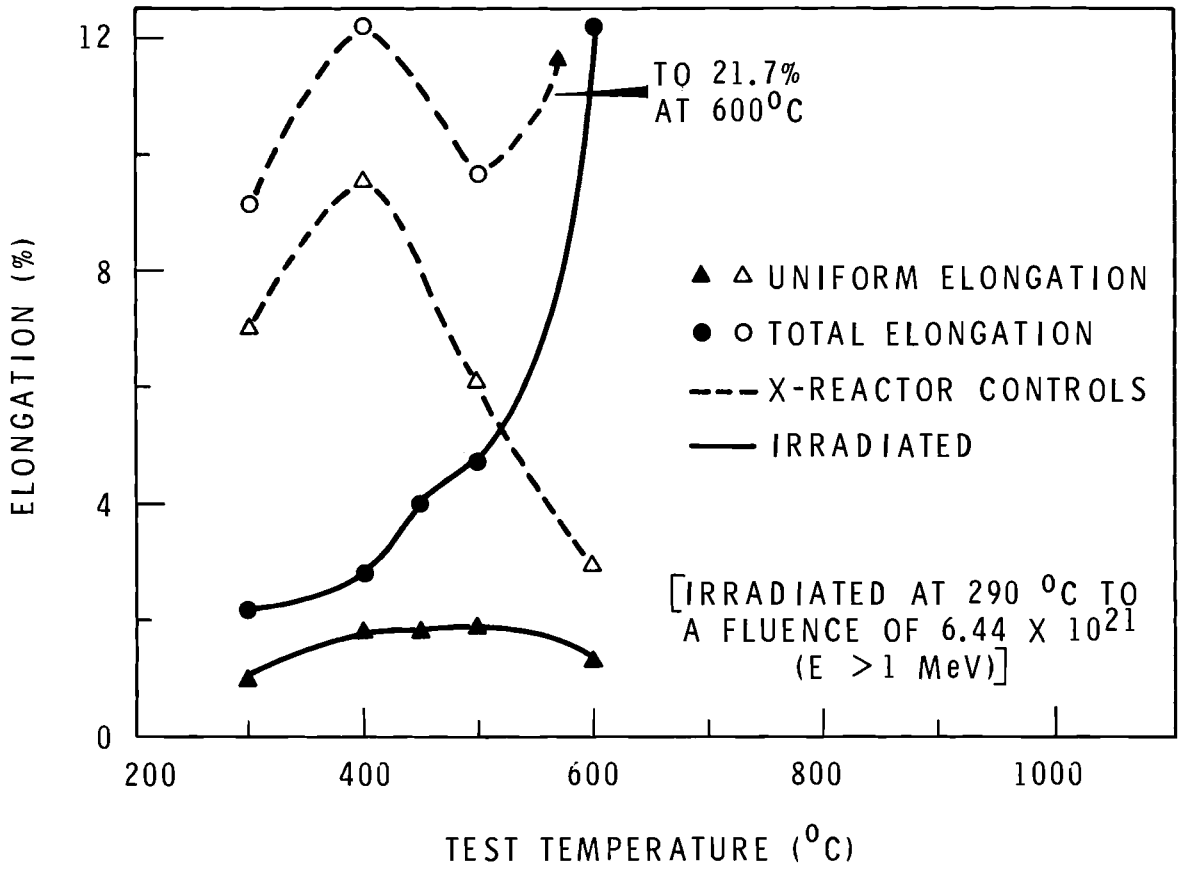

Neg 0680368-3

FIGURE 12.8. The Effect of Test Temperature on the Ductility of Irradiated 410 SS in the Martensitic Condition

ELECTRON MICROSCOPY OF ETR - IRRADIATED STAINLESS STEEL

H. R. Brager

The electron microscopy examination was continued on AISI type 304 SS irradiated in the ETR to 6 x 10^{21} n/cm^2 (E > 1 MeV) at 290 °C. This material was examined to determine the microstructure responsible for the high temperature irradiation hardening which persisted to the highest test temperature, 750 °C.

Photomicrographs presented in the last quarterly report[4] were analyzed. These picture the gage section of the material as tested at 750 °C and the same material having an additional 1 hr vacuum anneal at 870 °C (Table 12.8). In addition, sections of the material tested at 750 °C were vacuum annealed 1 hr at 980 °C or 1090 °C, (Table 12.8) and examined by electron microscopy Figures 12.9 and 12.10, respectively). The significant observations were:

TABLE 12.8. Electron Microscopy Observations of Type 304 SS Irradiated in the ETR to 6 x 10^{21} n/cm^2 (>1.0 MeV) at 290 °C

Material tensile tested at 750 °C, plus a vacuum anneal 1 hr at the indicated temperature	Anneal Temperature, °C			
	As Tested	870	980	1090
Cavity density (cm^3)$^{-1}$	2 x 10^{15}	3 x 10^{14}	2 x 10^{14}	1.5 x 10^{14}
$\Delta V/V$ (%)	0.17	0.25	0.50	1.2
Helium in equilibrium with surface tension of cavities (ppm)	300	275	400	600
Average cavity diameter (Å) (First moment/third moment)	110/115	210/250	270/350	460/575
Total cavity surface area (10^{19} Å^2/cm^3) (Calculated using first moment average cavity) diameter/third moment average cavity diameter)	2.5/3.0	1.5/2.0	2.2/2.7	3.0/4.0
Total cavity volume (10^{21} Å^3/cm^3) (Calculated using first moment average cavity diameter/third moment average cavity diameter)	3.0/3.5	2.5/4.5	4.5/9.2	13.5/21

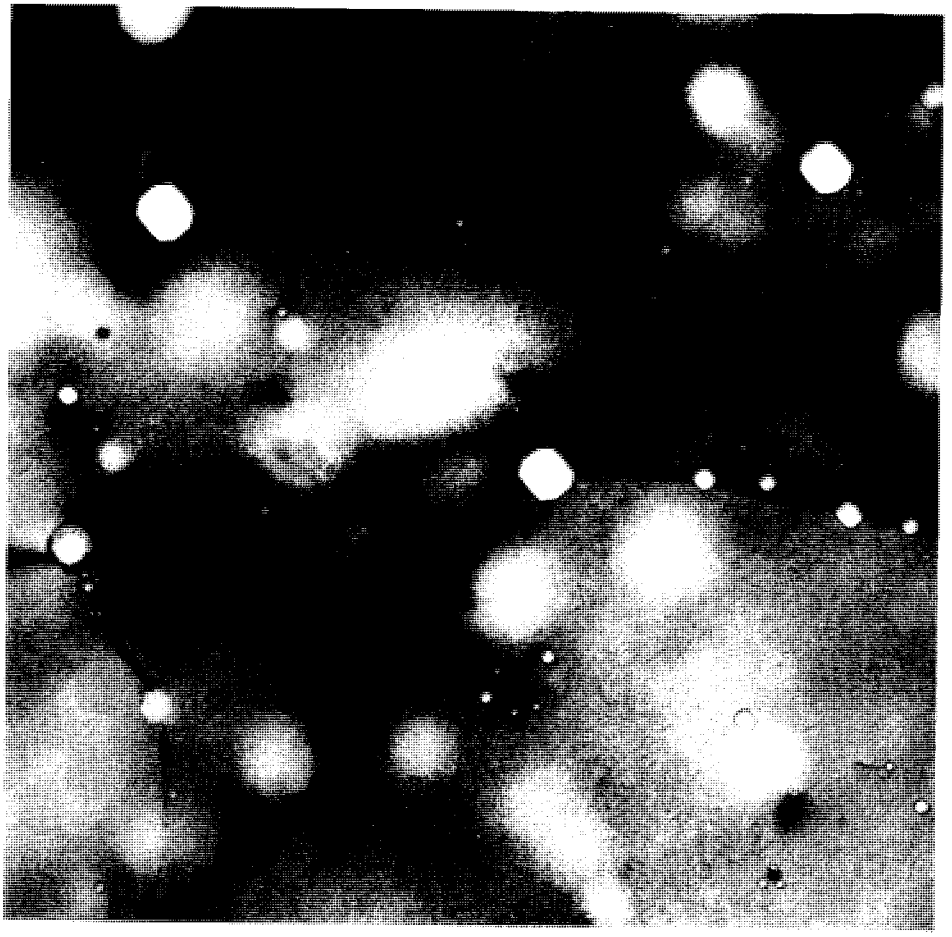

Neg 5255-A *96,000X*

FIGURE 12.9. Microstructure of AISI 304 SS Irradiated in the ETR at 290 °C to a Fluence of 6 x 10^{21} n/cm^2, Tested at 750 °C, and then Annealed at 980 °C for 1 hr

Neg 5301-B *98,000X*

FIGURE 12.10. Microstructure of AISI 304 SS Irradiated in the ETR at 290 °C to a Fluence of 6 x 10^{21} n/cm^2, Tested at 750 °C, and then Annealed at 1090 °C for 1 hr

- The cavities were present after vacuum annealing at temperatures up to 1090 °C.
- The cavities were uniformly located throughout the matrix and on grain boundaries. The grain boundaries did not have a denuded zone, and the size distribution of the cavities at the grain boundaries was not significantly different than for cavities in the matrix.
- No strain fields were observed around the cavities for material vacuum annealed within the temperature range of 750 to 1090 °C and furnace cooled.
- The total surface area of the cavities was constant over the investigated temperature range of 750 to 1090 °C while the total volume of the cavities increased with increased annealing temperature. The consistency of

macroscopic cavity surface area indicates that the cavities surface tensions are balanced by an internal gas pressure.

- The amount of helium gas produced by transmutation (about 12 ppm) was less than one-tenth the amount required to balance the cavities surface tension (assuming γ = 1500 ergs/cm^2).

The first four observations support the conclusion that the ETR irradiation produced cavities that behave like gas filled bubbles. However, the last observation suggests that the cavities are helium stabilized vacancy clusters. To provide additional information about the nature of the cavities, a sample of the ETR irradiated stainless steel was vacuum annealed 1 hr at 980 °C, annealed 1 hr at 820 °C in NaK at a pressure of 10,000 atm, and examined by transmission electron microscopy, Figure 12.11. The 980 °C vacuum anneal should have provided a high concentration (2 x 10^{14}/cm^3) of large cavities (300 Å). The 1-hr, 820 °C high-pressure (10,000 atm) anneal should have promoted the removal of soluable and chemically reactant gases which could help stabilize the cavities. The preliminary examination of the electron micrographs of the high pressure annealed steel provided the following observations:

- Approximately 2 x 10^{13} cavities/cm^3 with an average diameter of about 700 Å were still present after annealing the material 1 hr at 820 °C and 10,000 atm.
- There were no observable strain fields around the cavities.
- About 10^{13} precipitates/cm^3 with an an average diameter of about 400 Å were observed. The majority of the polyhedral precipitates were attached to cavities.
- Approximately 10^{14} small particles/cm^3 with an average diameter of 100 Å were observed. These small uniformly dispersed particles are not vacancy- or interstitial-clusters.

The preliminary estimate of the amount of helium gas required to balance the 10,000 atm applied pressure plus the cavity surface tension (assuming γ = 150 ergs/cm^2) is about 800 ppm. The concentration of the helium required to balance the surface tension of the cavities in the steel before the high pressure anneal was 400 ppm (Table 12.8). The factor of two discrepancies probably arises from the preliminary results so far obtained from analyses of the electron micrographs of samples after the high pressure anneal. Nevertheless, the recent results definitely confirm earlier results that the cavities do not respond like voids, but do behave like gas-filled bubbles.

IRRADIATION DAMAGE TO NICKEL-BASE ALLOYS

I. S. Levy

The requirements for corrosion resistance and high temperature strength place nickel-base alloys among the more promising materials for advanced nuclear reactor applications. When these alloys are irradiated at service temperatures, however, they generally suffer embrittlement and re-

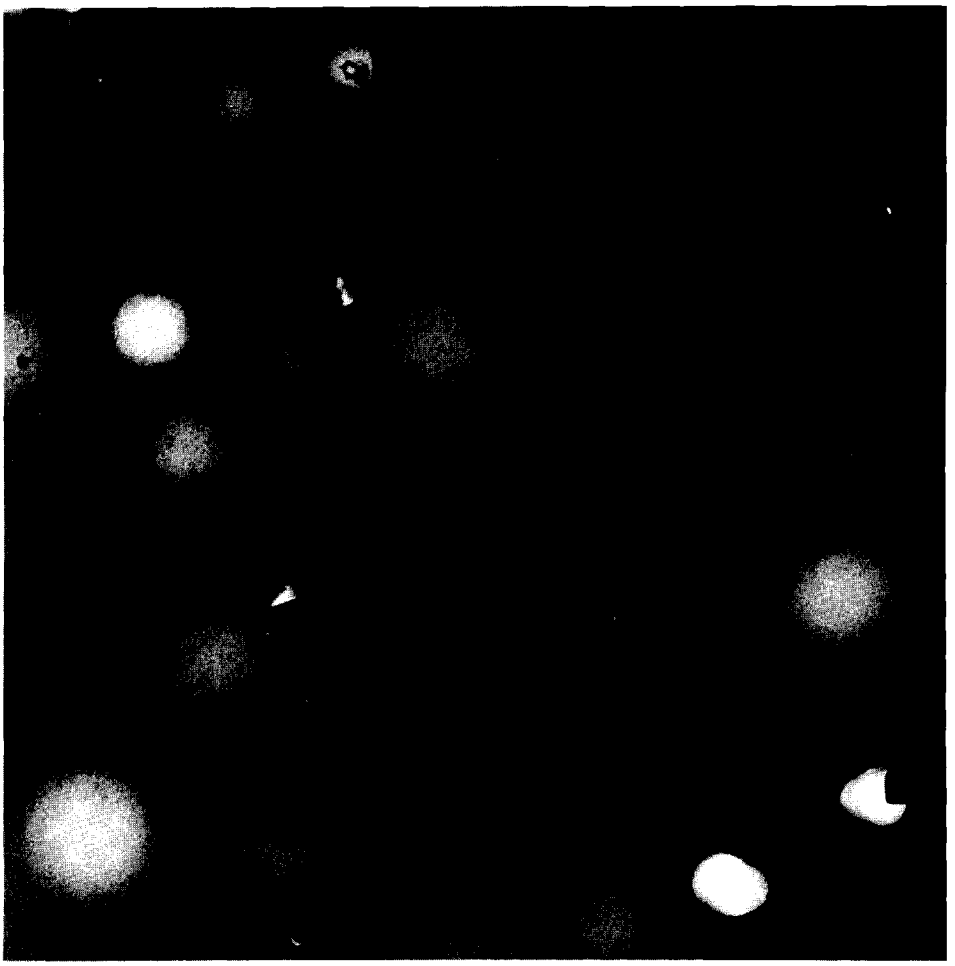

Neg 5452-D *96,000X*

FIGURE 12.11. Microstructure of Specimen Depicted in Figure 12.9, but After a 1 hr Anneal at 820 °C Under 10,000 atm Hydrostatic Pressure

duction in rupture life. The purpose of this program is to determine the effects of modified microstructures upon the irradiation stability of nickel-base alloys. These structural modifications are made by preirradiation thermal or thermomechanical treatments and are evaluated by tensile and stress-rupture tests and by microstructural examinations.

Recent studies on the three alloys in this program, Hastelloy X-280, Inconel 600, and Inconel X-750, have been concerned with the effects of pretreatments and long-term (>1500 hr) irradiation at 1250 °F (fast fluence of approximately 1 x 10^{20} n/cm^2). It has been found that the thermal exposure alone produces extensive matrix precipitation in Hastelloy X-280 and Inconel 600,[5] thus causing increases in yield strength and reductions in ductility in both alloys.

Preliminary data from stress-rupture tests on the control specimens of the three alloys at 1350 °F

show little change in rupture life after this thermal exposure compared with data after exposure at 540 °F. In fact, some treatments of Inconel X-750 that resulted in poor rupture properties after 540 °F exposure (because they produced an under-aged structure) showed, after the >1500 hr exposure at 1250 °F, better properties more closely related to those of the standard treatment. Presumably, this is the result of aging reactions during exposure.

The lack of reduction in rupture life in Hastelloy X-280 and Inconel 600, after this thermal exposure, may be caused by the opposing effects upon rupture life of the lowered ductility and increased strength indicated in tensile tests.

However, after irradiation, preliminary data show that compared to control specimens, the rupture lives of all three alloys were markedly reduced. Reductions ranged from about a factor of 10 for Hastelloy X-280 (36 hr vs 320 hr) and Inconel 600 (43 hr vs 515 hr) to about a factor of 300 for Inconel X-750 (2.5 hr vs 700 hr). These reductions in rupture life are larger than those found after exposure at 540 °F; compared to control specimens, the latter were only of the order of a factor of 3 for all three alloys. Thus, irradiation at 1250 °F increased these reductions (compared to 540 °F irradiation) by a factor of 3 for the solution-hardened alloys (Hastelloy X-280 and Inconel 600) to 25 for the precipitation-hardened alloy (Inconel X-750). The higher reductions may be associated with the combined effect of thermal and irradiation-induced instabilities. The fact that Inconel X-750 suffered a greater reduction in rupture life than did the two solution-hardened alloys might be expected, since a precipitation-hardened alloy would be more susceptible to aging reactions.

IN-REACTOR MEASUREMENTS OF MECHANICAL PROPERTIES

E. R. Gilbert and N. E. Harding

The in-reactor measurements program is intended to determine the effects of irradiation on the mechanical properties of reactor structural materails, to establish property data suitable for design purposes, and to consider mechanisms through irradiation effects on macroscopic deformation. The program currently involves conducting in-reactor creep measurements on annealed 304 SS, Hastelloy X, heat treated Zr—2.5 wt % Nb, and Zircaloy-2. Capsule development is being pursued so that program capabilities may be extended.

304 Stainless Steel

Loading curves for creep tests conducted at 450 °C are shown in Figure 12.12. The curves are similar for both an in-reactor test and an unirradiated control test and show discontinuous yielding independent of time. At 450 °C, a serrated stress-strain curve, due to strain aging, is observed in tensile tests. The discontinuous curve observed in the loading of the creep tests is probably a consequence of the same

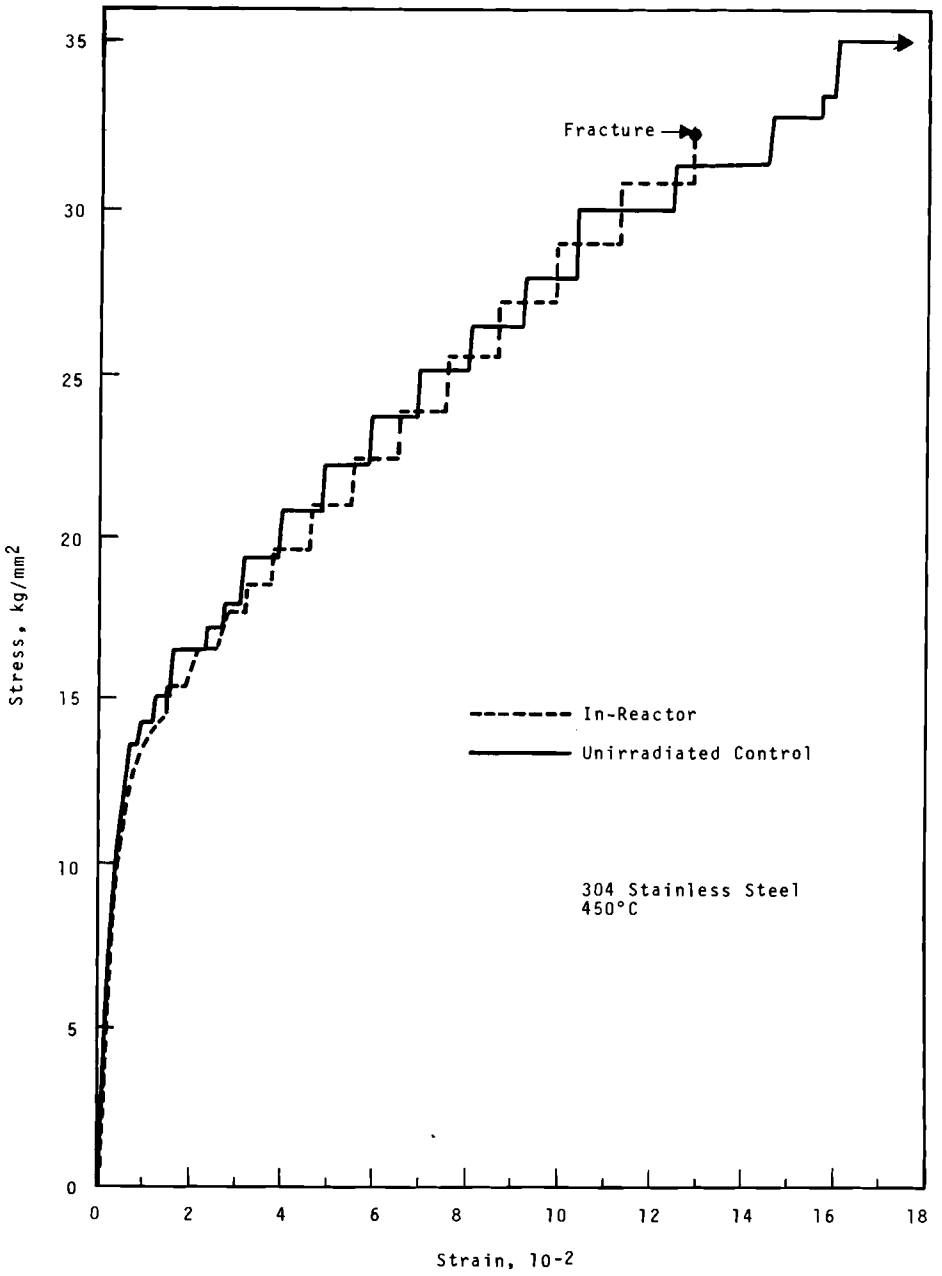

Neg 0680746

FIGURE 12.12. Loading Curves for Annealed 304 SS Tested During Neutron Irradiation and Without Irradiation at 450 °C

phenomenon that causes the serrated stress strain curve in tensile tests. However, it appears as steps under the constant load applied in the creep test in contrast to serrations under the constant cross head speed used in the tensile test. Neutron irradiation did not influence the discontinuous yielding but it did cause decreased fracture strain.

Zircaloy-2

An in-reactor creep test was conducted on 750 °C annealed Zircaloy-2 in the PRTR with a neutron flux of approximately 5 x 10^{12} nv (E > 1 MeV). The strain-versus-time curve and corresponding unirradiated control creep data are shown in Figure 12.13. The in-reactor creep appears to be increased over the unirradiated control test. The creep rates for the annealed Zircaloy-2 are plotted on a semilogarithmic plot of strain rate-versus-stress in Figure 12.14 along with data by Fidleris and Williams[6] for cold worked Zircaloy-2. It appears that both cold-worked and annealed Zircaloy-2 exhibit faster creep rates during neutron irradiation.

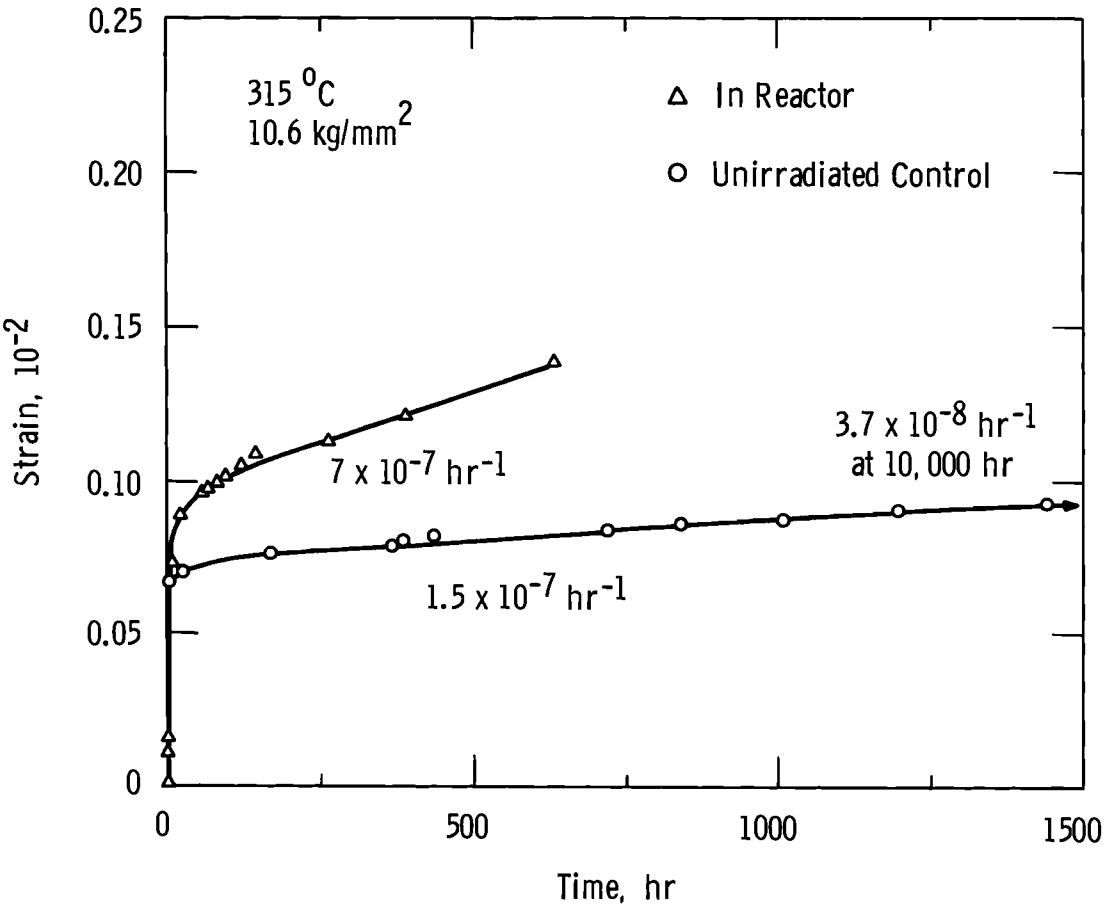

Neg 0672975-2

FIGURE 12.13. Strain Versus Time for Creep of Zircaloy-2 Tested in the PRTR in a Neutron Flux of Approximately 5 x 10^{12} nv (E>1 MeV). Specimens Cut in Longitudinal Direction from Plate, Annealed for 20 hr at 750 °C, and Furnace Cooled.

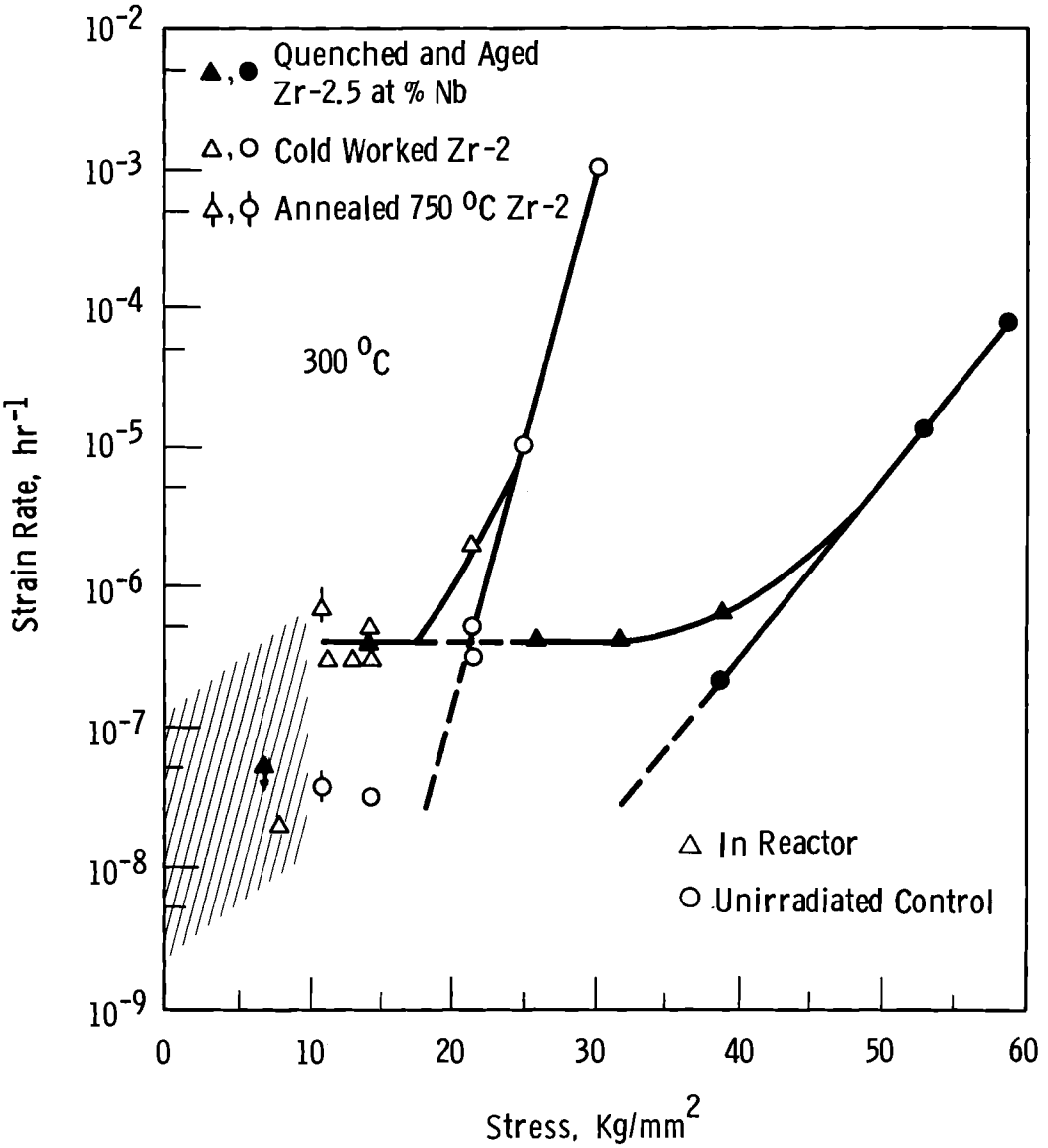

Neg 0673372-1

FIGURE 12.14. Strain-Rate Versus Stress on Semilogarithmic Coordinates for Zr–2.5 wt% Nb

Zr–2.5 wt% Nb

In-reactor creep rates for Zr–2.5 wt% Nb are plotted (Figure 12.14) against stress on semilogarithmic coordinates along with data for cold-worked Zircaloy-2 by Fidleris and Williams.[6] The in-reactor creep rates for Zr–2.5 wt% Nb show little if any dependence on stress between 14 and 32 kg/mm^2 and are similar in value to those for cold-worked Zircaloy-2 between 10 and 15 kg/mm^2. Appreciably slower in-reactor creep rates are observed at stresses below 10 kg/mm^2.

GRAIN BOUNDARY STABILIZATION

E. R. Bradley

A study was recently initiated to investigate the recrystalization and grain growth characteristics of metals containing small concentrations of inert gases.

Since impurities generally inhibit the motion of grain boundaries in metals, a large amount of work has been directed toward this problem. However, very few investigations of the interaction of the inert gases with boundaries have been conducted. Observations on uranium[7] and AL–0.7 wt% Li alloy[8] after neutron irradiation indicate that grain boundaries are stabilized during irradiation. One proposed mechanism for this stabilization is a "locking" of the boundaries by inert gases produced during irradiation.

Bubbles have been observed along grain boundaries and dislocation lines in irradiated structural materials. These bubbles are proposed to contain helium which is produced by $n \rightarrow \alpha$ fast reactions, or they are caused by boron impurities in the materials by the thermal reactions $^{10}B + n^{1} \rightarrow \alpha$. Postirradiation annealing of these materials also indicates a stabilized grain structure.

Inert gases are presently considered important in determining the properties of iron and nickel base alloys. The extreme loss of ductility in these alloys has been attributed to the buildup of helium gas bubbles. If a small concentration of inert gas can be introduced into a material, stabilizing the grain structure should be possible without detrimentally affecting the mechanical properties of the material. This would produce a material acceptable for prolonged service at high temperatures without catastrophic grain growth occurring.

Ion bombardment is one method of introducing small quantities of inert gas into a metal. An apparatus, shown schematically in Figure 12.15, has been constructed and shown to be effective in introducing small quantities of helium into a metal. Nickel is a convenient metal to demonstrate the practicality of the grain stabilization technique; therefore, nickel powder in the size range 3 to 7 μ was used. The bombardment apparatus consists of an evacuable chamber with a variable leak vacuum valve to maintain a dynamic helium pressure of 100 μ during bombardment. The anode is a 1/8 in. diam nickel rod; the powder sample in contact with a nickel rod is the cathode. The potential source for the glow discharge is a 5 kV power supply whose voltage and current is monitored with an x-y recorder.

The amount of helium injected into the nickel powder is determined by

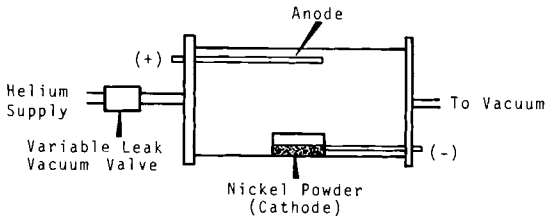

FIGURE 12.15. Schematic of Glow Discharge System for Injecting Helium into Metal Powders

heating the powder in vacuum and measuring the helium liberated as a function of temperature with a mass spectrometer type leak detector. The heating rate used is 20 °C/min. A typical graph of helium liberated versus temperature is shown in Figure 12.16.

Two distinct peaks occur as the temperature is increased from 50 to 800 °C. The relative size and position of these two peaks depend on the time and potential used during bombardment. The low temperature peak occurs between 100 to 400 °C and the high temperature peak between 500 to 800 °C. This technique and the apparatus available provide information only to a temperature of 800 °C. For higher temperature data, tin is alloyed with the nickel powder to determine the amount of helium remaining after heating to 800 °C. Up to 5% of the total helium released is found to be retained after heating in vacuum to 800 °C. The temperature at which this helium would be released from the metal powder cannot be determined by this method, but processing and compaction of the powders at temperatures up to 800 °C without complete loss of helium are feasible.

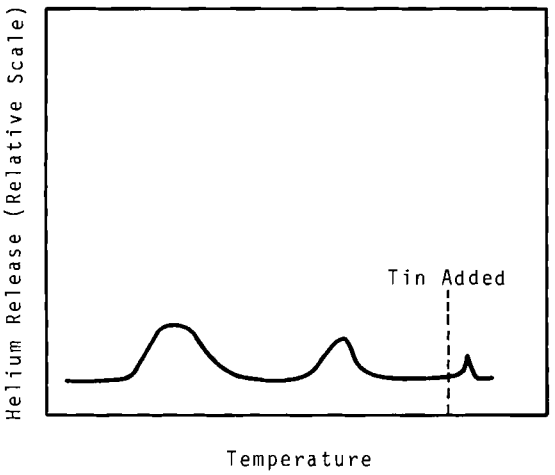

FIGURE 12.16. A Typical Chart Showing Helium Release from Nickel Powder Following Helium Ion Bombardment as a Function of Increasing Temperature During Heating at a Constant Rate

Nickel powder, with and without helium, is being hydrostatically compacted at various pressures and temperatures. Recrystallization and grain growth in these compacts will be studied by microscopy, hardness, and X-ray techniques.

FRACTURE STUDIES

J. A. Williams

Size Effects of the DCB Specimen on the Fracture Toughness of ASTM A533-B Steel

A major task of the HSST* irradiation damage program is to determine size effects of various types of fracture mechanics specimens. The objectives of this task are to determine as a function of neutron fluence:

- The smallest specimen size that will provide a valid measure of plane-strain fracture toughness at a given temperature
- The limiting temperature at which plane-strain fracture cannot be measured regardless of specimen size
- The influence on gross fracture toughness of microstructural and neutron fluence gradients in

* *Heavy Section Steel Technology*

heavy-section plates. Fracture mechanics specimens of the DCB, WOL, and notch bend types will be used in this task.

An initial plate, 1 in. thick x 1 in. wide x 2 in. long (RD) of ASTM A533-B Class 1 steel Lukens Heat A1008-1, was supplied by Oak Ridge National Laboratory in the heat treated condition. Heat treatment consisted of normalizing at 1600 to 1750 °F, austenitize at 1650 °F for 4 hr, water quenching, tempering at 1225 °F for 4 hr, and furnace cooling.

Double cantilever beam specimens 0.5 and 1.0 in. thick were machined from the 1/2 T plate position, with the fracture plane normal to the plate surfaces and in the rolling direction. The results of the fracture toughness tests are tabulated in Table 12.9. Fracture toughness tests at -160 and -140 °C were made on the 0.5 in. specimen. The second test at -140 °C resulted in fracture of both specimens arms. The 1.0 in. specimen was tested at -160, -140 and -120 °C. Specimen arm breakage occurred at -120 °C during the second test. The remainder of the 1.0 in. specimen was remachined (Figure 12.17) and tested at -160 °C to the end of the specimen. Arm breakage of both the 0.5 and the 1.0 in. specimens occurred at values less than 1.5 for $B/(K_{I_c}/\sigma_{ys})^2$.

The fracture toughness (K_{I_c}) of A533-B is plotted as a function of $B/(K_{I_c}/\sigma_{ys})^2$ in Figure 12.18d. An increase in K_{I_c} as a function of the crack length for the DCB specimen was observed (Table 12.9 and

TABLE 12.9. Results of DCB Fracture Toughness Tests of A533-B Class 1 Steel Specimens from 1/2 T Position in 12 in. Plate

Specimen Number	Thickness,[e] B, in.	Temperature, °C	Yield[a] Strength, ksi	Crack Length, C, in.	$\frac{B}{(K_{I_c}/\sigma_{ys})^2}$	K_{I_c}, ksi $\sqrt{in.}$	K_{I_a}, ksi $\sqrt{in.}$
01KA9	0.5	-160	95	2.23	4.3	32.1	29.9
01KA9	0.5	-160	95	2.27	4.2	32.8	30.8
01KA9	0.5	-160	95	2.43	3.0	38.6	29.8
01KA9	0.5	-160	95	2.59	3.5	35.8	32.8
01KA9	0.5	-140	86	2.78	1.1	58.5	31.3
01KA9	0.5	-140	86	3.95	0.8	68.0	(b)
01KA22	1.0	-160	95	3.06	9.7	30.4	29.9
01KA22	1.0	-160	95	3.17	7.9	33.7	31.1
01KA22	1.0	-160	95	3.55	5.5	40.5	35.7
01KA22	1.0	-160	95	4.47	5.5	40.5	37.8
01KA22	1.0	-160	95	4.75	4.9	42.8	36.3
01KA22	1.0	-140	86	5.52	3.2	48.1	37.8
01KA22	1.0	-120	79	6.92	1.7	61.1	56.0
01KA22	1.0	-120	79	7.32	1.0	77.5	(b)
01KA22[c]	1.0	-160	95	2.40	5.1	42.2	33.6
01KA22	1.0	-160	95	3.07	5.4	41.0	39.0
01KA22	1.0	-160	95	3.49	4.7	43.9	(d)

(a) *Yield strength data taken from Reference 10 for SA533-B 8 in. plate*

(b) *Both arms fractured*

(c) *5 1/2 in. long specimen machined from end of 01KA22 (Figure 12.17)*

(d) *Fracture run to end of specimen*

(e) $B_N/B = 0.33$

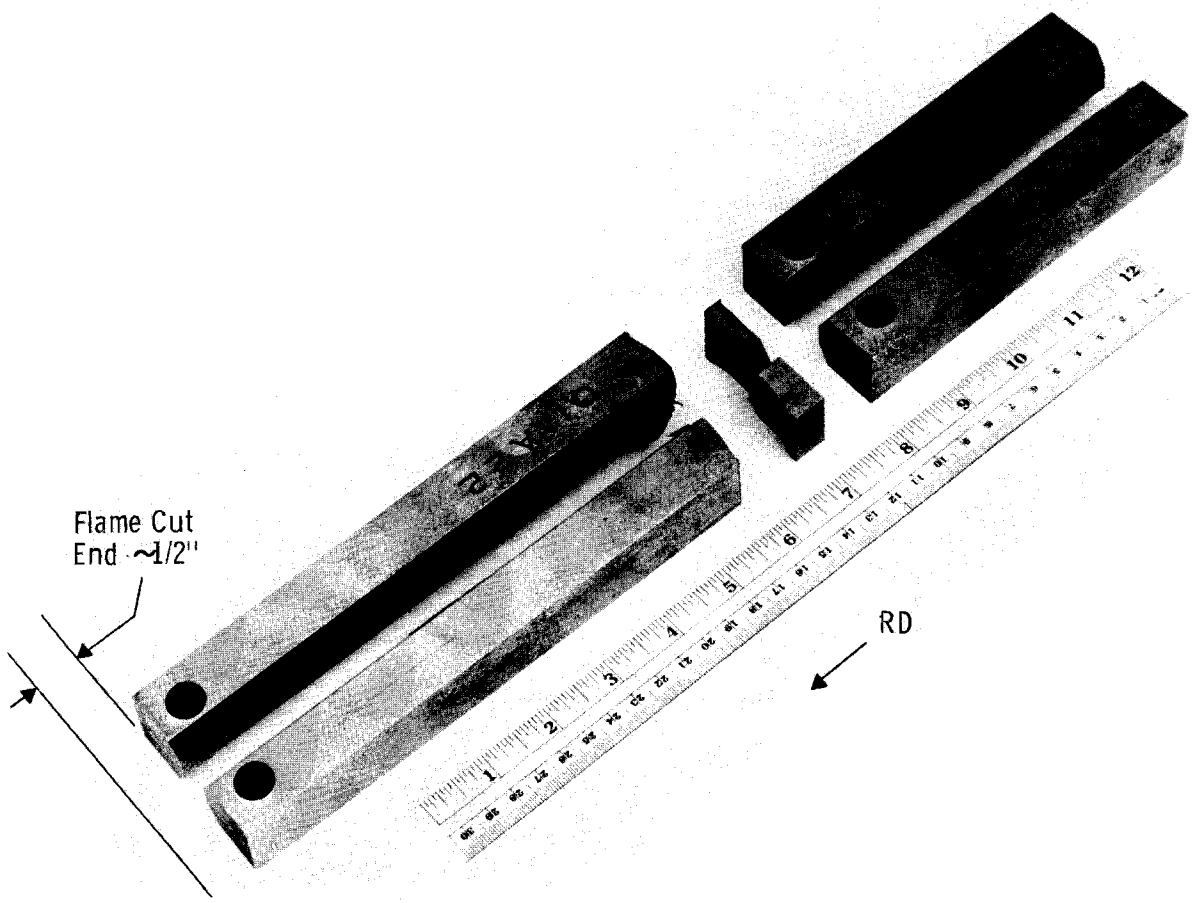

Neg 0680889

FIGURE 12.17. DCB (1 in. thick) Specimen of A533-B. Short Specimen Was Machined after Fracture of Both Arms

Figure 12.18d). To determine if the observed increase was a geometry effect or a material gradient, the remachined specimen from the end of 01KA22 was tested at -160 °C. The fracture toughness results of all tests at -160 °C are plotted as a function of crack length in Figure 12.18a and as a function of the distance from the flame cut end of the plate in Figure 12.18b. From these data, the observed change in K_{I_c} does not appear to be geometry dependent, but rather a result of material gradient. Whether the material gradient is a result of flame cutting or a gradient of the original plate is inconclusive. Metallographic examinations have been made that indicate that microstructural changes occur only to a depth of about 1/4 in. from the flame cut surface.[9] When the DCB specimen is used for plane-strain fracture toughness testing, the requirement $B/(K_{I_c}/\sigma_{ys})^2$ being equal to or greater than 2.5 appears to be a valid criteria (Figure 12.18d). Whether this requirement can be decreased by using a different net thickness (B_N) is yet to be determined.

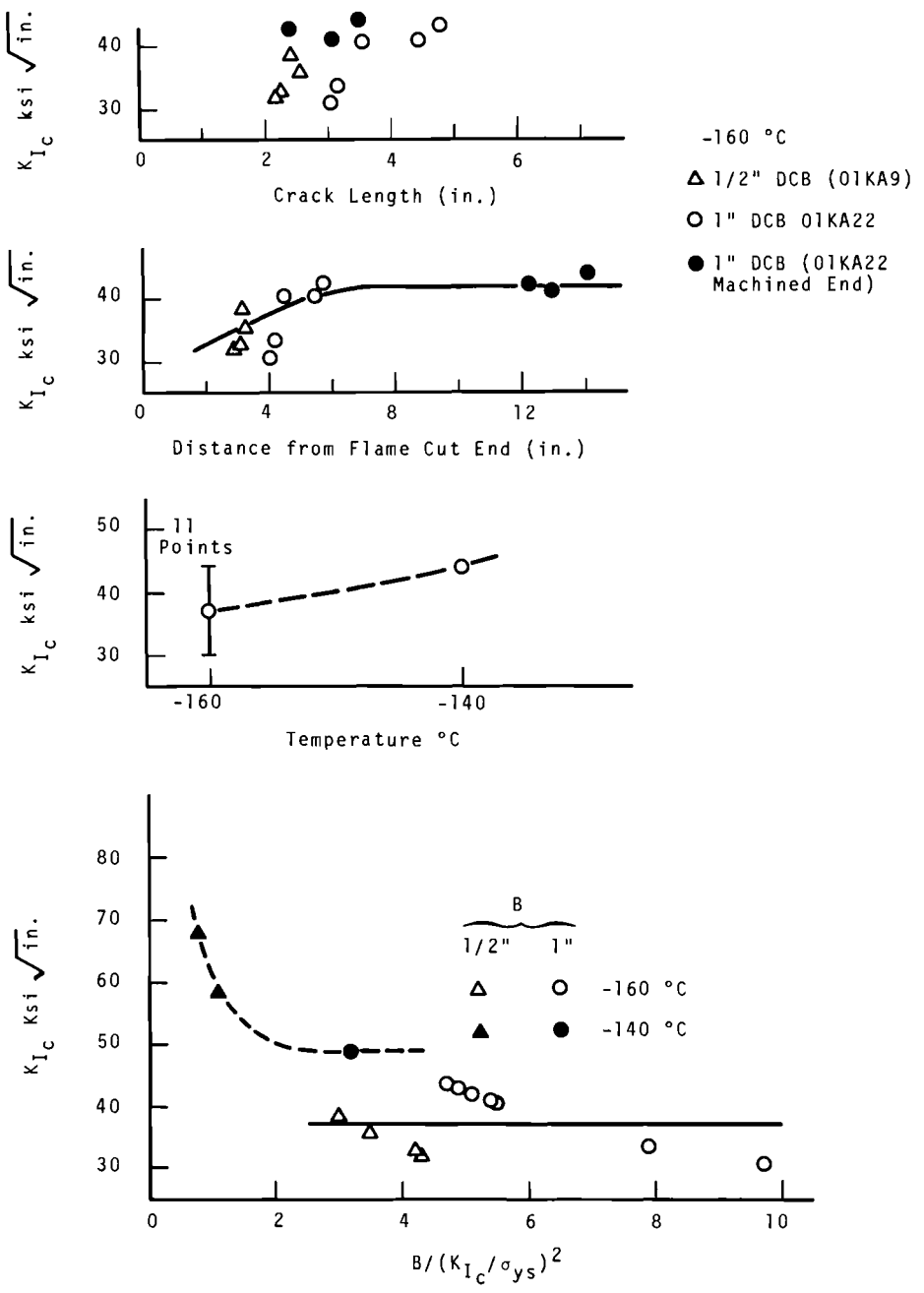

Neg 0680847-1

FIGURE 12.18. Fracture Toughness (K_{I_c}) of Q & T A533-B as a Function of (2a) Crack Length, (2b) Distance from Flame Cut Surface (2c) Temperature, and (2d) $B/(K_{I_c}/\sigma_{ys})^2$. All Measurements Made at 1/2 T Position of 12 in. Plate with the Crack Plane Normal to the Plate Surfaces and in the Rolling Direction of the Plate. (a through d progresses from top to bottom)

HEAVY SECTION STEEL

F. A. Smidt

This portion of the Heavy Section Steel Program (HSST) emphasized studies in support of the testing program on heavy sections of reactor pressure vessel steels. The objective was to gain insight into the conditions that might lead to catastropic fractures of this material during neutron irradiation.

During this report period, some time was spent in a literature survey of fracture mechanics and processes and mechanisms of crack nucleation and propagation.

The relationship between deformation temperature and the development of dislocation networks is being studied experimentally as a function of purity and neutron exposure of iron under another program (IDRM). Having direct bearing on the HSST program, this work should lead to a better understanding of the loss in work hardenability in the neighborhood of the crack tip, which is essential in determining the fracture toughness of a material. A paper on this subject, presented at the AIME Annual Meeting in New York, February 26-29, 1968,[11] describes some of the changes in internal stress fields (which are associated with dislocation networks) that accompany a change in the temperature at which iron is deformed. It also interprets these changes in terms of work-hardening mechanisms.

Tensile testing of iron specimens irradiated to a fast fluence of approximately 2 x 10^{20} n/cm^2 (E > 1 MeV) has also been initiated and should be completed within the next quarter. These data should contribute to our understanding of the modification of deformation mechanisms by higher neutron exposures. These data together with previously obtained data on iron will be included in a paper* describing the effects of neutron irradiation on the deformation mechanisms in iron.

HIGH PRESSURE STUDIES

G. L. Kulcinski

High Temperature-Pressure Annealing of Irradiated 304 SS

It has been found[12] that when 304 SS is irradiated to a high fluence in a thermal reactor and heated to temperatures above 750 °C, numerous cavities form in the matrix. Furthermore, these cavities enlarge as the metal is heated to higher temperatures.

The nature of these cavities has not been clear. When they are filled with gas, roughly 30 times more gas atoms are present than predicted by transmutation calculations. When they are voids, they should disappear upon heating but do not.[12] To determine more about the nature of the cavities, samples in which they had already formed, due to a 980 °C vacuum anneal, were subjected to a temperature of 820 °C and a pressure of 150,000 psi (10 kbars) for 1 hr

* *The Japanese-American Information Exchange Meeting on Effects of Irradiation in Iron and Steel is to be held in San Francisco, June 23-26, 1968.*

while immersed in NaK. A posttest electron microscopy examination indicated that the high pressure treatment failed to collapse the cavities but did cause changes in the size and distribution of the cavities. Detailed results are published elsewhere in this report.[12] The conclusion of the microscopy study is that the cavities are filled with gas and that they may be properly called bubbles in the solid.

Aside from the importance of the above conclusion, another interesting fact is that these samples were successfully contained in a hydrostatic medium at 820 °C under such a large pressure.

To study the effects of pressure annealing on microscopic defects produced by irradiation, it is extremely important that the sample be subjected to no shear stresses while under pressure. Defects such as vacancies, interstitials, or dislocations generated by such shear components would interfere with (and complicate) the interpretation of those defects already present due to irradiation. To insure that an external stress is transmitted hydrostatically to a sample, the sample is usually immersed in a substance that remains a liquid during the entire time of the test. At room temperature, this can be accomplished by using various organic fluids up to ∿300,000 psi (∿20 kbars). However, as the temperature is raised above 300 to 400 °C, the organics decompose or polymerize, thus forcing the use of other liquids. Liquid metals such as Li, Na, K, NaK, Ga, or Hg have much better thermal stability than organics, but Ga and Hg are extremely corrosive at high temperatures and attack iron or iron alloys quite readily above 600 °C.[13,14] NaK was picked because it is liquid at room temperature (mp = -11 °C) and is also relatively unreactive to stainless steel at temperatures to 900 °C.[14]

A schematic of the pressure cell assembly used is shown in Figure 12.19. The samples, contained in a perforated tantalum basket, were encapsulated in a NaK-filled can. This can was placed into a preassembled pressure cell (Figure 12.19), which was then placed into the tungsten-carbide die of a piston-cylinder high pressure device, described previously.[15] As the pressure cell was crushed under an advancing tungsten-carbide piston, the can collapsed and increased the pressure in the NaK. This pressure was then transmitted hydrostatically to the sample.

The pressure was first raised to 150,000 psi (10 kbars), and the temperature then raised to 820 °C. After 1 hr at these conditions, the temperature was lowered at a rate of approximately 300 °C/min, and the pressure was released. Figure 12.20 shows the can assembly before and after the test. Although there was some shortening of the can, no NaK leakage was evident.

A measure of the hydrostaticity of the pressure transmitting media is shown in Figure 12.21, where the microstructure of the steel is shown before and after the test. The white spots are bubbles and the black spots are precipitates. The

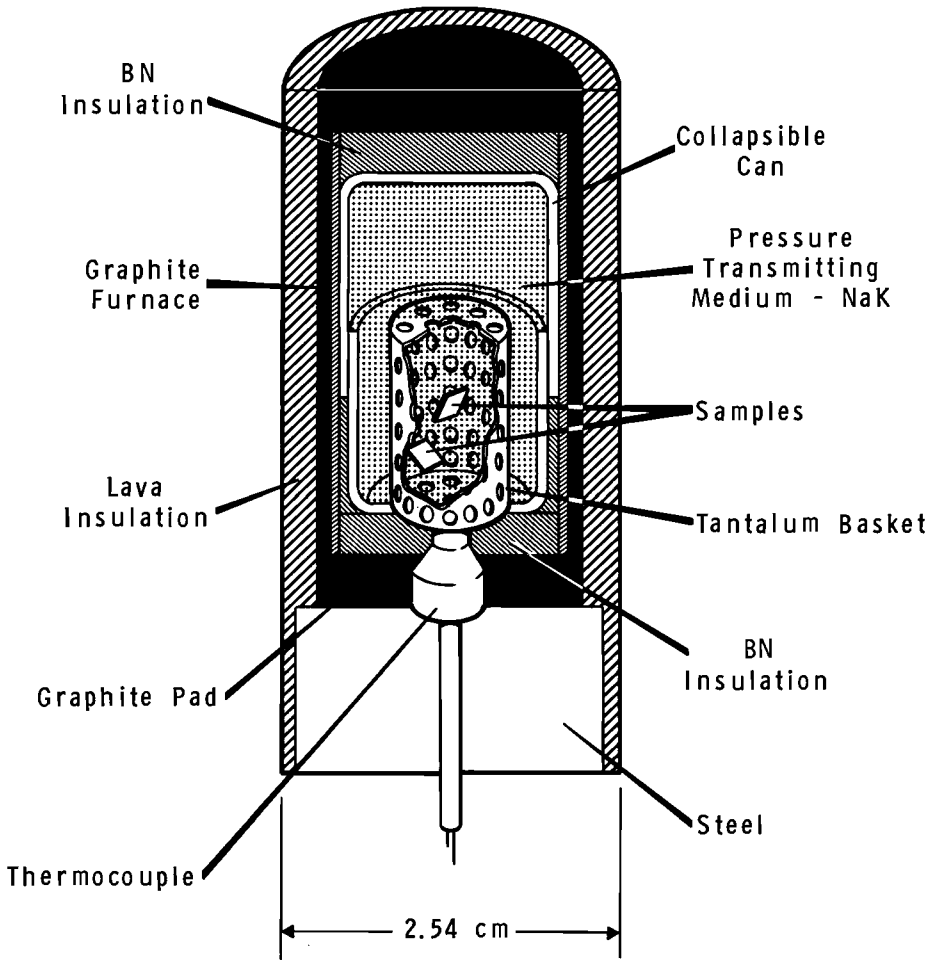

Neg 0680861

FIGURE 12.19. Pressure Cell Assembly for Annealing Irradiated 304 SS at 820 °C and 10 kbars (150,000 psi)

relatively low concentration of dislocations in the compressed sample is proof that there are few, if any, shear stresses acting on the sample. An increased amount of precipitate is also noted in the pressure annealed sample (Figure 12.21B); the association of bubbles with precipitates is much more prevalent in this sample than in the vacuum annealed case (Figure 12.21A).

The significance of the microstructure in the pressure annealed sample is currently under investigation.

IN-REACTOR CORROSION OF ZIRCONIUM ALLOYS

A. B. Johnson

The in-flux corrosion behavior of three lots of Zircaloy-2 was extensively characterized in pH-10 LiOH, ~1 ppm O_2.[16] The specimens, exposed in the G-7 loop of the Engineering Test Reactor, corroded at greatly accelerated rates. After the G-7 loop coolant was converted to pH-10 NH_4OH <0.05 ppm O_2, one set of specimens exposed in the pH-10 LiOH environment was transferred to

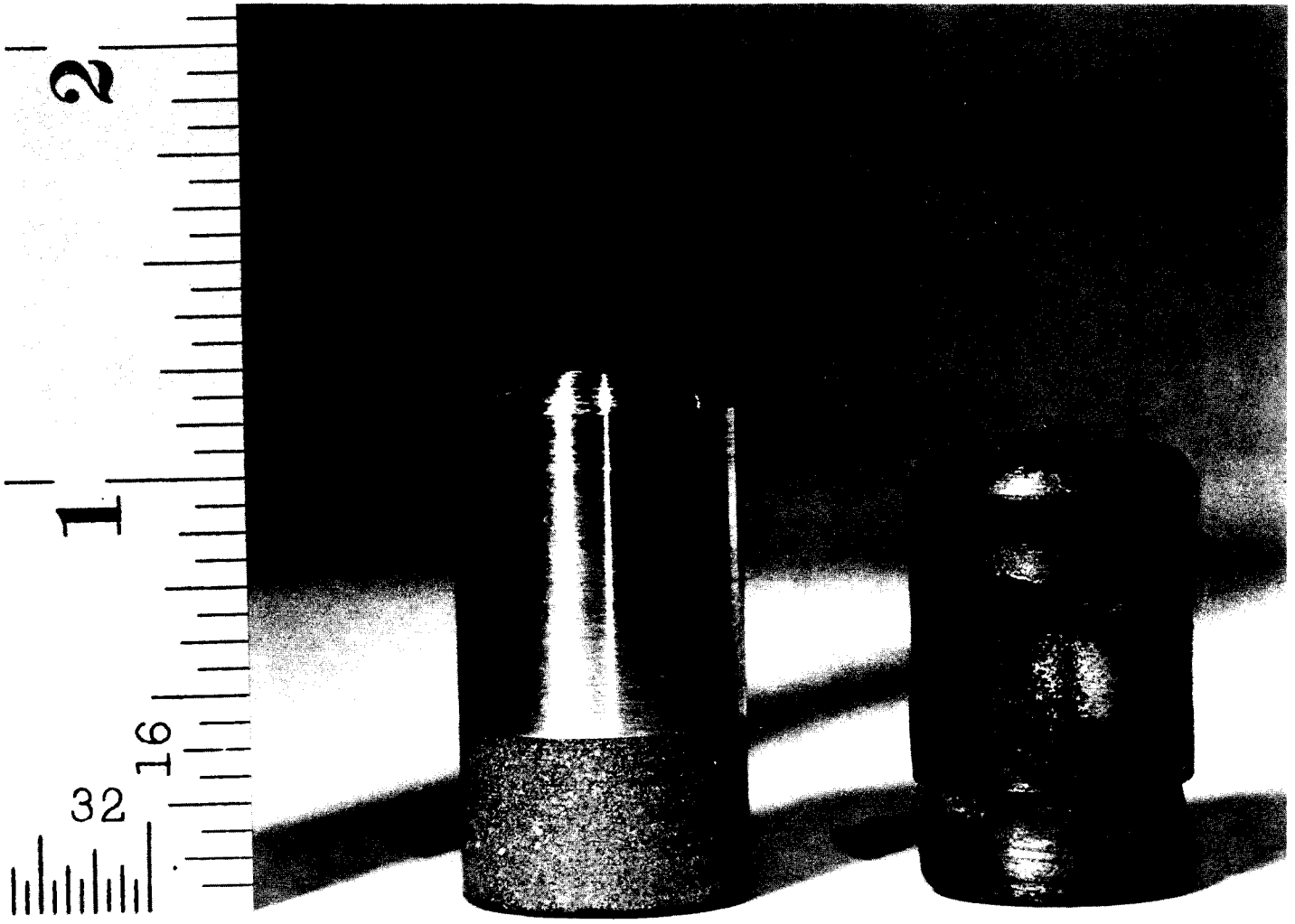

Neg 0670478

FIGURE 12.20. A Comparison of Collapsible Can Assemblies Before (Left) and After (Right) a High Pressure, High Temperature Test

Neg 5254-C

FIGURE 12.21A. Microstructure of 304 SS Irradiated to 6 x 10^{21} n/cm^2 (>1 MeV) at 290 °C and Subjected to a 980 °C, 1 hr Vacuum Anneal

Neg 5493-D

FIGURE 12.21B. Microstructure of Sample in 12.21A After a 1 hr, 10 kbar (150,000 psi), 820 °C Anneal in NaK

the ammoniated coolant. Corrosion of the transferred specimens continued at the high rates established in the high-oxygen lithiated environment. Recently, specimens of the three Zircaloy-2 lots were exposed in the ammoniated G-7 loop environment without prior exposure in the lithiated system. The samples were fabricated in the form of tensile specimens from the same stock used in the previous G-7 loop tests.[16] However, all specimens in the previous tests were prefilmed three days in water at 300 °C. The conditions of the 6-cycle G-7 loop exposure are summarized in Table 12.10.

TABLE 12.10. G-7 Loop Exposure Conditions

Temperature, °C	270-280
Time at Temperature, days	131
ETR Cycles	87 thru 92
Flux, n/cm^2 sec, >1 MeV	9.4×10^{13}
Fluence, n/cm^2 sec, >1 MeV	1.1×10^{21}
Fluence, n/cm^2 sec, thermal	2.6×10^{21}
Coolant	pH-10 NH_4OH
O_2, ppm	<0.05
H_2 (mean), cm^3/kg	45
C_s-138, dis/min ml	2×10^4
NH_3, ppm	10

The 6-cycle Zircaloy-2 specimens were exposed in as-etched and prefilmed surface conditions. The metallurgical and surface conditions are summarized in Table 12.11.

TABLE 12.11. Metallurgical and Surface Conditions

As-Etched Surface Conditions
- As-Fabricated[16]
- Alpha Annealed (8 hr, 760 °C)
- Beta Quenched (10 min, 1010 °C)

Prefilmed Surface Conditions (As-Fabricated)
- 300 °C, 3 days - 13 mg/dm^2 (Lots AT & CT only)
- 400 °C, 3 days - 24 mg/dm^2
- 400 °C, 210 days - 192 to 258 mg/dm^2

Control samples for certain metallurgical and surface conditions were exposed in an out-of-reactor autoclave operated at the G-7 loop temperature in pH-10 NH_4OH. Weight gains for the in-flux and out-of-reactor specimens are summarized in Figure 12.22.

Weight gains on as-etched G-7 loop specimens were only slightly higher than weight gains on the controls. In-flux weight gains were not affected by heat treatment, nor did in-flux corrosion resistance on as-etched specimens vary significantly as a function of Zircaloy-2 lot.

Corrosion rates were accelerated on all prefilmed G-7 loop specimens, but the response varied with the prefilm treatment. We are attempting to resolve uncertainties in the in-flux weight gains on 400 °C, 72 hr specimens by metallography. The least accelerated of the three prefilm conditions appears to have been the 300 °C, 73 hr surface condition. Corrosion rates were markedly accelerated on specimens with thick films formed out-of-reactor (400 °C, 210 days). The corresponding out-of-reactor,

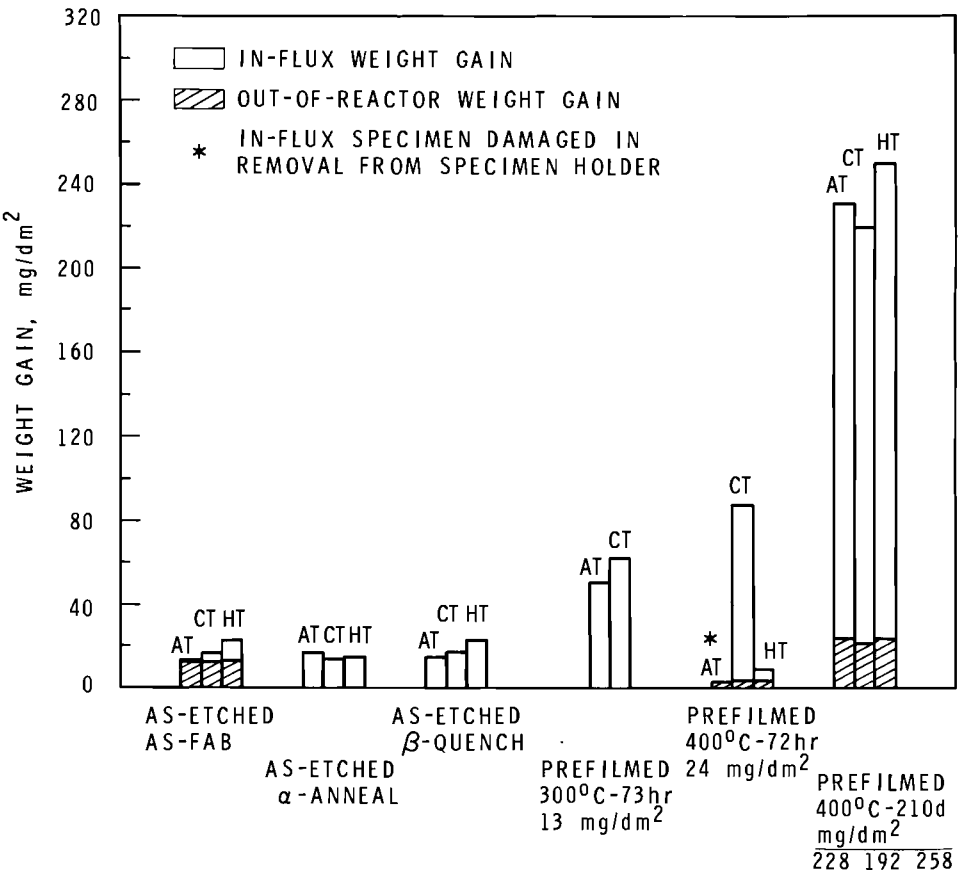

Neg 0680247-1

FIGURE 12.22. Heat Treatment and Prefilm Effects Exposure: G-7 Loop; pH-10 NH_4OH; 131 Days; 1 x 10^{21} n/cm² (>1 MeV) Est.

thick filmed specimens showed a "memory effect" in the transfer from 400 to 280 °C. A memory effect did occur for 400 °C thin film (72 hr) specimens; this agrees with the observations of Kass[17] that the memory effect occurs only on specimens with posttransition oxides.

The high rates on the 400 °C thick-film specimens suggest that the high rates on the in-reactor specimens transferred from pH-10 LiOH to pH-10 NH_4OH were probably due to the thick films on the specimens at the time of transfer.

The adverse effect of prefilming on in-reactor corrosion in pH-10 NH_4OH agrees with previous G-7 loop results.[18] The explanation for the accelerated corrosion on transferred and prefilmed specimens may involve the generation of local chemistry effects in the oxides.[19] The thick, porous oxides appear to promote the generation and/or entrapment of oxidizing species.

Weight gains are compared in Table 12.12 as a function of G-7 loop environment for specimens with the same prefilm treatment (300 °C) and fluence (~1 x 10^{21} n/cm², >1 MeV).

TABLE 12.12. In-Flux Weight Gains in the G-7 Loop

Alloy Lot	pH-10 LiOH, ∿1 ppm O_2	pH-10 NH_4OH, <0.05 ppm O_2
AT	250	50
CT	350	62
HT	225	-

The higher corrosion rates in the lithiated system are probably not caused by the lithium content of the coolant. There is evidence[18-22] that dissolved oxygen in the coolant increases the in-flux corrosion rate. Comparative experiments at ∿1 ppm and <0.05 ppm O_2 are planned to test the oxygen hypothesis. The experiments will be conducted in the north loop of the Advanced Test Reactor.

Hydrogen absorption is compared in Table 12.13 as a function of Zircaloy-2 lot, surface pretreatment, heat treatment and G-7 loop environment.

In the pH-10 NH_4OH environment, lot effects are not pronounced although they were significant in the pH-10 LiOH environment. Hydrogen pickups were higher for specimens prefilmed at 400 °C than for corresponding as-etched specimens and specimens prefilmed at 300 °C. However, the thick out-of-reactor film promoted a remarkable increase in the in-reactor hydriding rate, corresponding to a pickup of nearly 100% of the hydrogen generated by in-reactor corrosion of the specimen. Transfer of specimens from the lithiated to the ammoniated G-7 loop environment also resulted in a substantial increase in hydrogen absorption for the three lots of Zircaloy-2.[16] Entrapment of hydrogen from the hydrogen-rich ammoniated coolant in the thick, porous oxides offers the most likely explanation for the observed hydrogen absorption characteristics of the thick-film specimens.

TABLE 12.13. Zircaloy-2 Hydrogen Absorption in the ETR G-7 Loop

		In-Flux Hydrogen Absorption					
		pH-10 NH_4OH			pH-10 LiOH		
Lot	Specimen Condition	ppm	mg/dm^2	%	ppm	mg/dm^2	%
HT	As-Etched, As-Fabricated	24	1.5	51			
HT	As-Etched, β Quenched	15	0.9	31			
HT	Prefilmed, 400 °C, 72 hr	49	3.1	(a)			
HT	Prefilmed, 400 °C, 210 days	501	30.1	97			
AT	Prefilmed, 400 °C, 72 hr	28	1.7	(a)			
AT	Prefilmed, 300 °C, 73 hr	14	0.9	14	46	2.8	10
CT	Prefilmed, 300 °C, 73 hr	12	0.8	10	23	1.4	4

(a) *Weight gain not available.*

FAST REACTOR SUPPORTING STUDIES

FAST NEUTRON MECHANISMS

R. P. Allen

The objective of this program is to determine the effects of fast neutron irradiation and in-core environmental and service conditions on fundamental aspects of hydrogen and helium behavior in fast reactor alloys. Special nonsteady-state gas permeation and evolution techniques are currently being developed and used to investigate the effects of irradiation, composition, deformation, stress gradients, phase instabilities, surface condition, and desorption environment on the normal hydrogen diffusion, occlusion, and effusion characteristics of the austenitic stainless steels.

In a previous quarterly progress report,[5] a nonsteady-state gas permeation technique was described that is quite valuable for simultaneously determining equilibrium hydrogen solubilities and diffusivities at a constant temperature. From these data, inferences can be drawn regarding the trapping of hydrogen atoms at defect sites in the metal lattice. The method is such that it is readily suited to use for in-pile measurements. However, because of the special fabrication required, the thin, disc-shaped, membrane used for the measurements is not optimum for screening tests. Consequently, other techniques, which can use small pieces cut from irradiated tensile specimens or other irradiated hardware, are being developed for screening tests. These are discussed in the following sections.

Isothermal Gas Evolution Techniques

Gas evolution or "hot vacuum extraction" techniques can be used to determine hydrogen solubilities, diffusivities, and departures from normal behavior occasioned by anomalous hydrogen interactions.[23] For diffusivity determinations, hydrogen-containing material is heated to a suitable temperature either in a vacuum or at a constant hydrogen pressure, with the resulting hydrogen effusion rate measured as a function of extraction time. Diffusion coefficients can be calculated directly from these isothermal rate data by use of the appropriate differential solution of Fick's second law of diffusion for the particular sample geometry employed. Exceptional care must be exercised, however, to ensure that the apparent diffusivities determined actually reflect matrix diffusion and not a rate limiting surface process or other experimental artifact.[24]

Isothermal evolution techniques have also been specifically adapted to study the effects of surface condition and desorption environment on the kinetics and mechanisms of the hydrogen effusion process as it relates to the removal of neutronically-generated hydrogen from fast reactor core materials.

The sample geometry used for this technique must be one for which appropriate boundary conditions to Fick's

law can be specified. Since almost any regular shape will meet these conditions, irradiated specimens can be recovered from unrelated experiments (i.e. discs cut from the grip section of irradiated tensile specimens) without need for a special irradiation experiment.

Equilibrium hydrogen solubility values are obtained by (1) equilibrating specimens with hydrogen under carefully controlled temperature and pressure conditions, followed by rapid quenching to preserve the equilibrium gas content, and (2) extracting and measuring the dissolved hydrogen. Phase boundary of other rate-affecting kinetic processes are important only insofar as they prevent the attainment of equilibrium during the hydrogen saturation period. The only requirement for the extraction step is that the total gas content be accurately determined. This method of obtaining hydrogen solubilities is capable of high sensitivity and has a number of inherent advantages over the more common Sieverts method, especially where small samples or low gas contents are involved.[25] The sample geometry employed is unimportant in this method of determining solubility. Any shape of specimen can be used.

Nonisothermal Gas Evolution Techniques

The initial emphasis has been on the development and evaluation of nonisothermal vacuum effusion techniques where the sample is heated at a constant rate and the effusion flux is concurrently determined as a function of both temperature and extraction time. The primary advantage of this approach is that it provides a simple, rapid means of determining the qualitative effects of various material and environmental conditions and variables on the combined hydrogen diffusion, occlusion, and effusion characteristics of materials over an extended temperature interval. Therefore, the results serve to identify those particular effects and temperature ranges that merit further investigation by use of other and more quantitative-permeation and isothermal-effusion methods.

The types of effusion rate versus temperature curves generated during typical nonisothermal effusion experiments are illustrated in Figures 12.23 and 12.24 for a set of polished discoid specimens, thermally-charged with deuterium and degassed under identical conditions. The effusion flux was measured directly with a mass spectrometer type leak detector (CEC 27-120B) modified for hydrogen and deuterium service. The use of deuterium rather than hydrogen eliminated background problems at the higher extraction temperatures.

Figure 12.23 compares the nonisothermal deuterium effusion characteristics of annealed AISI types 316 and 348 SS. Neither curve is representative of a simple, matrix-diffusion controlled gas evolution process, and both show distinct, temperature-sensitive effusion stages. Although the particular mechanisms involved have not yet

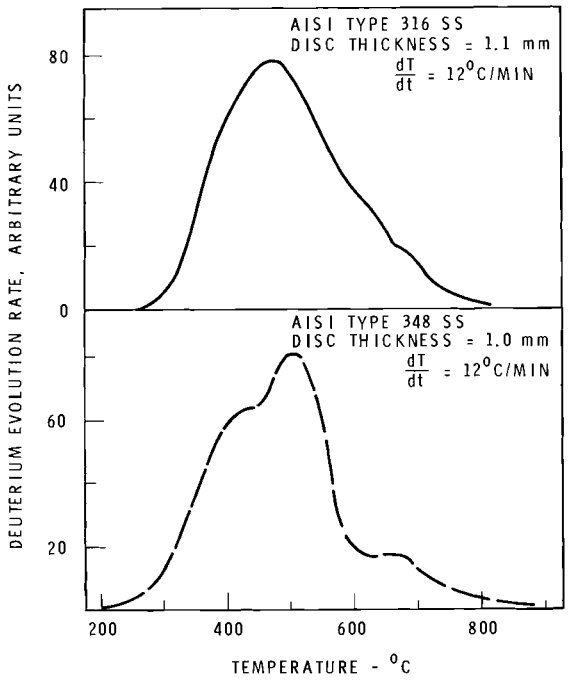

Neg 0680793-2

FIGURE 12.23. Characteristic Deuterium Effusion Curves for AISI Types 316 and 348 SS

been identified, the data illustrate both the significant effect that small differences in alloy composition can have on hydrogen behavior and the extreme sensitivity of the nonisothermal effusion technique to these differences.

Figure 12.24 similarly shows the effect of room temperature deformation on the nonisothermal deuterium effusion characteristics of AISI 348 SS. Hydrogen evolution appears to be enhanced rather than retarded by the deformation treatment, and the higher temperature maxima of the annealed state are eliminated or obscured. Here also, permeation and isothermal effusion studies are required to completely clarify the observed behavior, but the nonisothermal approach has

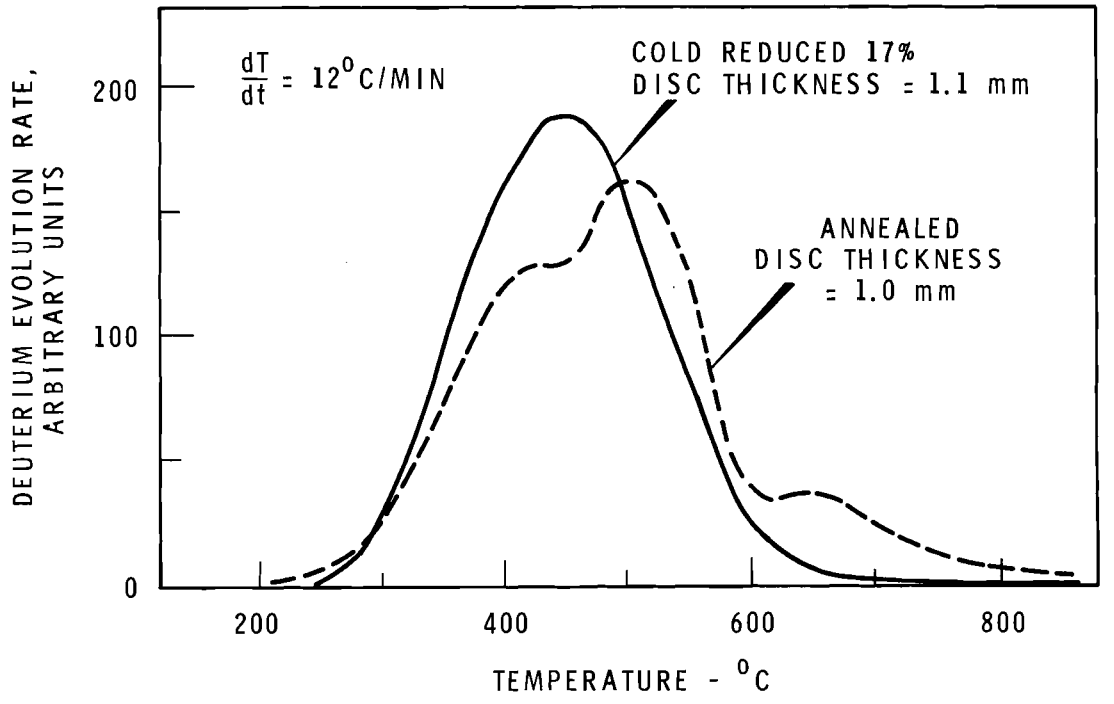

Neg 0680793-4

FIGURE 12.24. Effect of Postcharging Cold Deformation on the Deuterium Effusion Characteristics of AISI Type 348 SS

served to both disclose the effect and reveal its essential characteristics.

EBR-II IRRADIATIONS

J. J. Holmes and R. E. Robbins

The objective of this program is to determine the combined effects of environment and fast-reactor irradiation on the mechanical and physical properties of candidate fast-reactor cladding and structural alloys. The current program is specifically directed at providing a basis for selection of optimum alloys for FFTF applications and at providing a description of material behavior in fast-reactor service.

Recent studies[26-27] have shown that irradiation of austenitic stainless steel in a fast reactor at temperatures near one-half the absolute melting temperatures creates large numbers of internal voids. The density and size of these voids are sufficient to cause as much as 7% volume change. Since the measured volume changes appear to approach the order of magnitude of 10%, this swelling effect is of major engineering significance to FFTF design. Unfortunately, the current swelling data are too fragmentary to allow the relationship between fluence, temperature, and swelling to be deduced. Consequently, PNL has initiated a study to develop the swelling information required to provide a complete and detached description of swelling in the range of temperatures, times, and fluence appropriate to the FFTF.

Both, actual density measurements and void counting utilizing the electron microscope, are being used at PNL to map out the swelling characteristics of both 304 and 316 SS. Since the swelling problem was not anticipated prior to the insertion of current EBR-II irradiation experiments, no well-planned group of controlled density specimens is available for examination. Specimens for density determination must come from mechanical test specimens, capsule parts, and various EBR-II components as they become available.

Density measurements have been made on the following:

A) One-fourth inch sections taken from an irradiation capsule irradiated to 2 x 10^{22}* n/cm^2 peak fluence. The 1/4 in. sections were cut as various positions along the capsule to investigate temperatures and fluence variations along the capsule (700 to 800 °F).
B) One inch sections taken from an irradiation capsule used for a cermet fuel irradiation (Pin 5-P-9), (700 to 840 °F).
C) A tensile specimen irradiated at 1000 °F ± 100 °F to 2 x 10^{22} n/cm^2.

All the above items are in the annealed condition. Items A and B are 304L while Item C is 304.

The mean density on the unirradiated tensile material was 7.927 ± 0.003 g/cm^3, where the limits given refer to the 95% confidence limit. After irradiation, the density of Item A was found to be 7.913 ± 0.004

---

* *EBR-II estimated*

g/cm^3. The difference between these two mean values is 0.014 ± 0.007 g/cm^3. In this case, the density decrease may be caused by irradiation damage or by surface effects in the irradiated samples that are not present in the control. The irradiated specimens were exposed in flowing sodium for 156 days while the control tube was not. This sodium exposure may have changed the surface chemistry sufficiently to cause the observed density change. In addition, the control tube may have slightly different initial chemistry than the irradiated material.

Results from the 2.8 x 10^{22} n/cm^2 capsule (Item B) indicate a maximum decrease in density of 0.34%, the actual measured density being 7.898 g/cm^2. In this latter capsule, the change in density corresponds to the fluence and temperature along the capsule; for this reason it appears to be unambiguously caused by irradiation damage. Density measurements on Item C reveal a 0.24% decrease in density.

A summary of current swelling data from PNL and other laboratories is given in Table 12.14. An inspection of this table reveals the absence of data for 304 SS at high exposures at temperature above 1000 °F and the lack of data for 316 at the lower exposures and temperatures above 1040 °F. Efforts are in progress to obtain an EBR-II control rod thimble (304L) that has reached about 4.5 x 10^{22} total fluence. This thimble will allow swelling determination on 304 SS irradiated in the temperature range of 700 to 800 °F. In addition, GE-APO has agreed to supply PNL with 304 SS specimens irradiated in the EBR-II to fluence

TABLE 12.14. Summary of Stainless Steel Density Data

Source	Material	Irradiated Temperature	Condition	Fluence	$\frac{\Delta V}{V}$, %	Density	Method
PNL, Tensile Spec.	304	1000 ± 100 °F	Ann	1.9 x 10^{22}	0.24		D
Capsule A	304L	750 ± 50 °F	Ann	1.7 x 10^{22}	0.14	7.913 ± 0.003	D
Capsule B (5-P-9)	304L	760	Ann	2.3 x 10^{22}	0.13	7.916 ± 0.002	D
	304L	786	Ann	2.7 x 10^{22}	0.27	7.904 ± 0.002	D
	304L	819	Ann	2.7 x 10^{22}	0.33	7.900 ± 0.001	D
	304L	840	Ann	1.7 x 10^{22}	0.34	7.898 ± 0.002	D
	304L	844	Ann	1.2 x 10^{22}	0.13	7.917 ± 0.002	D
ORNL, EBR Driver Fuel[28]	304L	698	Ann	0.8 x 10^{22}	0.07		EM
		752	Ann	1.2 x 10^{22}	0.15		EM
		806	Ann	1.4 x 10^{22}	0.17		EM
		852	Ann	1.3 x 10^{22}	0.16		EM
		881	Ann	0.9 x 10^{22}	0.08		EM
Dounreay[26]	AISI 316	842	Ann	5.2 x 10^{22}	0.8		EM
		950	Ann	4.5 x 10^{22}	1.5		EM
		1040	Ann	3.2 x 10^{22}	0.2		EM
		932	Ann	7.8 x 10^{22}	6.8		EM, D

levels of from 1 x 10^{22} to 2.5 x 10^{22} at temperatures from 700 °F to 1200 °F. It is anticipated that studies on the thimble and GE-APO specimens will allow a rudimentary description of swelling as a function of fluence and temperature to be given.

Aging furnaces have been installed and are operating to provide a facility for obtaining control (unirradiated) specimens for EBR-II irradiations. The facility will also be used to carry out a program for determining the effect of aging time and temperature on the microstructure and tensile, uniaxial stress-rupture, and biaxial stress-rupture, properties of AISI Types 304 and 316 SS. All aging will be performed in sodium at temperatures of 800, 900, 1000, 1100, 1200, and 1400 °F for times of 20, 200, 2160, 6480, and 12960 hr. The last three aging times are not firm because they will depend on the in-reactor time of the subassemblies in the EBR-II irradiation program.

Ten EBR-II fuel jackets, without the fuel elements, have been received from ANL for evaluation. The irradiation temperature profiles of the jackets range from 740 to 945 °F, and the range of estimated cladding fluences is from about 0.92 to 1.32 x 10^{22} n/cm^2. Density measurements and biaxial stress rupture tests will be performed on selected sections from the jackets. Testing will be performed at 1100 and 1200 °F for rupture times of 10, 100, and 1000 hr.

FUEL CLADDING CHARACTERIZATION

M. M. Paxton and J. A. Yount

The purpose of this program is to determine the lot-to-lot variation in two lots of AISI 304 SS, seamless tubing 0.250 in. OD x 0.016 in. wall, that will be used in future fuel pin experiments.

The testing program as presented previously[5] is progressing smoothly. The chemical analyses of tubing Lots "E" and "F" have been completed by Lukens Steel Company. The analyses (Table 12.15) agree with those provided by the manufacturer.

The metallographic examination of the as-received tubing has been completed. Tubing Lot "E" has undergone intergranular attack on the OD surface. The reason for this attack is unknown. Both "E" and "F" lots were purchased under the same specifications; however, tubing Lot "E" has a grain size approximately ASTM #6; whereas, Lot "F" has a grain size approximately ASTM #10. In addition, Lot "F" contains 5 to 7 times more nonmetallic inclusion as Lot "E". Fabrication histories are being obtained from the manufacturers to

TABLE 12.15. Chemical Composition

	C	Mn	P	S	Si	Ni	Cr	N_2
Lot "E"	0.056	1.73	0.038	0.011	0.47	9.90	18.50	0.10
Lot "F"	0.052	1.72	0.024	0.013	0.48	9.21	18.75	0.057

help establish the cause for these differences. Typical photomicrographs are shown in Figure 12.25.

Room temperature uniaxial tension tests on full size tubular sections have been completed for Lots "E" and "F", and the results are summarized in Table 12.16.

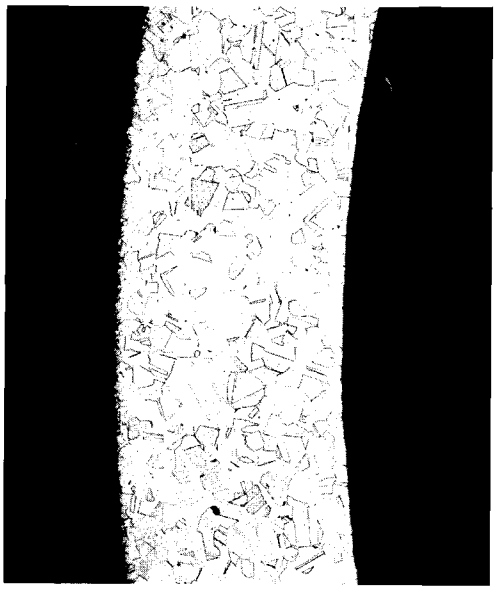

Neg 467-1724A *80X*

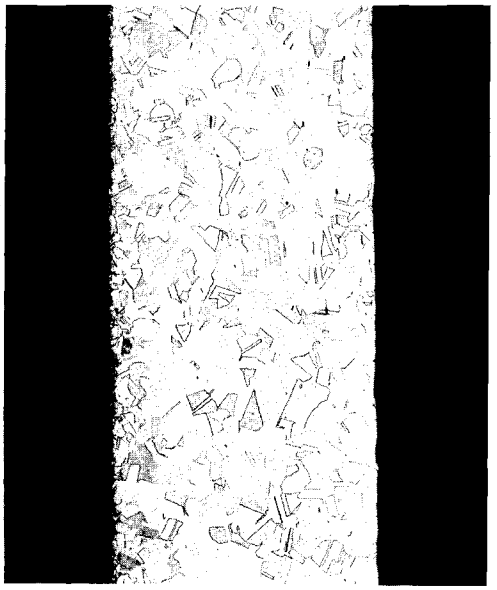

Neg 467-1725A *80X*

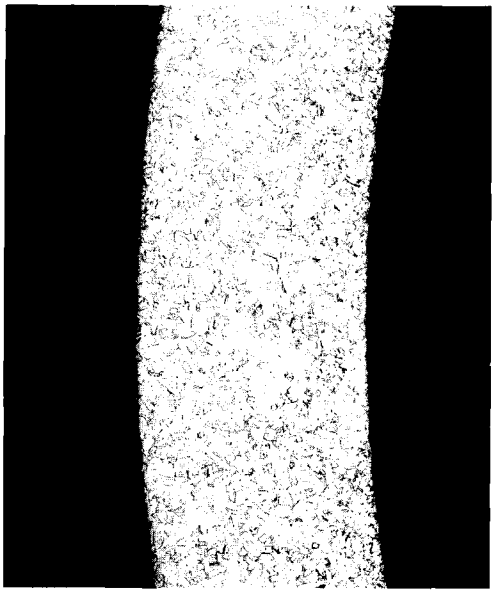

Neg 467-1753A *80X*

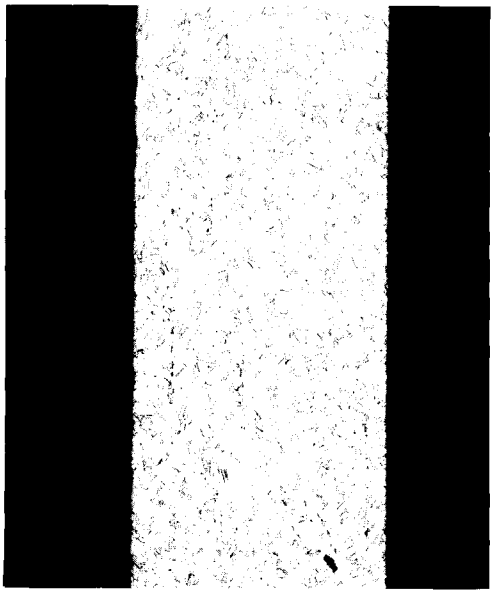

Neg 467-1755A *80X*

FIGURE 12.25. A Comparison of Microstructure of Tubing Lot "E" (Top) and Tubing Lot "F" (Bottom) Type 304 SS Fuel Cladding

TABLE 12.16. Tensile Properties of Tubing Lots "E" and "F" at Room Temperature

Spec. No.	0.2% YS, ksi	UTS, ksi	UE, %	Total Elongation, %
1E	41.36	95.34	68.05	87.69
2E	44.49	102.54	65.00	84.46
3E	43.64	99.58	69.99	91.06
1F	49.32	104.66	65.74	82.80
2F	46.61	102.80	68.62	79.23
3F	48.73	104.66	66.27	81.03

Room temperature burst tests have been completed on "E" tubing only (Table 12.17). Burst test at 1800 °F have been completed on defective and nondefective specimens from Lots "E" and "F". Specimens are classified defective if there is a surface defect more than one mil deep, as determined by NDT methods. The data are summarized in Table 12.17.

The presence of a defect apparently has no effect on burst strength at 1800 °F. Some defective specimens ruptured in the defect zone and others did not.

TABLE 12.17. Burst Data for Defective and Nondefective "E" and "F" Tubing

Tube Lot	Test Temp	Burst Pressure, psi	Hoop Stress, psi	Measurable Post OD
E	RT	10,700	72,870	0.300
		10,700	72,870	0.305
		10,700	72,870	0.298
		10,800	73,550	0.304
		10,800	73,550	0.305
E	1800 °F	1,365	9,296	--
		1,390	9,465	0.316
		1,395	9,500	0.303
		1,410	9,620	0.305
		1,450	9,865	0.294
E (Defective)	1800 °F	1,375	9,365	0.327
		1,380	9,400	0.321
		1,385	9,435	0.325
		1,420	9,670	0.305
		1,425	9,705	0.315
		1,440	9,805	0.303
F	1800 °F	1,170	7,968	0.305
		1,180	8,036	0.292
		1,185	8,070	0.315
		1,225	8,342	0.314
		1,180	8,036	0.317
F (Defective)	1800 °F	1,275	8,660	0.295
		1,150	7,832	0.295
		1,195	8,138	0.310
		1,150	7,832	0.317
		1,200	8,172	0.292

To accommodate the vast characterization program previously outlined,[5] it has been necessary to further modify the CANEL test stands with a resultant increase in testing capability. The plan remains to make full utilization of the CANEL biaxial test stands. However, close inspection of those frames has shown certain parts damaged and others missing entirely. Instead, it was decided to substitute six $167 Skutt ceramic kilns, each operating at one of six test temperatures. Each furnace is controlled by the same instrument configuration that was supplied with the CANEL test frames, but due to the increase in furnace size, eight specimen retorts may be installed per Skutt furnace instead of one per CANEL frame. The essential features are outlined as follows:

	CANEL	Skutt
Retorts	12	48
Specimens	48	384 (maximum)
		192 (normal
Furnaces Required	12 (6 available)	6
Recorder/Controllers Required	12 (6 available)	6
Temperature Profile	±5 °F/3.75 in.	±3 °F/6 + in.

The cost of purchasing all six Skutt kilns is roughly equivalent to replacing two of the original CANEL furnaces.

STRUCTURAL MATERIALS AND FUEL CLADDING STUDIES

R. W. Barker

The objective of this program is to determine the combined effects of environment and fast reactor irradiations on the mechanical properties of candidate fast-reactor cladding and structural alloys. The current program is specifically directed at providing a basis for selection of optimum alloys for FFTF applications and at providing a description of material behavior in fast-reactor service.

Pre- and postirradiation rupture properties will be determined on FFTF prototype fuel clad material (0.208 in. OD x 0.008 in. wall tubing). Types 304 and 316 SS are to be studied.

A limited quantity of unirradiated stress-to-rupture data for the type 304 SS has been developed for 1400 °F (760 °C) test temperature in a helium atmosphere. The condition of primary interest is the as-received condition, containing a slight degree of cold work from the final fabrication step. The as-received material has been tested at stresses sufficient to cause rupture in 0.1 to 139 hr (Figure 12.26). Identical material, annealed at 1950 °F (1066 °C) for 30 min in vacuum, has been tested at stresses sufficient to cause rupture in 0.2 to 78 hr. Ten additional tests on annealed type 304 SS, report previously,[29] were stressed at 10,000 psi at 1400 °F (760 °C), with failure occurring in all 10 tests in 88 to 120 hr. These data, however, are not recorded on the accompanying plots. The data clearly establish the tendency of the as-received and annealed curves to merge at rupture times of about 100 hr. The annealed stress-to-rupture curve indicates that the material is representative of typical type 304 SS, with respect to rupture stress and rupture times.

It can be observed in Figure 12.27 that the rupture strain for the annealed material is significantly less than for the as-received material of those specimens exhibiting intergranular failure. The same phenomena is observed in the room temperature tensile values (Table 12.18) where the as-received material (slightly cold worked) possesses 50% greater ductility than the annealed material.

The decreased ductility of the annealed material has been attributed to the selective grain growth occurring during annealing of the only slightly cold-worked material. A comparison of the grain size of the two conditions is shown in Figure 12.28. (Note, in the annealed material, bands of fine grains are adjacent to grains whose diameters are approximately equal to the wall thickness.)

Posttest comparisons of grain size and microstructural characteristics with untested material can be made in Figure 12.29 (as-received condition) and in Figure 12.30 (annealed

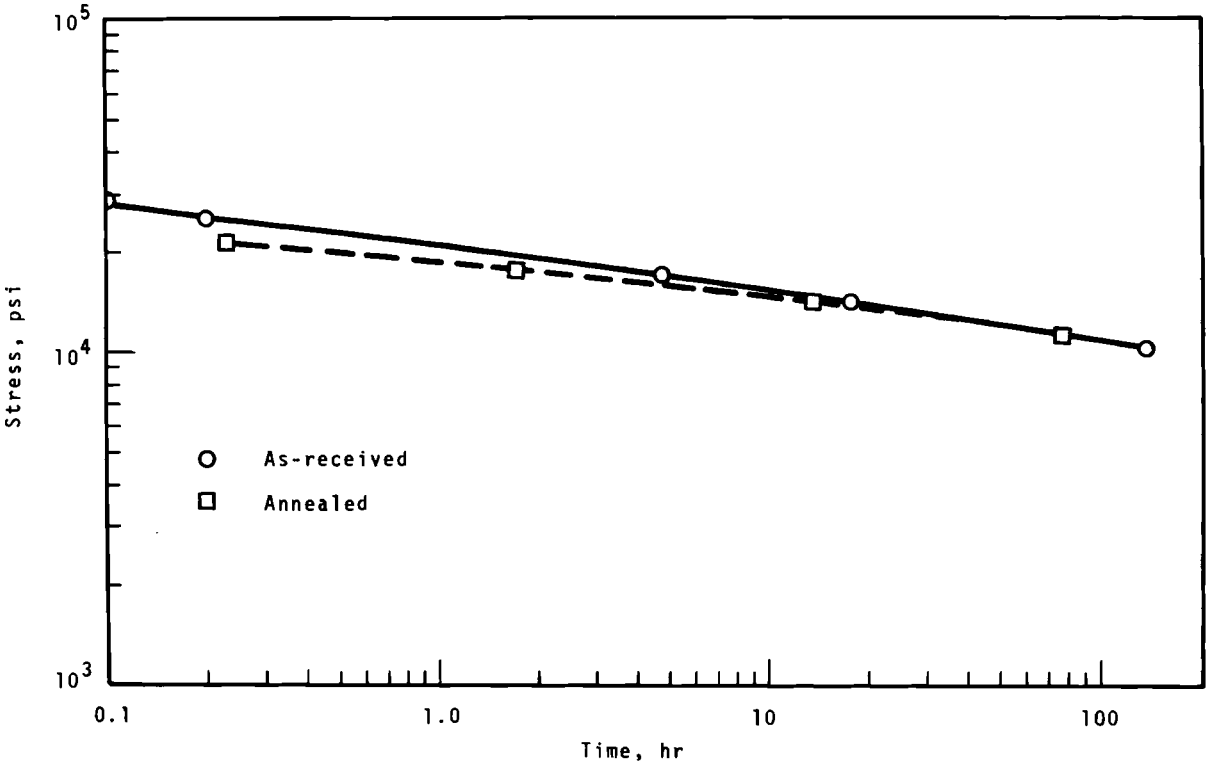

Neg 0680842-1

FIGURE 12.26. Stress to Rupture Properties of As-Received (slightly cold worked) and Annealed Type 304 SS Prototype FFTF Fuel Cladding

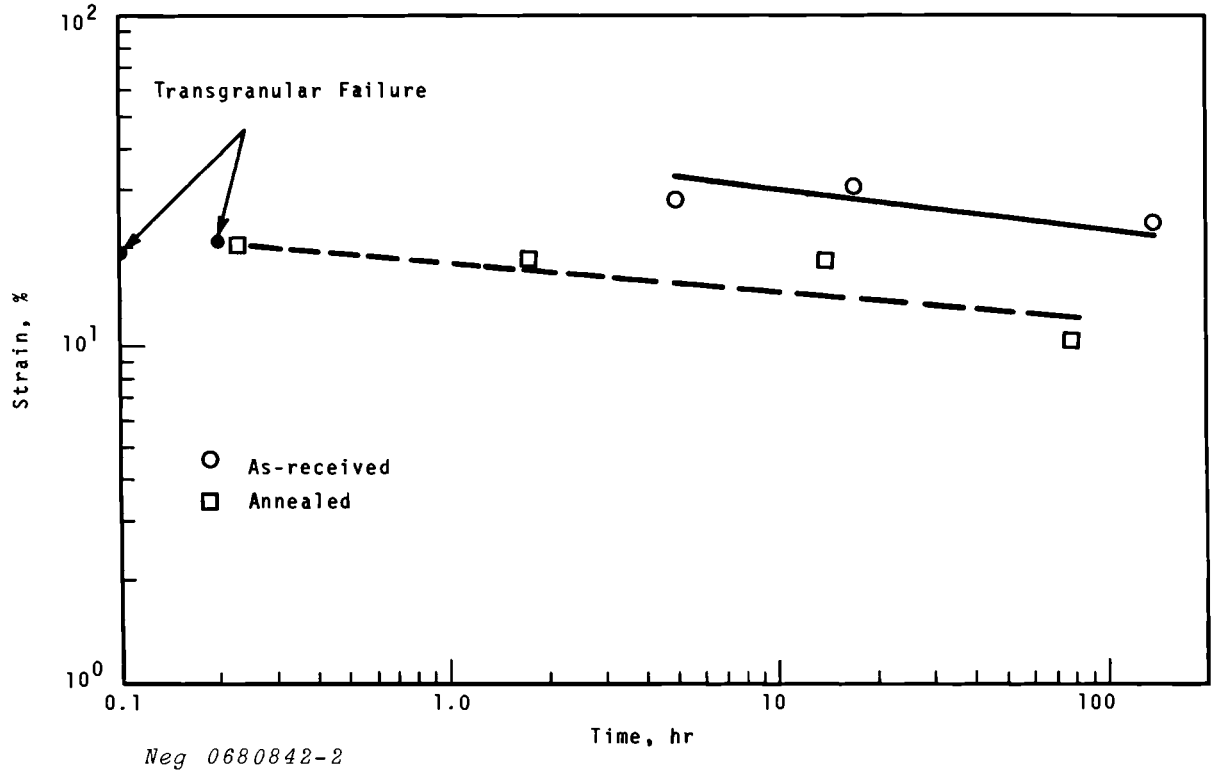

Neg 0680842-2

FIGURE 12.27. Rupture Strain of As-Received (slightly cold worked) and Annealed Type 304 SS Prototype FFTF Fuel Cladding

TABLE 12.18. Tensile Properties of As-Received and Annealed Type 304 SS Tubular Material, 0.208 in. OD x 0.008 in. Wall

Material	0.2% Yield Stress, psi	Ultimate Stress, psi	Uniform Elongation, %	Total Elongation, %
304 As Received	40,000	100,000	65	76
304 As Received	41,000	99,400	66	73
304 Annealed	35,800	89,000	43	52
304 Annealed	34,800	88,400	37	45

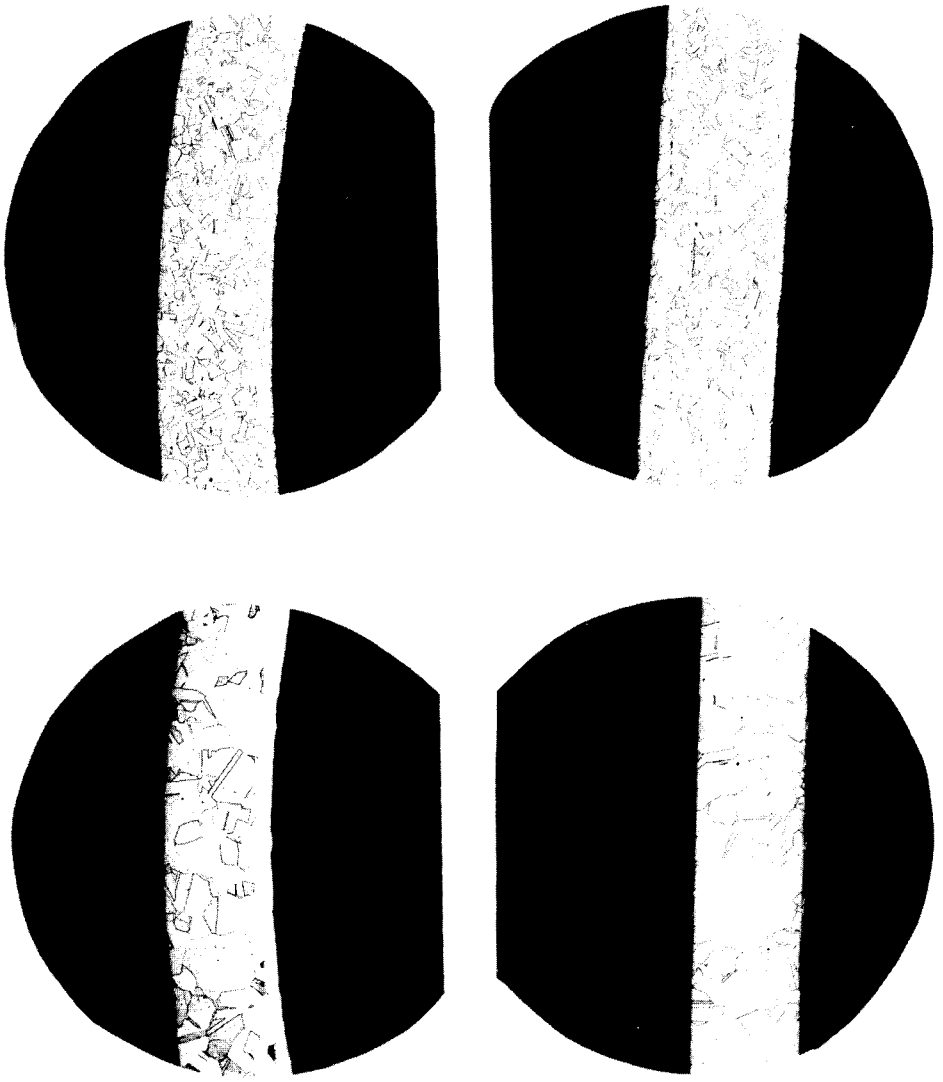

Neg 0680842-5

FIGURE 12.28. A Comparison of the Grain Size of the As-Received (Top) and Annealed (Bottom) Type 304 SS Fuel Cladding

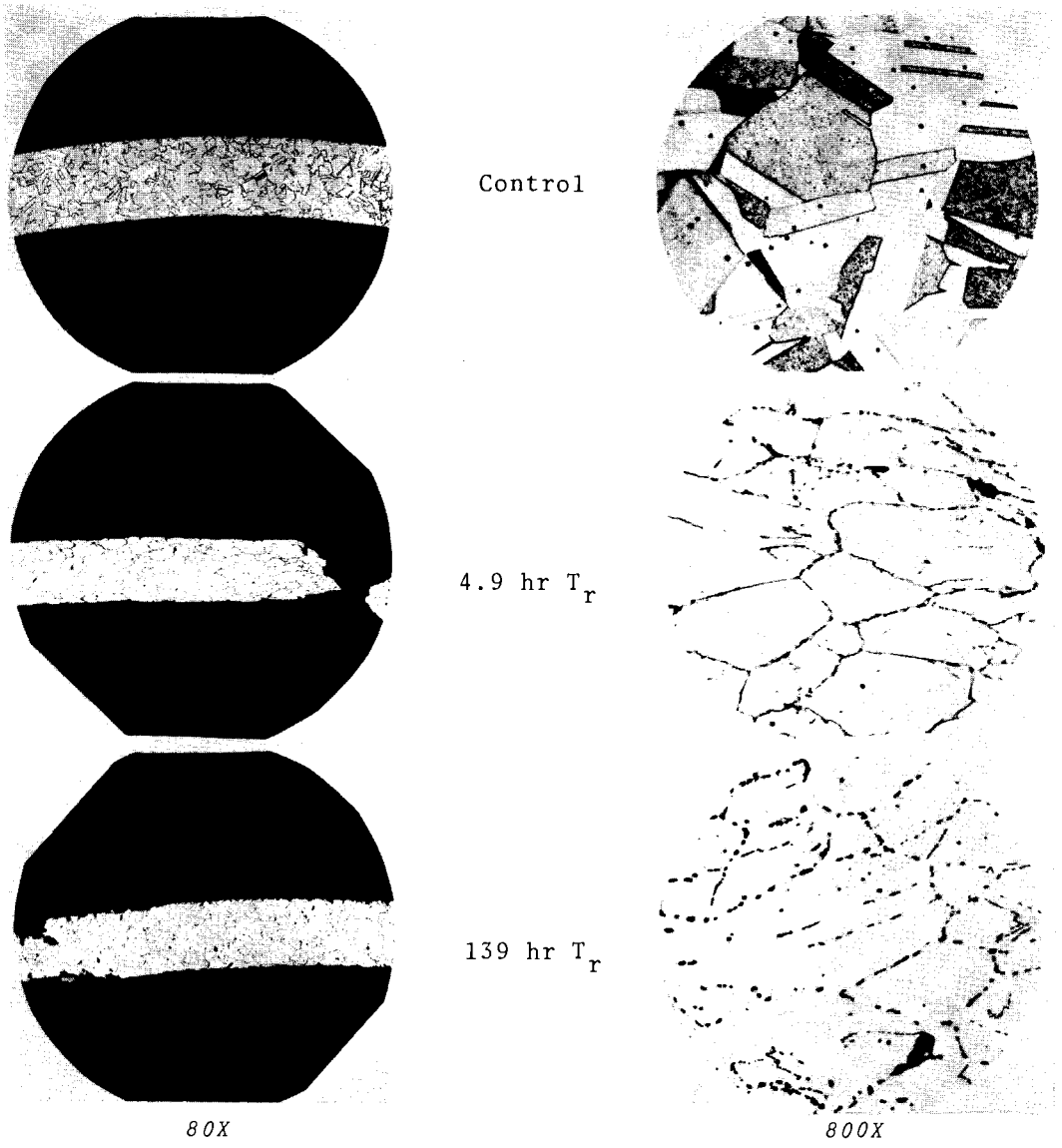

Neg 0680842-4

FIGURE 12.29. Grain Size and Microstructure of As-Received Type 304 SS Prototype Fuel Cladding in Untested Condition and After Rupture at 1400 °F (760 °C).

condition). The following general observations can be made for both material conditions.

- The growth of carbides increases with time-at-temperature. Cold work present in the as-received test material has had no observable effect on the size or location of the carbide precipitate.
- For the test times available, the nominal grain size remains unchanged throughout the test.

Further examination will proceed on these materials and on additional

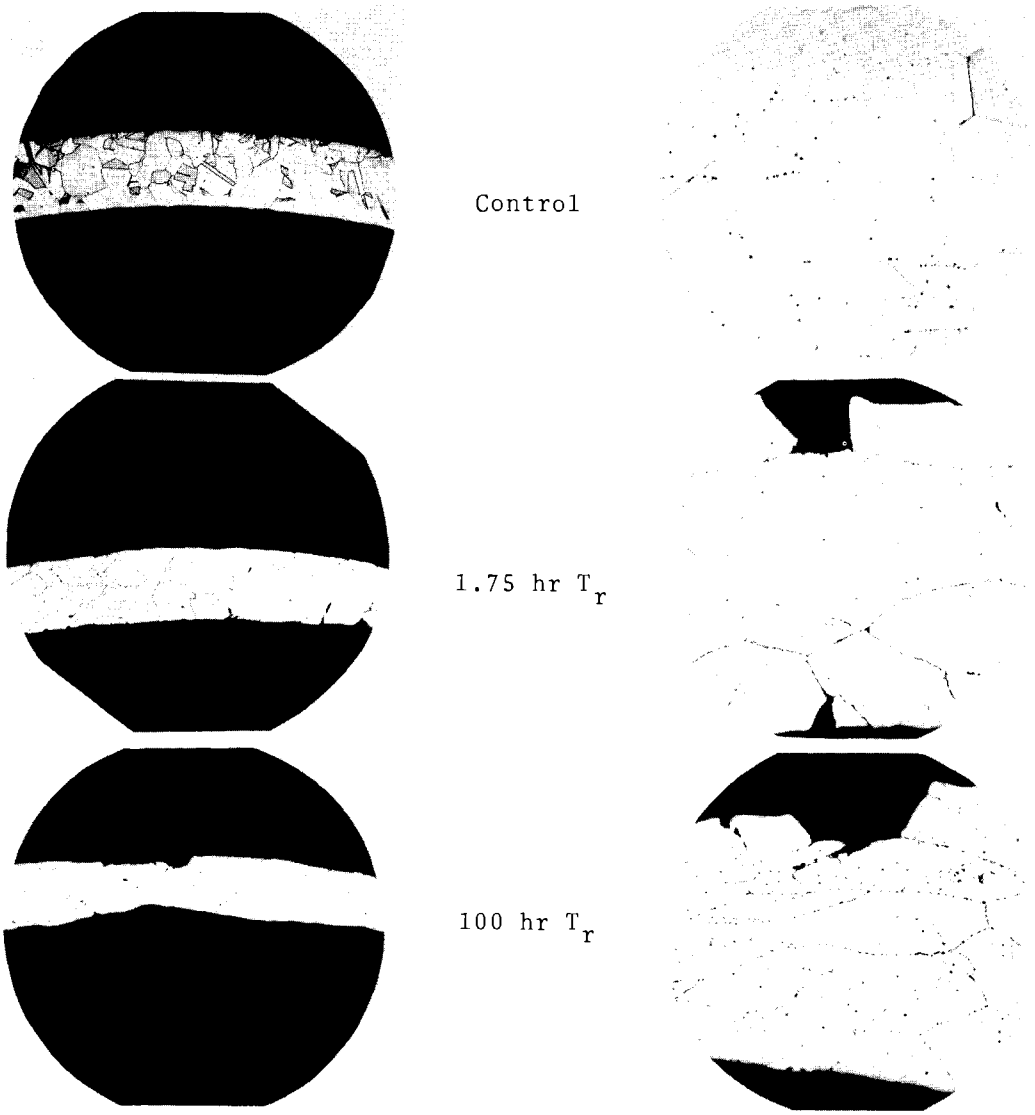

Neg 0680842-3

FIGURE 12.30. Grain Size and Microstructure of Annealed Type 304 SS Prototype Fuel Cladding in Untested Condition and After Rupture at 1400 °F (760 °C)

specimens as ruptured specimens become available.

Ultimately, stress-to-rupture testing will be performed to establish base curves for types 304 and 316 SS at temperatures of 1400, 1200, and 900 °F (760, 649, and 482 °C).

TEST FACILITIES

R. H. Todd

To comprehensively investigate the effects of irradiation and environment on candidate, structural and cladding materials for the FFTF, a

facility was needed that could provide the necessary test environments. Such facility for testing irradiated specimens in sodium and controlled gas atmospheres is now under construction, and as of March 1, 1968, was 85% complete. With construction 3% ahead of schedule, most of the remaining work involves installation of the heating and air conditioning equipment (due for delivery in March). The piping trenches will be covered with concrete which, after curing, will be covered with floor tile. Present plans call for the main transformer for this facility to be moved to a new location next to the building. Full power cannot be supplied to this facility until this move is made, so it is expected in the very near future.

Tests performed by the test stands, temporarily located in the mezzanine work shop, have given the following results in air environment (Table 12.19).

The complete analysis of these tests will be made by A. J. Lovell. The first of two test stands for static sodium environment has been aligned to provide uniaxial stress on the specimen with less than 10% bending moment. All parts of the machine had to be cleaned and realigned; also some parts of the sodium containment vessel had to be redesigned to meet the above specification. Although more stringent than the 15% limit prescribed by the ASTM specification for conducting creep and time-for-rupture tension tests of materials (ASTM E 139-66T), the 10% limit eliminates a great deal of scatter in the test results. A pair of short term tests will be run with type 304 SS to determine the proper stress level for a test of about 1000 hr duration at 650 °F (1202 °C). Emphasis will be placed on the long term tests, since the effect of sodium-versus-inert gas environment is nearly negligible in short term tests. As soon as the second static sodium test stand can meet testing standards, it also will be placed in service on this program.

Generally, the ASTM recommended practice for creep tests is a set of

TABLE 12.19. Creep Tests of Type 304 SS at 1200 °F in Air

Material	Prior History	Diameter, in.	Stress	Test Temp, °F	Hr to Rupture	Total Elongation, %
304 SS	20% Cold Worked Sol Treated 1 hr 1950 °F	0.160	25,000 psi	1202	113.9	54
304 SS	As-Received; Sol Treated 1 hr 1950 °F	0.125	25,000 psi	1202	60.3	45
304 SS	As-Received; Sol Treated 1 hr 1950 °F	0.125	22,000 psi	1202	625	41

operating rules that actual tests attempt to meet. Much useful data can be obtained without meeting the requirements of the ASTM specification, but such data have an inherent scatter difficult to deal with. Two of the most important parameters are the axiality of the applied stress and temperature control. The requirement for axiality of the applied stress (bending moment) is being exceeded in this laboratory as described above. The problem of temperature control has been solved with the invention of a furnace liner filled with sodium. The ASTM specification calls for a temperature uniformity of ±3 °F along the length of the specimen. The temperature profile of most furnaces make this condition very difficult to meet, and even more difficult to maintain for the duration of a test. The liner, placed in service here, is a tubular container made of stainless steel and filled with sodium. The liner fits inside the standard furnace and admits the specimen, grips, and pullrods through the ID of the liner. The liner and the specimen train do not touch one another. With suitable baffling and use of loose packing materials to restrict the flow of air through the channel, this new liner has reduced the temperature variation across a 2 in. specimen to less than 1 °F total variation. Operator time required to achieve temperature balance (in the region of 1200 °F) has been reduced to essentially zero. To date, the data from the two tests run with this liner show a definite reduction in the amount of scatter in the plot of creep data. Efforts are being made to provide each test furnace with a liner of this type as soon as possible.

The support section of the liquid metal loop has been assembled in working position with controllers and recorders attached. This section contains one unshielded test leg, along with the electromagnetic pumps and cold trap for circulating and purifying the sodium. Work on the supporting utilities progressed far enough to allow start-up of the sodium loop for operational acceptance tests and operator check-out. Some deficiencies were found, and these are now being corrected. Design work for the shielded test loops was completed, while design work on the radiation shield was begun in February. A date for start of construction on this portion of the sodium loop has not yet been set.

An inert atmosphere glove-box for handling high purity alkali metals has been built by Vacuum Atmospheres Corporation and will be shipped in March. This glove-box will provide a high-purity inert atmosphere with evacuable transfer port and a vacuum oven large enough to handle any of the alkali metal capsules or containers now in use on testing programs.

Recent experiments with the sodium filling apparatus with receiving vessels closed to air atmosphere have shown that helium does dissolve in liquid sodium. The solubility of helium is sufficient to cause bubbles to form when the sodium is exposed to vacuum. The possibility of the bubbles being formed by sodium vapor was considered, but sodium vapor pressure at the highest temperatures involved

(600 °F) would support a column of sodium less than 1 mm high; whereas, the observed effects require pressure to support a column of sodium several centimeters high. Special procedures for outgassing the helium from liquid sodium and for the removal of bubbles entrained in liquid sodium have been developed. Since the problem is of sufficient magnitude, if the special procedures are not followed, accurate measurements of sodium within closed vessels cannot be done reliably.

The vacuum manifold for the interior of the prototype cell has been completed and installed, but work in and around the prototype cell is still being held up by building construction. A prototypical testing unit, ready for installation in the cell and for attachment to the vacuum manifold, will be installed as soon as the building construction items are cleared up.

REFERENCES

1. *I. P. Bell, J. Standrig, P. C. L. Pfeil, G. H. Broomfield, K. Q. Bagley, and A. S. Fraser. "The Effects of Irradiation on the High Temperature Properties of Austenitic Steels and a Precipitation Hardened Nickel Alloy," 69th Annual Meeting of ASTM, Atlantic City, N. J., June 27-July 1, 1967.*

2. *F. A. Comprelli and J. E. Lewis. Microstructural Evaluation of Superheat Cladding Materials, GEAP 4751, General Electric Company, San Jose, California.*

3. *Interim Data Sheet, IN 102 Alloy, The International Nickel Co., Inc.*

4. *J. J. Cadwell, D. R. de Halas, R. E. Nightingale, and D. C. Worlton. Quarterly Progress Report, October, November, December, 1967, Reactor Fuels and Materials Branch of USAEC Division of Reactor Development and Technology, BNWL-668, Pacific Northwest Laboratory, Richland, Washington, March, 1968.*

5. *J. J. Cadwell, D. R. de Halas, R. E. Nightingale, and D. C. Worlton. Quarterly Progress Report, July, August, September, 1967, Reactor Fuels and Materials Branch of USAEC Division of Reactor Development and Technology, BNWL-658, Pacific Northwest Laboratory, Richland, Washington, February, 1968.*

6. *V. Fidleris and C. D. Williams. "In-Reactor Creep of Zircaloy-2," Electrochemical Technology, vol. 4 p. 258. 1966.*

7. *Quarterly Progress Report, Metallurgy Research Operation, October, November, December 1963, HW-79766, General Electric Company, Richland, Washington, p. 3.39. 1964.*

8. *G. T. Murray and H. Kuzuu. "Precipitation of Helium During Annealing of Cold-Worked and Irradiated Al-Li Alloy," Journal of Nuclear Materials, vol. 9, p. 107. 1963*

9. *F. J. Witt. "An Investigation of the Structural Reliability of Heavy Section Steels for Light-Water Reactor Pressure Vessel Applications," Inter American Conference on Material Technology, San Antonio, Texas, May, 1967.*

10. *L. F. Cochrun. Fracture Mechanics Evaluation of Reactor Vessel Steels Quarterly Progress Report for Period Ending September 30, 1967," WCAP-3677-5, Westinghouse Electric Corporation, Pittsburgh, Pennsylvania, 1967.*

11. *F. A. Smidt. "Dynamic Changes in the Internal Stress Fields of High Purity Iron," AIME Annual Meeting in New York February 26-29, 1968.*

12. *H. R. Brager. "Electron Microscopy of ETR-Irradiation Stainless Steel," Quarterly Report January, February, March 1968, BNWL-768, Pacific Northwest Laboratory, Richland, Washington, 1968.*

13. W. D. Wilkinson. Effects of Ga on Materials at Elevated Temperatures, ANL-5027, Argonne National Laboratory, Argonne, Illinois, 1953.

14. LeRoy Kelmen, W. D. Wilkinson, and F. L. Yaggee. Resistance of Materials to Attack by Liquid Metals, ANL-4417, Argonne National Laboratory, Argonne, Illinois, 1950.

15. G. L. Kulcinski. Design, Calibration, and Capabilities of Solid State Piston-Cylinder and 'Belt' Ultra High Pressure Equipment, BNWL-465, Pacific Northwest Laboratory, Richland, Washington, 1967.

16. A. B. Johnson, Jr. and J. E. Irvin. Radiation-Enhanced Oxidation of Zircaloy-2 in pH-10 LiOH and pH-10 NH_4OH, BNWL-463, Pacific Northwest Laboratory, Richland, Washington, July 1967.

17. S. Kass. "Corrosion of Prefilmed Zircaloy," Corrosion, vol. 23, No. 12, pp. 374-378. December, 1967.

18. A. B. Johnson, Jr. "In-Reactor Oxidation of Zirconium Alloys in pH-10 LiOH and pH-10 NH_4OH, 23rd Annual Meeting, National Association of Corrosion Engineers, BNWL-SA-822, Pacific Northwest Laboratory, Richland, Washington, March 16, 1967.

19. W. A. Burns. Effects of Fast Neutron Irradiation, Fabrication History and Water Oxygen on the Environmental Behavior of Zirconium Alloys, BNWL-88, Pacific Northwest Laboratory, Richland, Washington, August 1965.

20. B. Cox. AECL Experiments on the Corrosion of Zirconium Alloys Under Irradiation, AECL-2257, Chalk River Laboratory, Ontario, Canada, May, 1965.

21. J. E. Le Surf. "The Effect of Water Chemistry on the Oxidation of Zirconium Alloys Under Reactor Radiation," 23rd Annual Meeting National Association of Corrosion Engineers, Los Angeles, California, March 16, 1967.

22. R. J. Davis, T. H. Mauney and R. J. Hart. "Corrosion of Zircaloy-2 by Hydrogen Peroxide at Elevated Temperature," J. Electrochem. Soc., vol. 113, No. 11 pp. 1222-23. November 1966.

23. M. L. Hill and E. W. Johnson. "Hydrogen in Cold Worked Iron-Carbon Alloys and the Mechanism of Hydrogen Embrittlement," Trans. Met. Soc. AIME, vol. 215, p. 717. 1959.

24. D. C. Carmichael, J. R. Hornaday, A. E. Morris, and N. A. Parlee. "The Absorption and Effusion of Hydrogen in Alpha Iron," Trans. Met. Soc. AIME, vol. 218, p. 826. 1960.

25. C. L. Thomas. "Solubility of Hydrogen in Solid Copper, Silver, and Gold Obtained by A Rapid Quench and Extraction Technique," Trans. Met. Soc. AIME, vol. 239, p. 485. 1967.

26. C. Cawthorne, E. J. Fulton. "Voids in Irradiated Stainless Steel," Nature, vol. 216, p. 575. 1967.

27. J. J. Holmes, R. E. Robbins, J. L. Brimhall, and B. Mastel. Elevated Temperature Irradiation Hardening in Austenitic Stainless Steel BNWL-SA-1318, Pacific Northwest Laboratory, Richland, Washington, October, 1967.

28. E. E. Bloom. Unpublished Data, ORNL personal communication.

29. F. W. Albaugh, S. H. Bush, J. J. Cadwell, D. R. de Halas, and D. C. Worlton. Quarterly Progress Report, October, November, December, 1966, Reactor Fuels and Materials Branch of USAEC Division of Reactor Development and Technology, BNWL-CC-957. Pacific Northwest Laboratory, Richland, Washington, January, 1967.

DISTRIBUTION

No. of Copies		No. of Copies	
5	Argonne National Laboratory F. Foote L. R. Kelman J. H. Kittel M. V. Nevitt P. Shewmon	2	Battelle Memorial Institute D. Keller S. Paprocki
		1	Bettis Atomic Power Laboratory E. J. Kreh
3	AEC Division of Technical Information Extension	2	Brookhaven National Laboratory Research Library 25 Brookhaven Avenue Upton, New York 11973 D. H. Gurinsky C. Klamut
4	AEC RDT Site Representative PNL P. G. Holsted (2) L. R. Lucas A. D. Toth	1	Bureau of Mines, Albany H. Kato
15	AEC Library, Washington Reactor Development and Technology G. W. Cunningham G. K. Dicker D. Erb J. Hunter R. E. Pahler R. C. Schwenk J. M. Simmons (2) S. A. Szawlewicz A. Van Echo C. E. Weber G. W. Wensch M. J. Whitman Division of Naval Reactors R. H. Steele Division of Research D. K. Stevens	2	Combustion Engineering, Inc. S. Christopher W. Chernock
		1	General Atomics J. F. Watson
		2	General Electric Company, Cincinnati V. P. Calkins J. Moteff
		3	General Electric, San Jose R. N. Duncan A. Klepfer R. B. Richards
1	AEC Richland Operations Office C. L. Robinson	1	General Electric Company, Pleasanton L. P. Bupp
2	AEC Chicago Patent Group G. H. Lee R. K. Sharp (Richland)	1	IIT Research Institute R. Van Thyne
		2	Knolls Atomic Power Laboratory N. W. Cayey Document Library
3	Ames Laboratory O. N. Carlson W. L. Larsen M. Smutz	1	Lawrence Radiation Laboratory, Berkeley L. Brewer
1	Atomics International S. Carniglia	2	Lawrence Radiation Laboratory, Livermore J. S. Kane A. J. Rothman
2	Babcock and Wilcox Company C. Baroch J. H. MacMillan		

No. of Copies		
2	Los Alamos Scientific Laboratory	R. D. Baker D. B. Hall
1	Mound Laboratory	R. G. Grove
1	National Reactor Testing Station (INC)	W. C. Francis
1	NASA, Lewis Research Center	J. J. Lambardo
2	Naval Research Laboratory	J. R. Hawthorne L. E. Steele
2	North Carolina University	J. Beehler R. E. Dahl
9	Oak Ridge National Laboratory	G. M. Adamson J. E. Cunningham J. H. Frye, Jr. D. B. Lloyd C. J. McHargue P. Patriarca O. Sisman M. S. Wechsler J. R. Weir
2	Ohio State University Dept. of Metallurgy Columbus, Ohio 43212	M. G. Fontana R. W. Staehle
1	Rensselaer Polytechnic Institute Department of Materials Engineering Troy, New York	C. B. Willingham, Jr.
2	Sandia Corporation, Albuquerque	R. P. Stromberg J. Jacobs
3	Westinghourse Atomic Power Division, Pittsburgh	R. J. Allio P. Cohen E. Landerman
2	Westinghouse Bettis Atomic Power Laboratory, West Mifflin	Document Library E. J. Kreh
2	Westinghouse Electric Corporation	R. J. Allio R. E. Olson
73	Battelle-Northwest	F. W. Albaugh H. J. Anderson E. R. Astley J. M. Batch J. L. Bates A. L. Bement C. A. Bennett T. K. Beirlein S. H. Bush J. J. Cadwell T. D. Chikalla J. A. Christensen T. T. Claudson P. D. Cohn J. L. Daniel F. G. Dawson D. R. de Halas R. L. Dillon D. G. Doran K. Drumheller E. A. Eschbach E. A. Evans P. L. Farnsworth J. J. Fuquay R. L. Gibby S. Goldsmith W. L. Hampson L. A. Hartcorn H. Harty B. R. Hayward S. S. Jones D. C. Kaulitz A. R. Keene R. S. Kemper H. A. Kornberg G. A. Last R. D. Leggett D. C. Lehfeldt C. E. McNeilly J. E. Minor R. P. Nelson R. E. Nightingale (2) D. P. O'Keefe R. S. Paul L. T. Pedersen W. D. Richmond W. E. Roake R. K. Robinson

Battelle-Northwest (contd)

C. A. Rohrmann
F. M. Smith
R. C. Smith
J. C. Spanner
R. W. Stewart
H. A. Taylor
G. L. Tingey
J. C. Tverberg
E. E. Voiland
R. E. Westerman
R. G. Wheeler
E. T. Weber
O. J. Wick
D. C. Worlton
H. H. Yoshikawa
Patent Section (2)
Technical Information File (5)
Technical Publications (2)